UNIVERSITY OF NAPLES "FEDERICO II"

PH. D. PROGRAMME in MATERIALS and
STRUCTURAL ENGINEERING

COORDINATOR: PROF. DOMENICO ACIERNO

PH. D. DISSERTATION

NUMERICAL ANALYSIS ON THE DEBONDING OF FRP FLEXURAL REINFORCEMENT OF RC MEMBERS

Fiorenzo De Cicco

TUTORS
Dr. ANDREA PROTA
Dr. GIULIO ALFANO

to

my parents

ACKNOWLEDGMENTS

I want to express my deep thanks to my major teacher, Professor Cosenza, because there are no good students without good teachers. He has taught me the love for the research, and above all, the critical examination of a problem.

I would like to extend my deepest regards to Professor Manfredi for his valuable support and contributing to my growth.

I wish to thank my tutor, Andrea Prota for his constant assistance. I have learned a lot of things from his experience since my universities studies. I will keep all the experiences with him in my mind for ever. He has been for me an older brother in these three years.

I feel sincerely grateful to my tutor and friend, Giulio Alfano for having welcomed me when I was in London at Brunel University. He has been fundamental for drawing up this dissertation. His valuable teachings will be engraved in my mind for ever.

I wish to thank my friends and colleagues at the Department of Structural Engineering: they have contributed to enrich myself by sharing interesting discussions and by spending nice moments together; also my degree students Simona, Luigi and Antonio, and all my students who unfortunately have met me in this experience: thanks to them I have understood how is important and difficult to judge another person.

Finally, I want to express a thought of deep gratitude to my family for believing in me anytime, in particular to my sisters Francesca and Alessia, you are in my heart.

Heartfelt thanks to Roberta, my "fellow traveller", your closeness gives me a lot of energy.

Naples, November 2008 *Fiorenzo*

INDEX

INTRODUCTION

Fibre reinforced polymers (FRP) have been used for many years in the aerospace and automotive industries. In the construction industry they can be used for cladding or for structural elements in a highly aggressive environment. The application of fiber-reinforced polymers (FRP) to existing Reinforced Concrete (RC) structural elements as external reinforcement is become very frequent in the last years. For this reason a lot of researches are been devoted to this topic, together with the development of national and international guidelines containing reliable design procedures.

Strengthening of a structure can be required because of change in its use or due to deterioration. In the past, strength would be increased casting additional reinforced concrete or dowelling in additional reinforcement. More recently, steel plates have been used to enhance the flexural strength of members in bending (the so-called “beton plaquet”). These plates are bonded to the tensile zone of RC members using bolts and epoxy resins.

As an alternative to steel plates, FRP plates, generally containing carbon fibres, can be used. FRP can be convenient compared to steel for a number of reasons. They are lighter than the equivalent steel plates. They can be formed on site into complicated shapes. The installation is easier and temporary support until the adhesive gains its strength is not required. They can also be easily cut to length on site. Fibres are also available in the form of fabric. Fabrics are convenient instead of plates where round surfaces, like columns, need to be wrapped. Other advantages in using FRPs are the higher ultimate strength and lower density of such materials with respect to steel. The lower weight makes handling and installation significantly easier than steel. Works to the underside of bridges and building floor slabs can often be carried out from man-access platforms rather than full scaffolding.

The main disadvantage of externally strengthening structures with FRP materials are the risks of fire and accidental damage, and the extra-cost of the materials. A particular concern for bridges over roads is the risk of soffit reinforcement being ripped off by over height vehicles. Comprehensive knowledge of the long term effectiveness of this kind of intervention is not yet available. This may be perceived as a risk by some engineers and

owners. The materials are relatively expensive but generally the extra cost of the material is balanced by the reduction in labour cost. Very often, the failure mechanisms of RC beams retrofitted with FRP sheets are due to debonding of the covercrete with the attached laminate or to FRP debonding, because of an advanced deterioration of concrete substratum and an uncorrected application of FRP sheets on it. Debonding failure can occur in four different ways: in the concrete, in the bonding material, at the interface between bonding material and FRP sheets, and at the interface between concrete and bonding material. This last case is the most common and can be easily observed in the practical applications; typically it involves the laminate together with a thin layer of concrete or even with the whole covercrete which remain attached to the sheet.

Debonding could start either in the terminal zone of the FRP sheet, where the shear stresses are large, or in the proximity of flexural and combined shear/flexural cracks and propagates towards the end zones. This last typology is denoted as mid-span debonding failure. This implies that, in general, the capacity of a structural element reinforced with FRP is more influenced by the performance of the interface between concrete and external reinforcement rather than by the strength of the latter.

The subject of this dissertation is the numerical analyses of RC structural elements strengthened in the way described above; in particular the theoretical and numerical investigation of the interface behaviour between concrete and FRP external reinforcement and the role of the cracking of concrete in the mid-span debonding resulting in the premature failure, which is quite frequent in RC beams if the anchorage length of the FRP sheet is fairly proportioned.

For this purpose, the finite-element method has been chosen as a basic framework for the analyses.

In fact, due to the particularly complex behaviour of RC beams retrofitted with FRP sheets, use of refined finite-element analysis has been often made in the recent decade.

Some of them perform a sensitivity analysis with respect to various material and geometry parameters using a linearly elastic model, and obtain results

which are clearly valid only for serviceability conditions, and only when an initial crack pattern in concrete is not present.
In other finite-element models based on smeared cracked models, the overall behaviour of the retrofitted beam is well captured with such approaches, but the stress concentrations along the FRP/concrete interface induced by the presence of cracks in the concrete are not well predicted. Hence, these methods are not well suited to reproduce the mid-span debonding failure. Detailed results for a finite-element models based on the discrete-crack approach are also available in literature.
The analysis have been carried out by using the finite element code ABAQUS, widely used in both the scientific research and the industrial design. However, it has not been developed an enhanced solver because the basic idea was to make use of the algorithms currently available in the ABAQUS.
The finite-element analysis of RC structures can be carried out using several models according to the purpose of the research and the size of the control volume relevant for the specific application. For example the analysis could be either used to calculate the deflections on the whole structure under a given loading condition or to investigate the local effects in a particular area of the structure. In the first case we can adopt a model that describes the overall stiffness of the reinforced concrete, either cracked or not, while in the second case we may find convenient to understand where the cracking will occur, how it will develop and to compute the distribution of stresses between concrete and steel and concrete and FRP. In general the overall behaviour of a structure can be successfully investigated using structural elements such as beams, shells, trusses. Their use will limit the computational onus and simplify the definition of the structure. When it comes to investigate a reduced volume of a bigger structure, solid elements combined if necessary with structural elements are more appropriate. This is the case for our analyses as the focus is on what happen within a single structural element.
The main structural material for the systems under investigation is concrete. Concrete gives a defined shape to the structural elements and the loads are, in fact, applied directly to the concrete. The standard and FRP

reinforcement, although essential, are auxiliary components. Correct modelling of the nonlinear behaviour of concrete is therefore essential. The mechanical behaviour of concrete has been investigated worldwide and today there is a general agreement among researchers on its characteristic properties. The most sophisticated ones include elasto-plastic constitutive laws with complex hardening laws, non-associative flow-rules, post yielding softening.

However these models can not be easily used within a finite-element code and simplified models have been developed to take into account only the particular aspects relevant to each specific application.

Several ABAQUS material models have been tested for modelling of plain concrete. The model adopted in this study is an advanced elasto-plastic isotropic constitutive models with a yielding criterion dependent upon the first and second invariants of the stress tensor with kinematic and isotropic hardening. Isotropy implies that the yield function depends only on either two invariants of the stress tensor. However, other more sophisticated materials, contains also the dependence upon the third stress invariant. The dependence upon the third invariant of yield functions suitable for concrete introduces further complications. As reported in Chapter III, the applications presented in this study are based on the Lubliner et al. yield criterion for concrete, with the modifications introduced by Lee and Fenves. In particular, as the confining stresses increase, the shape of the Lubliner et al. yield surface in the deviatoric plane changes from triangular to circular, in accordance with the experimental results. The criterion depends upon four parameters which can be specialized to obtain other criteria such as Huber-Mises, Drucker-Prager, Rankine, Mohr-Coulomb, which are available in the ABAQUS material library.

A very important aspect in the modelling of RC beams retrofitted with FRP is the representation of the interfacial behaviour between the different materials. Correct modelling of the interface FRP/concrete is necessary as debonding of the FRP is a typical failure mode for these systems. Moreover debonding is affected by cracking of concrete. To allow the cracks to open it is necessary to model relative displacements between concrete and reinforcement. This is possible by mean of special interface in conjunction

with a non-linear constitutive model available for this kind of elements, which belong to the class of cohesive-zone model.
Starting from a brief description on the fundamentals of Linear Elastic Fracture Mechanics (LEFM), the main cohesive-zone approaches and existing closed-form models for the modelling of FRP/concrete and steel bars/concrete interface behaviours will be reported in Chapters IV and V.
The behaviour at the interface, as mentioned, is strongly influenced by the localization of stresses due to cracking or interruption of the composite at the end of the plates. Because cracking is important in the analysis of the RC beams retrofitted with FRP, it has to be conveniently included in the models. All the models based on a uniform distribution of cracks (smeared) within a volume of cracked concrete are not dealt with in this dissertation. It is only interesting to underline that in this approach cracking is reduced to a constitutive problem. Basically the cracks are modelled by a sudden local stiffness loss in a band of a width comparable with the crack width.
For applications to RC beams retrofitted with FRP, the local effects at the interfaces are critical and the modelling must feature discrete cracking. The problem has been tackled by inserting preset cracks in the finite element mesh. This approach is justified as the crack pattern of the beams investigated was known from experiments and as the main focus was rather on the interfacial behaviour between FRP and concrete than on the onset and propagation of cracking.
In Chapter VII, the numerical results obtained by performing numerical non-linear analyses on the two-dimensional finite-element models developed in ABAQUS and based on a discrete-crack approach will be compared with the results inherited from a previous experimental campaign on RC beams retrofitted with FRP tested up to failure.
The experimental campaign, which have not yet be published, was conducted in the laboratory of the Department of Structural Engineering of University of Naples “Federico II” within the research project “New cohesive-zone models and solution algorithms for the numerical analysis of delamination and decohesion problem” funded by Regione Campania (Legge 5/2002). The experimental tests consist in carrying out a four point

bending on RC beams, with different geometrical dimensions and type of steel reinforcement.

The current guidelines for the design of this type of strengthening works tend to extend the principles for the design of standard RC elements to the case of FRP retrofitted ones: in fact, it is widely accepted that the conventional RC theory, in the case of full composite action, for the ultimate limit state analysis can be easily applied by simply adding the composite as additional resisting element in traction. However, when failure occurs because the adhesion between composite and FRP is lost, either in proximity of vertical/inclined cracks or at the end of the composite laminate, the codes of practice propose different analytical models based on the extensive research done in the last two decades. The proposed models all involve different types of approximation and often different proposed methods yield quite different results. For this reason, the results of analytical calculations based on the models proposed in the main codes of practice will be presented in Chapter VIII and will provide a further element of comparison and discussion with the experimental and numerical results.

The principal aims of this dissertation can be summarized in the follows:

- showing that, despite some simplified assumptions made, the model is able to well capture, both qualitatively and quantitatively, the structural response of RC beams retrofitted with FRP laminates, in particular the post-peak behaviour of the reinforced beams;
- highlighting the importance of accounting for the cracks in order to well capture the stress concentrations at the concrete/steel and concrete/FRP interfaces;
- showing that the use of a simple bilinear cohesive-zone model for the modelling of nonlinear behaviour of the above mentioned interfaces can effectively predict the mid-span debonding failure, in the proximity of localized cracks
- show the effectiveness of the proposed methodology of analysis through the ability of the model to numerically reproduce the available experimental results in order to capture those kind of information, which are not easily measurable experimentally, like the interface-stress profile or the stress-strain fields within reinforced beams.

CHAPTER II
The USE of FRP for the RETROFITTING of RC STRUCTURES

2.1 INTRODUCTION

Fibre reinforced polymers (FRP) have been used for many years in many high tech fields such as the aerospace, navy and automotive industries. In the construction industry they have been used and tested for the first time in the ’80 at the Swiss Federal Laboratory for Materials Testing and Research (EMPA) as a new strengthening of structural elements in an highly aggressive environment. These materials are now becoming popular mostly for the strengthening of existing structures.

The upgrading of existing civil engineering infrastructure has been an issue of great importance for over a decade. Deterioration of bridge decks, beams, girders and columns, buildings, parking structures and others may be attributed to ageing, environmentally induced degradation, poor initial design and/or construction, lack of maintenance, and to accidental events such as earthquakes. Frequently, the infrastructure’s increasing decay needs the upgrading, so that structures meet more stringent design requirements (i.e., increased traffic volumes in bridges exceeding the initial design loads). The civil engineering infrastructure renewal has received considerable attention over the past few years throughout the world. At the same time, seismic retrofit has become as important as infrastructure renewal, especially in areas of high seismic risk. Strengthening of a structure can be required for:

- the growth of loads as well as dead or live load (change of the use of building) or traffic load of a bridge,
- structural damage due to corrosion of the bars in RC and deterioration of concrete,
- structural damage due to exceptional events as explosions, fire and crashes,
- changes of the structural system,

- design or fabric flaw,
- the need to reduce tensions, deformations or crack spacing,
- increasing of ultimate strength and of rigidity.

In the past, the strength was increased casting additional reinforced concrete or dowelling in additional reinforcement or using the technique of "Betòn plaque" (steel plates bonded to the tensile zone of RC members using bolts and epoxy resins to enhance the flexural strength of members in bending).
FRP plates, generally containing carbon fibres, can be used as an alternative to steel plates.
Fibre reinforced polymers can be compared to steel for a number of reasons:

- they are lighter than the equivalent steel plates,
- they can be formed on site into complicated shapes,
- the installation is easier and temporary support until the adhesive gains its strength is not required,
- they can also be easily cut to length on site,
- fibres are also available in the form of fabric, which are convenient instead of plates where round surfaces, like columns, need to be wrapped.

The materials are relatively expensive but generally the extra cost of the material is balanced by the reduction in labour cost.
There are a lot of advantages in using FRP:

- these materials have higher ultimate strength and lower density than steel;
- the lower weight makes handling and installation significantly easier than steel,
- works to the underside of bridges and building floor slabs can often be carried out from man-access platforms rather than full scaffolding;

The quality of the workmanship is essential in this strengthening technique.
The main disadvantage of externally strengthening structures with FRP materials are the risks of fire and accidental damage and the few knowledge of the effect of periodical strain.
The most application fields of FRP as strengthening tool are shown in Figure 2.1.1:

- flexural strengthening of RC beams or plates and masonry wall,

- shear strengthening of RC beams and masonry wall,
- confinement of RC or masonry columns.

Composite materials for strengthening of civil engineering structures are available today mainly in the form of:

- thin unidirectional strips (with thickness in the order of 1 mm) made by pultrusion
- flexible sheets or fabrics, made of fibres in one or at least two different directions, respectively (and sometimes pre-impregnated with resin).

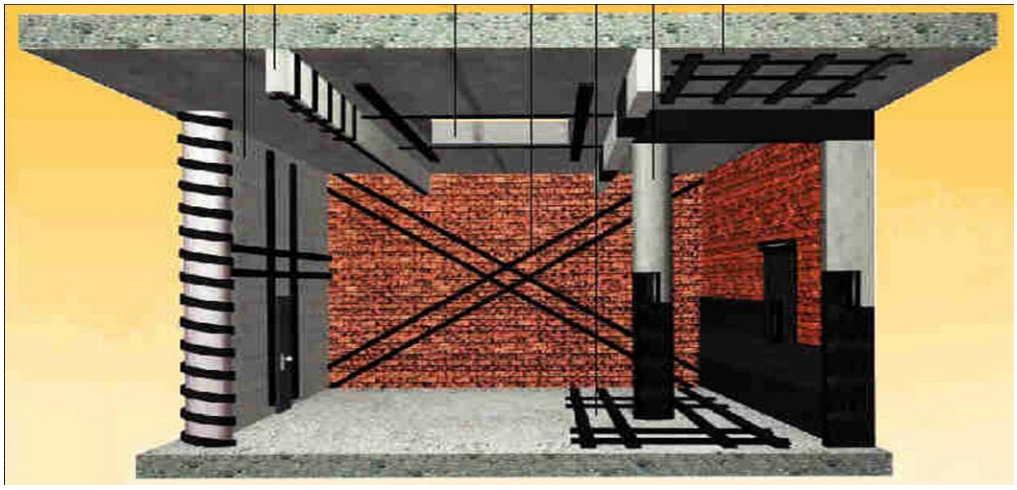

Figure 2.1.1: Typical applications of FRP in the strengthening of RC structures

Figure 2.1.2 shows typical stress-strain diagrams for unidirectional composites under short-term monotonic loading compared to steel.

Composites suffer from certain disadvantages which are not to be neglected by engineers: contrary to steel, which behaves in an elasto-plastic manner, composites in general are linear elastic to failure (although the latter occurs at large strains) without any significant yielding or plastic deformation, leading to reduced ductility.

Additionally, the cost of materials on a weight basis is several times higher than steel's cost (but when cost comparisons are made on a strength basis, they become less unfavourable).

Moreover, some FRP materials, i.e. carbon and aramid, have incompatible thermal expansion coefficients with concrete. Finally, their exposure to high temperatures (e.g. in case of fire) may cause premature degradation and collapse (some epoxy resins start softening at about 45-70 °C, the corresponding temperature is named "glass transition temperature").
The FRP materials should not be thought as a blind replacement of steel (or other materials) in structural intervention applications. Instead, the advantages offered by them should be evaluated against potential drawbacks, and final decisions regarding their use should be based on consideration of several factors, including not only mechanical performance aspects, but also constructability and long-term durability.

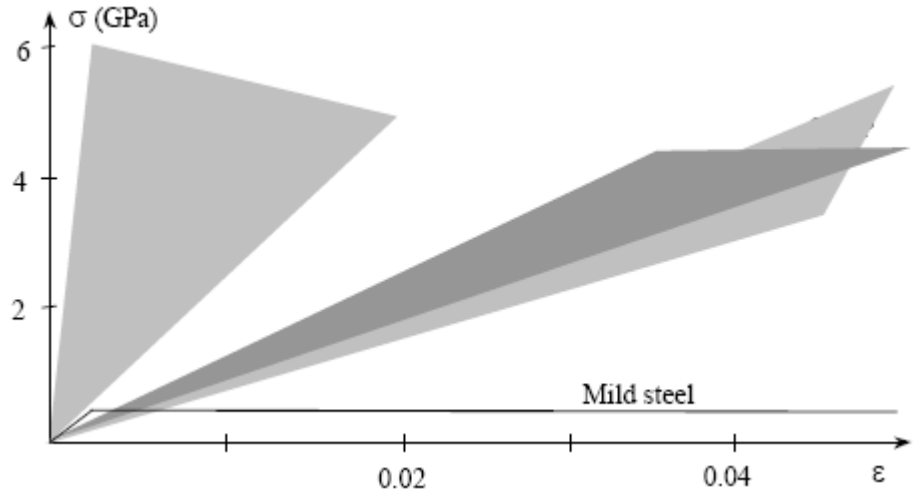

Figure 2.1.2: Uniaxial tension stress-strain diagrams for different unidirectional FRPs and steel (CFRP = carbon FRP, AFRP = aramid FRP, GFRP = glass FRP)

2.2 MATERIALS

Composites materials are formed of two or more materials (phases) of different nature and macroscopically distinguishable. In fibre composites the two phases are high performance fibres, and an appropriate resin.

The mechanical properties of the composites mainly depend on the type, amount and orientation of the fibres. The role of resin is to transfer stresses to and from the fibres. It also provides some protection from the environment.
This section provides a general introduction on the fibres and resins used for strengthening. Further information can be found in the trade literature.

2.2.1 Fibres

Fibres typically used for strengthening applications are glass, carbon, or aramid (also known as Kevlar).
Typical values for the properties of fibres are given in Table 2.2.1. These values are for the fibres only and the correspondent values for the composite are significantly lower. All the fibres are linear elastic to failure with no significant yielding.
The selection of the type of fibre to be used for a particular application will depend on factors like the type of structure, the expected loading, the environmental conditions, etc.

Table 2.2.1. Typical fibre properties.

Fibre	Tensile strength [MPa]	Modulus of elasticity [GPa]	Elongation [%]	Specific density
Carbon: high strength	4300-4900	230-240	1.9-2.1	1.80
Carbon: high module	2740-5490	294-329	0.7-1.9	1.78-1.81
Carbon: ultra high module	2600-4020	540-640	0.4-0.8	1.91-2.12
Aramid	3200-3600	124-130	2.4	1.44
Glass	2400-3500	70-85	3.5-4.7	2.60

Carbon fibres are used for high performance composites and are characterised by high value of stiffness and strength but they are not very sensible to creep and fatigue and exhibit negligible loss of strength in the long term.

These fibres have a crystalline structure similar to graphite's one. Graphite's structure is hexagonal, with carbon atoms arranged in planes held together by Van Der Waals forces.
Atoms in each plane are held together by covalent bonds, much stronger than Van Der Waals forces, resulting in high strength and stiffness in any direction within the plane.
The modern technology of production of carbon fibres is based on the thermal decomposition in absence of oxygen of organic substances, called precursors. The most popular precursors are polyacrilonitrile and rayon fibres. Fibres are stabilised first, through a thermal treatment inducing a preferential orientation of their molecular structure, then they undergo a carbonisation process in which all components other than carbon are eliminated. The process is completed by a graphitization during which, as the word indicate, the fibres are crystallised in a form similar to graphite.
Fibres with carbon content higher than 99% are sometime called graphite fibres.
Aramid fibres are organic fibres, made of aromatic polyamides in an extremely orientated form. Introduced for the first time in 1971 as "Kevlar", these fibres are distinguished for their high tenacity and their resistance to manipulation. They have a strength and stiffness between glass and carbon fibres. Their compression strength is usually around 1/8 the tensile one. This is due to the anisotropy of the structure of the fibre, because of which compression loads trigger localised yielding and buckling resulting in the formation of kinks. This kind of fibres undergoes degradation under sunlight, with a loss of strength of up to 50%. They can also be sensitive to moisture. They exhibit creep and are fatigue sensitive.
The technology of fabrication is based on the extrusion at high temperature of the polymer in a solution and subsequent rapid cooling and drying. The synthesis of polymer is done before the extruding equipment by using very acid solutions. It is finally possible to apply a thermal orientation treatment to improve the mechanical characteristics.
Glass fibres are widely used in the naval industry for the fabrication of composites with medium to high performance. They are characterised by high strength. Glass is made mainly of silica (SIO_2) in thetrahedrical

structure (SIO_4). Aluminium and other metal oxides are added in different proportions to simplify processing or modify some properties. The technology of production is based on the spinning of a batch made essentially of sand, alumina and limestone. The components are dry mixed and melted at 1260 ^oC. Fibres are originated from the melted glass. Glass fibres are less stiff than carbon and aramid fibres and are sensitive to abrasion. Due to the latter care must be used when manipulating fibres before impregnation. This kind of fibres exhibit non negligible creep and are fatigue sensitive.

2.2.2 Fabrics

Fabrics are available in two basic forms:

- Sheet material, either fibres (generally unidirectional, though bi-axial and tri-axial arrangements are available)on a removable backing sheet or woven rovings,
- Fibres pre-impregnated with resin ("prepreg" material), which is cured once in place, by heat or other means.

The selection of the appropriate fabric depends on the application.
The properties of the sheet materials depend on the amount and type of fibre used. An additional consideration is the arrangement of fibres; parallel lay gives unidirectional properties while a woven fabric has two-dimensional properties.
In woven fabrics, perhaps 70% of the fibres are in the 'strong' direction and 30% in the transverse direction. It should be noted that the kinking of the fibres in the woven material significantly reduces the strength.
The thickness of the material can be as low as 0.1 mm (with the fibres fixed to a removable backing sheet) and is available in widths of 500 mm or more.

2.2.3 Plates

Unidirectional plates are usually formed by the pultrusion process. Fibres in the form of continuous rovings are drawn off in a carefully controlled pattern through a resin bath which impregnates the fibres bundle. They are then pulled through a die which consolidates the fibres-resin combination

and forms the required shape. The die is heated which sets and cure the resin, allowing the completed composite to be drawn off by reciprocating clamps or a tension device. The process enables a high proportion of fibres (generally about 65%) to be incorporated in the cross section. Hence in the longitudinal direction, relatively high strength and stiffness are achieved, approximately 65% of the relevant figures in Table 2.1.1. Because most, if not all, of the fibres are in the longitudinal direction, transverse strength will be very low.

Plates formed by pultrusion are 1-2 mm thick and are supplied in a variety of widths, typically between 50 and 100 mm. As pultrusion is a continuous process, very long lengths of material are available. Thinner material is provided in the form of a coil, with a diameter of about 1 m. It can be easily cut to length on site using a common guillotine. Plates can also be produced using the prepreg process, which is widely used to produce components for the aerospace and automotive industries. Typically plates have a fiber volume fraction of 55 %, and can incorporate 10% fibres (usually glass aligned at an angle of 45o to the longitudinal axis) to improve the handling strength.

Lengths up to 12 m can be produced, with a thickness being tailored to the particular application. Widths up to 1.25 m have been produced and thickness up to 30 mm.

2.2.4 Resins

The most popular types of resins used for the production of FRP are polymeric thermo-hardening resins. These are available in a partially polymerised form and are liquid or creamy at ambient temperature. Mixed with an appropriate reagent they polymerise until they become a solid glassy material.

Because the reaction can be accelerated heating up the material, these resin are also termed thermo-hardening resins.

The advantages of their use are:

- low viscosity at the liquid state resulting in easy of fibre impregnation;

- very good adhesive properties, the availability of types capable of polymerising at ambient temperature;
- good chemical resistance;
- absence of a melting temperature.

The principal disadvantages, are, on the other hand, related to the range of serviceability temperatures, with an upper limit given by the glassy transition temperature, brittle fracture properties and moisture sensitivity during application.

The most common resins used in the field of civil engineering are epoxy resins. In some cases polyester or vinyl resins can be used. If the matrix is mixed with the fibres on site (if fabrics are used) specialist contractors should be appointed.

Polymeric materials with thermo-plastic resins are also available. The have the advantage the can be heated up and bent on site at any time. These materials are more convenient for the production of bars to be embedded in concrete like ordinary reinforcement.

Epoxy resins have good resistance to moisture and to chemicals. Besides, they have very good adhesive properties. Their maximum working temperature is depends on the type but is typically below 60 ^{o}C. However epoxy resins with higher working temperatures are available. Usually there are no limits on the minimum temperature.

The main reagent is composed by organic liquids with low molecular weight containing epoxy groups, rings composed by two atoms of carbon and one atom of oxygen.

The pre-polymer of the epoxy is a viscous fluid, with a viscosity depending on the degree of polymerisation. A polymerising agent is added to the above mix to solidify the resin. This can be done at low or high temperatures depending on practicalities and on the final properties desired.

Polyester resins are characterised by a lower viscosity compared to epoxy resins. However, chemical resistance and mechanical properties are not as good as for epoxy. Polyesters are polymers with high molecular weight with double bonds between carbon atoms C=C, capable of reacting chemically. At ambient temperature the resin is usually solid. To be used, a solvent must

be added. The latter also reduces the viscosity of the resin and facilitates the impregnation of the fibres.
The reaction is exothermal and does not generate secondary products.
Solidification can happen at low or high temperatures depending on practicalities and on the final properties desired.
The intrinsic limits of thermo-hardening resins, described above (in particular the limited tenacity), the low service temperatures and the tendency to absorb moisture from the environment, have lead in recent years to the development of thermo-plastic resins.
These resins are characterised by their property of softening when heated up to high temperatures. The shape of the components can be, therefore modified after heating.
Even though their use in the civil engineering field is quite limited at the moment, their use has been proposed for the production of reinforcement bars similar to the ordinary steel ones. They have higher tenacity than epoxy and polyester resins and generally can withstand higher temperatures. Besides they are more resistant to environmental agents.
The main limitation for their application is the high viscosity that renders difficult the impregnation of the fibres.
There are also special resins developed for aggressive environment and high temperatures. They are mainly vinyl-ester resins with intermediate properties between polyester and epoxy resins.
Finally, inorganic matrices can be used; these can be cementitious, ceramic, metallic etc. Their use in civil engineering, though, pertain areas other than the retrofitting of structural elements.

2.3 EXPERIMENTAL BEHAVIOUR of RC BEAMS RETROFITTED with FRP

The role of the composite in retrofitted structures is similar to that of ordinary steel reinforcement. The composite enhances both the stiffness and the strength of the structural elements.

Methods of analysis for ordinary RC can be easily generalised to include FRP reinforcement. Accordingly the gain in the structural capacity of the strengthened structure is generally significant. However researchers have observed that the real capacity is limited by modes of failure not observed in ordinary RC structures. These failures are often brittle, involving delamination of the FRP, debonding of concrete layers, and shear collapse. Failure can occur at loads significantly lower than the theoretical strength of the retrofit system. Specific failure criteria are therefore required for the analysis of these structures. To set these out a thorough understanding of the behaviour of these systems is required. Until now we have referred to structural elements in general.

2.3.1 Failure modes of RC beams externally reinforced with FRP

Failure modes of RC beams retrofitted with FRP fall into six distinct categories (Figure 2.3.1). The mode of failure marked as a) in Figure 2.3.1 is characterised by yielding of tensile steel followed by rupture of the FRP.
This is a brittle failure due to the brittle nature of the FRP rupture but in this case the material is used at its maximum capacity and the failure load can be accurately predicted using strain and stress compatibility equations.
For the mode marked as b) the failure is due to the crushing of concrete in compression. In this case the maximum failure load can be accurately predicted too. Failure is still brittle.
The mode marked as c) is a shear failure mode. A shear crack initiating usually at the tip of the FRP sheets propagate until the beam fails. Failure often occurs when the laminate detaches from the beam ceasing to contribute to its strength. Failures of this type are marked as d) and e) in Figure 2.3.1. In case d), known as bond split, the entire cover-concrete is ripped off. This generally happen by formation of a shear crack that propagate along the line of the reinforcement. In case e), known as laminate peeling, the laminate detaches because of the formation and propagation of a fracture along the interface with the concrete.

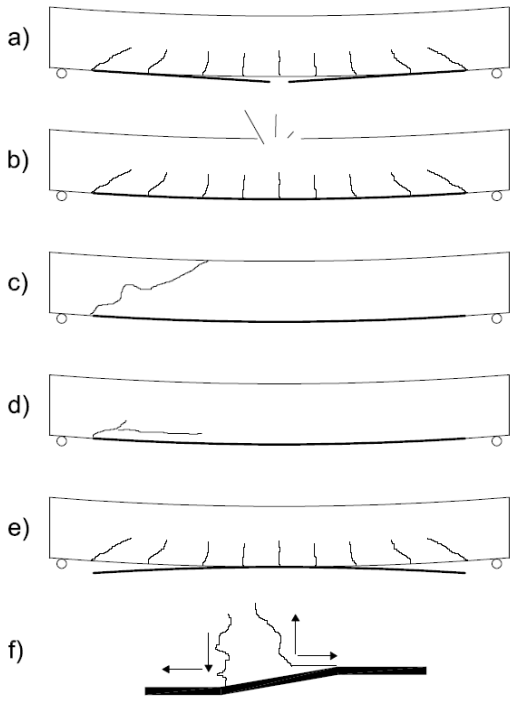

Figure 2.3.1: Failure Modes in FRP Retrofitted Concrete Beams

The fracture at the interface is usually a cohesive fracture within the concrete adjacent to the epoxy. This is usually because epoxy is stronger than concrete. In this case the same material is visible on both the fracture surfaces. The fracture can also be an adhesive fracture at the interface between epoxy and concrete. In this case the materials visible on the two fracture surfaces are different. This happens when the face of the concrete has not been properly treated before the application of the epoxy.
The fracture could also be at the interface epoxy/FRP for similar reasons.
A mixed type of fracture with irregular surfaces and both the materials visible on both the fracture surface is also possible.
Laminate peeling can initiate at the tip of the laminate (end peeling) where the stiffness of the section changes and tensile forces are transferred into the laminate. Stresses at this location are essentially shear stresses but due to the little but non zero bending stiffness of the laminate, and the eccentric

application of the tensile force, normal stresses can arise, activating also mode I delamination (Figure 2.3.2).

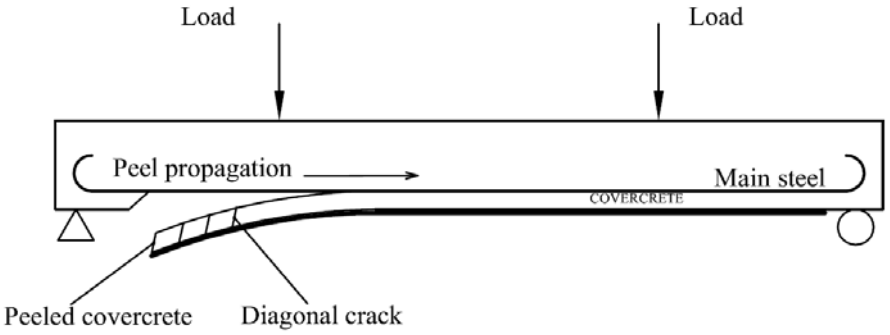

Figure 2.3.2: End peeling failure mode

Whereas end peel involves the entire depth of covercrete and propagates from the ends of the plates inwards, another debonding mode exists that fractures, in the main, only part of the depth of covercrete and initiates at the toes of flexural cracks in the mid-span region of the beam with propagation out to the ends of the plates. This latter mode, termed mid-span debonding, is illustrated in Figure 2.3.3 for one initiating flexural crack. As shown in Figure 2.3.3 (a), the delaminated concrete, adhesive, and plate remain a single unit after debonding, with the remaining covercrete staying an integral part of the original beam. There are two phases to mid-span debonding process, namely the initiation phase, inclined cracks form in the covercrete near the toes of flexural cracks Figure 2.3.3 (b) shows that opening of these inclined cracks induces local bending (or dowel actions) of the plate, thereby causing the plate to exert a vertical pull on the adjacent adhesive and covercrete to one side of the inclined crack. This pull eventually fractures a thin layer of cover-concrete along a roughly horizontal plane.

Note that since the FRP plates used in strengthening applications are typically very thin, the plates are quite flexible under bending in a vertical

plane. Hence, propagation of mortarcrete fracture away from the base of the inclined crack due to this local bending action is limited.
During the second phase, the debonding process is a self propagating mechanism of development of vertical stresses near ends of plate. The length of the mortarcrete fracture zone along the beam increases first in a stable, incremental manner with each subsequent increment of load on the beam. Eventually, the mortarcrete fracture process suddenly runs along the remaining bonded length of plate, resulting in complete unzipping of the plate from the beam. The energy released by unzipping is sometimes sufficient to dislodge from the beam the wedges of concrete bounded by the inclined crack and flexural cracks.

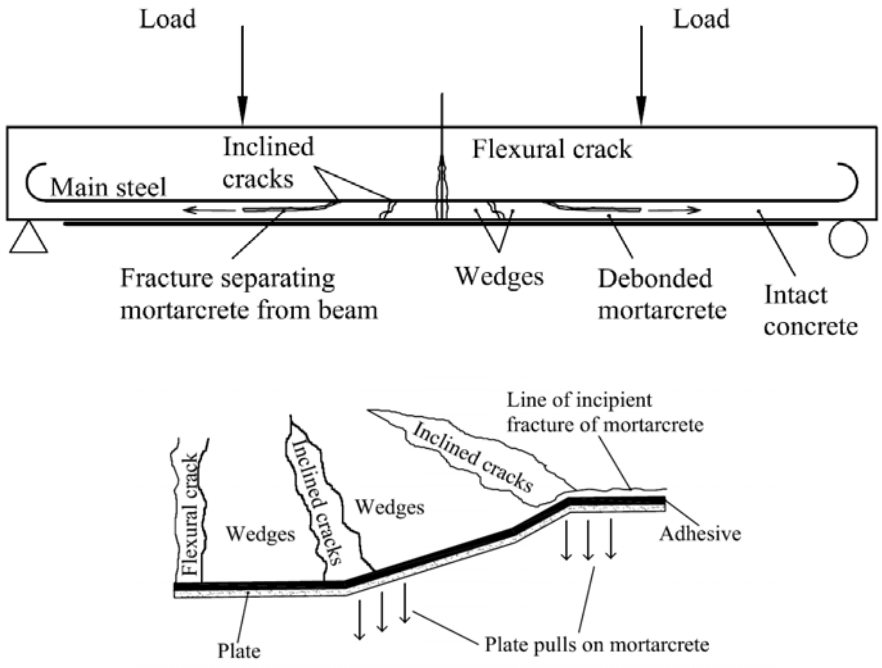

Figure 2.3.3: Mid-span debonding: mode of failure and dowel effect in plate

Besides the failure types commonly observed in ordinary RC beams, retrofitted beams can fail because transfer of forces between the composite

and the concrete is not possible beyond a certain limit and the two structural components separate causing the FRP cease to be effective.
This mode of failure introduces a great deal of complication into the problem because its associated failure load is much more difficult to predict than those associated with crushing of concrete or rupture of the retrofit material.
Even though, with reasonable accuracy, the problem of the interface can be locally cast into a simple set of equations, considerable difficulties arise in the treatment of this aspect due to the influence of cracking of concrete in tension that continuously alter the boundary conditions. Because of this, failure due to FRP detachment cannot be dealt with by a local stress or strain check at a certain cross section of the beam but requires analysis of the structural element as a whole.
As far as mid-span debonding is concerned, currently available guidelines try to overcome this difficulty in a simplified manner introducing a limit on the maximum working strain of the composite as a failure criterion to be added to the usual check of the maximum compressive strain in the concrete (0.35%), maximum tensile strain in the steel (1%) and maximum stress in the FRP. The maximum tensile strain in the concrete to be used in the check at a given section is the one derived imposing the equilibrium at that section considering perfect adherence between the different materials and the concrete as a no tension material.
Even if this principle makes the check conservative, it is obviously somewhat coarse and provides little understanding of the behaviour of the system.
Also delamination in the terminal zones of FRP is to be addressed. The typical approach derived by the practice for ordinary reinforced concrete is to make sure that the plates have enough anchorage length to transfer the axial forces from the concrete to the FRP.
This approach suffers from two major shortcomings:

- differently from ordinary bars, the maximum force that can be transferred into the FRP plates does not increase indefinitely with increasing anchorage length but reaches a maximum at a specific length and than does not increase anymore,

- the effects of the local distribution of stresses are much more important than in the case of the anchorage of ordinary bars.

The behaviour at the interface between the different materials in an RC beam retrofitted with FRP, being to a certain extent an element of novelty with respect to ordinary RC, will be widely analysed in the following chapters.

This will require the abandonment of the concept of the section and in general of the beam as opposed to the general solid.

CHAPTER III
CONCRETE MODELLING

3.1 INTRODUCTION

Concrete is a heterogeneous, cohesive-frictional material and exhibits complex non-linear inelastic behaviour under multi-axial stress states. The increased use of concrete as primary structural material in building complex structures such as reactor vessels, dams, offshore structures, etc., necessitates the development of sophisticated material models for accurate prediction of the material response to a variety of loading situations.

Concrete contains a large number of micro-cracks, especially at the interface between aggregates and mortar, even before the application of the external load. Many theories proposed in the literature for the prediction of the concrete behaviour such as empirical models, linear elastic, nonlinear elastic, plasticity based models, models based on endochronic theory of inelasticity, fracturing models and continuum damage mechanics models, micromechanics models, etc. Some of them will be discussed in this sections.

There exist an incredible amount of models for concrete. Although the physical properties of the material are relatively well established, regularly, researchers develop new variants of existing models. Available models are usually tailored around a specific application.

There are two basic approaches to nonlinear modelling of concrete: finite (or total) material characterization in the form of secant formulation and incremental (or differential) models in the form of tangential stress-strain relations. Finite constitutive equations of the first category are restricted to path-independent, reversible processes causing a uniqueness problem in the case of non-proportional loading. The most prominent models of this class are hyperelastic formulation and the deformation theory of plasticity. In contrast, differential or incremental material descriptions of the second category do not exhibit the shortcomings of reversibility and path

dependency. The most prominent models of this class are hyperelastic models and models based on the flow theory of plasticity.
There are also models based on elastic degradation in the form of continuum damage mechanics.

3.2 EXPERIMENTAL BEHAVIOUR

Concrete is a composite material mainly consisting of different sized aggregate particles embedded in a cement past matrix and its mechanical behaviour is strongly affected by the microstructure properties. In order to give physical explanations to the experimental behaviour observed during tests, the knowledge of microstructure becomes fundamental. The main aspects to consider:

1. A large number of bond micro cracks exist at the interface between coarser aggregates and mortar;
2. The cement paste has a high porosity, the pores being filled with water or air;
3. At all dimensional levels, above the molecular level, air and or water voids exists.

Many of the microcracks in concrete are caused by segregation, shrinkage or thermal expansion in the mortar and therefore exist even before any load has been applied. Some of the microcracks can be developed during loading because of the difference in stiffness between aggregates and mortar.
Therefore, the aggregate-mortar interface constitutes the weakest link in the composite system. This is the primary reason for the low tensile strength of concrete materials.
For example the propagation of micro cracks during loading contributes to the non linear behaviour of concrete at low stress levels and causes volume increases near failure and uniaxial compressive state of stress. For high hydrostatic pressure the intrusion of voids and paste pores becomes increasingly important in affecting the behaviour and strength of concrete.
Thus, in order to create an appropriate mathematical model it is essential to understand the behaviour of plain concrete under uniaxial, biaxial and

triaxial states of stress. Typical tests results are illustrated in the next paragraph and they all refer to normal weight concrete under short term quasi-static loading conditions.

3.2.1 Uniaxial compressive behaviour

Results from uniaxial compression tests are generally represented as stress strain curves as shown in Figure 3.2.1. The shape of stress strain curves is similar for low-, normal-, and high-strength concretes as shown in Figure 3.2.2.

The key observations are :

1. The concrete behaviour is nearly linear elastic up to about 30% of its maximum compressive strength f'_c. For stresses above $0.3f'_c$ concrete begins to soften and the stress-strain curve shows a gradual increase in curvature up to about $0.75f'_c$ to $0.9f'_c$, after which the curve bends more sharply until it approaches the peak point at f'_c. Beyond this point the curve has a descending part until crushing failure occurs at some ultimate strain value ε_u (Figure 3.2.1);

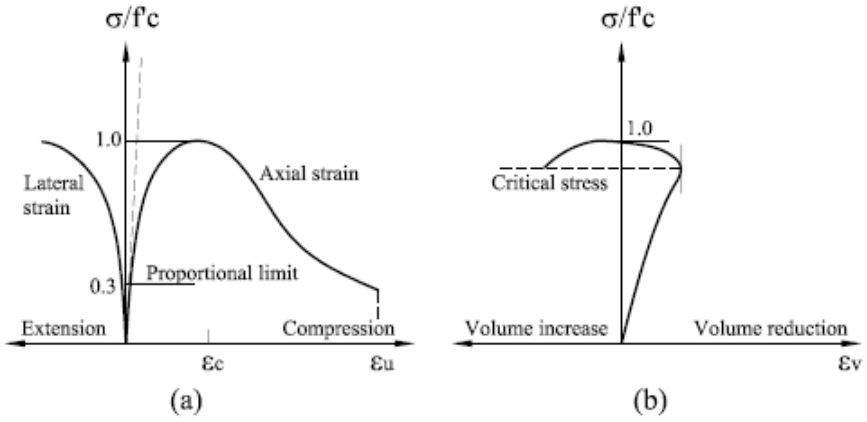

Figure. 3.2.1: Typical stress-strain curves for concrete in uniaxial compression test. (a) Axial and lateral strains. (b) Volumetric strain ($\varepsilon_v = \varepsilon_1 + \varepsilon_2 + \varepsilon_3$)

2. The volumetric strain $\varepsilon_v = \varepsilon_1 + \varepsilon_2 + \varepsilon_3$ is almost linear up to about $0.75f'_c$ to $0.9f'_c$. At this point the direction of the volumetric strain is reversed and the material starts dilating (Figure 3.2.1). The stress corresponding to the minimal volumetric strain is defined as critical stress [Richart et al. 1929];
3. Concrete with higher strength behave as linear to a higher stress level than low strength concrete, but seems to be more brittle on the descending portion of the stress strain curve. All peak point correspond approximately to a value of 0.002 (Figure 3.2.2).

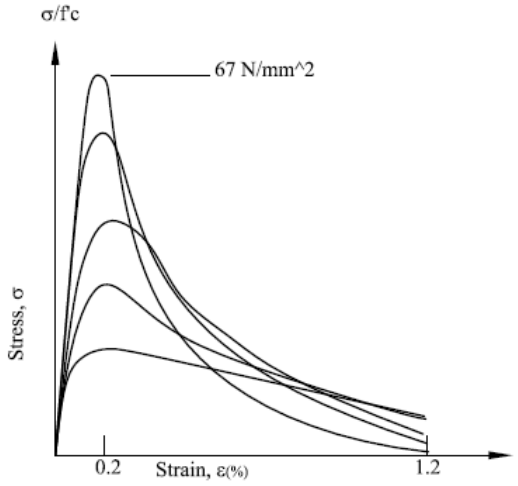

Figure 3.2.2: Uniaxial compressive stress-strain

The first two points are associated with the mechanism of internal progressive micro cracking. When the stress is still in the region of $0.3f'_c$ the internal energy is not sufficient to create new micro crack surfaces and the cracking existing in the concrete before loading remain nearly unchanged.

The stress level corresponding to $0.3f'_c$ has been defined as onset of localized cracking and has been proposed as the limits of elasticity [Kotsovos & Newman 1977]. For stress between 30 and 50 % of f'_c the bond cracks start to extend because of the stress concentration at the crack

tips. Mortar cracks remain negligible and the available internal energy is approximately balanced by the required crack release energy. At this stage the crack propagation is stable in the sense that cracks rapidly reach their final lengths, if the applied stress is maintained constant.
For the next stress range 50-70 % of f'_c some cracks at nearby aggregates surfaces start to bridge in the form of mortar cracks. Meanwhile other bond cracks keep growing. If the load is maintained constant the crack continue to propagate with a decreasing rate to their final lengths.
For higher stress levels the system is unstable and complete disruption can occur even if the load is maintained constant. Microcracks through the mortar in the direction of the applied stress bridge together the bond microcracks at the surface of the nearby aggregates and form macroscopic cracks. This stage correspond to the descending portion of the concrete stress-strain curve (softening). The stress level of about $0.75f'_c$ is termed as "onset of unstable fracture propagation" or "critical stress" since it corresponds to the minimum value of the volumetric strain ε_v.
The initial modulus of elasticity E_0 is generally correlated to the uniaxial compressive strength and can be approximated with the empirical formula:

$$E_0 = 5700\sqrt{f'_C}\, N/mm \qquad (3.2.1)$$

which gives a reasonable accuracy. The poissons ratio ν also varies with the compressive strength f'_c, with 0.19 or 0.20 being representative values.

3.2.2 Uniaxial tensile behaviour

The stress-strain curves for uniaxial tension tests are similar in shape to those observed for uniaxial compression (Figure 3.2.3).
However the tensile strength f'_t is significantly lower than the corresponding strength in compression f'_c, with a ratio of 0.05-0.1. The concrete behaviour is nearly linear elastic up to about 60% of its maximum tension strength f_{0t}. The following interval of stable crack propagation is very short and the system becomes unstable around $0.75f'_t$.

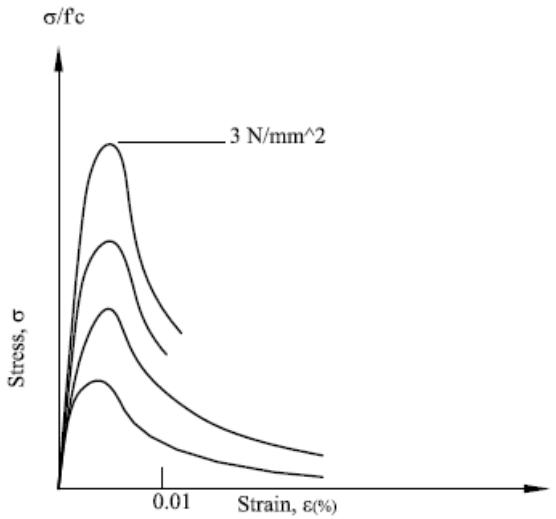

Figure 3.2.3: Typical tensile stress-strain curves for concrete

The direction of cracks propagation is transversal to the applied stress direction. The descending portion of the stress-strain curve is difficult to follow because the crack propagation is very rapid. The value of f'_t is difficult to measure experimentally and there are several formulae to estimate it from the corresponding value of the compression strength.
The modulus of elasticity and the poissons ratio under uniaxial tension are respectively higher and lower than the case of uniaxial compression.

3.2.3 Biaxial behaviour

The strength and ductility of the concrete under biaxial states depends on the nature of stress state: compressive type or tensile type. The biaxial strength envelope (Figure 3.2.4) represented by Kupfer et al. [1969] suggests that the biaxial compression strength of the material increases compared to the equivalent uniaxial state. Equally from the stress-strain curves it is possible to recognize that the tensile ductility of concrete is greater under biaxial compression state than uniaxial compression (Figure3.2.5).

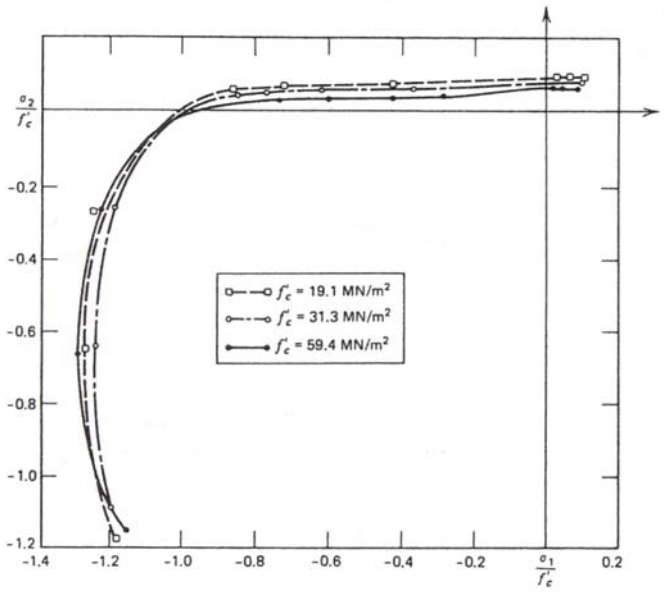

Figure 3.2.4: Biaxial strength envelope of concrete [Kupfer et al. 1969]

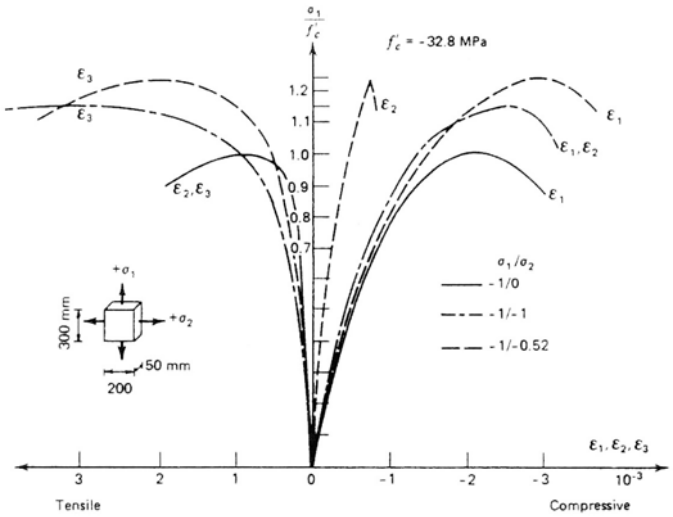

Figure 3.2.5: Stress-strain relationships for concrete under biaxial compression [Kupfer et al. 1969]

The biaxial tension strength is very similar to what measured for uniaxial tension state. Under biaxial compression-tension state the compressive strength decreases almost linearly as the applied tensile strength is increased.
Some studies suggest that the maximum strength envelope is almost independent of load path.
The growth of major microcracks is associated with an inelastic volume increase defined dilatancy. This phenomenon becomes visible when the failure point is approached. The failure will occur along surfaces orthogonal to the direction of the maximum tensile stress or strain. In particular the tensile strains are critical in defining the failure criterion of concrete.
Typical stress-strain results from triaxial tests on concrete indicate that the ultimate axial strength increases considerably with the confining stress. As the hydrostatic stress increases, the behaviour of the concrete moves from quasi-brittle to plastic softening to plastic hardening. This happens because under higher hydrostatic stresses the possibility of bond cracking is reduce and the failure rather explained with the crushing of cement paste. During hydrostatic compression tests the concrete behaves as nonlinear during the loadings stages, while upon unloading the slope of the curve is almost constant and approximately equal to the initial tangent of the loading curve (Figure 3.2.5).
Typical stress-strain results from triaxial tests on concrete indicate that the ultimate axial strength increases considerably with the confining stress. As the hydrostatic stress increases, the behaviour of the concrete moves from quasi-brittle to plastic softening to plastic hardening. This happens because under higher hydrostatic stresses the possibility of bond cracking is reduce and the failure rather explained with the crushing of cement paste. During hydrostatic compression tests the concrete behaves as nonlinear during the loadings stages, while upon unloading the slope of the curve is almost constant and approximately equal to the initial tangent of the loading curve Figure 3.2.5.
The failure surface can be defined as a function of the three principal stresses. The elastic limit and failure surfaces of concrete representation in the three principal stresses space is shown indicatively in Figure 3.2.5,

assuming the material is isotropic. For small hydrostatic pressures the deviatoric sections are convex and non circular, becoming more or less circular for increasing compressions (along the $\sigma_1 = \sigma_2 = \sigma_3$ axis). Finally, the failure surface appears to be independent of the load path [Kotzovos 1979].

3.3 UNIAXIAL MONOTONIC CONSTITUTIVE MODELS

3.3.1 Yassin model (1994)

The monotonic curve for concrete in compression of Yassin's model, follows the monotonic stress-strain relation model of Kent & Park [1971] as extended by Scott et al. [1982]. Even though more accurate and complete monotonic stress-strain models have been published since, the so-called "modified Kent-Park model" offers a good balance between simplicity and accuracy, and is widely used.

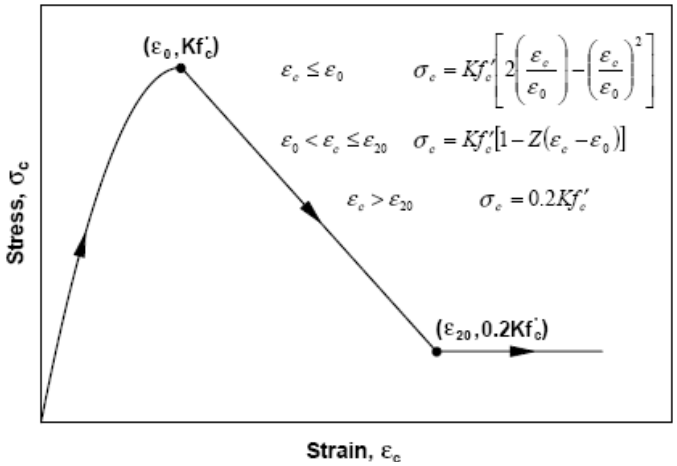

Figure 3.3.1: Modified Kent & Park model [1982] for concrete in compression

In the modified Kent-Park model (Figure 3.3.1), the monotonic concrete stress-strain (σ_c-ε_c) relationship in compression is described by three regions. Adopting the convention that compression is positive, the three regions are:

Region OA: $\varepsilon_c \le \varepsilon_0$

$$\sigma_c = Kf'_c \left[2\left(\frac{\varepsilon_c}{\varepsilon_0}\right) - \left(\frac{\varepsilon_c}{\varepsilon_0}\right)^2 \right] \tag{3.3.1}$$

Region AB: $\varepsilon_0 < \varepsilon_c \le \varepsilon_{20}$

$$\sigma_c = Kf'_c \left[1 - Z\left(\varepsilon_c - \varepsilon_0\right) \right] \tag{3.3.2}$$

Region BC: $\varepsilon_c > \varepsilon_{20}$

$$\sigma_c = 0.2Kf'_c \tag{3.3.3}$$

The corresponding tangent moduli E_t are given by the following expressions:

$\varepsilon_c \le \varepsilon_0$

$$E_t = \frac{2Kf'_c}{\varepsilon_0}\left(\frac{\varepsilon_c}{\varepsilon_0}\right) \tag{3.3.4}$$

$\varepsilon_0 < \varepsilon_c \le \varepsilon_{20}$

$$E_t = -ZKf'_c \tag{3.3.5}$$

$\varepsilon_c > \varepsilon_{20}$

$$E_t = -ZKf'_c \tag{3.3.6}$$

where:

$$\varepsilon_0 = 0.002K \tag{3.3.7}$$

$$K = \rho_s \frac{f_{yk}}{f'_c} \tag{3.3.8}$$

$$Z = \frac{0.5}{\frac{3 + 0.29 f'_c}{145 f'_c - 1000} + 0.75\rho_s \sqrt{\frac{h'}{s_h}} - 0.002K} \tag{3.3.9}$$

In the equations above, ε_0 is the concrete strain at maximum compressive stress, ε_{20} is the concrete strain at 20% of maximum compressive stress, K is a factor that accounts for the strength increase due to confinement, Z is the strain softening slope, f'_c is the concrete compressive cylinder strength (unconfined peak compressive stress) in MPa, f_{yh} is the yield strength of transverse reinforcement in MPa, ρ_s is the ratio of the volume of transverse reinforcement to the volume of concrete core measured to the outside of stirrups, h' is the width of concrete core measured to the outside of stirrups, and s_h is the center to center spacing of stirrups or hoop sets.

3.3.2 Chang & Mander model (1994)

The compression envelope curve of the model developed by Chang & Mander [1994] (referred to as C-M model in the sequel) is defined by the initial slope E_c , the peak coordinate (ε'_c , f'_c), a parameter r from Tsai's equation [1988] defining the shape of the envelope curve, and a parameter $x_{cr} > 1$ to define the spalling strain (Figure 3.3.2).

Both the compression and tension envelope curves can be written in nondimensional form by the use of the following equations:

$$y(x) = \frac{nx}{D(x)} \tag{3.3.10}$$

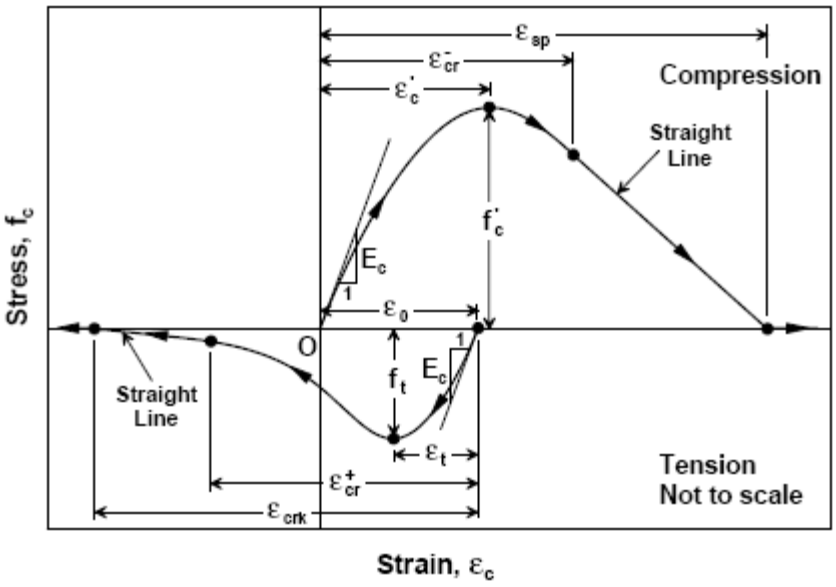

Figure. 3.3.2: Compression and tension envelopes [Chang & Mander 1994]

$$z(x) = \frac{(1-x')}{\left[D(x)\right]^2} \tag{3.3.11}$$

where:

$$D(x) = 1 + \left(n - \frac{r}{r-1}\right)x + \frac{x'}{r-1} \tag{3.3.12}$$

if $r \neq 1$, and

$$D(x) = 1 + (n - 1 + \ln x)x \tag{3.3.13}$$

if $r = 1$;

n and x are defined for the compression envelope as:

$$x^{-} = \left| \frac{\varepsilon_c}{\varepsilon'_c} \right| \tag{3.3.14}$$

$$n^{-} = \left| \frac{E_c \varepsilon'_c}{f'_c} \right| \tag{3.3.15}$$

The non-dimensional spalling strain can be calculated by:

$$x_{sp} = x_{cr}^{-} - \frac{y\left(x_{cr}\right)}{n^{-} z\left(x_{cr}^{-}\right)} \tag{3.3.16}$$

In the equations above, ε_c is the concrete strain, ε'_c is the concrete strain at peak unconfined (or confined) stress, f'_c is the unconfined (or confined) concrete strength, E_c is the concrete initial Young's modulus, x is the nondimensional strain on the compression envelope, x_{cr}^{-} is the nondimensional critical strain on the compression envelope curve (used to define a tangent line up to the spalling strain), x_{sp} is the non-dimensional spalling strain, $y(x)$ is the nondimensional stress function, $z(x)$ is the nondimensional tangent modulus function (Figure 3.3.2).
The stress f_c and the tangent modulus E_t at any given strain on the compression envelope curve are defined by:

$$f_c = f_c^{-}\left(x^{-}\right) \tag{3.3.17}$$

$$E_t = E_t^{-}\left(x^{-}\right) \tag{3.3.18}$$

where $f_c^{-}\left(x^{-}\right)$ and $E_t^{-}\left(x^{-}\right)$ are defined as:

$$f_c^{-} = f'_c \, y\left(x^{-}\right) \tag{3.3.19}$$

$$E_t^{-} = E_c z\left(x^{-}\right) \tag{3.3.20}$$

if $x^- < x_{cr}^-$ (Tsai's equation), as:

$$f_c^- = f'_c\left[y\left(x_{cr}^-\right) - n^- z\left(x_{cr}^-\right)\left(x^- - x_{cr}^-\right)\right] \tag{3.3.21}$$

$$E_t^- = E_c z\left(x_{cr}^-\right) \tag{3.3.22}$$

if $x_{cr}^- \le x^- \le x_{sp}$ (Straight line), and as:

$$f_c^- = E_t^- = 0 \tag{3.3.23}$$

if $x > x_{sp}$ (Spalled).

Once the concrete is considered to be spalled, the stresses are zero from that moment on. Confined concrete can be considered not to spall, in such a case a large value of x_{cr}^- should be defined. The minus superscript in the equations above refers to the stress-strain behaviour in compression.
The material parameters associated with the compression envelope curve of the model are the concrete strength f'_c , the concrete strain at peak stress ε'_c, the concrete initial Young's modulus E_c , the Tsai's parameter *r* defining the shape of the compression envelope, and the nondimensional critical strain x_{cr}^- where the envelope curve starts following a straight line. All of these parameters can be controlled and manipulated based on specific experimental results for a refined calibration of the compression envelope. Nevertheless, Chang and Mander have proposed empirical relations for the parameters E_c, ε'_c, and *r* defined based on a detailed review of previous research. Parameters E_c, ε'_c, and *r* associated with the unconfined compression envelope can be empirically related to the unconfined concrete strength f'_c (MPa) as:

Initial Young modulus,

$$E_c = 8200 f'_c \, Mpa \tag{3.3.24}$$

Strain at peak stress,

$$\varepsilon_c = \frac{\left(f'_c\right)^{1/4}}{28} \tag{3.3.25}$$

Shape parameter,

$$r = \frac{f'_c}{5.2} - 1.9 \tag{3.3.26}$$

The compressive envelope of the C-M model for confined concrete complies with the generalized confinement model developed by Mander et al. [1988a], which is applicable to RC members with either circular or rectangular cross sections and any general type and configuration of reinforcement (Figure 3.3.3). For rectangular sections, the effectively confined concrete area is given by the expression:

$$A_c = \left(b_c d_c - \sum_{i=1}^{n} \frac{\left(w'_i\right)^2}{6} \right) \left(1 - 0.5 \frac{s'}{d_c} \right) \tag{3.3.27}$$

whereas the concrete core area is given by:

$$A_{cc} = b_c d_c - A_{st} \tag{3.3.28}$$

The lateral confinement pressure (imposed by the transverse steel) for each direction is calculated as:

$$f'_{lx} = k_c \rho_x f_{yh} \tag{3.3.29}$$

$$f'_{ly} = k_c \rho_y f_{yh} \tag{3.3.30}$$

in which k_c is the confinement effectiveness coefficient defined as:

$$k_c = \frac{A_c}{A_{cc}}, \tag{3.3.31}$$

and

$$\rho_x = \frac{A_{xx}}{s \cdot d_e} \tag{3.3.32}$$

where A_{xx} is the total area of transverse reinforcement parallel to the x-axis,

$$\rho_y = \frac{A_{yy}}{s \cdot d_e} \tag{3.3.33}$$

where A_{yy} is the total area of transverse reinforcement parallel to th y-axis.
The equation proposed in C-M model in order to represent the analytical confinement coefficient K takes the form (as an approximation of the ultimate strength surface proposed by Mander et al. [1988a]):

$$K = \frac{f'_{cc}}{f'_c} = A\bar{x}\left(0.1 + \frac{0.9}{1 + B\bar{x}}\right) \tag{3.3.34}$$

with

$$\bar{x} = \frac{f'_{l1} + f'_{l2}}{2f'_c} \tag{3.3.35}$$

$$r = \frac{f'_{l1}}{f'_{l2}} \tag{3.3.36}$$

with $f'_{l2} \geq f'_{l1}$,

$$A = 6.8886 - (0.6096 + 17.175r)e^{-4.989r} \tag{3.3.37}$$

$$B = \frac{4.5}{\frac{5}{A}\left(0.9849 - 0.6306e^{-3.8939r}\right) - 0.1} \tag{3.3.38}$$

where the analytical confinement coefficient K is the ratio of the confined concrete strength f'_{cc} to the unconfined concrete strength f'_c.

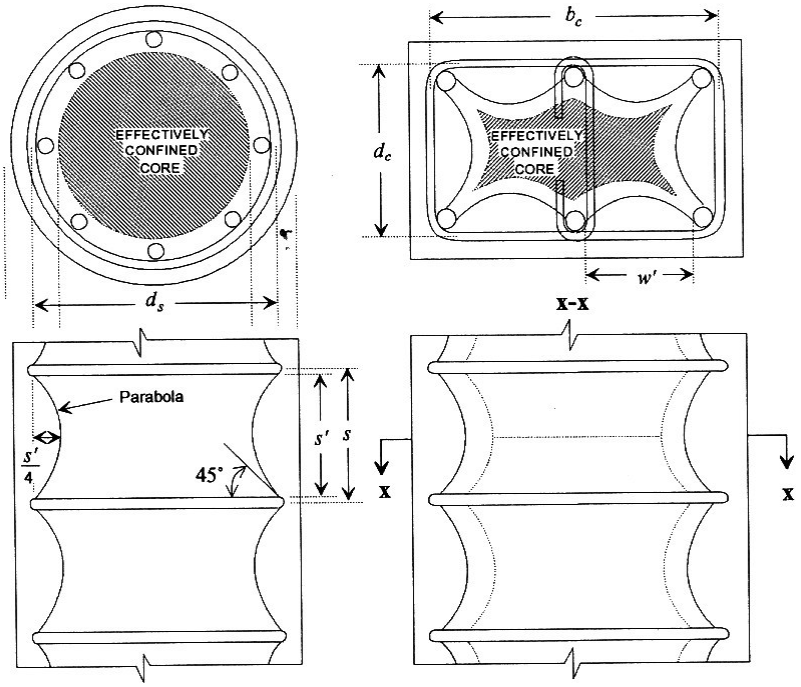

Figure. 3.3.3: Confinement mechanism for circular and rectangular cross sections [Chang & Mander 1994]

Eq. (3.3.34) can be represented in the form of:

$$K = f'_c + k_1 f_l \tag{3.3.39}$$

By taking f_l as the average of f_{l1} and f_{l2} this can be rewritten as:

$$K = \frac{f'_{cc}}{f'_c} = 1 + k_1 \bar{x} \tag{3.3.40}$$

where

$$k_1 = A\left(0.1 + \frac{0.9}{1 + B\bar{x}}\right) \tag{3.3.41}$$

The strain at peak stress for confined concrete (ε'_{cc}) takes the form:

$$\varepsilon'_{cc} = \varepsilon'_c \left(1 + k_2 \bar{x}\right) \tag{3.3.42}$$

with

$$k_2 = 5k_1 \tag{3.3.43}$$

where ε'_c is the strain at peak unconfined stress.
The confinement parameters described above were validated by Mander et al. [1988b] and Chang & Mander [1994] against extensive experimental data from tests on RC column specimens under eccentric loading.
The shape of the tension envelope curve in C-M model is the same as that of the compression envelope curve (Figure 3.3.1). The curve is shifted to a new origin ε_0 (such procedure will not be explained in this dissertation for brevity). The non-dimensional parameters for the tension envelope curve are given by:

$$x^+ = \left|\frac{\varepsilon_c - \varepsilon_0}{\varepsilon_t}\right| \tag{3.3.44}$$

$$n^+ = \frac{E_c \varepsilon_t}{f_t} \tag{3.3.45}$$

The non-dimensional cracking strain is given by:

$$x_{crk} = x_{cr}^{+} - \frac{y\left(x_{cr}^{+}\right)}{n^{+} z\left(x_{cr}^{+}\right)} \tag{3.3.46}$$

where ε_c is the concrete strain, ε_t is the concrete strain at peak tension stress, f_t is the concrete tensile strength, E_c is the concrete initial Young's modulus, x^{+} is the non-dimensional strain on the tension envelope curve, x_{cr}^{+} is the critical strain on the tension envelope curve (used to define a tangent line up to the cracking strain), and x_{crk} is the cracking strain (Figure. 3.3.1).
The stress f_c and the tangent modulus E_t for any given strain on the tension envelopecurve are defined as:

$$f_c = f_c^{+}(x^{+}) \tag{3.3.47}$$

$$E_c = E_t^{+}(x^{+}) \tag{3.3.48}$$

where $f_c^{+}\left(x^{+}\right)$ and $E_t^{+}\left(x^{+}\right)$ are defined as:

$$f_c^{+} = f'_t\, y\left(x^{+}\right) \tag{3.3.49}$$

$$E_t^{+} = E_c z\left(x^{+}\right) \tag{3.3.50}$$

if $x^{+} < x_{cr}^{+}$ (Tsai's equation), as:

$$f_c^{+} = f'_t\left[y\left(x_{cr}^{+}\right) - n^{+} z\left(x_{cr}^{+}\right)\left(x^{+} - x_{cr}^{+}\right)\right] \tag{3.3.51}$$

$$E_t^{+} = E_c z\left(x_{cr}^{+}\right) \tag{3.3.52}$$

if $x_{cr}^{+} \le x^{+} \le x_{crk}$ (Straight line), and as:

$$f_c^{+} = E_t^{+} = 0 \tag{3.3.53}$$

If $x > x_{crk}$ (Cracked).

The functions y and z are defined by Equations 3.3.10-3.3.11. When the concrete is cracked it is considered no longer to resist any tension stress, as a result of crack opening, but on the other hand a gradual crack closure is considered to take place. Concrete experiencing tension stiffening can be considered not to crack completely, that is, a large value of x_{cr}^{+} can be defined. The plus superscript refers to the stress-strain behaviour in tension.
The parameters associated with the tension envelope curve include the concrete tensile strength f_t , the strain at peak tensile stress ε_t , and the parameter r defining the shape of the tension envelope curve. The critical strain on the tension envelope curve x_{cr}^{+} (where the envelope curve starts following a straight line) can be controlled and calibrated based on either experimental results or empirical relations (i.e., Collins & Mitchell 1991; Belarbi & Hsu 1994) to model the behaviour of concrete in tension and the tension-stiffening phenomenon.

3.3.3 Modelling of Tension Stiffening

The contribution of cracked concrete to the tensile resistance of RC members is known as the effect of tension stiffening. The concrete between the cracks, which is still bonded to the reinforcing steel bars, contributes to the tensile resistance of the member. The tension-stiffening phenomenon plays a significant role in reducing the post-cracking deformations of reinforced concrete structures, and has been proven by researchers (i.e., Vecchio & Collins 1982; Collins & Mitchell 1991; Belarbi & Hsu 1994; Pang & Hsu 1995; Hsu & Zhang 1996; Mansour et al. 2001; Hsu & Zhu 2002) to considerably influence the post-cracking stiffness, yield capacity, and shear behavior of reinforced concrete members.
In the model developed by Vulcano et al. [1988], for example, tension stiffening was modeled using an axial-element-in-series model (Figure 3.3.4) to describe the response of the uniaxial sub-elements of the model. The two elements in series represented the segment along the uniaxial elements in which the bond remained active (Element 1) and the segment for which the bond stresses were negligible (Element 2). The concrete within Element 1 was considered to be un-cracked and modelled with a

linear elastic behaviour. The cracked concrete within Element 2 was considered to have no contribution (zero stresses) to the axial stiffness of the whole model under increasing tensile strains. A dimensionless parameter λ was introduced to define the relative length of the two elements (representing cracked and uncracked concrete) to account for tension stiffening. Under monotonic tensile loading, the tension-stiffening effect was incorporated by manipulating the value of the dimensionless parameter λ such that the tensile stiffness of the uniaxial model in Figure 3.3.4 would be equal to the actual (experimentally observed) tensile stiffness of a tension stiffened uniaxial element evaluated on the basis of an empirical law suggested by proposed by Rizkalla & Hwang [1984].

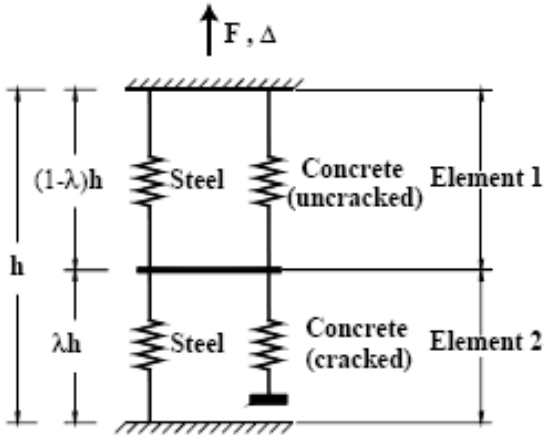

Figure 3.3.4: Axial-element-in-series model [Vulcano et al. 1988]

Such law relates the ratio of the steel strain within cracks to the average strain of a reinforced concrete member under monotonic axial tensile loading. Under cyclic loading, it was assumed that the value of λ was kept constant during unloading from the tensile stress state, equal to the value corresponding to the maximum tensile strain previously attained; if this maximum strain was exceeded during a tensile reloading, the value of λ was updated as for the case of monotonic tensile loading.

In other studies, such as formulation proposed by Colotti [1993], instead of an axial-element-in-series model, a two-parallel-component model (Figure 3.3.5) is adopted for the uniaxial elements of the present wall model, and concrete and steel within each uniaxial element are subjected to the same average (smeared) strains.
The tension-stiffening effects are directly incorporated into the constitutive stress-strain relations implemented for concrete and steel.

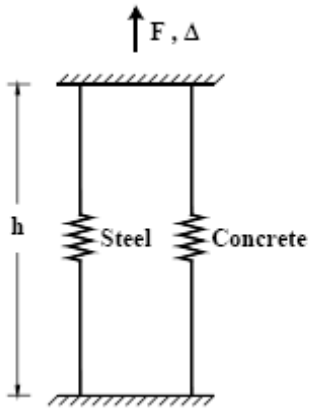

Figure 3.3.5: Two-parallel-component-model [Colotti 1993]

As investigated in detail by Belarbi & Hsu [1994], the modelling of the tension-stiffening phenomenon must consider two effects simultaneously. First, an average (smeared) tensile stress-strain curve must be considered for cracked concrete; and second, the stress-strain curve of bare mild steel bars must be replaced by an average (smeared) stress-strain curve for steel bars stiffened by concrete between cracks. Accordingly, based on extensive tests of reinforced concrete panels subjected to normal stresses, Belarbi and Hsu developed two constitutive models: one for the average tensile stress-strain relation of concrete and one for the average tensile stress-strain relation of steel reinforcing bars stiffened by concrete. The tension-stiffening models proposed by Belarbi and Hsu have also been used and validated experimentally in more recent studies to model the shear behaviour of RC

membrane elements (i.e., Pang & Hsu 1995; Hsu & Zhang 1996; Mansour et al. 2001; Hsu & Zhu 2002).

The average stress-strain relation proposed by Belarbi and Hsu for concrete in tension takes the form (Figure 3.3.6):

$$\sigma_c = E_c \varepsilon_c \tag{3.3.54}$$

if $\varepsilon_c \le \varepsilon_{cr}$, and

$$\sigma_c = f_{cr} \left(\frac{\varepsilon_{cr}}{\varepsilon_c} \right)^{0.4} \tag{3.3.55}$$

if $\varepsilon_c > \varepsilon_{cr}$,

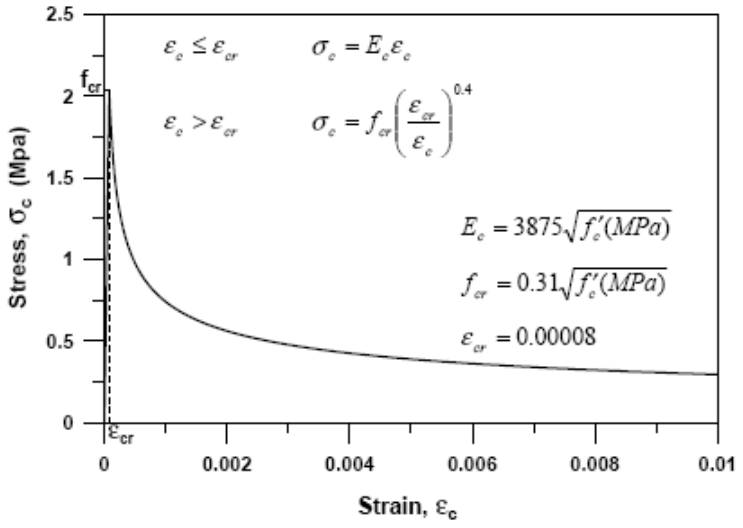

Figure 3.3.6: Average stress-strain relation for concrete in tension [Belarbi & Hsu 1994]

where

$$E_c = 3875\sqrt{f'_c(MPa)} \tag{3.3.56}$$

$$f_{cr} = 0.31\sqrt{f'_c(MPa)} \tag{3.3.57}$$

$$\varepsilon_{cr} = 0.00008 \tag{3.3.58}$$

In the equations above, ε_c is the average concrete tensile strain, σ_c is the average concrete tensile stress, E_c is the initial Young's modulus of the average stress-strain relation, f_{cr} is concrete the tensile cracking stress, and ε_{cr} is the concrete strain at cracking.

The relation consists of an ascending straight line before cracking and a descending curve to the power of 0.4 after cracking (Figure 3.3.6).

The expressions for f_{cr}, ε_{cr}, E_c , and the power constant 0.4 in Equation (3.3.55) are obtained from the average and best fit of experimental results from testing 17 RC panels with concrete cylinder compressive strengths ranging between 36.9 MPa and 47.7 MPa.

It seems interesting underlining that, Belarbi and Hsu also identified how the average stress-strain relation of reinforcing steel bars surrounded by concrete is different than the stress-strain relation of bare steel bars (Figure 3.3.7). The most important difference was found to be the lowering of the yield stress, σ_y, as yielding of a reinforced concrete element occurs when the steel stress at the cracked section reaches the yield strength of the bare bar. At the same time, the average steel stress smeared along the length of the element reaches a level lower than that of the yield stress of the bare bar.

Based on experimental data from the RC panels, the reduction of the yield stress of bars embedded in concrete were found to be empirically dependent on the cross-sectional area ratio of the longitudinal steel in the panel (ρ) and the ratio of concrete cracking stress (f_{cr}) to the steel yield stress (σ_y). The strain-hardening slope (plastic modulus) of the steel bars embedded in concrete was also observed to differ from the plastic modulus of bare bars with the variation also dependent on the above parameters. Based on evaluation and characterization of experimental data from the RC panels, they proposed a simple bilinear constitutive model for steel bars embedded in concrete, which is not reported here.

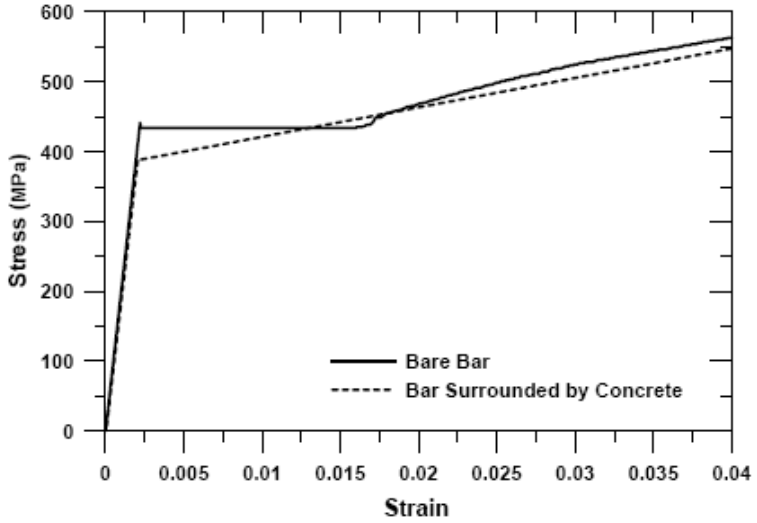

Figure 3.3.7 :Effect of tension stiffening on reinforcing bars [Belarbi & Hsu 1994]

3.4 MULTIAXIAL MATHEMATICAL ELASTO-PLASTIC DAMAGED MODELS

3.4.1 Etse-William model (1994)

The model described here, used as a base to discuss the main aspects of multi-axial concrete modelling, is an incremental one and is based on the flow theory of elasticity. The model has been introduced by Etse & Willam [1994], it is an attempt to define an omni-comprehensive representation of the material.

The model features refined failure criterion and plastic loading conditions, a non-associated flow rule, and specifically designed hardening and softening rules. Softening is based on a fracture energy formulation.

The proposed failure criterion uses the Hoek & Brown [1980] criterion, originally developed for rock materials.

The criterion is expressed in terms of three scalar invariants $\sqrt{2J_2}$, $\cos(3\theta) = \sqrt{27}J_3 \Big/ (2J_2)^{3/2}$, directly related to the Haigh-Westergaard coordinates $\xi = \sqrt{3}\sigma$, ρ, θ, which permit a convenient geometric representation of the failure surfaces.

The meridional sections of the failure surface are, in fact, readily traced, for different values of θ in the (ξ, ρ) plane, and the sections in the deviatoric planes can be also represented in a polar diagram.
The expression for the failure criterion proposed is:

$$F(\sigma,\rho,\theta)=\frac{3}{2}\left[\frac{\rho r(\theta)}{f'_c}\right]^2+\frac{m_c}{f'_c}\left[\sigma+\frac{\rho r(\theta)}{f'_c}\right]-1=0 \qquad (3.4.1)$$

where $r(\theta)$ is the Klisinsky function:

$$r(\theta)=\frac{4(1-e^2)\cos^2(\theta)+(2e-1)^2}{2(1-e^2)\cos(\theta)(2e-1)\sqrt{4(1-e^2)\cos^2(\theta)+5e^2+4e}} \qquad (3.4.2)$$

with $0.5\le e\le 1$ to preserve convexity of the yield function.
The parameter e is called eccentricity and represent the ratio between the radius of the deviatoric section along tensile and compressive meridians ρ_t/ρ_c (tensile and compressive meridians correspond to $\theta=0$ and $\theta=\pi/3$ and are represented in Figure 3.4.1).

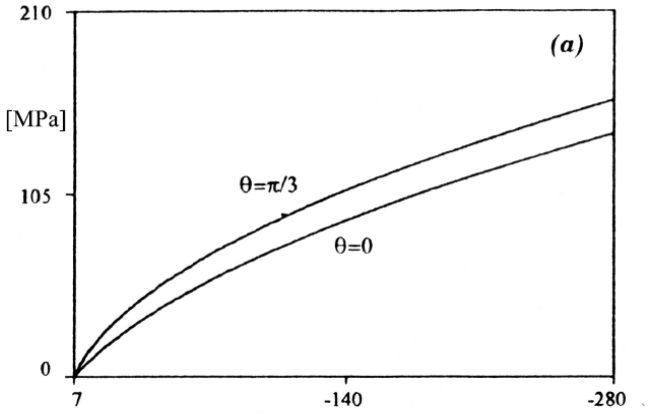

Figure 3.4.1: Meridian sections of concrete failure surface

The Klisinsky function was introduced to smoothen the Hoek and Brown failure surface and its effect can be seen in Figure 3.4.2.
The difference between the proposed criterion and the Hoek and Brown's one is best appreciated by comparing the failure locus in plane stress (Figure 3.4.3).

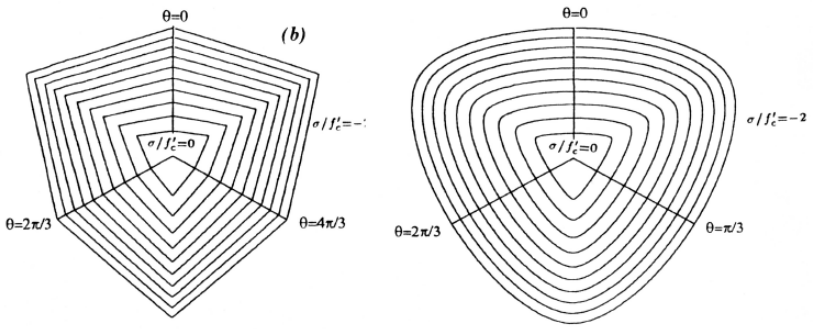

Figure 3.4.2: Deviatoric sections of Hoek and Brown failure criterion (left) and the proposed Extended Leon Criterion (right) [Etse & William 1994]

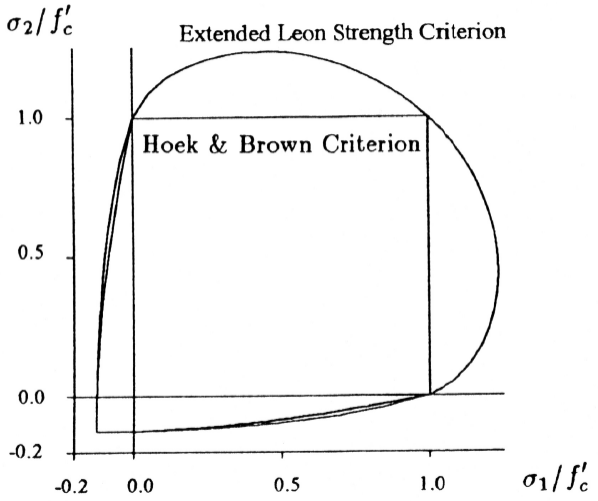

Figure 3.4.3: Plane stress sections of smoothened and polygonal failure envelopes

Also the loading function was derived by modifying the Hoek and Brown criterion. The same loading function is used for pre-peak and post-peak response.
The model is isotropic and remain isotropic during the loading history and degradation of the elastic properties during plastic flow is neglected.
The total strain is composed of a plastic and an elastic component ($\dot{\varepsilon} = \dot{\varepsilon}_c + \dot{\varepsilon}_p$). The elastic response is linear, and the plastic response is governed by the flow rule:

$$\dot{\varepsilon}_p = \dot{\lambda} m \tag{3.4.3}$$

with $m = \frac{\partial Q}{\partial \sigma}$, where $\dot{\lambda}$ denotes the plastic multiplier and Q is the plastic potential. A non associative flow rule is used to avoid overprediction of dilatancy. Therefore Q differs from the loading function. The expression of the loading function proposed is:

$$F(\sigma,\rho,\theta,k,c) = \left\{(1-k)\left[\frac{\rho}{f'_c} + \frac{\rho r(\theta)}{\sqrt{6} f'_c}\right]^2 + \sqrt{\frac{3}{2}}\frac{\rho r(\theta)}{f'_c}\right\}^2 +$$

$$+\frac{k^2 m}{f'_c}\left[\sigma + \frac{\rho r(\theta)}{\sqrt{6}}\right] - k^2 c = 0 \tag{3.4.4}$$

where m is the friction parameter, while softening is represented varying the decohesion parameter c from unity to zero.
In the hardening regime the evolution of the loading surface is varied by the parameter k ($0 \le k \le 1$), namely "normalized strength parameter". The linear elastic response is therefore bounded by the initial value of k (for instance k_0 = 0.1). Note that for $k=1$ the loading function reduces to the failure one.
The shape of the hardening surfaces for different values of k is depicted in Figure 3.4.4. Note that initially the loading surface are closed to allow for cap action. The hardening function is smooth everywhere except at its intersection with the hydrostatic axis. In Figure 3.4.5 the same surface are represented during softening (for c ranging from zero to unit).

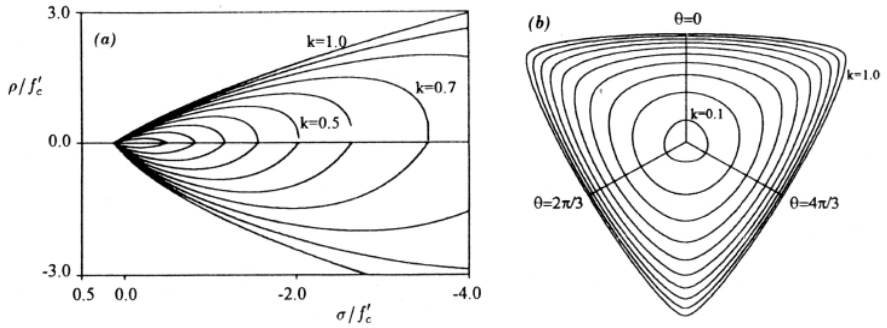

Figure 3.4.4: Loading surface of Etse-William model in hardening regime: (a) Meridian sections; (b) deviatotic sections at $\sigma / f_c' = -0.3$.

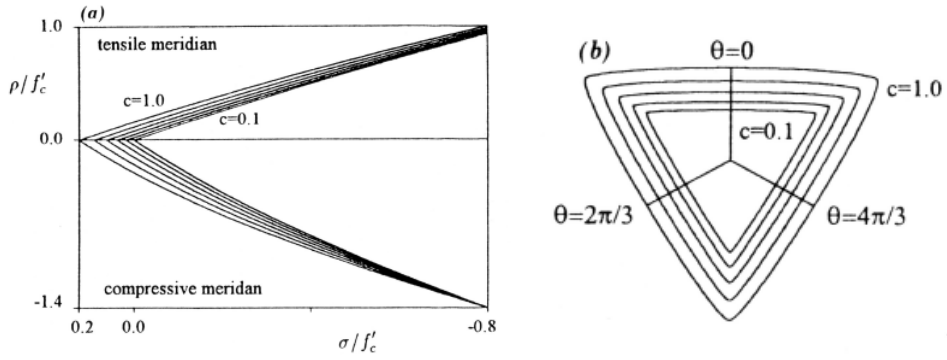

Figure 3.4.5: Loading surface of Etse-William model in softening regime: (a) Meridian sections; (b) deviatoric sections at $\sigma / f_c' = 0$.

A non associated flow rule is used to control inelastic dilatancy. This is required because it is seen experimentally that the use of an associative flow rule, over predicting the dilatation, over predicts the confinement, as well, leading to overestimation of structural element affected by passive confinement.

The plastic potential used is based on a volumetric modification of the yield condition. Therefore, the deviatoric component of the plastic strain rate follows an associated flow rule. The plastic potential has the following form:

$$Q\left(\sigma,\rho,\theta,k,c,m_Q\right)=\left\{\left(1-k\right)\left[\frac{\sigma}{f'_c}+\frac{\rho r\left(\theta\right)}{\sqrt{6}f'_c}\right]+\sqrt{\frac{3}{2}}\frac{\rho r\left(\theta\right)}{f'_c}\right\}^2+$$

$$+\frac{k}{f'_c}\left[m_Q+m\frac{\rho r\left(\theta\right)}{\sqrt{6}}\right]-k^2c \qquad (3.4.5)$$

where m_Q is defined in terms of its gradient:

$$\frac{\partial m_Q}{\partial\sigma}=D\exp(Ex^2)+G \qquad (3.4.6)$$

Where $x=\dfrac{-\sigma+f'_t/3}{f'_c}$.

The material parameters *D*, *E* and *G* are to be calibrated from three different experiments using dilatancy measurements at different levels of the hydrostatic component of the stress.

For the hardening formulation the model introduces a scalar variable α such that:

$$\dot{\alpha}=\frac{1}{x_p}\dot{\varepsilon}_p \qquad (3.4.7)$$

where $\dot{\varepsilon}_p$ is the Euclidean norm of the of the plastic strain rate:

$$\dot{\varepsilon}_p=\sqrt{\dot{\varepsilon}_p\bullet\dot{\varepsilon}_p}=\dot{\lambda}\left\|m\right\|, \qquad (3.4.8)$$

x_p is a function of the confinement through the stress invariant σ and have the following polynomial expression:

$$x_p=x_p\left(\sigma\right)=A\left(\frac{\sigma}{f'_c}\right)^2+\left(\frac{\sigma}{f'_c}\right)+C, \qquad (3.4.9)$$

therefore, Eq. (3.4.7) defines the rate of strain hardening $\dot{\sigma}$ in terms of x_p and $\dot{\varepsilon}_p$, with α=0 at the beginning of the inelastic deformation process. The peak strength is reached for α=1.
The normalized strength parameter k which controls the evolution of the yield surface in the pre-peak regime, is finally expressed by the following function of the variable α:

$$k = k(\alpha) = k_0 + (1 - k_0)\sqrt{\alpha(2 - \alpha)}\,, \qquad (3.4.10)$$

Finally, it is worth considering that the correct modelling of softening is a very important aspect of concrete modelling. It is widely recognized, in fact, that the most relevant source of nonlinearity in structural problems involving concrete is cracking of concrete.
In the smeared crack concept, in which the cracked medium is represented as an equivalent continuum, a good representation of the softening of the material in tension is of key importance for the correct prediction of crack propagation and spacing. However, softening does not occur only in tension and its different characteristics for different confinement regimes determine brittle or ductile response of the material in compression.
Concrete softening is the manifestation of drastic changes of the micro and mesostructure of the heterogeneous material, when micodefects propagate and coalesce into macrodefects. Softening is then a structural phenomenon rather than a material property.
Because of this, in a smeared crack based formulation for softening behaviour there is a difficulty in determining softening relations that are independent on test configuration and boundary conditions.
A possible strategy is the use of a fracture energy base softening description. Softening is represented through a reduction of the decohesion parameter c and the friction parameter m and is assumed to take place only for values of confinement below a determined transition point. The decohesion factor c varies from 1 to 0 during the softening process and the shear parameter m is a function of the decohesion one as the deviatoric strength at the transition point is assumed to be constant during the softening process.
The intermediate softening surface after failure is defined by:

$$F_s(\sigma,\rho,\theta,c)=\frac{3}{2}\left[\frac{\rho r(\theta)}{f'_c}\right]^2+\frac{m_s}{f'_c}\left[\sigma+\frac{\rho r(\theta)}{\sqrt{6}}\right]-c_s=0\,, \quad (3.4.11)$$

Imposing the constraint that the deviatoric strength at the transition point is fixed we get that the parameter m_s have the following expression:

$$m_s=m_r-(m_r-m_0)c_s\,, \quad (3.4.12)$$

where m_r is the residual shear parameter and m_0 is the initial one.
The ratio c_s is defined as:

$$c_s=\frac{\sigma_t}{f'_t}\,, \quad (3.4.13)$$

it varies in the field [0, 1].

3.4.2 Menetrey-William yield criterion (1995)

The model described in the previous section include all the main aspects characterizing the behaviour of plain concrete. A model of this type can be implemented in a computer program to trace, given a straining history, the corresponding stress history.
However a program of this kind does not necessarily have the stability and efficiency required for the inclusion within a finite element architecture. This is due to two basic reasons.
First, the computational time is not an issue if the sole purpose of the program is to reproduce a stress history for a given strain history, in order to validate a constitutive law.
Second, in a finite element model it is desirable to assemble a tangent operator necessary for the use of a Full Newton Raphson solution alghoritm. This tangent modulus should be assembled in efficient manner to speed up, rather the slowing down, the solution. On the other hand softening, as it is well known, leads to negative stiffnesses in local areas whose propagation in the analysed domain renders the tangential stiffness of the problem

singular and leads to failure of the procedures for solving non linear problems.

To circumvent these issues, as typical in engineering, may be convenient to renounce to completeness and make use of a model embodying only the aspects deemed to be decisive. The choice of the characteristics of a model depends on implementation issues, computational effort required, numerical convergence performance, but also on the purpose of the analysis and the range of application of the model.

The model adopted is an isotropic elastoplastic model with standard isotropic hardening. It features an associative flow rule as dilatancy is not thought to be a key parameter for the investigation carried out (limited passive confinement is involved).

The Menetrey-William plasticity model [1995] is based on the hypothesis of material isotropy, whereby the yield function can be expressed in terms of the three invariants, J_1, J_2 and J_3 of the stress state, σ:

$$J_1 = tr\sigma = \sigma \bullet 1; \quad J_2 = \frac{1}{2} trS^2 = \frac{1}{2} S^2 \bullet 1; \quad J_3 = \frac{1}{3} trS^3 = \frac{1}{3} S^3 \bullet 1, \tag{3.4.14}$$

with S denoting the deviatoric part of σ, 1 the rank-two identity tensor and the symbol $\bullet$ indicating the operation of scalar product.

For geometrical interpretation it is convenient to introduce the three Haigh-Westergaard cylindrical coordinates:

$$\xi = \frac{1}{\sqrt{3}} I_1; \quad \rho = \sqrt{2J_2}; \quad \theta = \frac{1}{3} \cos^{-1} \left(\frac{3\sqrt{3} J_3}{2 J_2^{\frac{3}{2}}} \right), \tag{3.4.15}$$

where ξ represents the mean stress, ρ is the norm of the deviatoric stress, and θ denotes the Lode angle.

The Menetrey-Willam yield function can then be written as follows:

$$\phi(\xi, \rho, \theta) = (A\rho)^2 + m\left[B\rho r(\theta, c) + C\xi \right] - c, \tag{3.4.16}$$

where *A, B, C, m* and *e* represent material parameters, *c* accounts for isotropic hardening and *r* indicates the Klisinski function, defined by:

$$r(\theta,e)=\frac{4\left(1-e^2\right)\cos^2\theta+\left(2e-1\right)^2}{2(1-e^2)\cos\theta+\left(2e-1\right)\sqrt{4\left(1-e^2\right)\cos^2\theta+5e^2-4e}} \tag{3.4.17}$$

for $\theta\in\left[0,\pi/3\right]$, and by assuming the following symmetry conditions:

$$\begin{aligned} r\left(\theta+n\frac{2\pi}{3},e\right)&=r(\theta,e)\\ r\left(-\theta,e\right)&=r(\theta,e)\end{aligned} \tag{3.4.18}$$

for $\theta\notin\left[0,\pi/3\right]$, with *n* being an arbitrary integer.
From the definition of the yield function (Eq. (3.4.16)) the following remarks on the yield surface can be made:

- It is convex and smooth everywhere except at a vertex located along the hydrostatic axis, that is for any value of θ, $\rho = 0$ and $\xi = c/(mC)$;
- its sections with the planes $\theta = \theta_0 =$ constant are parabolic curves;
- if $A=0$, its section with the plane $\xi=\xi_0=$constant is a curve whose equation in polar coordinates ρ, θ is given by:

$$\rho=\rho\left(\theta\right)=\frac{c-mC\xi_0}{mB}\frac{1}{r\left(\theta,e\right)} \tag{3.4.19}$$

Hence, to within the factor $(c-mC\xi_0/mB)$, the function defined by equation (3.4.19) coincides with the inverse of the Klisinski function (3.4.17).
It has been shown in the work published by Menetrey & William [1995] that the parameters in Eq. (3.4.16) can be suitably fixed so as to specialize the Menetrey-Willam yield criterion to the Hencky-von Mises, Drucker-Prager, Rankine and Leon criteria. Mohr-Coulomb criterion can also be well approximated.

3.4.3 Lee-Fenves model (1998)

The model is based on an internal variable formulation of plasticity theory for the nonlinear analysis of concrete. The model makes use of the fact that concrete eventually exhibits strain-softening in tension and compression, leading to complete loss of strength. In this regard, concrete resembles such materials as cohesive soils, and may be classified with them as frictional materials with cohesion, where the eventual loss of strength may be thought of as the vanishing of the cohesion.

For such a model to be capable of representing the behaviour of concrete materials, the yield criterion must be of the form in which the concept of cohesion is clear, and the hardening rule should be such that it will eventually lead to vanishing of the cohesion (total damage).

The model of Lee & Fenves [1998], makes use of the yield function of Lubliner et. al. [1989]. The modifications proposed by Lee and Fenves was introduced in order to account for different evolution of strength under tension and compression.

The model has the following characteristics:

- The shape of the yield surface is assumed to remain constant and is defined by a modified Mohr-Coulomb criterion;
- The evolution of the elastic domain is defined by a hardening rule that is calibrated on the basis of experimental data;
- Plastic strain is defined on the basis of an associated flow rule;
- Damage is assumed to be isotropic and defined by a single scalar damage variable, $\tilde{\varepsilon}^{pl}$, that is a measure of the accumulated damage;
- Damage is assumed to accumulated as a function of plastic strain.

An additive strain rate decomposition is assumed for this rate-independent model:

$$\dot{\boldsymbol{\varepsilon}} = \dot{\boldsymbol{\varepsilon}}^{el} + \dot{\boldsymbol{\varepsilon}}^{pl}, \tag{3.4.20}$$

where $\dot{\boldsymbol{\varepsilon}}$ is the total strain rate, $\dot{\boldsymbol{\varepsilon}}^{el}$ is the elastic part of the strain rate, and $\dot{\boldsymbol{\varepsilon}}^{pl}$ is the plastic part of the strain rate. The stress-strain relations are governed by a scalar damaged elasticity:

$$\boldsymbol{\sigma} = \left(1-d\right)\mathbf{D}_0^{el} : \left(\dot{\boldsymbol{\varepsilon}} - \dot{\boldsymbol{\varepsilon}}^{pl} \right), \tag{3.4.21}$$

where $\mathbf{D}_0^{el}$ is the initial (undamaged) elastic stiffness matrix of the material, $\mathbf{D}^{el} = \left(1-d\right)\mathbf{D}_0^{el}$ is the degraded elastic stiffness matrix, and d is the scalar stiffness degradation variable, which can take values in the range from zero (undamaged material) to one (fully damaged material). Damage associated with the failure mechanisms of the concrete (cracking and crushing) therefore results in a reduction in the elastic stiffness. Within the context of the scalar-damage theory, the stiffness degradation is isotropic and characterized by a single degradation variable, d. The effective stress is defined as:

$$\overline{\boldsymbol{\sigma}} = \mathbf{D}_0^{el} : \left(\boldsymbol{\varepsilon} - \boldsymbol{\varepsilon}^{pl} \right), \tag{3.4.22}$$

The Cauchy stress tensor is related to the effective stress tensor through the scalar degradation relation:

$$\boldsymbol{\sigma} = \left(1-d\right)\overline{\boldsymbol{\sigma}}, \tag{3.4.23}$$

For any given cross-section of the material, the factor $\left(1-d\right)$ represents the ratio of the effective load-carrying area (i.e., the overall area minus the damaged area) to the overall section area. In the absence of damage, $d = 0$, the effective stress tensor $\overline{\boldsymbol{\sigma}}$ is equivalent to the Cauchy stress tensor, $\boldsymbol{\sigma}$. When damage occurs, however, the effective stress is more representative than the Cauchy stress because it is the effective stress area that is resisting the external loads. It is, therefore, convenient to formulate the plasticity problem in terms of the effective stress. As discussed later, the evolution of the degradation variable is governed by a set of hardening variables, $\tilde{\boldsymbol{\varepsilon}}^{pl}$, and the effective stress, that is, $d = d\left(\overline{\boldsymbol{\sigma}}, \tilde{\boldsymbol{\varepsilon}}^{pl}\right)$.

Damaged states in tension and compression are characterized independently by two hardening variables, $\tilde{\varepsilon}_t^{pl}$ and $\tilde{\varepsilon}_c^{pl}$, which are referred to as equivalent plastic strains in tension and compression, respectively. The evolution of the hardening variables is given by an expression of the form:

$$\dot{\tilde{\boldsymbol{\varepsilon}}}^{pl} = \mathbf{h}\left(\bar{\boldsymbol{\sigma}}, \tilde{\boldsymbol{\varepsilon}}^{pl}\right) \cdot \dot{\boldsymbol{\varepsilon}}^{pl}, \tag{3.4.24}$$

with:

$$\tilde{\boldsymbol{\varepsilon}}^{pl} = \begin{bmatrix} \tilde{\varepsilon}_t^{pl} \\ \tilde{\varepsilon}_c^{pl} \end{bmatrix}, \tag{3.4.25}$$

Micro-cracking and crushing in the concrete are represented by increasing values of the hardening variables. These variables control the evolution of the yield surface and the degradation of the elastic stiffness. They are also intimately related to the dissipated fracture energy required to generate micro-cracks.
In terms of effective stresses, the yield function takes the form:

$$F\left(\bar{\boldsymbol{\sigma}}, \tilde{\boldsymbol{\varepsilon}}^{pl}\right) = \frac{1}{1-\alpha}\left(\bar{q} - 3\alpha\bar{p} + \beta\left(\tilde{\boldsymbol{\varepsilon}}^{pl}\right)\left\langle\hat{\bar{\sigma}}_{\max}\right\rangle - \gamma\left\langle\hat{\bar{\sigma}}_{\max}\right\rangle\right) - \bar{\sigma}_c\left(\tilde{\varepsilon}_c^{pl}\right) \le 0, \tag{3.4.26}$$

where α and γ are dimensionless material constants;

$$\bar{p} = -\frac{1}{3}\bar{\boldsymbol{\sigma}} : \mathbf{I} = -\,1/3\left(\bar{\sigma}_1 + \bar{\sigma}_2 + \bar{\sigma}_3\right), \tag{3.4.27}$$

is the effective hydrostatic pressure;

$$\bar{q} = \sqrt{\frac{3}{2}\bar{\mathbf{S}} : \bar{\mathbf{S}}}, \tag{3.4.28}$$

is the Mises equivalent effective stress;

$$\bar{\mathbf{S}} = \bar{p}\mathbf{I} + \bar{\boldsymbol{\sigma}}, \tag{3.4.29}$$

is the deviatoric part of the effective stress tensor $\bar{\boldsymbol{\sigma}}$; and $\hat{\bar{\sigma}}_{\max}$ is the algebraically maximum eigenvalue of $\bar{\boldsymbol{\sigma}}$.
The Macauley bracket $\langle\cdot\rangle$ is defined by $\langle x\rangle = 1/2\left(|x| + x\right)$.

The function $\beta\left(\tilde{\boldsymbol{\varepsilon}}^{pl}\right)$ is given as:

$$\beta\left(\tilde{\boldsymbol{\varepsilon}}^{pl}\right)=\frac{\bar{\sigma}_c\left(\tilde{\varepsilon}_c^{pl}\right)}{\bar{\sigma}_t\left(\tilde{\varepsilon}_t^{pl}\right)}\left(1-\alpha\right)-\left(1+\alpha\right), \tag{3.4.30}$$

where $\bar{\sigma}_c$ and $\bar{\sigma}_t$ are the effective tensile and compressive cohesion stresses, respectively.

In biaxial compression, with $\hat{\bar{\sigma}}_{\max}=0$, Eq. (3.4.26) reduces to well-known Drucker-Prager yield condition. The coefficient α can determined from the initial equibiaxial and uniaxial compressive yield stress, σ_{b0} and σ_{c0}, as:

$$\alpha=\frac{\left(\sigma_{b0}/\sigma_{c0}\right)-1}{2\left(\sigma_{b0}/\sigma_{c0}\right)-1}, \qquad \left(0\le\alpha\le 0.5\right), \tag{3.4.31}$$

The coefficient γ enters the yield function only for stress state of tri-axial compression, when $\hat{\bar{\sigma}}_{\max}\neq 0$. It can be determined by comparing the yield conditions along the tensile and compressive meridians. By definition, the tensile meridian (TM) is the locus of stress states satisfying the condition $\hat{\bar{\sigma}}_{\max}=\hat{\bar{\sigma}}_1>\hat{\bar{\sigma}}_2=\hat{\bar{\sigma}}_3$ and the compressive meridian (CM) is the locus of stress states such that $\hat{\bar{\sigma}}_{\max}=\hat{\bar{\sigma}}_1=\hat{\bar{\sigma}}_2>\hat{\bar{\sigma}}_3$, where $\hat{\bar{\sigma}}_1$, $\hat{\bar{\sigma}}_2$ and $\hat{\bar{\sigma}}_3$ are the eigenvalues of the effective stress tensor.

With $\hat{\bar{\sigma}}_{\max}<0$ the corresponding yield conditions are:

$$\left(\frac{2}{3}\gamma+1\right)\bar{q}-\left(\gamma+3\alpha\right)\bar{p}=\left(1-\alpha\right)\bar{\sigma}_c \qquad \left(TM\right) \tag{3.4.32}$$

$$\left(\frac{1}{3}\gamma+1\right)\bar{q}-\left(\gamma+3\alpha\right)\bar{p}=\left(1-\alpha\right)\bar{\sigma}_c \qquad \left(CM\right) \tag{3.4.33}$$

Let $K_c=\bar{q}_{(TM)}/\bar{q}_{(CM)}$ for any given value of the hydrostatic pressure $\bar{p}$ with $\hat{\bar{\sigma}}_{\max}<0$; then:

$$K_c = \frac{\gamma + 3}{2\gamma + 3}, \tag{3.4.34}$$

The coefficient γ is, therefore, evaluated as:

$$\gamma = \frac{3(1 - K_c)}{2K_c - 1}, \tag{3.4.35}$$

If $\hat{\bar{\sigma}}_{\max} > 0$, the yield conditions along the tensile and compressive meridians reduce to:

$$\left(\frac{2}{3}\beta + 1\right)\bar{q} - (\beta + 3\alpha)\,\bar{p} = (1 - \alpha)\,\bar{\sigma}_c \qquad (TM) \tag{3.4.36}$$

$$\left(\frac{1}{3}\beta + 1\right)\bar{q} - (\beta + 3\alpha)\,\bar{p} = (1 - \alpha)\,\bar{\sigma}_c \qquad (CM) \tag{3.4.37}$$

Let $K_t = \bar{q}_{(TM)} / \bar{q}_{(CM)}$ for any given value of the hydrostatic pressure $\bar{p}$ with $\hat{\bar{\sigma}}_{\max} > 0$; then

$$K_t = \frac{\beta + 3}{2\beta + 3}, \tag{3.4.38}$$

Typical yield surfaces are shown in Figure 3.4.6 in the deviatoric plane and in Figure 3.4.7 for plane-stress conditions.
For sake of simplicity, the equations which define the damage and stiffness degradation are conveniently reported by considering uniaxial loading conditions.
The uniaxial degradation variables (d_t and d_c) are increasing functions of the equivalent plastic strains. They can take values ranging from zero, for the undamaged material, to one, for the fully damaged material.

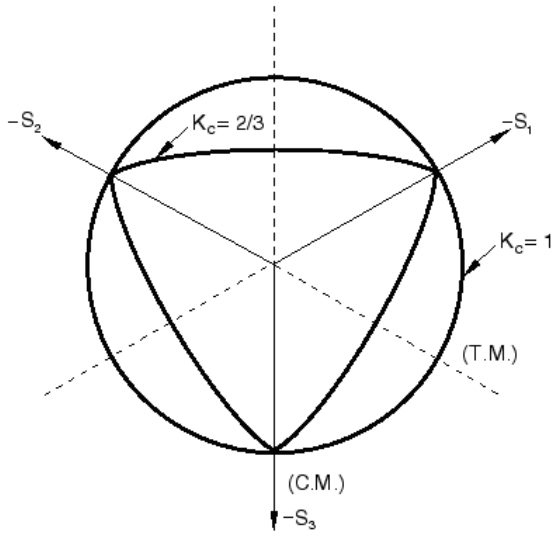

Figure 3.4.6: Yield surfaces in the deviatoric plane, corresponding to different values of K_c [Lee & Fenves 1998]

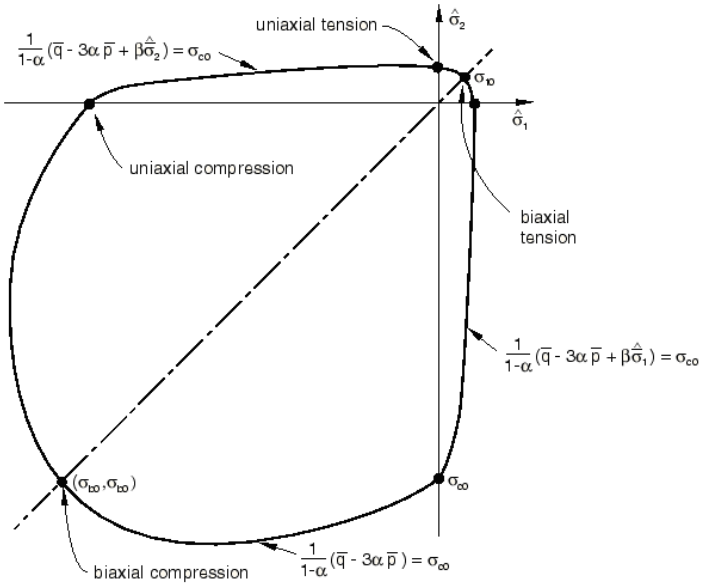

Figure 3.4.7: Yield surface in plane stress [Lee & Fenves 1998]

If E_0 is the initial (undamaged) elastic stiffness of the material, the stress-strain relations under uniaxial tension and compression loading are, respectively:

$$\sigma_t\left(\tilde{\varepsilon}_t^{pl}\right)=\left(1-d_t\right)E_0\left(\varepsilon_t-\tilde{\varepsilon}_t^{pl}\right) \tag{3.4.39}$$

$$\sigma_c\left(\tilde{\varepsilon}_c^{pl}\right)=\left(1-d_c\right)E_0\left(\varepsilon_c-\tilde{\varepsilon}_c^{pl}\right) \tag{3.4.40}$$

Under uniaxial loading cracks propagate in a direction transverse to the stress direction. The nucleation and propagation of cracks, therefore, causes a reduction of the available load-carrying area, which in turn leads to an increase in the effective stress. The effect is less pronounced under compressive loading since cracks run parallel to the loading direction; however, after a significant amount of crushing, the effective load-carrying area is also significantly reduced. The effective uniaxial cohesion stresses, $\bar{\sigma}_t$ and $\bar{\sigma}_c$, are given as:

$$\bar{\sigma}_t\left(\tilde{\varepsilon}_t^{pl}\right)=\frac{\sigma_t}{\left(1-d_t\right)}=E_0\left(\varepsilon_t-\tilde{\varepsilon}_t^{pl}\right) \tag{3.4.41}$$

$$\bar{\sigma}_c\left(\tilde{\varepsilon}_c^{pl}\right)=\frac{\sigma_c}{\left(1-d_c\right)}=E_0\left(\varepsilon_c-\tilde{\varepsilon}_c^{pl}\right) \tag{3.4.42}$$

The effective uniaxial cohesion stresses determine the size of the yield (or failure) surface.

It should be noted here that for tensile loading, damage and plasticity are initiated when the equivalent applied stress reaches the uniaxial tensile strength σ_{b0} as shown in Figure 3.4.8(a). However, under compressive loading, damage is initiated at a different stage than plasticity. Once the equivalent applied stress reaches σ_{c0} (i.e. when nonlinear behaviour starts) damage is initiated, whereas plasticity occurs once σ_{cu} is reached (Figure 3.4.8(b).

Therefore, generally $\sigma_{tu}=\sigma_{b0}$ for tensile loading, but this is not true for compressive loading (i.e. $\sigma_{cu}\neq\sigma_{c0}$).

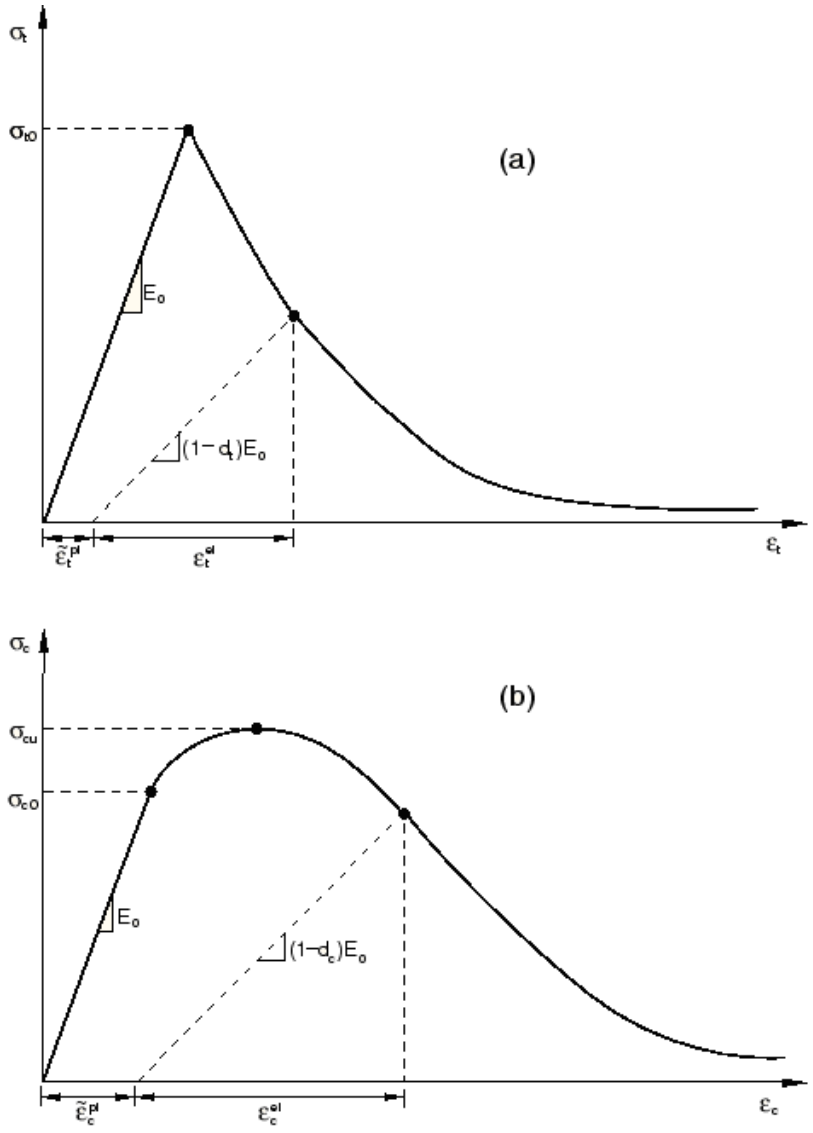

Figure 3.4.8: Concrete behaviour under uniaxial loading in, (a) tension, (b) compression [Lee & Fenves 1998]

The concrete damaged plasticity model assumes a non-associated potential plastic flow rule:

$$\dot{\boldsymbol{\varepsilon}}^{pl} = \dot{\lambda} \frac{\partial G(\bar{\boldsymbol{\sigma}})}{\partial \bar{\boldsymbol{\sigma}}}, \tag{3.4.43}$$

The flow potential G used for this model is the Drucker-Prager hyperbolic function:

$$G = \sqrt{(e\sigma_{t0} tg\psi)^2 + \bar{q}^2} - \bar{p} tg\psi\,, \tag{3.4.44}$$

which makes use of two stress invariants of the effective stress tensor, like yield surface.

Parameter ψ is the dilation angle measured in the p–q plane at high confining pressure; σ_{t0} is the uni-axial tensile stress at failure; and e is an eccentricity parameter, that defines the rate at which the function approaches the asymptote (the flow potential tends to a straight line as the eccentricity tends to zero). When the value of e increases, the curvature to the flow potential becomes greater, implying that the dilation angle increases more rapidly as the confining pressure decreases.

This flow potential, which is continuous and smooth, ensures that the flow direction is always uniquely defined.

The function asymptotically approaches the linear Drucker-Prager flow potential at high confining pressure stress and intersects the hydrostatic pressure axis at 90°.

As it is known, the non associative flow rule is necessary to control the dilatancy in modelling frictional materials like concrete [Chen & Han 1988], but this requires the solution of non-symmetric equations.

In summary, the elastic-plastic response of the concrete damaged plasticity model is described in terms of the effective stress and the hardening variables:

$$\begin{cases} \overline{\boldsymbol{\sigma}} = \mathbf{D}_0^{el} : \left(\boldsymbol{\varepsilon} - \boldsymbol{\varepsilon}^{pl} \right) & \in \left\{ \overline{\boldsymbol{\sigma}} \middle| F\left(\overline{\boldsymbol{\sigma}}, \tilde{\boldsymbol{\varepsilon}}^{pl} \right) \right\} \\ \dot{\tilde{\boldsymbol{\varepsilon}}}^{pl} = \mathbf{h}\left(\overline{\boldsymbol{\sigma}}, \tilde{\boldsymbol{\varepsilon}}^{pl} \right) \cdot \dot{\boldsymbol{\varepsilon}}^{pl} \\ \dot{\boldsymbol{\varepsilon}}^{pl} = \dot{\lambda} \dfrac{\partial G\left(\overline{\boldsymbol{\sigma}} \right)}{\partial \overline{\boldsymbol{\sigma}}} \end{cases} \tag{3.4.45}$$

where $\dot{\lambda}$ and F obey the Kuhn-Tucker conditions $\dot{\lambda} F = 0; \quad \dot{\lambda} \geq 0; \quad F \leq 0$.
The Cauchy stress is calculated in terms of the stiffness degradation variable, $d\left(\overline{\boldsymbol{\sigma}}, \tilde{\boldsymbol{\varepsilon}}^{pl} \right)$, and the effective stress through Eq. (3.4.23).
The constitutive relations for the elastic-plastic response (Eq. (3.4.45)) are decoupled from the stiffness degradation response (Eq. (3.4.23)) which makes the model attractive for an effective numerical implementation.
It's to be noted that, unlike concrete models based on the smeared crack approach, the concrete damaged plasticity model does not have the notion of cracks developing at the material integration point. However, in order to introduce the concept of an effective crack direction with the purpose of obtaining a graphical visualization of the cracking patterns in the concrete structure, different criteria can be adopted within the framework of scalar-damage plasticity for the definition of the direction of cracking.
Lubliner et. al. [1989] assumed that cracking initiates at points where the tensile equivalent plastic strain is greater than zero, $\tilde{\varepsilon}_t^{pl} > 0$, and the maximum principal plastic strain is positive. The direction of the vector normal to the crack plane is assumed to be parallel to the direction of the maximum principal plastic strain.

3.4.4 Oliver et al. model (1991)

Damage models have become, recently, popular techniques for simulating various nonlinear effects in materials. The isotropic damage model of Oliver et al. [1991] includes degradation of the material both in tension and in compression.
The onset of damage is established by imposing a damage condition similar to a yield function in elastoplasticity.

Different tensile and compressive strengths can be specified and the model, even though very simple, has been used, also by others, to attempt a smeared crack type modelling of concrete.
Damage accumulation is represented by using a function of the complementary energy:

$$G(\tau_t) = 1 - \frac{\tau_0}{\tau_t} \exp\left[A\left(1 - \frac{\tau_0}{\tau_t} \right) \right], \tag{3.4.46}$$

where τ_0 is a damage threshold and has the expression:

$$\tau_0 = \left[\frac{(\sigma_t)}{(E_0)^{1/2}} \right], \tag{3.4.47}$$

and τ_t (the term containing the complementary energy) is the current damage strength and has the expression:

$$\tau_t = \max\left\{ \tau_0, \gamma\left(\sigma_t^T \mathrm{E}^{-1} \right)^{\frac{1}{2}} \right\}, \tag{3.4.48}$$

where E denotes as usual the elastic compliance tensor of the undamaged material and is a scalar function of the stresses. For the case of no damage $G(\tau_t) = G(\tau_0) = 0$.
The parameter A in (3.4.46) is a material parameter and has the following expression in Oliver's model:

$$A = \left[\left(\frac{G_f E_0}{\sigma_d^t} \right) - 0.5 \right]^{-1}, \tag{3.4.49}$$

With E_0 initial modulus of elasticity of concrete and G_f fracture energy in mode I of concrete.
Eventually, the secant stiffness matrix of the material is given as:

$$E^{sec} = (1-G)E_0, \tag{3.4.50}$$

From which the current stresses can be easily calculated.
The model has been used because no difficulty whatsoever has been encountered in terms of convergence. It is, admittedly too simplistic, for concrete, but was useful to obtain preliminary results against which to compare those obtained with more sophisticated models.

3.5 MODELLING OF CONCRETE CRACKING

Because of its influence on the mechanism of stress transfer between the FRP and the concrete, cracking of concrete has a great influence on the behaviour of RC beams retrofitted with FRP. Within the framework of the finite element method, there exist several techniques to model crack onset and propagation.
For problems in which the local distribution of stresses is not very important, methods considering the cracks like uniformly spread on a portion of material affected by cracking have become popular. Stresses and strains in such a volume (large enough to contain a few cracks) are represented by averaged values, calculated in some cases taking into account also the reinforcement and its interaction with the base material. In this approach cracking is reduced to a constitutive problem and the continuity is not lost at the element or mesh level with obvious advantages from the implementation point of view.
More precisely models of this kind are referred to as models using the smeared crack concept. The denomination is due to the fact that cracks are somehow smeared into a finite volume rather than localised as discrete discontinuity.
It is opportune, now, to clarify that such an approach is currently used in two, quite different, contexts. One case is the modelling of a large portion of a structure in which a finite element is representative of a volume actually containing series of parallel cracks in one or more directions, for which the smearing is quite a natural operation. In this context the control volume

includes generally also reinforcement uniformly spread in different directions and the constitutive law used is representative of the entire assemblage of uncracked concrete, cracks and reinforcement (note that we deliberately refer to cracks like to a sort of frictious structural unit). The other case is the modelling of the onset and growth of localised cracks into a plain concrete volume.

Although the two applications of the smeared crack concept are quite different they are both developed on the same basic framework. The main difference being mainly the strategy used, in the latter, for the localization of the strains representative of cracking within narrow bands (ideally with the width of a single element).

The first reinforced concrete finite element model which includes the effect of cracking was developed by Ngo and Scordelis [1967], who carried out a linear elastic analysis of beams with predefined crack patterns. The cracks were modelled by separating the nodal points of the finite element mesh and thus creating a discrete crack model (Figure 3.5.1). Although, the lack of generality in crack orientation has made the discrete crack model unpopular, the use of discrete crack models in finite element analysis offers certain advantages over other methods. For those problems that involve a few dominant cracks, the discrete crack approach offers a more realistic description of the cracks, which represent strain discontinuities in the structure.

Such discontinuities are correctly characterized by the discrete crack model. The need for a crack model that offers automatic generation of cracks and complete generality in crack orientation, without the need of redefining the finite element topology, has led the majority of investigators to adopt the smeared crack concept also to model discrete cracks.

Rather than representing a single crack, as shown in Figure 3.5.1 (a), the smeared crack model represents many finely spaced cracks perpendicular to the principal stress direction, as illustrated in Figure 3.5.1 (b).

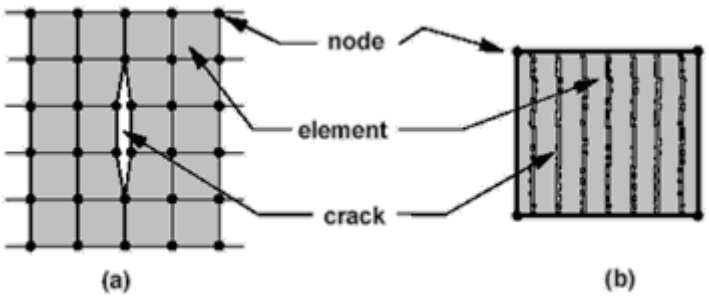

Figure 3.5.1: Cracking models: (a) discrete; (b) smeared

The smeared crack model first used by Rashid [1968] represents cracked concrete as an elastic orthotropic material with reduced elastic modulus in the direction normal to the crack plane. With this continuum approach the local displacement discontinuities at cracks are distributed over some tributary area within the finite element and the behaviour of cracked concrete can be represented by average stress-strain relations. In contrast to the discrete crack concept, the smeared crack concept fits the nature of the finite element displacement method, since the continuity of the displacement field remains intact.

As far as the reinforced concrete beams retrofitted with FRP are concerned local effects are relevant as they largely influence the behaviour of the interface.

In the case of uniform stress distribution and under the spreading action exerted by the reinforcement (both ordinary and external FRP reinforcement) inelastic strains do not localise in the zones where cracks are expected, but tend to spread over the volume, missing to give a good representation of local effects. This behaviour of this kind of model is known to researchers, who recognise that the problem cannot be effectively solved without the introduction a random dishomogeneity of the material .

Because of this tendency to spread the damage into the volume interested by tensile stresses, the smeared cracking models proved to be not suitable for the detailed investigation of the behaviour of RC beams retrofitted with FRP and in particular for the prediction of the interfacial behaviour at the FRP to

concrete joint. The initial approach of resorting to preset cracks proved to be therefore more adequate.

In the finite element analysis carried out in this work, cracking of concrete has been dealt with by introducing preset cracks in the finite element mesh. This approach was justified because the crack pattern on the beams analysed was known from experimental records and because the main focus was not on the prediction of the formation and propagation of cracks, but on their effect on the performance of the structure once formed and fully developed.

It is important to note that there exist, nowadays, techniques enabling the introduction of discontinuities in the displacement field within a finite element and therefore a more realistic modelling of cracking. The implementation of these techniques, likewise that of others involving automatic generation of a new mesh, when a crack forms, is outside the scope of this research work.

CHAPTER IV
FRACTURE MECHANICS and COHESIVE-ZONE MODELS

4.1 INTRODUCTION to BASIC CONTINUUM MECHANICS

Considering an initial position **X** of a material point and the next position **x**, given by **x**=**X**+**u**, and the elementary displacements *d***x** and *d***X** we can write that:

$$d\mathbf{x} = \frac{\partial \mathbf{x}}{\partial \mathbf{X}} d\mathbf{X} = \mathbf{F} d\mathbf{X} \tag{4.1.1}$$

We define the Green Lagrange strain tensor as:

$$\mathbf{E} = \frac{1}{2}\left(\mathbf{F}^T\mathbf{F} - \mathbf{I}\right) \tag{4.1.2}$$

By differing the expression of **x** according to **X** we obtain **F**=**I**+**D** where **D**=**gradu**. So:

$$\mathbf{E} = \frac{1}{2}\left[\mathbf{D}^T + \mathbf{D}\right] + \frac{1}{2}\mathbf{D}^T\mathbf{D} \tag{4.1.3}$$

In a crack problem, we often deal with small deformations. Consequently, **E** can be linearised at the first order and we introduce the small strain tensor ε defined as:

$$\boldsymbol{\varepsilon} = \frac{1}{2}\left[\mathbf{D}^T + \mathbf{D}\right] \tag{4.1.4}$$

The mechanical equilibrium in small strains is given by the principle of virtual work:

$$W = W_i^* - W_e^* = \int_V \boldsymbol{\sigma} : \delta\boldsymbol{\varepsilon}_v dV - W_e^* \tag{4.1.5}$$

Where W^*_e is the virtual work due to the external load, W^*_i is the virtual work due to the internal forces, and $\delta\boldsymbol{\varepsilon}_v$ is a virtual strain change. So we need to know the change, $\delta\boldsymbol{\varepsilon}$, in order to have a simpler expression of the virtual work.

$$\delta\boldsymbol{\varepsilon} \approx \boldsymbol{\varepsilon}\left(\mathbf{u} + \delta\mathbf{u}\right) - \boldsymbol{\varepsilon}\left(\mathbf{u}\right) \tag{4.1.6}$$

After calculus, we obtain the expression:

$$\delta\boldsymbol{\varepsilon} = \frac{1}{2}\left(\delta\mathbf{D}^T + \delta\mathbf{D}\right) \tag{4.1.7}$$

Where $\delta\mathbf{D}$ is equal to **grad**($\delta\mathbf{u}$). Considering equation (4.1.7), the virtual strain $\delta\boldsymbol{\varepsilon}_v$ becomes:

$$\delta\boldsymbol{\varepsilon}_v = \frac{1}{2}\delta\mathbf{D}_v^{\,T} + \delta\mathbf{D}_v \tag{4.1.8}$$

Finally we have the following expression of the virtual work:

$$W = \int_V \boldsymbol{\sigma} : \delta\mathbf{D}_v dV - \mathbf{P}_e^* \tag{4.1.9}$$

The equation (4.1.9) will allow the formulation of the out-of-balance force vector **g** used in non-linear procedures, while to form the tangent stiffness matrix, we can use the change in (4.1.9):

$$W \approx W_0 + \delta W \tag{4.1.10}$$

Accordingly, the virtual work need to be differentiated:

$$\delta W = \int_V \delta\boldsymbol{\sigma} : \delta\mathbf{D}_v dV \tag{4.1.11}$$

Knowing the behaviour law $\boldsymbol{\sigma}=\boldsymbol{C}\,\boldsymbol{\varepsilon}$ we can express the change in $\boldsymbol{\sigma}$ as:

$$\delta\boldsymbol{\sigma} \approx \mathbf{D}_t \delta\boldsymbol{\varepsilon} \tag{4.1.12}$$

Inserting this equation in the change of the virtual work, it results:

$$\delta W = \int_V \mathbf{D}_t \delta\boldsymbol{\varepsilon} : \delta\boldsymbol{\varepsilon}_v dV - \delta W_e^* \tag{4.1.13}$$

This decomposition allows the use of a finite-element formulation and the study small strain problems with linear or non-linear materials. In general, dealing with large strains leads to a second term in the formulation, which introduces consequently non-linear geometry.

4.2 BASIC FINITE-ELEMENT ANALYSIS OF CONTINUA

In this section the approximation of the continuum formulation by means of a finite element discretisation will be illustrated considering for simplicity a two-dimensional formulation. The structure is then divided into a finite number N_e of elements. For each of them, equation (4.1.7) can be separately written and then an assembly procedure is used in order to obtain the complete system of equations. Focusing the attention to a simple element, where the displacement *u* and *v* are related to nodal values **u** and **v** via shape function **h** as follows:

$$u = \mathbf{hu} \tag{4.2.1}$$

$$v = \mathbf{hv} \tag{4.2.2}$$

The deformation ε can be expressed as follows:

$$\boldsymbol{\varepsilon} = \mathbf{B}_1 \mathbf{p} \tag{4.2.3}$$

and

$$\delta\boldsymbol{\varepsilon} = \mathbf{B}_1 \delta\mathbf{p} \tag{4.2.4}$$

Where $\mathbf{p}$ contains the vector of element nodal displacement and $\mathbf{B_1}$ is a matrix. Substituting (4.2.4) into (4.1.7) it gives:

$$W_e = \delta\mathbf{p}_v^T \int_V \mathbf{B}_1 : \boldsymbol{\sigma} dV - \delta\mathbf{p}_v \delta\mathbf{q}_e = \delta\mathbf{p}_v^T \mathbf{g} \tag{4.2.5}$$

With the notation $\mathbf{q}_i = \int_V \mathbf{B}_1 : \boldsymbol{\sigma} dV$, where $\mathbf{q_i}$ represent the internal forces, from equation (4.2.5), the out-of-balance force vector $\mathbf{g}$ is given by:

$$\mathbf{g} = \mathbf{q}_i - \mathbf{q}_e \tag{4.2.6}$$

As W=0 for each $\delta\mathbf{p}_v$, Eq. (4.2.5) gives $\mathbf{g}=\mathbf{0}$, and this problem is referable to the problem just explained in the first section.
It needs also to know the tangent stiffness matrix $\mathbf{K_t}$ in order to use non-linear methods. From $\delta W = \delta\mathbf{p}_v^T \delta\mathbf{g}$, it results:

$$\delta W = \delta\mathbf{p}_e^T \frac{\partial \mathbf{g}}{\partial \mathbf{p}} \delta\mathbf{p} \tag{4.2.7}$$

The tangent stiffness matrix defined by $\mathbf{K}_t = \frac{\partial \mathbf{g}}{\partial \mathbf{p}}$ can be used in order to solve the mechanical problem.

4.3 LEFM and DAMAGE MECHANICS

4.3.1 Linear Elastic Fracture Mechanics

The linear elastic fracture mechanics (LEFM) is based on an elastic analysis of the stress field for small strains. It gives excellent results for brittle-elastic materials. With the occurrence of plasticity or visco-plasticity, we enter into the field of non-linear fracture mechanics, which uses more complicated

methods. The analysis of stresses and strains in the vicinity of crack tips constitutes a necessary basis for studying crack behaviour. Fracture mechanics assumes the existence of an initial crack in the structure.

4.3.1.1 Global Energy Balance

For fracture to occur, the energy stored in the structure must be sufficient to overcome the surface energy of a material. It can be defined by the Griffith energy balance for an incremental increase in the crack area *dA* under equilibrium condition:

$$\frac{dE}{dA} = \frac{d\pi}{dA} + \frac{dW_s}{dA} = 0 \qquad (4.3.1)$$

E is the total energy, π is the potential energy supplied by the internal strain energy and external forces, W_s is the work required to create new surfaces. Two different approaches can be considered for studying fractures.

4.3.1.2 The energy approach

The energy approach is equivalent to the Griffith model. The energy release rate G is a measured of the energy available for an increment of crack extension:

$$G = -\frac{d\pi}{dA} \qquad (4.3.2)$$

Thus, G is also indicated as the crack extension force.

Crack extension occurs when G reaches a critical value $G_c = \frac{dW_e}{dA} = 2\omega_f$, called critical energy release rate or fracture energy.

4.3.1.3 The stress analysis of cracks

One can show that the stress field in any linear elastic cracked body for an infinite plate is:

$$\sigma_{ij} = \frac{k}{\sqrt{r}} f_{ij}(\theta) + \sum_{m=0}^{\infty} A_m r^{\frac{m}{2}} g_{ij}^{(m)}(\theta) \qquad (4.3.3)$$

with a polar coordinate axis with the origin at the crack tip. Near the crack tip, σ_{ij} varies with $r^{1/2}$ and introducing the stress intensity factor $K=k(2\pi)^{1/2}$, the stress fields ahead of a crack tip in an isotropic linear elastic material can be written as:

$$\lim_{r\to\infty} \sigma_{ij}^{\,n} = \frac{K_n}{\sqrt{2\pi r}} f_{ij}^{\,n}(q), \qquad (4.3.4)$$

where n corresponds to mode I, II, or III. The knowledge of K_n enables to find all the components of the stress tensor or the displacement components in a cracked structure which is assumed to behave elastically.
Although stress intensity solutions are given in a variety of forms, K_n can always be related to the crack through the correction factor:

$$K = Y\sigma\sqrt{\pi a}\,, \qquad (4.3.5)$$

where σ is a characteristic stress, a is a characteristic crack dimension and Y is a dimensionless constant that depends on geometry and mode loading.

4.3.1.4 Relation between K and G

The term G quantifies the net change in potential energy that accompanies an increment of crack extension, and K characterises the stresses strains and displacements near the crack tip. Meaningfully, G is for a global behaviour while K is for a local analysis.
For example, considering a two-dimensional mode I problem, and denoting by E and ν the Young modulus and the Poisson ratio, the following formula holds:

$$G = \frac{K_I^2}{E}, \qquad (4.3.6)$$

with $E' = E$ for plane stress and $E' = \frac{E}{1-\nu^2}$ for plane strain.

4.3.2 Fracture Based Approaches

A number of relationships are available that attempt to quantify the critical relationship between stress, flaw size, and toughness, but each of these approaches is only suitable in limited situations. Analytical values of crack variables are only available for very simple geometries. Thus, it becomes necessary to resort to finite-element analysis. The setting up of a mesh constitutes a difficult problem since it must represent the singular stress field in the vicinity of the crack tip. The global approach to crack growth uses the crack variables *K*, *G* or *J*.
A brief outline of some finite element procedures to analyse fracture process will be done in the follows. Most of these approaches are formulated in the hypotheses of linear and elastic material.

4.3.2.1 Local analysis: direct method

In the direct method, the stress intensity factor is determined directly from the computed stresses, or the displacement field, in the vicinity of the crack tip. This technique requires a high accuracy in calculations due to the presence of the singularities. Once the displacement field has been determined, a simple way of obtaining the stress intensity factors is by using, for example, relations in plane stress:

$$K_n = \lim_{r \to 0} \left[\frac{E}{8} \left(\frac{2\pi}{r} \right)^{1/2} \left[\left| u_n \right| \right] \right], \qquad (4.3.7)$$

Other methods are based on the calculation of the energy release rate for a unit growth of the crack. These indirect methods use nodal information to obtain the energy release rate, which can be used to calculate **K**.

4.3.2.2 Virtual crack extension

This method enables to compute G for a very small crack extension. The potential energy is given as follows:

$$\boldsymbol{\pi} = \frac{1}{2}\mathbf{p}^T\mathbf{K}\mathbf{p} - \mathbf{p}^T\mathbf{F}\,, \tag{4.3.8}$$

where **p** are the nodal displacement, **K** is the stiffness matrix and **F** are the external nodal forces. Then the energy release rate is computed as:

$$G = -\frac{d\boldsymbol{\pi}}{dA} = -\frac{d\mathbf{p}^T}{dA}\left[\mathbf{K}\mathbf{p} - \mathbf{F}\right] - \frac{1}{2}\mathbf{p}^T\frac{d\mathbf{K}}{dA}\mathbf{p} + \mathbf{p}^T\frac{d\mathbf{F}}{dA} \tag{4.3.9}$$

Using the equilibrium **Kp-F=0**, we obtain:

$$G = -\frac{1}{2}\mathbf{p}^T\frac{d\mathbf{K}}{dA}\mathbf{p} \tag{4.3.10}$$

Generating a finite-element mesh for a body with crack length a, the extension of crack by Δa, assuming that the small crack has only a local effect, can be obtained through the following expression for the energy release rate:

$$G = -\frac{1}{2}\mathbf{U}^T\sum_{i=1}^{N_c}\frac{d\mathbf{K}}{dA}\mathbf{U} \tag{4.3.11}$$

4.3.2.3 The virtual crack closure method

The formulation was originally addressed by Rybicki and Kanninen for two-dimensional problems. The crack closure method is based on the fact that the energy needed to extend a crack of length a by an infinitesimal amount Δa is equal to the energy needed to close the crack to its original length. In the follows this method will be briefly explained. The energy release rate is computed with the sole use of nodal forces and displacements. For simplicity, a two-dimensional problem with a unit thickness will be considered. The energy release rate is expressed as follows:

$$G = \lim_{\Delta a \to 0} \frac{\left(W(a+\Delta a) - W(a)\right)}{\Delta a} = \lim_{\Delta a \to 0} \frac{1}{2\Delta a} \int_0^{\Delta a} \sigma_{yy} v(r)\, dr \quad (4.3.12)$$

where σ_{yy} is the distribution of normal stress and *v(r)* is the crack profile of a flaw in y-direction (Figure 4.4.1 (a)). The integral is then derived analytically in terms of nodal forces and displacements. For a linear element, the energy release rates can be computed as (Figure 4.4.1 (b)):

$$G_I = \frac{1}{2\Delta a} F_y^i \left(v_k^{top} - v_k^{bot}\right) \quad (4.3.13)$$

$$G_{II} = \frac{1}{2\Delta a} F_x^i \left(u_k^{top} - u_k^{bot}\right) \quad (4.3.14)$$

where F_i is the nodal force at node *I*, v_k is the nodal displacement at node k and v_{ktop} - v_{kbot} is the difference in displacement in y direction between the top and the bottom surface of opposite crack tip elements.

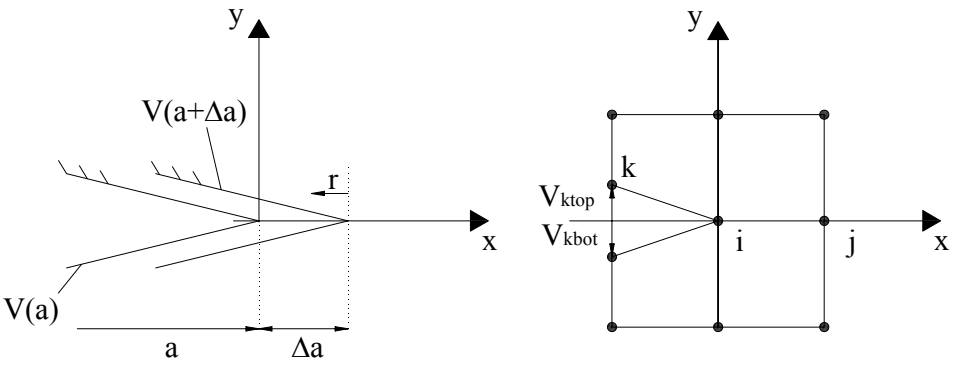

Figure 4.3.1: (a) geometry at crack tip; (b) linear element at crack tip

4.3.2.4 The J contour integral

Another way of characterising the singularity of the stress field in the vicinity of a crack tip consists in studying certain contour integrals deduced

on the basis of the law of conservation energy. Rice presented a path-independent contour integrals for analysis of cracks. He then showed that the value of this integral, which is called **J**, is equal to the energy release rate in a linear or non-linear elastic body that contains a crack. The J-integral has enjoyed a great success as a fracture characterizing parameter for non-linear materials. Also this method will be briefly described. Considering an arbitrary counter-clockwise path Γ around the crack tip (Figure 4.4.2). The J-integral is given by:

$$J = \int_{\Gamma} \left(w dy - T_i \frac{\partial u_i}{\partial x} ds \right), \tag{4.3.15}$$

where w is the strain energy density, T_i are components of the traction vector, u_i are the displacement vector components and ds is a length increment along Γ. The strain energy density is defined as:

$$w = \int_0^{\varepsilon_{ij}} \sigma_{ij} d\varepsilon_{ij} \tag{4.3.16}$$

The traction is a stress vector normal to the contour.

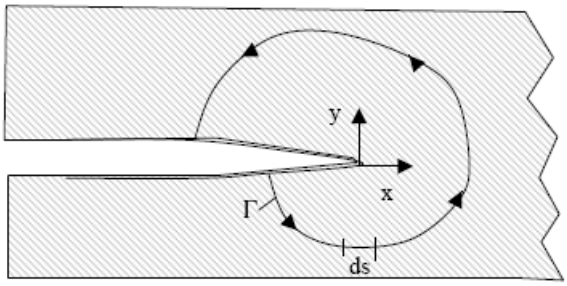

Figure 4.3.2: Arbitrary contour around the crack tip

This integral is independent of the contour of the integration. Having such a method, the J-integral method can be used in a finite-element formulation by evaluating the stresses and strains that must be evaluated on the contour, which is, in general, formed by the sides of the finite elements. An

interpolation process must therefore be used to obtain the edge values from the known values at the Gauss points.

4.4 SOLID ELEMENTS

In this section a brief description of the formulation at the basis of solid elements approach will be done. They will be used for the modelling of concrete, steel bars and FRP reinforcement in the numerical analyses of the RC beams retrofitted with composite sheets because they provide a detailed distribution of stresses and strains within the beams, as it will be explained in Chapter VII.

4.4.1 Introduction

Any combination of elements can be used to make up a model. Sometimes multi-point constraints are required for application of the necessary kinematic relations to form the model.

All elements use numerical integration to allow complete generality in material behaviour. All of the elements can be formulated in a global Cartesian coordinate system except the axisymmetric elements, which are formulated in terms of *r–z* coordinates. In almost all elements, primary vector quantities (such $\boldsymbol{u}$ as displacements and rotations Φ) are defined in terms of nodal values with scalar interpolation functions. For example, in elements with a two-dimensional topology the interpolation can be written as:

$$u(g,h) = N^N(g,h)u^N \tag{4.4.1}$$

where the interpolation functions $N^N(g,h)$ are written in terms of the parametric coordinates *g* and *h*. In most element types the same parametric interpolation is used for the coordinate vector:

$$\mathbf{x}(g,h) = N^N(g,h)\mathbf{x}^N \tag{4.4.2}$$

Such *isoparametric* elements are able to represent all rigid body modes and homogeneous deformation modes exactly.
All elements are integrated numerically. Hence, the virtual work integral will be replaced by a summation:

$$\int_V \sigma : \delta D dV \rightarrow \sum_{i=1}^{n} \sigma_i : \delta D_i dV_i \qquad (4.4.3)$$

where n is the number of integration points in the element and V_i is the volume associated with integration point i. It can be used either "full" or "reduced" integration. For full integration the number of integration points is sufficient to integrate the virtual work expression exactly, at least for linear material behaviour. For triangular and tetrahedral elements may be used a full integration.
The reduced integration can be used for quadrilateral and hexahedral elements; in this procedure the number of integration points is sufficient to integrate exactly the contributions of the strain field that are one order less than the order of interpolation. The (incomplete) higher-order contributions to the strain field, which are present in these elements, are neglected.
The advantage of the reduced integration elements is that the strains and stresses are calculated at the locations that provide optimal accuracy, the so-called Barlow points [Barlow, 1976]. A second advantage is that the reduced number of integration points decreases the computational cost in terms of CPU time and storage requirements. The disadvantage is that the reduced integration procedure can admit deformation modes that cause no straining at the integration points. These zero-energy modes make the element rank-deficient and cause a phenomenon called "hourglassing," where the zero energy mode starts propagating through the mesh, leading to inaccurate solutions. To prevent these excessive deformations, an additional artificial stiffness is added to the element. In this so-called hourglass control procedure, a small artificial stiffness is associated with the zero-energy deformation modes.
Most fully integrated solid elements are unsuitable for the analysis of (approximately) incompressible material behaviour. The reason for this is

that the material behaviour forces the material to deform (approximately) without volume changes. Fully integrated solid element meshes, and in particular lower-order element meshes, do not allow such deformations (other than purely homogeneous deformation).
The "selectively reduced" integration in these elements is used for the volume strain and full integration for the deviatoric strains. As a consequence the lower-order elements give an acceptable performance for approximately incompressible behaviour.

4.4.2 Solid Elements Overview

Solid elements are of two-dimensional and three-dimensional kind. The two-dimensional elements allow modelling of plane and axisymmetric problems and include extensions to generalized plane strain.
The solid elements can be isoparametric: quadrilaterals in two dimensions and "bricks" in three dimensions. These isoparametric elements are generally preferred for most cases because they are offered with first- and second-order interpolation: thus they should be used in any critical region (such as an area where the strain must be predicted accurately).
Solid elements are provided with first-order (linear) and second-order (quadratic) interpolation. The first-order elements are essentially constant strain elements: the isoparametric forms can provide more than constant strain response, but the higher-order content of the solutions they give is generally not accurate and, thus, of little value. The second-order elements are capable of representing all possible linear strain fields. This observation logically leads to the use of the "hierarchical" finite element technique: refining the model by increasing the interpolation order in the elements in critical regions.
The argument is readily extended to higher-order interpolation (cubic, quartic, etc), but the rapid increase in cost per element for higher-order forms means that, even though the accuracy per degree of freedom is higher, the accuracy per computational cost may not be increasing. Practical experience suggests that, except in special cases, little is gained by going beyond the second-order elements.

4.4.3 Solid Elements Formulation (Hughes & Winget 1962)

All the solid elements allow for finite strain and rotation in large-displacement analysis.
For kinematic linear analysis the strain is defined as:

$$\boldsymbol{\varepsilon} = sym\left(\frac{\partial \mathbf{u}}{\partial \mathbf{X}}\right) \tag{4.4.4}$$

Where ***u*** is the total displacement and ***X*** is the spatial position of the point under consideration in the original configuration. This measure of strain is useful only if the strains and rotations are small (all components of the strain and rotation matrices are negligible compared to unity).
When the hyperelastic or hyperfoam material definition is used with an element, the stretch values are calculated directly from the deformation gradient matrix to compute the material behaviour. With any other material behaviour it is assumed that any elastic strains are small compared to unity, so the appropriate reference configuration for the elasticity is only infinitesimally different from the current configuration and the appropriate stress measure is, therefore, the Cauchy ("true") stress. More precisely, the appropriate stress measure should be the Kirchhoff stress defined with respect to the elastic reference configuration, but the assumption that this reference configuration and the current configuration are only infinitesimally different makes the Kirchhoff and Cauchy stress measures almost the same: the differences are on the order of the elastic strains compared to unity.
The conjugate strain rate to Cauchy stress is the rate of deformation, $\mathbf{D} = sym\left(\frac{\partial \mathbf{v}}{\partial \mathbf{x}}\right)$.

Where **v** is the velocity at a point and **x** are the current spatial coordinates of the point. The strain is, therefore, defined as the integral of the rate of deformation. The total strain is constructed by integrating the strain rate approximately over the increment by the central difference algorithm; and, when the strain components are referred to a fixed coordinate basis, the

strain at the start of the increment must also be rotated to account for the rigid body rotation that occurs in the increment.
This is also done approximately, using the Hughes & Winget method [1980]. This integration algorithm defines the integration of a tensor associated with the material behaviour as:

$$\mathbf{a}_{t+\Delta t} = \Delta R \bullet \mathbf{a} \bullet \Delta R^T + \Delta \mathbf{a}\left(\Delta D\right), \tag{4.4.5}$$

where a is the tensor; $\Delta\mathbf{a}$ is the increment in the tensor associated with the material's constitutive behaviour, and, therefore, dependent on the strain increment, $\Delta\mathbf{D}$, defined by the central difference formula as:

$$\Delta\mathbf{D} = sym\left(\frac{\partial\Delta\mathbf{u}}{\partial\mathbf{x}_{t+\Delta t}}\right), \tag{4.4.6}$$

where

$$\mathbf{x}_{t+\Delta t} = \frac{1}{2}\left(\mathbf{x}_t + \mathbf{x}_{t+\Delta t}\right), \tag{4.4.7}$$

and $\Delta\mathbf{R}$ is the increment in rotation, defined by Hughes and Winget as:

$$\Delta\mathbf{R} = \left(\mathbf{I} - \frac{1}{2}\Delta\mathbf{W}\right)^{-1}\left(\mathbf{I} + \frac{1}{2}\Delta\mathbf{W}\right), \tag{4.4.8}$$

where $\Delta\mathbf{W}$ is the central difference integration of the rate of spin:

$$\Delta\mathbf{W} = asym\left(\frac{\partial\Delta\mathbf{u}}{\partial\mathbf{x}_{t+\Delta t/2}}\right) \tag{4.4.9}$$

A somewhat different algorithm to calculate $\Delta\mathbf{R}$ is used for the Green-Naghdi rate. For example, the stress is integrated by this method as:

$$\boldsymbol{\sigma}_{t+\Delta t} = \Delta\mathbf{R} \bullet \boldsymbol{\sigma}_t \bullet \Delta\mathbf{R}^T + \Delta\boldsymbol{\sigma}\left(\Delta\mathbf{D}\right), \tag{4.4.10}$$

where $\Delta\boldsymbol{\sigma}(\Delta\mathbf{D})$ is the stress increment caused by the straining of the material during this time increment and $\boldsymbol{\sigma}$ is the Cauchy stress. The subscripts t and $t+\Delta t$ refer to the beginning and the end of the increment, respectively.
The contribution of the internal work terms to the Jacobian of the Newton method that is often used is:

$$\int_V \left(d\boldsymbol{\sigma} : \delta\mathbf{D} + \boldsymbol{\sigma} : d\delta\mathbf{D} \right) dV, \tag{4.4.11}$$

where $d\boldsymbol{\sigma}$ and $\boldsymbol{\sigma}$ are evaluated at the end of the increment.
Using the integration definition above, it can be shown that:

$$d\boldsymbol{\sigma}_{t+\Delta t} = d\Delta\mathbf{R}\bullet\Delta\mathbf{R}^T \left(\boldsymbol{\sigma}_{t+\Delta t} - \Delta\boldsymbol{\sigma} \right) + \left(\boldsymbol{\sigma}_{t+\Delta t} - \Delta\boldsymbol{\sigma} \right) \Delta\mathbf{R}\bullet d\Delta\mathbf{R}^T + \mathbf{C} : d\Delta\mathbf{D}, \tag{4.4.12}$$

where $\mathbf{C}$ is the Jacobian matrix of the constitutive model:

$$\mathbf{C} = \frac{\partial\Delta\boldsymbol{\sigma}}{\partial\Delta\mathbf{D}} \tag{4.4.13}$$

However, rather than computing the tangent matrix for the Newton method on this basis, this can be approximated by using:

$$d\boldsymbol{\sigma}_{t+\Delta t} = d\mathbf{W}\bullet\boldsymbol{\sigma}_{t+\Delta t} + \boldsymbol{\sigma}_{t+\Delta t}\bullet d\mathbf{W}^T + \mathbf{C} : d\mathbf{D}, \tag{4.4.14}$$

which yields the Jacobian:

$$\int_V \left(\delta\mathbf{D} : \mathbf{C} : d\mathbf{D} - \boldsymbol{\sigma} : \left(2\delta\mathbf{D}\bullet d\mathbf{D} - \frac{\partial\delta\mathbf{v}^T}{\partial\mathbf{x}} \frac{\partial\delta\mathbf{v}}{\partial\mathbf{x}} \right) \right) dV \tag{4.4.15}$$

This Jacobian is the tangent stiffness of the rate form of the problem. Experience with practical cases suggests that this approximation provides an acceptable rate of convergence in the Newton iterations in most applications with real materials.

The strain and rotation measures described above are approximations. Probably the most limiting aspect of these approximations is the definition of the rotation increment $\Delta\mathbf{R}$. While this measure does give a representation of the rotation of the material at a point in some average sense, it is clear that each of the individual material fibres at a point has a different rotation. This suggests that the integration methods described above are not suitable for such material models at large strains (for practical purposes with typical material parameters this means that the solutions will be quite wrong when the strains are greater than 20%-30%).

4.5 INTERFACE ELEMENTS and COHESIVE-ZONE MODELS

4.5.1 Introduction of the interface problem

Actually, the interfacial interaction concrete/FRP and concrete/steel bars is not a phenomenon localised at the physical joint between the two materials but involves a small volume around it. The observable slip between the materials is due in reality to inelastic deformation of a small portion of concrete (and of the adhesive for the FRP case). For the simulation of the interaction between the two materials through a finite-element approach, involving such a number of sources of nonlinearity as the analysis of RC beams retrofitted with FRP, it is convenient to represent the interfacial interaction in global terms through the introduction of an interfacial stress and a relative slip between the two materials which is a measure of the relative movement between two points in the two material associated with the location at which the interfacial stress is evaluated.

In order to study such problems, one can use the direct application of fracture energy. When non-linearities can be neglected, methods based on linear elastic fracture mechanics (LEFM) are quite effective for two-dimensional problems. It does however need to assume that the stress field, when a crack is perturbed, is self similar. This forces the use of very small elements at a crack front and poses essential difficulties where a curved

crack front develops due to spatially varying energy release rates. As in all fracture mechanics models, it is necessary to assume an initial flaw, which introduces an indeterminacy, thus these methods are restricted to problems in which the initial position of the crack is known.
The problems due to the direct application of the fracture mechanics based techniques (i.e., virtual crack closure method) for the study of delamination of composite, such as the curved fronts and the initial flaws, can be overcome by using hypothetical "interface elements" which are embedded at potential delamination sites.
Progressive delamination is then modelled by introducing a softening traction/relative displacement relationship as a "material model" for the interface elements. Fracture mechanics is indirectly introduced because the area under the softening curve is equated (as an input parameter) to the critical fracture energy.
Thus, the interfacial behaviour FRP/concrete and the bond slip behaviour of steel bars can be effectively modelled by using interface elements. Using this approach we define a surface of separation (a line in two-D problems) between different materials and describe their interaction by defining a relative displacement at each contact point and the associated dual stress component.
These procedures are based on the assumption of a "cohesive zone" and the method is applied in conjunction with interface elements and is modelled on the basis of the damage mechanics combined with an indirect introduction of fracture mechanics.
Considering two layers of a composite structure, we can define at the interface Γ the forces $t = \sigma n$ applied by one part on the other when the normal n of the interface is given (Figure 4.5.1 (a)). We assume that the interface can be progressively damaged until complete separation of the two parts, initially glued together. The interface is initially divided in a completely cracked part Γ_{0d} and a part Γ_{0nd} where the cohesion between the two layers is complete. During the loading process, the delaminated part can increase and we assume the existence of a new zone corresponding to the cohesive zone where the traction are not zero and relative displacements can appear (Figure 4.5.1 (b)).

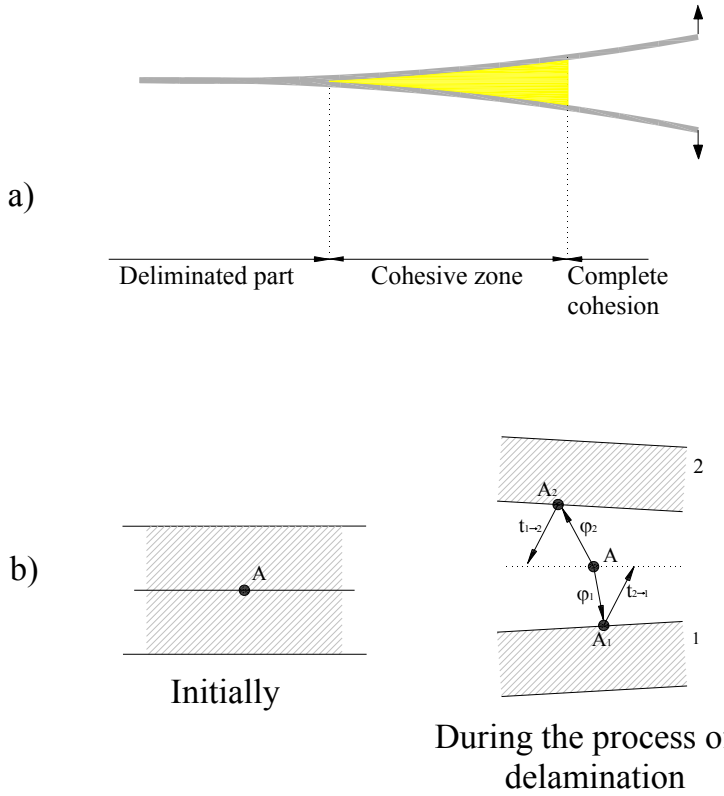

Figure 4.5.1. (a) Different parts of an interface; (b) Tractions and relative displacements for an interface

A constitutive law for the interface needs then to connect the traction vector *t* to the relative displacement vector between the two layers.

Tractions and relative displacements are the key components of the "cohesive model" and appear in the equilibrium equation of the body.

In order to introduce the cohesive-zone model approach let us consider two layers denoted as $\Omega_i \left(i=1,2\right)$, and an interface between these layers denoted as Γ. Applied the principle of virtual work for each layer, it can be written:

$$\int_{\Omega_i} \boldsymbol{\sigma}_i \mathbf{grad}\left(\phi\right) dV = \int_{\Omega_i} \rho \mathbf{f} \phi dV + \int_{\partial\Omega_i} \mathbf{F} \phi dS \qquad (4.5.1)$$

where **F** are the boundary tractions, ρ**f** are body forces applied to the layer Ω_i, and ϕ is a virtual displacement field.
According to the principle of reciprocal actions, at the interface we have the following relation:

$$\mathbf{t}_{1\to 2} = -\mathbf{t}_{2\to 1} \Rightarrow \|\mathbf{t}\| = \mathbf{0} \tag{4.5.2}$$

Adding the different equations (4.5.1), the term using boundary tractions can be written as follows:

$$\sum_i \int_{\partial\Omega_i} \mathbf{F}\phi dS = \sum_i \int_{\partial\Omega_i - \Gamma} \mathbf{F}\phi dS + \sum_i \int_{\Gamma} \mathbf{F}\phi dS \tag{4.5.3}$$

Making use of Eq. (4.5.2), the second term in the above equation (integration over Γ) can be expressed as:

$$\sum_i \int_{\Gamma} \mathbf{F}\phi dS = \int_{\Gamma} \mathbf{t}_{1\to 2}\phi_1 dS + \int_{\Gamma} \mathbf{t}_{2\to 1}\phi_2 dS = \int_{\Gamma} \mathbf{t}_{1\to 2}\left(\phi_1 - \phi_2\right) dS \tag{4.5.4}$$

Setting $\delta^* = \left(\phi_2 - \phi_1\right)$ the principle of the virtual work for the whole structure is finally:

$$\int_{\Omega_i} \boldsymbol{\sigma}_i \mathbf{grad}\left(\phi\right) dV + \int_{\Gamma} \mathbf{t}_{1\to 2}\delta^* dS = P_e^* \tag{4.5.5}$$

Where P_e^* is the power of external loads.
As may be seen in Eq. (4.5.5), the presence of an interface results in the addition of a new term to the virtual power of internal forces. This terms links the relative displacement δ to the corresponding traction t. The relative displacement δ plays the role of a deformation measure, with the tractions furnishing the conjugate stress measure. This expression is fundamental for methods based on the existence of a "cohesive-zone" and particularly for the interface elements methods.
It must be noticed that, along the interface, the displacements can be large, but the relative displacements are small in the non-fully delaminated part or

in the laminated part of the specimen. This hypothesis of small relative displacements allows the use of interface laws formulated in the small perturbation case and enables to use finite-element formulation, as already discussed in section 4.1 and 4.2, for the "interface" term in Eq. (4.5.5).
Depending on the direction of the load with respect to the direction of the crack, three important mechanisms for the relative displacements of the crack tips can occur. In other words, t and δ have three components and each of them corresponds to one mode: mode I is the opening mode parallel to the axis y, mode II is the sliding mode parallel to the axis x and mode III is the tearing mode parallel to the axis z. A cracked body can be loaded in any one of these modes (uncoupled delamination) or a combination of two or three modes (mixed-mode delamination).

4.5.2 Interface Elements

To introduce the interface elements let us focus the attention on two dimensional problems. In the interface-elements approach to debonding and delamination problems it is assumed that the interface has a null thickness (Figure 4.5.2), whereby the interface can be viewed as a couple of lines which exactly occupy the same position in the initial configuration domain. These two lines will be indicated as bottom (b) line and top (t) line so that, on each point of the initial configuration of the interface, there exist two points, one point on the bottom line and one other on the top line. Accordingly, two displacement vectors can be defined, namely a displacement u_b of the point on the bottom line and a displacement u_t of the point of the top line.
In this way, a discontinuity for the displacement field is introduced on the interface and the relative displacement vector at each point of the interface, referred to as s, and is given by $s = u_t - u_b$. The relative displacement is obviously null in the initial configuration.
A local reference system is point wise introduced, with axis x_0 tangent and axis y_0 normal to the interface, and the relative displacement can be decomposed into two components along the axes, s_{0x} and s_{0y}. The component s_{0y} physically represents the 'opening' component of the relative

displacement (mode-I), and will be later indicated as s_I , while the component s_{0x} represents the 'sliding' component (mode-II), and will be later indicated as s_{II} .

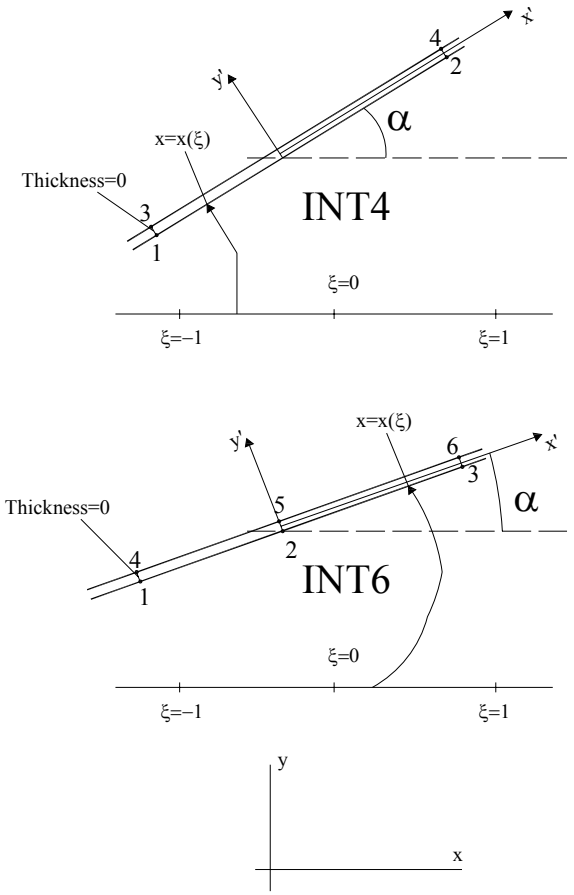

Figure 4.5.2: Initial configuration.

In a finite-element model, the interface is discretized into a finite number of interface elements. Each element is characterised by an even number N of nodes, because for each node placed on the bottom line of the element there must exist an other node on the top part of it.
Here 4-noded (INT4) and 6-noded (INT6) interface elements will be considered. For the INT4 element the initial configuration must necessarily be a straight line, while the initial shape of the INT6 element can also

describe a curved line. However, also for the INT6 element it will be initially assumed, for the sake of simplicity, that the three couples of nodes initially stay on a straight line. For both elements a reference element domain is defined, consisting in the interval $[-1, 1]$ of $\mathbb{R}$. An isoparametric mapping relates the abscissas ξ in the reference element to the position $x(\xi)$ of the points in the interface element (see Figures 4.5.3-4.5.4).

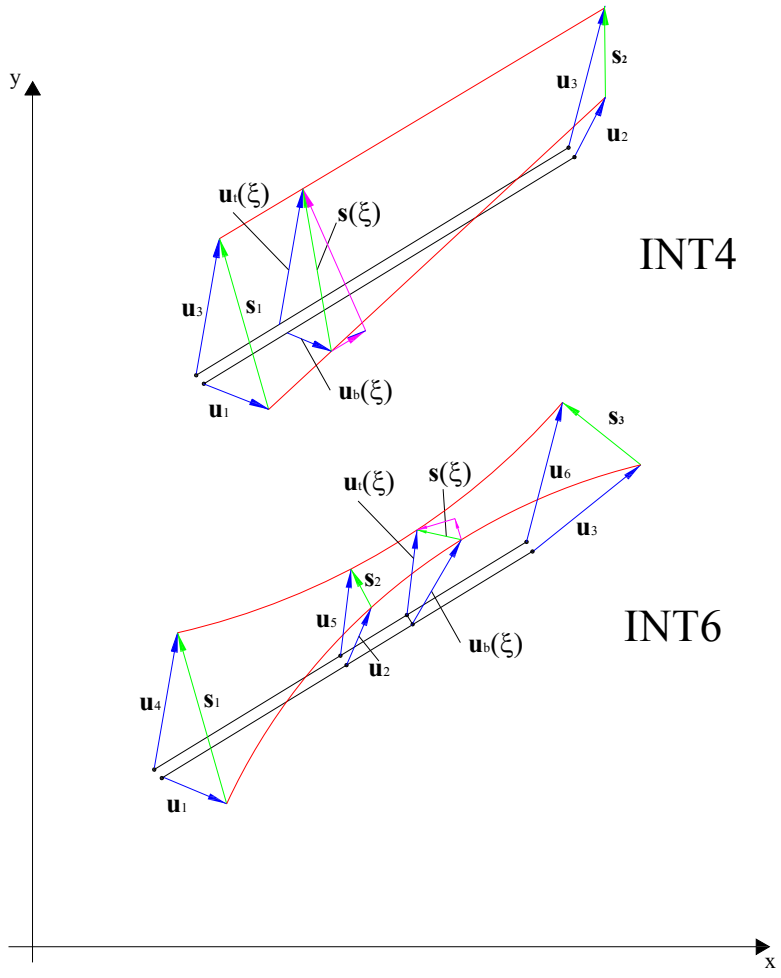

Figure 4.5.3: Deformed configuration.

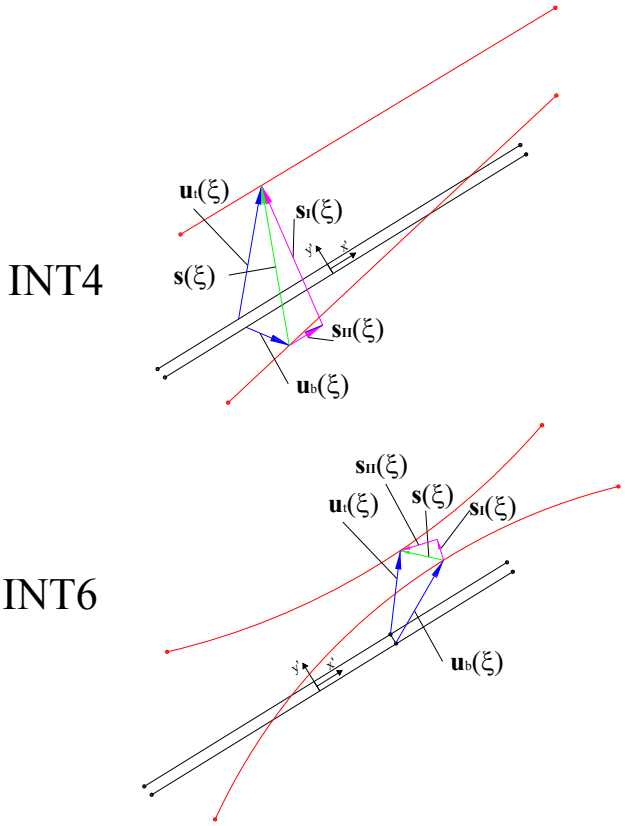

Figure 4.5.4: Decomposition of the relative displacement s(ξ) into its components, or 'modes', that is the opening mode s_I and the sliding mode s_{II}.

4.5.2.1 INT4 element

Let us focus the attention on the INT4 element, as all the results obtained for this element will easily be extended to the case of the INT6 element. The isoparametric mapping is given by:

$$x(\xi) = \sum_{1}^{N/2} \Phi_i(\xi) x_i = \frac{1-\xi}{2} x_1 + \frac{1+\xi}{2} x_2 \qquad (4.5.6)$$

where x_1 is the initial (coincident) position vector of nodes 1 and 3 with respect to a preset origin O of the 2D Euclidean space, x_2 is the initial

position vector of nodes 2 and 4 while Φ_1 and Φ_2 are the shape functions and N/2 = 2 in this case.
The relative displacement at each point x of the initial configuration can be defined as a function of ξ through the isoparametric mapping as follows:

$$s(\xi) = \sum_{1}^{N/2} \Phi_i(\xi) s_i \tag{4.5.7}$$

with s_i being the nodal relative displacements. More in detail it results:

$$\begin{aligned} s(\xi) &= \begin{bmatrix} s_{II}(\xi) \\ s_I(\xi) \end{bmatrix} = \Phi_1(\xi) \begin{bmatrix} s_{1,II} \\ s_{1,I} \end{bmatrix} + \Phi_2(\xi) \begin{bmatrix} s_{2,II} \\ s_{2,I} \end{bmatrix} = \\ &= \Phi_1(\xi)\left(u_3' - u_1'\right) + \Phi_2(\xi)\left(u_4' - u_2'\right) = \\ &= \Phi_1(\xi) \begin{bmatrix} u_{3x}' - u_{1x}' \\ u_{3y}' - u_{1y}' \end{bmatrix} + \Phi_2(\xi) \begin{bmatrix} u_{4x}' - u_{2x}' \\ u_{4y}' - u_{2y}' \end{bmatrix} \end{aligned} \tag{4.5.8}$$

where

$$\begin{aligned} \Phi_i &= \begin{bmatrix} \Phi_i(\xi) & 0 \\ 0 & \Phi_i(\xi) \end{bmatrix} \\ u_i' &= \begin{bmatrix} u_{ix}' \\ u_{iy}' \end{bmatrix} \end{aligned} \tag{4.5.9}$$

It is now convenient to introduce the transformation from the global system {x, y} to the local system {x_0, y_0}:

$$u_i' = R u_i \tag{4.5.10}$$

And more in detail:

$$u_i' = \begin{bmatrix} u_{ix}' \\ u_{iy}' \end{bmatrix} = \begin{bmatrix} \cos\alpha & \sin\alpha \\ -\sin\alpha & \cos\alpha \end{bmatrix} \begin{bmatrix} u_{ix} \\ u_{iy} \end{bmatrix} \tag{4.5.11}$$

where α is the angle formed by x_0 with x (see Figure 4.5.2).
The 2×8 matrix B(ξ) which relates the element nodal displacements to the relative displacement s(ξ) is then obtained as follows:

$$B(\xi)=\left[-\Phi_1(\xi)R \quad -\Phi_2(\xi)R \quad -\Phi_1(\xi)R \quad -\Phi_2(\xi)R\right] \tag{4.5.12}$$

being R:

$$R=\begin{bmatrix}\cos\alpha & \sin\alpha\\ -\sin\alpha & \cos\alpha\end{bmatrix} \tag{4.5.13}$$

In a displacement-based finite-element analysis the internal work in the interface element is then given by:

$$\begin{aligned} W_{\text{int}} &= \int_{\xi=-1}^{\xi=1} t\left[s(\xi), history\right]\bullet\delta s(\xi)J(\xi)d\xi = \\ &= \int_{\xi=-1}^{\xi=1} t\left[B(\xi)u, history\right]\bullet B(\xi)\delta u J(\xi)d\xi \end{aligned} \tag{4.5.14}$$

where *δs(ξ)* denotes the virtual relative displacement at the interface and *t[s,history]* is the value of the traction obtained for an assigned relative displacement *s* and an assigned history. Furthermore, *J(ξ)* represents the Jacobian $\|dx/d\xi\|$ of the isoparametric mapping.
By transposing matrix B and omitting the dependence of t on the history of the relative displacement, one then obtains:

$$W_{\text{int}} = \int_{\xi=-1}^{\xi=1} B(\xi)^T t(\xi)J(\xi)d\xi\bullet\delta u = q_{\text{int}}\cdot\delta u \tag{4.5.15}$$

The internal force vector is then given by:

$$q_{\text{int}} = \int_{\xi=-1}^{\xi=1} B(\xi)^T t(\xi)J(\xi)d\xi \tag{4.5.16}$$

By differentiating the function *t = t[s, history]* with respect to *s* the tangent material stiffness dt/ds is obtained. By the chain rule of differentiation the element tangent stiffness is then given by the following expression:

$$K_t = \int_{\xi=-1}^{\xi=1} B(\xi)^T \frac{dt}{ds} B(\xi) J(\xi) d\xi \tag{4.5.17}$$

The integrals contained in equations (4.5.16) and (4.5.17) must of course be numerically evaluated. To this end, Newton-Cotes integration rule is typically used instead of the Gauss rule, because spurious traction oscillations have been often observed with the latter. Denoting by M the number of integration points and by ξ_i and W_i the abscissa and the weighting factor associated with the i^{th} integration point, one obtains:

$$q_{\text{int}} = \sum_{i=1}^{M} W_i J(\xi_i) B(\xi_i)^T t(\xi_i) \tag{4.5.18}$$

$$K_t = \sum_{i=1}^{M} W_i J(\xi_i) B(\xi_i)^T \frac{dt}{ds} B(\xi_i) \tag{4.5.19}$$

From an operative point of view, the implementation of the INT4 element can be summarized as follows:

- Loop on the element integration points i = 1, . . . ,M;
- For each integration point compute the value of the shape function:

$$\Phi_1 = \frac{1-\xi_i}{2}; \Phi_2 = \frac{1+\xi_i}{2} \tag{4.5.20}$$

- For each integration point evaluate the Jacobian. In this case the Jacobian is constantly equal to:

$$J(\xi) = J = \frac{\|x_2 - x_1\|}{2} = \frac{L}{2} \tag{4.5.21}$$

  with L being the length of the element in its initial configuration;
- Compute matrix $B(\xi_i)$ by substituting Eq. (4.5.20) into Eq. (4.5.12)
- Evaluate the relative displacement $s(\xi_i)$ with the formula:

$$s(\xi_i) = B(\xi_i) u \tag{4.5.22}$$

With $u^T = \begin{bmatrix} u_1^T & u_2^T & u_3^T & u_4^T \end{bmatrix}$.

Compute the traction t and the material stiffness as a function of the current relative displacement $s(\xi_i)$ and also of the history of the relative displacements. Apart from the last point of the bullet point list of operations detailed above, all the other steps are valid whatever interface law is used.
Interesting contributions, where many different interface models are either proposed or revisited, are given in [Needlemann 1990, Tvergaard & Hutchinson 1992-1993, Corigliano 1993, Schellekens & de Borst 1993, Allix et al. 1995, Allix & Corigliano 1996-1999, Chaboche et al. 1997, Bolzon & Corigliano 1997, Corigliano & Ricci 2001, Champaney & Valoroso 2001, Chandra et al. 2002], in the sequel only the most used by finite-element analysis programs will be illustrated.

4.5.2.2 INT6 element

For the INT6 element the shape function are the following quadratic functions:

$$\Phi_1(\xi) = \frac{1}{2}\xi(\xi - 1);\ \Phi_2(\xi) = 1 - \xi^2;\ \Phi_3(\xi) = \frac{1}{2}\xi(1 + \xi) \quad (4.5.23)$$

The matrix $B(\xi)$ is given by:

$$B(\xi) = \begin{bmatrix} -\Phi_1(\xi)R & -\Phi_2(\xi)R & -\Phi_3(\xi)R & \Phi_1(\xi)R & \Phi_2(\xi)R & \Phi_3(\xi)R \end{bmatrix} \quad (4.5.24)$$

with R again given by Eq. (4.5.13).
The relative displacement $s(\xi_i)$ is then given by:

$$s(\xi_i) = B(\xi_i)u \quad (4.5.25)$$

with $u^T = \begin{bmatrix} u_1^T & u_2^T & u_3^T & u_4^T & u_5^T & u_6^T \end{bmatrix}$

All the remaining part follows analogously as for the INT4 element.

4.5.3 Cohesive-zone model: Crisfield et al. (1997)

It is considered that there is a process zone or cohesive-zone ahead of the delamination tip. Physically, the cohesive-zone represents the coalescence of crazes in the resin rich layer located at the delamination tip and reflects the way by which the material loses load-carrying capacity.
In order to be consistent with the original work published by Crisfield et al. [1997] in the following, we will refer to tractions across the interface elements as "stresses" ($\bar{\sigma}$) and will refer to the relative displacements across the interface as "strains" ($\bar{\varepsilon}$). Figure 4.5.5 illustrates the constitutive behaviour for pure mode I, pure mode II, and pure mode III loading by imputing the tensile strength, $\bar{\sigma}_t$, the "cracking strain", $\bar{\varepsilon}_0$, and the "maximum strain", $\bar{\varepsilon}_{\max}$.

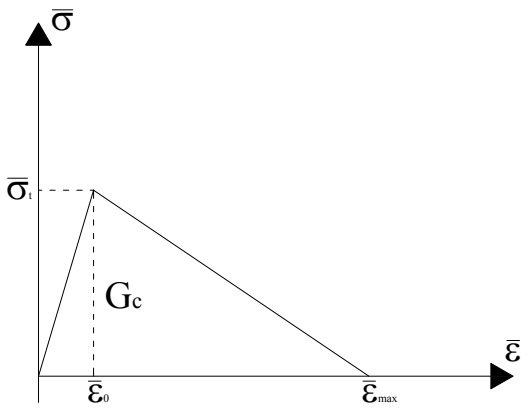

Figure 4.5.5: Softening "traction- relative displacement " relationship

In the finite-element simulations, the strain can exceed $\bar{\varepsilon}_{\max}$, but the equivalent stress is then zero, that is the crack opening is complete. The elements where softening take place are in the region $\bar{\varepsilon}_0 < \bar{\varepsilon} < \bar{\varepsilon}_{\max}$.
The opening strain $\bar{\varepsilon}_{\max}$ is chosen such that the area under the curve is equal to the critical fracture energy G_c which is a material property. In practice, the adopted $\bar{\varepsilon}_0$ is very small and $\bar{\varepsilon}_{\max} = 2G_c / \bar{\sigma}_t$.

Crisfield showed that when the relative displacements $\bar{\varepsilon}_0$ and $\bar{\varepsilon}_{\max}$ (Figure 4.5.5) are coincident (corresponding to a sudden load drop to zero) a perfectly brittle fracture is simulated. A model for brittle fracture must be able to capture the high stress gradients at the crack tip with sufficiently fine mesh densities or singular elements. This observation lead to the use of a bilinear softening material behaviour.
The method has some similarities with the original cohesive-zone procedure of Barrenblatt [1962] and Dugdale [1960] but they imposed a constant stress distribution in the cohesive zone so that to cause the stress intensity factor to be zero at the tip of the cohesive zone. In contrast, in the current method the stress drops from $\bar{\sigma}_t$ at the tip of the cohesive zone to zero (Figure 4.5.6).

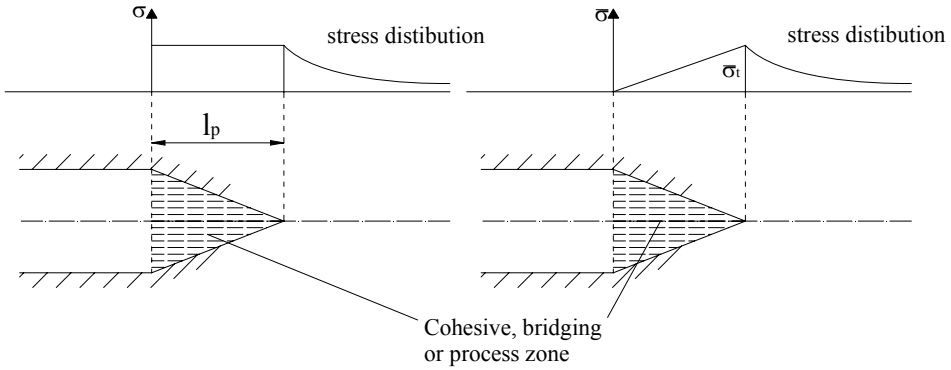

Figure 4.5.6: (a) Barrenblatt/Dugdale model; (b) Crisfield model

In order to define the material model, we must specify the unloading response. A simple elastic damage model has been adopted so that, with reversing strains, the material is assumed to unload directly towards the origin.
Considering an individual material point and subject it to increasing tensile strain increments, it is easy to show that:

$$\int_0^{\bar{\varepsilon}_{\max}} \bar{\sigma} d\bar{\varepsilon} = G_c \qquad (4.5.26)$$

So that once the stress has been reduced to zero, the critical fracture energy has been consumed.
When combined with the proposed criterion for the interaction between mode I and II (mixed-mode delamination), the resulting damage formulation leads to a very simple numerical algorithm.
In these circumstances, analysts often use a linear interaction relationship which is given by Wu & Reuter [1965]:

$$f_L = \frac{G_I}{G_{Ic}} + \frac{G_{II}}{G_{IIc}} = 1 \tag{4.5.27}$$

Experimental results indicate that a significant number of results lie between the previous linear relationship and a quadratic relationship given by:

$$f_Q = \left(\frac{G_I}{G_{Ic}}\right)^2 + \left(\frac{G_{II}}{G_{IIc}}\right)^2 = 1 \tag{4.5.28}$$

Finite element computations are "strain-driven" and hence, in place of Eq. (4.5.26) to simulate Eq. (4.5.27), it requires:

$$f_L = \frac{\int \bar{\sigma}_I d\bar{\varepsilon}_I}{G_{Ic}} + \frac{\int \bar{\sigma}_{II} d\bar{\varepsilon}_{II}}{G_{IIc}} = 1 \tag{4.5.29}$$

With a view to the satisfaction of Eq. (4.5.29) it can be proposed a "damage model" whereby in place of the usual "scalar damage" relationship, $\sigma = (1-d)E_0\varepsilon$, we write:

$$\bar{\boldsymbol{\sigma}} = \begin{Bmatrix} \bar{\sigma}_I \\ \bar{\sigma}_{II} \end{Bmatrix} = [\mathbf{I} - \mathbf{D}]\mathbf{E_0} \begin{Bmatrix} \bar{\varepsilon}_I \\ \bar{\varepsilon}_{II} \end{Bmatrix} = \left[\mathbf{I} - \frac{\kappa}{1+\kappa}\mathbf{F}\right]\mathbf{E_0}\bar{\varepsilon} \tag{4.5.30}$$

In Eq. (4.5.30), $\mathbf{E_0}$ is a diagonal matrix containing the initial stiffnesses in modes I and II respectively while **F** is another diagonal matrix with diagonal entries given by:

$$F_{ij} = \left[\frac{\overline{\varepsilon}_{\max}}{\overline{\varepsilon}_{\max} - \overline{\varepsilon}_0} \right]_{I,II} \tag{4.5.31}$$

And κ is a scalar to be chosen, depending on the interaction model. Choosing for mode II, the terms $\overline{\varepsilon}_0$ and $\overline{\varepsilon}_{\max}$ in the same manner as previously described for mode I, we obtain the area under the curve as G_{IIc}, so that $\left[\overline{\varepsilon}_{\max}\right]_{II} = \left[2G_c / \overline{\sigma}_t\right]_{II}$. Setting $\overline{\varepsilon}_{0I} = \overline{\varepsilon}_{0II}$, the scalar κ in Eq. (4.5.30) will be defined as:

$$\kappa = \left[\overline{\boldsymbol{\varepsilon}}^T \mathbf{A} \overline{\boldsymbol{\varepsilon}} \right]^{1/2} - 1 \tag{4.5.32}$$

$$\mathbf{A} = \begin{bmatrix} \dfrac{1}{\overline{\varepsilon}_{0I}^2} & 0 \\ 0 & \dfrac{1}{\overline{\varepsilon}_{0II}^2} \end{bmatrix} \tag{4.5.33}$$

In order to generalise the method, Eq. (4.5.32) must be recovered by:

$$\kappa = \sqrt{\left(\frac{\overline{\varepsilon}_I}{\overline{\varepsilon}_{0I}} \right)^a + \left(\frac{\overline{\varepsilon}_{II}}{\overline{\varepsilon}_{0II}} \right)^a} - 1 \tag{4.5.34}$$

which coincides with Eq. (4.5.32) when $\alpha = 2$.

To embed the material model within a conventional non-linear finite element computer program, the tangent modular matrix $\mathbf{D_t}$ is required, it stems from the variation of Eq. (4.5.30). Considering the linear formulation of equation (or Eq. (4.5.34) with $\alpha = 2$), this process leads to the relationship.

$$\delta\overline{\sigma} = D_t \delta\overline{\varepsilon} = \left[\left[I - \frac{\kappa_{old}}{1+\kappa_{old}} F \right] E_0 - \frac{1}{\left(1+\kappa_{old}\right)^3} F E_0 \overline{\varepsilon}\overline{\varepsilon}^T A \right] \delta\overline{\varepsilon} \tag{4.5.35}$$

4.5.4 Cohesive-zone model: Camanho & Davila (2002)

In order to model the initiation and non-self-similar growth of delamination, they proposed decohesion model with mixed-mode capability.

The simulation of delamination in composites is usually divided into delamination initiation and delamination propagation. Delamination initiation analyses are usually based on stresses and use criteria such as the quadratic interaction of the interlaminar stresses in conjunction with a characteristic distance.

As usual in the formulation of the cohesive-zone models, the need for an appropriate constitutive equation is fundamental for an accurate simulation of the interlaminar cracking process. Figure 4.5.7 represents the cohesive zone in specimens loaded in pure Mode II (Figure 4.5.7-a)) and in pure Mode I (Figure 4.5.7-b)).

For pure mode I and pure mode II or mode III loading the bi-linear softening constitutive behaviour represented in Figure 4.5.7 is used. A high initial stiffness (penalty stiffness, K) is used to hold the top and bottom faces of the decohesion element together in the linear elastic range (point 1 in Figure 4.5.7). For pure mode I, II or III loading, after the interfacial normal or shear tractions attain their respective interlaminar tensile or shear strengths (point 2 in Figure 4.5.7), the stiffnesses are gradually reduced to zero. The onset displacements are obtained as: $\delta_3^0 = N/K$, $\delta_2^0 = S/K$ and $\delta_1^0 = T/K$, where N is the interlaminar tensile strength, and S and T are the interlaminar shear strengths.

The area under the traction-relative displacement curves is the respective (mode I, II or III) fracture toughness (G_{IC}, G_{IIC} and G_{IIIC}, respectively) and defines the final relative displacements, δ_3^f, δ_2^f and δ_1^f, corresponding to complete decohesion:

$$\int_0^{\delta_3^f} \tau_3 d\delta_3 = G_{IC} \tag{4.5.36}$$

$$\int_0^{\delta_2^f} \tau_2 d\delta_2 = G_{IIC} \tag{4.5.37}$$

$$\int_0^{\delta_1^f} \tau_1 d\delta_1 = G_{IIIC} \tag{4.5.38}$$

The final displacements are then obtained as: $\delta_3^f = 2G_{IC}/N$, $\delta_2^f = 2G_{IIC}/S$ and $\delta_1^f = 2G_{IIIC}/T$.

Once a crack is unable to transfer any further load (point 5 in Figure 4.5.7), all the penalty stiffnesses revert to zero. However, it is necessary to avoid the interpenetration of the crack faces. The contact problem is addressed by re-applying the normal penalty stiffness when interpenetration is detected. In order to formulate the complete constitutive equation, the unloading behaviour must be defined. It is considered that a softening point unloads towards the origin, as shown in Figure 4.5.7. Using the following operator:

$$\langle x \rangle = \begin{cases} 0 \Leftarrow x \le 0 \\ x \Leftarrow x > 0 \end{cases} \tag{4.5.39}$$

the loading condition can be formulated in terms of a state variable defined as the "maximum relative displacement", δ^{max}, suffered by the point:
for mode II or III

$$\delta_i^{\max} = \max\left\{\delta_i^{\max}, |\delta_i|\right\}, i = 1,2 \tag{4.5.40}$$

for mode I:

$$\delta_3^{\max} = \max\left\{\delta_3^{\max}, |\delta_3|\right\}, with\ \delta_3^{\max} \ge 0 \tag{4.5.41}$$

and using a "loading function", F, defined as:
for mode II or III

$$F\left(|\delta_i| - \delta_i^{\max}\right) = \frac{\left\langle |\delta_i| - \delta_i^{\max} \right\rangle}{|\delta_i| - \delta_i^{\max}}, i = 1,2 \tag{4.5.42}$$

for mode I:

$$F\left(\delta_3-\delta_3^{\max}\right)=\frac{\left\langle \delta_3-\delta_3^{\max}\right\rangle}{\delta_3-\delta_3^{\max}},\ with\ \delta_3^{\max}\geq 0 \qquad (4.5.43)$$

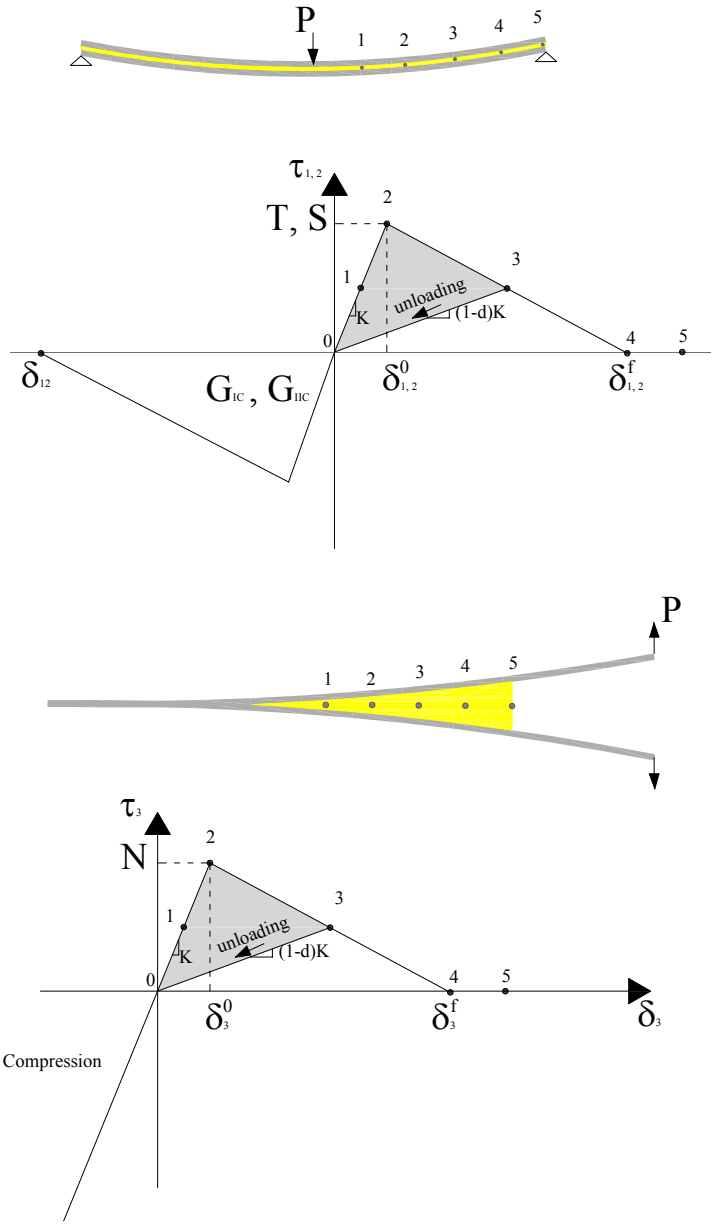

Figure 4.5.7: Pure mode constitutive equation, (a) mode II or mode III;(b) Mode I

Using δ^{max} in the constitutive equation, the irreversibility of damage is taken into account. This is shown in Figure 4.5.7: if the relative displacement decreases, the point unloads elastically towards the origin with a reduced, secant, stiffness (point 3 in Figure 4.5.7).
The irreversible, bi-linear, softening constitutive behaviour shown in Figure 4.5.7 was developed in previous works as Chen et al. [1999], Alfano & Crisfield [2001], Davila et al. [2001], and can be defined as:

$$\tau_i = \begin{cases} K\delta_i \Leftarrow \delta_i^{\max} \le \delta_i^0 \\ (1-d_i)K\delta_i \Leftarrow \delta_i^0 < \delta_i^{\max} < \delta_i^f \\ 0 \Leftarrow \delta_i^{\max} \ge \delta_i^f \end{cases} \tag{4.5.44}$$

$$d_i = \frac{\delta_i^f \left(\delta_i^{\max} - \delta_i^0\right)}{\delta_i^{\max}\left(\delta_i^f - \delta_i^0\right)}, i = 1,2,3; d_i \in [0,1] \tag{4.5.45}$$

In order to avoid interpenetration of the crack faces, the following condition is introduced:

$$\tau_3 = K\delta_3 \Leftarrow \delta_3 \le 0 \tag{4.5.46}$$

The properties required to define the interfacial behaviour are the penalty stiffness, K, the corresponding fracture toughness, G_{IC}, G_{IIC} and G_{IIIC}, and the corresponding interlaminar normal tensile or shear strengths, N, S or T, respectively.
Under pure mode I, II or III loading, the onset of damage at the interface can be determined simply by comparing the traction components with their respective allowable values. However, under mixed-mode loading damage onset and the corresponding softening behaviour may occur before any of the traction components involved reach their respective allowables, which is an issue that is usually neglected in the formulation of decohesion elements. Cui et al. [1992] have highlighted the importance of the interactions between interlaminar stress components when predicting delamination. It was shown that poor results are obtained using the maximum stress

criterion. Therefore, a mixed-mode criterion accounting for the effect of the interaction of the traction components in the onset of delamination was proposed by Camanho & Davila [2002].
It is assumed that the initiation of the softening process can be predicted using the quadratic failure criterion, considering that compressive normal tractions do not affect delamination onset and using the operator defined in Eq. (4.5.39):

$$\left(\frac{\langle \tau_3 \rangle}{N}\right)^2 + \left(\frac{\tau_2}{S}\right)^2 + \left(\frac{\tau_1}{T}\right)^2 = 1 \qquad (4.5.47)$$

This criterion has been successfully used to predict the onset of delamination in previous investigations.
The total mixed-mode relative displacement δ_m is defined as:

$$\delta_m = \sqrt{\delta_1^2 + \delta_2^2 + \langle \delta_3 \rangle^2} = \sqrt{\delta_{shear}^2 + \langle \delta_3 \rangle^2} \qquad (4.5.48)$$

where δ_{shear} represents the norm of the vector defining the tangential relative displacements of the element.
Using the same penalty stiffness in modes I, II and III, the tractions before softening onset are:

$$\tau_i = K\delta_i, \; i = 1,2,3 \qquad (4.5.49)$$

Assuming S=T, the single-mode relative displacements at softening onset are:

$$\delta_3^o = N / K \qquad (4.5.50)$$

$$\delta_1^o = \delta_2^o = \delta_{shear}^o = S / K \qquad (4.5.51)$$

For an opening displacement δ_3 greater than zero, the mixed-mode ratio β is defined as:

$$\beta = \frac{\delta_{shear}}{\delta_3} \tag{4.5.52}$$

The mixed-mode relative displacement corresponding to the onset of softening, δ_m^0, is obtained by substituting Equations (4.5.48)-(4.5.52) into Eq. (4.5.48) and solving for δ_m, which gives:

$$\delta_m^o = \begin{cases} \delta_3^o \delta_1^o \sqrt{\dfrac{1+\beta^2}{\left(\delta_1^o\right)^2 + \left(\beta \delta_3^o\right)^2}} \Leftarrow \delta_3 > 0 \\ \delta_{shear}^o \Leftarrow \delta_3 \le 0 \end{cases} \tag{4.5.53}$$

Clearly, pure mode loading is a particular case of the proposed formulation as $\delta_m{}^0 = \delta_3^0$ for $\beta=0$ (mode I), and $\delta_m^0 = \delta_{shear}^0$ for $\delta_3=0$ (or when $\beta\rightarrow\infty$, shear mode).

The criteria used to predict delamination propagation under mixed-mode loading conditions are usually established in terms of the energy release rates and fracture toughness. There are established test methods to obtain the Mode I and II interlaminar fracture toughness. The Double Cantilever Beam Specimen (DCB) is used for Mode I. The End Notched Flexure (ENF) or the End Loaded Split (ELS) specimens are used for Mode II. For mixed-mode I and II, the Mixed-Mode Bending (MMB) test specimen is normally used. However, further research is required to assess the Mode III Interlaminar fracture toughness, G_{IIIC}. Although some test methods have been suggested for the measurement of Mode III interlaminar fracture toughness, such as the Edge Crack Torsion (ECT), there are important issues that need clarification, such as the determination of the transverse shear modulus G_{23}, which is a parameter required for the analysis. Furthermore, there is no reliable mixed-mode delamination failure criterion incorporating Mode III because there is no mixed-mode test method available incorporating Mode III loading. Therefore, most of the failure criteria proposed for delamination growth were established for mixed-mode I and II loading only. For these reasons the concept of energy release rate related with shear loading, $G_{shear} = G_{II} + G_{III}$, is used for the mixed-mode.

In order to predict delamination propagation under mixed-mode loading, the widely used "power law" criterion and the mixed-mode criterion proposed by Benzeggagh & Kenane [1996] (referred to as B-K criterion) are used in this model.
The former is established in terms of an interaction between the energy release rates:

$$\left(\frac{G_I}{G_{IC}}\right)^{\alpha}+\left(\frac{G_{II}}{G_{IIC}}\right)^{\alpha}=1 \qquad (4.5.54)$$

The latter is expressed as a function of the mode I and mode II fracture toughness and a parameter η obtained from MMB tests at different mode ratios:

$$G_{IC}+\left(G_{IIC}-G_{IC}\right)\left(\frac{G_{II}}{G_T}\right)^{\eta}=G_C, with\ G_T=G_I+G_{II}, \qquad (4.5.55)$$

if mode III loading occurs the criterion is:

$$G_{IC}+\left(G_{IIC}-G_{IC}\right)\left(\frac{G_{shear}}{G_T}\right)^{\eta}=G_C, with\ G_T=G_I+G_{shear} \qquad (4.5.56)$$

The energy release rates corresponding to total decohesion are obtained from:

$$G_{IC}=\int_0^{\delta_m^{3f}}\tau_3 d\delta_3 \qquad (4.5.57)$$

$$G_{IIC}=\int_0^{\delta_m^{2f}}\tau_2 d\delta_2 \qquad (4.5.58)$$

$$G_{IIIC}=\int_0^{\delta_m^{1f}}\tau_1 d\delta_1 \qquad (4.5.59)$$

Using Equations (4.5.43), (4.5.46) and (4.5.51) in Equations (4.5.57)-(4.5.59) and substituting in (4.5.57) or in (5.3.59), the criterion for total decohesion can be established in terms of δ_m and β.

Solving the equation for δ_m, the mixed-mode displacements corresponding to total decohesion, δ_m^f, are obtained for the B-K criterion as:

$$\delta_m^f = \begin{cases} \dfrac{2}{K\delta_m^o}\left[G_{IC} + \left(G_{IIC} - G_{IC}\right)\left(\dfrac{\beta^2}{1+\beta^2}\right)^{\eta}\right] \Leftarrow \delta_3 > 0 \\ \sqrt{\left(\delta_1^f\right)^2 + \left(\delta_2^f\right)^2} \Leftarrow \delta_3 \le 0 \end{cases} \tag{4.5.60}$$

and for the power law criterion as:

$$\delta_m^f = \begin{cases} \dfrac{2\left(1+\beta^2\right)}{K\delta_m^o}\left[\left(\dfrac{1}{G_{IC}}\right)^{\alpha} + \left(\dfrac{\beta^2}{G_{IIC}}\right)^{\alpha}\right]^{\frac{1}{\alpha}} \Leftarrow \delta_3 > 0 \\ \sqrt{\left(\delta_1^f\right)^2 + \left(\delta_2^f\right)^2} \Leftarrow \delta_3 \le 0 \end{cases} \tag{4.5.61}$$

Regardless of the criterion used, pure mode loading is a particular case of the proposed formulation, as $\delta_m^f = \delta_3^f$ for $\beta=0$ (mode I), and $\delta_m^f = \delta_{shear}^s$ for $\delta_3=0$ (or when $\beta\rightarrow\infty$, shear mode).

The constitutive equation for mixed-mode loading is defined by the penalty parameter K, the damage evolution function d, and the mixed-mode relative displacements corresponding to damage initiation and total decohesion, δ_m^0 and δ_m^f, respectively, as:

$$\tau_s = D_{sr}\delta_r\,, \tag{4.5.62}$$

with the constitutive operator given by:

$$D_{sr} = \begin{cases} \\ \bar{\delta}_{sr} K \Leftarrow \delta_m^{\max} \le \delta_m^o \\ \bar{\delta}_{sr}\left[\left(1-d\right)K + Kd\bar{\delta}_{s3}\dfrac{\left\langle -\delta_3 \right\rangle}{-\delta_3}\right] \Leftarrow \delta_m^o < \delta_m^{\max} < \delta_m^f \\ \bar{\delta}_{s3}\bar{\delta}_{3r}\dfrac{\left\langle -\delta_3 \right\rangle}{-\delta_3} K \Leftarrow \delta_m^{\max} \ge \delta_m^f \end{cases}, \quad (4.5.63)$$

$$d = \frac{\delta_m^f\left(\delta_m^{\max} - \delta_m^o\right)}{\delta_m^{\max}\left(\delta_m^f - \delta_m^o\right)}, d \in \left[0,1\right]$$

where $\bar{\delta}_{sr}$ is the Kronecker delta.

It is worth noticing that Eq. (4.5.63) avoids the interpenetration of the crack faces of the decohesion element for softening and fully open conditions.

In order to define the loading and unloading conditions the state variable maximum mixed-mode relative displacement, $\delta_m^{\max}$, and the loading function, *F*, are defined as:

$$\delta_m^{\max} = \max\left\{\delta_m^{\max}, \delta_m\right\} \quad (4.5.64)$$

$$F\left(\delta_m - \delta_m^{\max}\right) = \frac{\left\langle \delta_m - \delta_m^{\max} \right\rangle}{\delta_m - \delta_m^{\max}} \quad (4.5.65)$$

The mixed mode softening law presented above is a single-variable response similar to the bilinear single-mode law illustrated in Figure 4.5.7, defined by a damage evolution law (Eq. (4.5.63)), by the maximum mixed-mode relative displacement (Eq. (4.5.64)), and by the loading function (Eq. (4.5.65)). Only one state variable, the maximum relative displacement variable $\delta_m^{\max}$, is used to track the damage at the interface. By recording the highest value attained by δ_m, the unloading response is such as shown in Figure 4.5.7. The relative displacements for initiation and ultimate failure are functions of the mixed-mode parameter β, the material properties, and the penalty stiffness.

The mixed-mode softening law can be illustrated in a single three-dimensional map by representing mode I on the Y-Z plane, and shear mode in the X-Z plane, as shown in Figure 4.5.8.

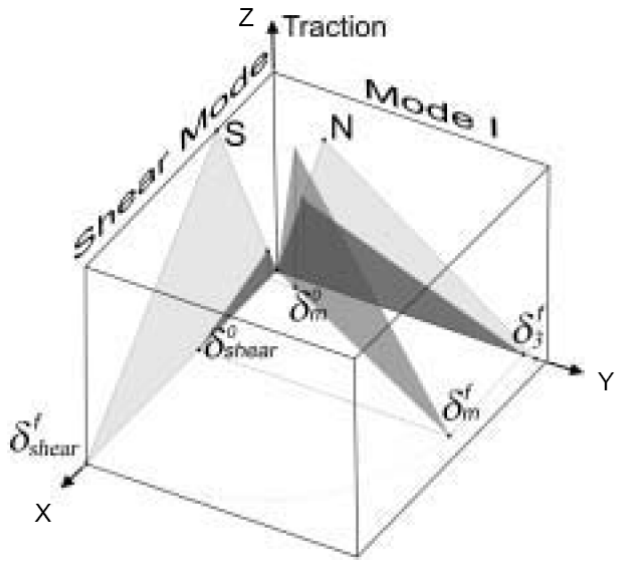

Figure 4.5.8: Mixed-mode softening law [Camanho & Davila 2002]

The triangles *0-N-*δ_3^f and 0-S-δ_{shear}^f are the bilinear response in mode I and in shear mode, respectively. In this three-dimensional map, any point on the 0-X-Y plane represents a mixed-mode relative displacement.

4.5.5 Damage elasto-plastic cohesive-zone model: Alfano & Rosati (2003)

It is assumed that the two elements can be well modelled through a linear, elastic law and in the hypothesis of small deformations, with the whole non-linear debonding process being due to the evolution of damage and plasticity within the adhesive material. As usual, the thickness of adhesive is assumed to be so small, with respect to the other geometric dimensions, that it can be neglected.

Hence, the structural model will be defined by a domain Ω of an Euclidean space, which can be viewed as the union of two closed, connected parts, Ω_1

and Ω_2, whose boundaries share an interface surface $\Gamma = \partial\Omega_1 \cap \partial\Omega_2$. Reference will be made here to a general three-dimensional problem, although the numerical results presented later relate to two-dimensional cases.

In the initial, undeformed configuration we assume that the two parts, which occupy Ω_1 and Ω_2 are bonded together along a connected part Γ_1 of Γ, and that the remaining part $\Gamma_2 = \Gamma - \Gamma_1$ is completely debonded, although in contact. Accordingly, a contact-type relationship without friction will be adopted along Γ_2, whereas the possible decohesion along Γ_1 will be modelled as detailed in this section.

Two opposite points P_1 and P_2 of the interface, which occupy the same position in the undeformed configuration, will move to two different positions P'_1 and P'_2 of the deformed configuration. The vector $\mathbf{s} = P'_2 - P'_1$ represents their relative displacement. This, in turn, can be decomposed into its three components $\mathbf{s}_i$ with $i=1,2,3$, parallel to a local, orthonormal reference system $\mathbf{e}_i$. Assuming that $\mathbf{e}_1$ is directed along the normal to the tangent plane π to Γ in $P_1 = P_2$, so that $\mathbf{s}_1$ represents the so called mode-I 'opening' displacement, and that $\mathbf{e}_2$ and $\mathbf{e}_3$ lay in π so that $\mathbf{s}_2$ and $\mathbf{s}_3$ represent the mode-II 'sliding' and mode-III 'tearing' components, respectively.

The total relative displacement is additively decomposed into the sum of an elastic part $\mathbf{s}_e$ and a plastic part $\mathbf{s}_p$:

$$\mathbf{s} = \mathbf{s}_e + \mathbf{s}_c \tag{4.5.66}$$

A vector $\mathbf{d}=[d_1, d_2, d_3]$ of damage parameters and a scalar hardening variable ζ are introduced as internal variables, and the free energy is written as follows:

$$\psi = \psi\left(\mathbf{s}_e, \mathbf{d}, \zeta\right) = \psi_e\left(\mathbf{s}_e, \mathbf{d}\right) + \psi_h\left(\zeta\right) \tag{4.5.67}$$

The elastic-damage part ψ_e of the free energy is assumed given by:

$$\psi_e\left(\mathbf{s}_e, \mathbf{d}\right) = \frac{1}{2}\left[\mathbf{I} - \mathbf{D}\left(\mathbf{d}\right)\mathbf{C}\right]\mathbf{E}\mathbf{s}_e \bullet \mathbf{s}_e \tag{4.5.68}$$

where $\mathbf{E}=diag(E_i)$ is a penalty stiffness matrix, which is taken high enough to model the undamaged behaviour of the interface, $\mathbf{I}$ is the identity 3x3 matrix and $\mathbf{D}(\mathbf{d})=diag(d_i)$. Furthermore, in order to avoid penetration for mode I in compression, the matrix $\mathbf{C}=diag[H(s_{e1}),1,1]$ has been introduced, with $H(s_{e1})$ defined by:

$$H\left(s_{e1}\right)=1 \;\; if \;\; s_{e1}\geq 0 \quad and \quad H\left(s_{e1}\right)=0 \;\; if \;\; s_{e1}<0 \tag{4.5.69}$$

The hardening part ψ_h of the free energy is assumed given by:

$$\psi_h\left(\zeta\right)=\frac{1}{2}h\zeta^2 \tag{4.5.70}$$

and accounts for a linear-isotropic type of hardening.
Differentiation of the free energy defines the variables t, Y and $\hat{\chi}$, which are conjugated to $\mathbf{s}_e$,$\mathbf{d}$ and ζ, respectively:

$$\begin{cases} \mathbf{t}=\dfrac{\partial\psi}{\partial\mathbf{s}_e}=\left[\mathbf{I}-\mathbf{D}\left(\mathbf{d}\right)\mathbf{C}\right]\mathbf{E}\mathbf{s}_e=\left[\mathbf{I}-\mathbf{D}\left(\mathbf{d}\right)\mathbf{C}\right]\mathbf{E}\left(\mathbf{s}-\mathbf{s}_p\right) \\ \mathbf{Y}=\dfrac{\partial\psi}{\partial\mathbf{d}}=\left[\dfrac{1}{2}H\left(s_{e1}\right)E_1s_{e1}^2,\dfrac{1}{2}E_2s_{e2}^2,\dfrac{1}{2}E_3s_{e3}^2\right]^T \\ \hat{\chi}=\dfrac{\partial\psi}{\partial\zeta}=h\zeta \end{cases} \tag{4.5.71}$$

In particular, $\mathbf{t}$ is the traction at the interface, each component Y_i of $\mathbf{Y}$ represents the conjugated variable to d_i. Finally, $\hat{\chi}$ denotes the increase in the yield threshold due to the isotropic hardening.
In the adopted damage model all of the damage variables turn out to coincide, that is $d_1=d_2=d_3=d$, and d can be obtained in closed form as a function of $\mathbf{s}_e$ as follows:

$$d=\frac{1}{\eta}\left(\frac{\kappa_{\max}}{\kappa_{\max}+1}\right) \tag{4.5.72}$$

with

$$\kappa_{\max} = \max \kappa \left[\left(\frac{\langle s_{e1} \rangle}{s_{01}} \right)^{\alpha} + \left(\frac{\langle s_{e2} \rangle}{s_{02}} \right)^{\alpha} + \left(\frac{\langle s_{e3} \rangle}{s_{03}} \right)^{\alpha} \right]^{\frac{1}{\alpha}} - 1 \qquad (4.5.73)$$

where $\langle x \rangle = \left(x + |x| \right) / 2$. For a single-mode debonding, the above-elastic damage law results in the two bilinear relationships depicted in Figure 4.5.9, and in the above relationship s_{0i} is the value of the relative-displacement component at which interface damage begins to grow in these cases. Furthermore, α is a material parameter and η is given by:

$$\eta = 1 - \frac{G_{o1}}{G_{c1}} = 1 - \frac{G_{o2}}{G_{c2}} = 1 - \frac{G_{o3}}{G_{c3}} \qquad (4.5.74)$$

where G_{ci} is the fracture energy in mode i and $G_{oi} = E_i s_{ei}^2 / 2$ is the specific elastic energy stored when the damage parameter d_i begins to increase to values greater than zero. Notice that Eq. (4.5.74) is based on the assumption that G_{oi}/G_{ci} is constant for all of the modes i. This hypothesis has been made in [Alfano & Crisfield 2001] on the grounds that, unlike G_{ci} which is an input parameter, G_{oi} can be changed in a certain range by changing the value of s_{oi} (see Figure 4.5.10).

The direct relationship between the damage parameter d and $\mathbf{s}_e$ can be derived from the general 'damage mechanics' framework described earlier in the previous section. This can be done by introducing the following convex function:

$$f(Y) = \left(\frac{Y_1}{G_{c1}} \right)^{\frac{\alpha}{2}} + \left(\frac{Y_2}{G_{c2}} \right)^{\frac{\alpha}{2}} + \left(\frac{Y_3}{G_{c3}} \right)^{\frac{\alpha}{2}} \qquad (4.5.75)$$

so as to define the damage domain $\mathcal{D}$:

$$\mathcal{D} = \left\{ Y : f(Y) \le \omega_c \right\} \qquad (4.5.76)$$

which depends on the non-dimensional threshold value ω_c.
A non-associative evolution law for the internal variables **d** and **Y** is then assumed:

$$\dot{d} = \dot{d}\begin{bmatrix}1 & 1 & 1\end{bmatrix}^T \tag{4.5.77}$$

with the Khun-Tucker conditions:

$$f(Y) \le \omega_c, \quad \dot{d} \ge 0, \quad \left[f(Y) - \omega_c\right]\dot{d} = 0 \tag{4.5.78}$$

and the additional constraint that $0 \le d \le 1$.
The condition $d_1=d_2=d_3=d$ is thus a consequence of Eq. (4.5.77) and of the fact that $d_i=0$ at the beginning of the process for all of the modes i. The zone of the interface where $0 < d < 1$ is classically denoted as the "process zone" and separates the still undamaged part from the fully damaged part of the interface.
The threshold ω_c is assumed as a function of d through the following relationship:

$$\begin{cases} \omega_c = (1-\eta)^{\alpha/2} & if \quad d = 0 \\ \omega_c = \left[\dfrac{(1-\eta)}{(1-\eta d)^2}\right]^{\alpha/2} & if \quad 0 < d < 1 \\ \omega_c = \bar{\omega} & if \quad d = 1 \end{cases} \tag{4.5.79}$$

in which $\bar{\omega} = \max f(Y)$. Hence, the damage domain D changes during the damage process, since the threshold ω_c has the initial value $(1-\eta)^{\alpha/2}$, approaches the value $(1-\eta)^{\alpha/2}$ when $d \to 1$ and can indefinitely increase when $d=1$, together with $\bar{\omega}$.
The choice of assuming a fixed threshold value ω_c, instead of relationship (Eq. (4.5.79)), would decrease the size of the process zone to zero, so that a discontinuity in the traction-relative displacement law would exists, with a jump from the maximum value of the elastic range to zero.

For a clearer understanding of the model, the geometric meaning of G_{01} and Y_{01} is shown in Figure 4.5.10, which refers to a pure mode-I case.
Furthermore, this formulation takes into account the plastic evolution law through the use of convex yield function ϕ, which is made dependent on the "effective traction" [Champaney & Valoroso 2001; Corigliano 1993] defined as:

$$\hat{\mathbf{t}} = \frac{\mathbf{t}}{1-d} = \mathbf{E}\left(\mathbf{s} - \mathbf{s}_p\right) \tag{4.5.80}$$

in accordance with the physical argument that plastic yielding occurs in the not-yet-damaged part of the interface.
Thus, the elastic domain $\mathcal{S}$ is implicitly defined as follows:

$$\mathcal{S} = \left\{\hat{t} \,\middle|\, \phi\left(\hat{t}, \hat{\chi}\right) \le 0\right\} \tag{4.5.81}$$

where ϕ is assumed to be convex and positively homogeneous while $\hat{\chi}$ represents the isotropic expansion of $\mathcal{S}$.

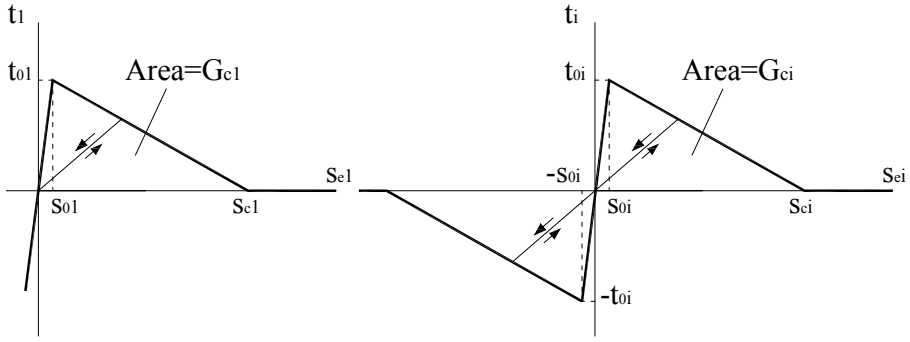

Figure 4.5.9: Traction-relative displacement relationship: (a) mode I; (b) modes II and III (i=2,3)

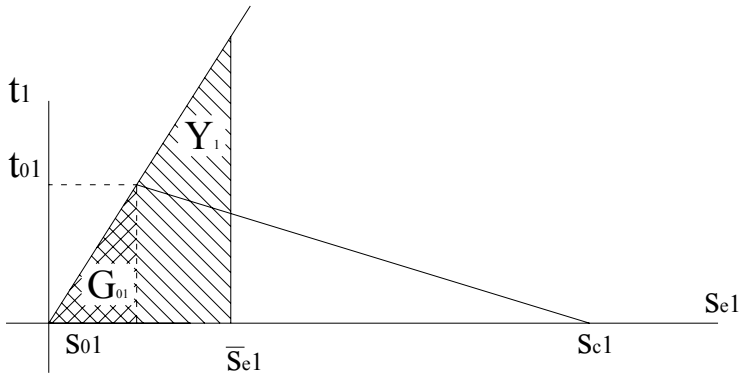

Figure 4.5.10: The two patterned areas are equal to G_{01} and $Y_{01}(s_{e1})$, respectively.

CHAPTER V
EXISTING MODELS for FRP/CONCRETE and STEEL/CONCRETE INTERFACES

5.1 INTRODUCTION

The main element of novelty of RC beams retrofitted with FRP, with respect to ordinary reinforced concrete beams, are the failure modes associated with debonding of the FRP external reinforcement.
This new aspect is recognised in the international guidelines for the design of this type of strengthening works, which give indications on how to prevent mid-span debonding.
A good model for RC beams retrofitted with FRP must be therefore capable of predicting debonding failure modes. Besides, as we have already explained, the model we are setting up is intended to be the more realistic and comprehensive is possible. This is because the model is not only intended for the assessment of the element capacity but also to supply information on these systems which are difficult to obtain experimentally.
A good model for the interfaces is therefore of key importance. This does not apply only to the sensitive interface FRP/concrete but also to the more robust one, steel rebar/concrete. This is due to the fact that bond slip of steel bars largely influence crack opening and spacing, and in turn, the performance of the FRP/concrete interface, as will be demonstrated in by the numerical results.
The correct modelling of the interfaces affects significantly also the stiffness performance of the system, that is also of interest, as often FRP are used to increase the stiffness of a structural element rather than its capacity.
In this chapter, some mathematical models available in literature on the interfacial behaviour of FRP/concrete and steel bar/concrete will be described.

5.2 EXISTING FRP/CONCRETE INTERFACE MODELS

5.2.1 Introduction

Several scientific contributions have been proposed by various researchers in the last ten years concerning both with the interface stress evaluation and adhesive-concrete bond interface behaviour.

Chen & Teng [2001] reported an overview of some models for evaluating the ultimate strength of FRP plates epoxy-bonded to concrete. They have been classified into three categories: empirical models, based directly on the regression of experimental data, fracture mechanics, based models design proposals that generally make use of some simplified assumptions. In particular, the models belonging to the second category consist in introducing various expressions for fracture energy, representing relationships between interface slip and tangential stress. Neubauer & Rostasy [1997] starting from previous researchers assumed a bi-linear relationship between slip and interface shear stress, simulating a first range of elastic behaviour, followed by a second and larger one accounting for the softening behaviour of concrete beneath the epoxy resin. In fact, concrete cracking due to high interface shear stress results in softening behaviour of the epoxy-concrete interface as a whole. Due to the greater importance of the softening range with respect to the elastic one for evaluating the ultimate strength of the FRP-to-concrete joint, a linear descending simplified relationship may be assumed. Bi-linear relationship has been chosen by Wu & Yin [2003] to model the fracturing behaviour of FRP-strengthened concrete structures: they studied the mode II crack (shear mode) occurring in the adhesive layer and proposed a smeared crack model for simulate the micro-cracking phenomena occurring at the adhesive-concrete interface, resulting in a progressive loss of strength of the epoxy FRP/concrete joint as a whole.

Several efforts have been carried out by various researchers about either evaluating stress concentration in the adhesive interface and estimating its strength.

Under the experimental standpoint, various testing techniques have been proposed for investigating the interface behaviour. Jones et al. [1988] tested scaled beams strengthened with steel plates characterized by different dimensions and arrangements of plates; Bizindavy [1999] carried out similar experiments on beams strengthened by FRP sheets: both observed premature beam failures due to interface debonding of the strengthening plates.

Instead of testing strengthened beams as a whole, Chajes et al. [1996] performed pull-out tests on FRP-to-concrete epoxy joints in order to evaluate the interface behaviour by reproducing the situation of the cut-off section in strengthened beams where stress concentrations arise. Faella et al. [2002, 2003] presented a series of suitably instrumented experimental pull-out tests on FRP/concrete joints; on the basis of the experimental results their investigation was addressed to carry out an indirect identification procedure for calibrating the bilinear ascending softening (τ-s) relationship chosen for characterizing the joint behaviour.

However, largely scattered results have been obtained for bond strength due to different testing methods adopted by the various researchers. Horigucki & Saeki [1997] just focused on the effect of testing methods by comparing the results in terms of (average) bond strength obtained with three types of tests; they found that tensile tests provide always the higher bond strength while shear pull-out tests give generally the lower values.

It is easy to understand that such a general trend is mainly due to the stress distribution induced by the two above mentioned tests: in particular, tensile tests results in uniform tensile stress at the interface while shear tests induce a normal and shear stress concentrations close to the pulling out force application point, as it will be widely shown in the following.

Under the theoretical point of view various one-dimensional models have been carried out for estimating stress concentrations in the adhesive layer. Roberts [1988] proposed one of the first formulation for evaluating normal and shear stress in the adhesive layer by means of a simple uncoupled approach. In the following years other proposals have been carried out among which the ones by Malek et al. [1998] and Täljsten [1997], both providing a closed form solution for shear and normal stress concentrations.

Moreover, Brosens & Van Gemert [2001] proposed a Mohr-Coulomb-like failure criterion for evaluating limit combinations of shear and normal stresses in the adhesive-concrete interface.

It is informative at this stage to give further explanation of the mechanism of transfer of forces between the concrete and the composite. As this section is intended to be descriptive, only basic equations shall be given to clarify the physics of the problem.

Separation of concrete and FRP is generally referred to, in the literature, as peeling or bond splitting depending on whether the entire covercrete is involved or not. In the following, when it is intended to make no distinction between the two modes the term delamination will be used.

In two dimensions, two modes of delamination are recognised.

They are conventionally named as mode I and mode II.

- Mode I is associated with normal relative displacements between the two surfaces connected by the interface and mode II is associated with transverse displacements. The two modes are generally coexistent in different proportions. In the case of the interface FRP/concrete in structural elements in bending mode II is dominant (Figure 5.2.1(a)).
- Mode II generate shear stresses. These shear stresses are transmitted to the covercrete via the adhesive. Axial equilibrium of an element plate gives:

$$\tau = t_p \frac{d\sigma_{mp}}{dx} = t_p E_p \frac{d\varepsilon_{mp}}{dx} \qquad (5.2.1)$$

where τ is the shear stress; and t_p, E_p, σ_{mp}, ε_{mp}, x, are the thickness, the Young's modulus , mean axial stress, mean axial strain, and distance along the plate, respectively (Figure 5.2.1(b)).

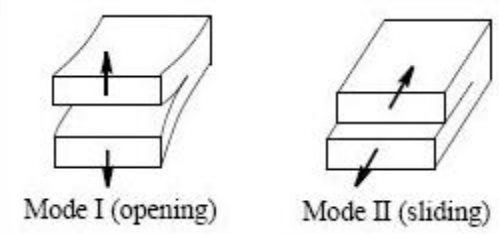

Figure 5.2.1: Modes of delamination; (a) Mode I, (b) Mode II

For a linear strain variation through the thickness of the plate, the average strain is that at mid thickness. The shear bond stresses which trigger mid-span debonding action can be generated by any influence inducing axial stress gradients in the plate. For initiation of debonding, one such source of axial stress gradient is tension stiffening, which refers to the axial variation of tensile stress in the concrete teeth between cracks, owing to the bond between the tension reinforcement and the cracked concrete. For equilibrium, axial stress gradients must also exist in the FRP plate bonded onto the cracked concrete, with such stresses diminishing away from the crack faces.

During debonding propagation, a change exists along the beam from sections with bonded plate to sections with debonded plates.

The presence of yielded steel at the debonded sections and elastic steel at bonded sections exacerbates the change. This induces high axial stress gradients along the plate in the transition region between the debonded and the bonded beam sections, which in turn induces further debonding. Hence, the mid-span process is self-propagating and can become particularly pronounced after yield of the embedded steel.

It is worth to observe that for simply supported beams, end peeling is likely to occur when the following conditions exist:

• low shear span loading (to generate high plate-to-beam shear bond stresses near the supports);

• curtailment of the plates far from the supports (for the end effects which amplifies the shear bond stresses);

• use of a stiff plate (to attract high bond stresses near plate curtailment) ;

Mid-span debonding, by contrast, requires:
• high shear span loading (to generate large moments near mid-span);
• plate curtailment very near to supports and thin plates.
The latter two conditions are required to minimize end peeling tendencies.
In practice uniformly distributed loads can generally be regarded as high shear span loads.

5.2.2 Elastic approach (Rasheed & Pervaiz 2002)

A variety of possible approaches have been proposed for the problem of the interface between concrete and FRP. Closed form solutions have been found for highly idealised linear elastic models [Rasheed & Pervaiz 2002; Yang et al. 2004], in which the relative movement between the two materials is due to elastic deformation of the bonding agent (epoxy) assumed with a finite thickness. At this level of idealization a closed form solution to the interface problem can be derived as follows.
The problem can be greatly simplified if the following assumptions are made:
• Linear elastic behaviour of all components;
• Unidirectional FRP plates with their fibres aligned with the beam axis;
• Bond line has no axial and bending stiffnesses;
• The adhesive is homogeneous and uniform along the bond line;
• Linear strain distribution is assumed in the beam and strengthening plate sections.
With reference to Figure 5.2.2 the following relation can be written:

$$-\gamma t_i = d\left(v' - \phi\right) \tag{5.2.2}$$

where γ is the shear strain in the adhesive layer, t_i is the thickness of the adhesive, d is the distance of the axis of the FRP plate from the axis of the concrete section, v' is the rotation of the concrete section and ϕ is the average cross sectional rotation defined by the difference of the axial displacement of the concrete section and the plate and the distance between their axes d (see Figure 5.2.2). Assuming small deformations:

$$\phi = \frac{u_2 - u_1}{d} \tag{5.2.3}$$

According to the convention used in the figure v' and ϕ are counter clockwise
while γ is a clockwise angle.

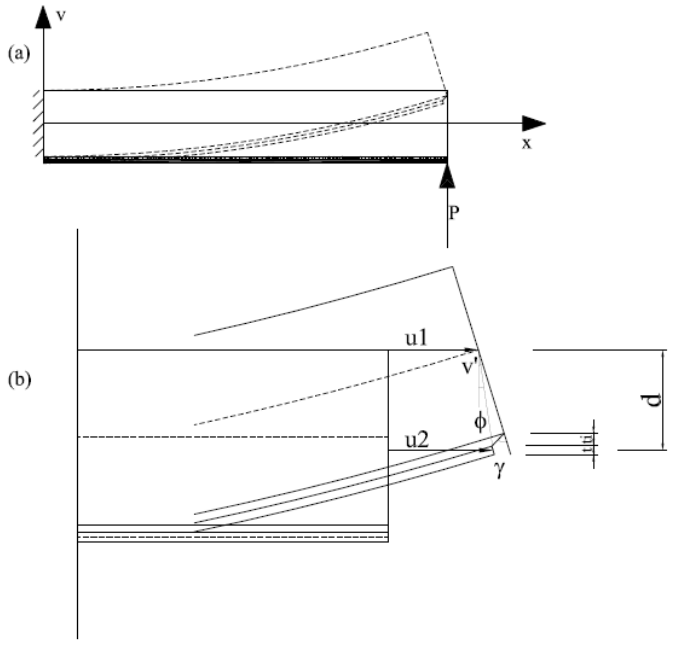

Figure 5.2.2: FRP strengthened beam considering interface slip: (a) beam layout; (b) cross section kinematics

The axial strains of beams and plate are given by:

$$u_1' = \frac{C}{EA_B}; \quad u_2' = \frac{T}{EA_p} \tag{5.2.4}$$

where C is the compressive axial force in the concrete, T is the tensile axial force in the FRP and all other symbols have their usual meaning with the suffix B for beam and p for plate.

Since the deflection is assumed to be the same for all points in the section, the curvature (v'') may be directly used to define the bending moments in the beam and the FRP plate, respectively (Figure 5.2.3(a)).

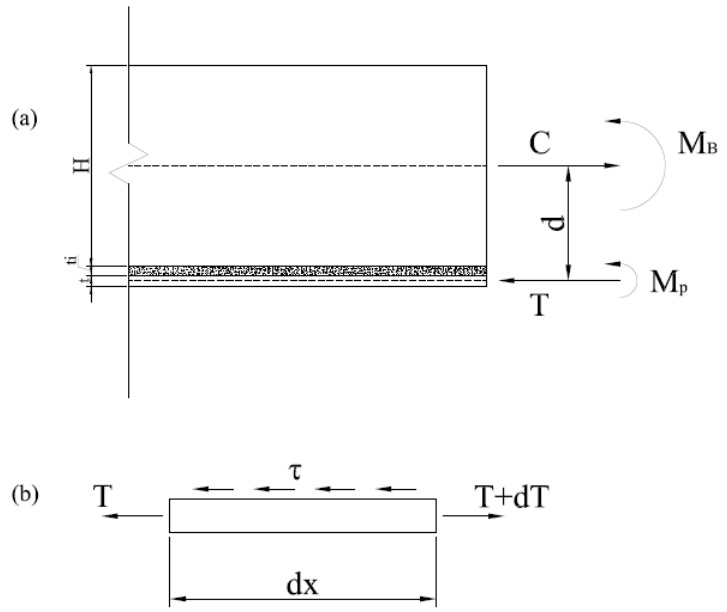

Figure 5.2.3: Equilibrium of forces: (a) force/moment distribution in cross section; (b) interface shear stress on differential plate element

$$M_B = EI_B v''; \quad M_p = EI_p v'' \tag{5.2.5}$$

The interface shear stress τ is related to the shear strain through the shear modulus G.

$$\tau = G\gamma \tag{5.2.6}$$

The equilibrium of an elemental segment of plate yields:

$$\tau = \frac{1}{b}\frac{dT}{dx} \tag{5.2.7}$$

Where *b* denotes the width of the FRP plate.
Taking the equilibrium of forces and moments at any cross section:

$$C = -T \tag{5.2.8}$$

$$M_x = M_b + M_p + Td \tag{5.2.9}$$

Differentiating ϕ with respect to x and using equation (5.2.8) we get:

$$\phi' = \frac{T}{dEA_s} \tag{5.2.10}$$

where $EA_s = 1/EA_b + 1/EA_p$.
Substituting Eq. (5.2.5) into Eq. (5.2.9) and rearranging:

$$T = \frac{M(x) - EI_s v''}{d} \tag{5.2.11}$$

where $EI_s = EI_b + EI_p$. Differentiating equation (5.2.13) with respect to x and substituting into Eq. (5.2.7):

$$v''' = \frac{M'(x) - bd\tau(x)}{EI_s} \tag{5.2.12}$$

Differentiating Eq. (5.2.2) twice with respect to x, substituting Eq. (5.2.10) and rearranging:

$$\gamma'' + \frac{d}{t_i}\left(v''' - \frac{T'}{dEA_s} \right) = 0 \tag{5.2.13}$$

Substituting Eq. (5.2.7) and Eq. (5.2.12) into Eq. (5.2.13), The shear differential equation is obtained:

$$\tau''(x) - \alpha^2 \tau(x) = -\frac{dG}{t_i EI_s} M'(x) \tag{5.2.14}$$

where

$$\alpha^2 = \frac{bG}{t_i}\left(\frac{1}{EA_s} + \frac{d^2}{EI_s}\right) \tag{5.2.15}$$

The solution of the above linear differential equation with constant coefficients has the well known form:

$$\tau(x) = A\cosh(\alpha x) + B\sinh(\alpha x) + \tau_p(x) \tag{5.2.16}$$

where τ_p is a particular solution.
To calculate the shear stresses as a function of x it is necessary to find a particular solution $\tau_p(x)$ and impose the appropriate boundary conditions.
In the case of a simply supported partially plated beam under uniform loading the solution has the following form:

$$\begin{aligned}\tau(x) = {} & \frac{dG}{\alpha^2 t_i EI_s} w\left[\left(\frac{L}{2} - x_p\right) + \frac{\sinh(\alpha x_p) - \tanh(\alpha L_p/2)\cosh(\alpha x_p)}{\alpha}\right] + \\ & - \frac{dG}{2\alpha^2 t_i EI_s} w(L - L_p)\frac{\cosh(\alpha x_p)}{\cosh(\alpha L_p/2)} + \\ & + \frac{Gw}{8\alpha t_i dEA_s}(L^2 - L_p)\left(1 - \frac{EI}{EI_b}\right)\left[\sinh(\alpha x_p) - \tanh(\alpha L_p/2)\cosh(\alpha x_p)\right]\end{aligned} \tag{5.2.17}$$

Other approaches [Yang et al. 2004] with less stringent kinematical assumptions giving also the possibility of considering more than three layers of different materials involve the use of Fourier series and are not reported for brevity.

5.2.3 Empirical models

Several experimental and theoretical work exists on the bond strength of FRP to concrete joints. The models presented below are based on simple shear tests.

Tanaka [1996] presented a simple expression similar to that presented by Sato [1996] as function of the bond length L:

$$\tau_u = 6.13 - \ln L \qquad \text{[MPa]} \qquad (5.2.18)$$

where L in mm.

Hiroyuki & Wu [1997] derived a set of double shear tests on RC members strengthened with carbon fibre sheets from which they derived the following empirical relationship:

$$\tau_u = 5.88 \cdot L^{-0.669} \qquad \text{[MPa]} \qquad (5.2.19)$$

where L in cm.

Maeda et al. [1997] developed a model function of the modulus of elasticity E_p and the thickness t_p of the bonded plate:

$$\tau_u = 110.2 \cdot 10^{-6} E_p \cdot t_p \qquad \text{[MPa]} \qquad (5.2.20)$$

with E_p in MPa and t_p in mm.

The ultimate strength P_u is given by multiplying the ultimate shear stress by the effective bond area $L_e\, b_p$, where:

$$L_e = e^{6.13 - 0.58 \ln E_p t_p} \qquad \text{[mm]} \qquad (5.2.21)$$

Maeda's model is obviously valid only for $L > L_e$.

5.2.4 Fracture-mechanics based models

Holzenkämpfer [1994] investigated the bond strength between steel and concrete using non-linear fracture mechanics (NLFM). To calculate the bond strength he used the modified expression of Niedermeier [1996]:

$$P_u = \begin{cases} 0.78 b_p \sqrt{2 G_f E_p t_p}, & \text{if } L \geq L_e \\ 0.78 b_p \sqrt{2 G_f E_p t_p}\, \dfrac{L}{L_e}\left(2 - \dfrac{L}{L_e}\right), & \text{if } L < L_e \end{cases} \tag{5.2.22}$$

with E_p in MPa, t_p in mm, and P_u in N.
The effective bond length L_e and the fracture energy G_f are given by:

$$L_e = \sqrt{\frac{E_p t_p}{4 f_{ctm}}} \qquad \text{[mm]} \tag{5.2.23}$$

$$G_f = c_f k_p^2 f_{ctm} \qquad \text{[Nmm/mm}^2\text{]} \tag{5.2.24}$$

in which, f_{ctm} in MPa, is the average tensile strength of the concrete determined in a pull-off test according to DIN 1048 [1991], c_f is a constant determined by linear regression analysis of experimental data; k_p is a geometrical factor related to the width of the bonded plate b_p and the width of the concrete beam b_c , both expressed in mm:

$$k_p = \sqrt{1.125 \frac{2 - b_p / b_c}{1 + b_p / 400}} \tag{5.2.25}$$

Täljsten [1994] developed a similar model, in which the bond strength is calculated as:

$$P_u = \sqrt{\frac{2 E_p t_p G_f}{1 + \alpha_T}} b_p, \tag{5.2.26}$$

where E_c and t_c are the elastic modulus and thickness of the concrete member. The ratio α_t is:

$$\alpha_T = \frac{E_p t_p}{E_c t_c} \tag{5.2.27}$$

Yuan & Wu [1999] and Yuan et al. [2001] studied the bond strength between FRP and concrete using linear elastic fracture mechanism (LEFM) and nonlinear fracture mechanics (NLFM).
The expression proposed is similar to Eq. (5.2.26) but includes the effects of width of the plate and the concrete member through the coefficient α_y which replaces α_T of Eq. (5.2.27). They solved the NLFM equation for five different shear stress-slip relationships, among which the bi-linear relationship (Figure 5.2.4 (e)) is the closest to reality.

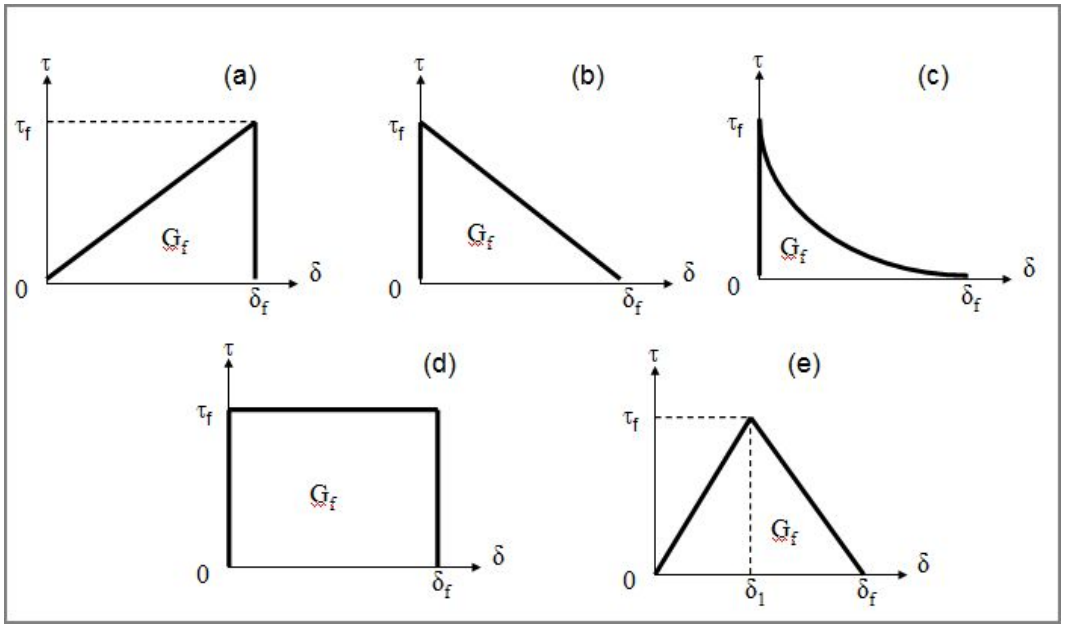

Figure 5.2.4: Shear-slip models for plate to concrete bonded joints

The maximum load-carrying capacity is:

$$P_u = \frac{\tau_f b_p}{\lambda_2} \frac{\delta_f}{\delta_f - \delta_1} \sin(\lambda_2 a) \qquad (5.2.28)$$

where a is the solution of the following equation:

$$\tanh\left[\lambda_1\left(L-a\right)\right]=\frac{\lambda_2}{\lambda_1}\tan\left(\lambda_2 a\right) \tag{5.2.29}$$

with τ_f is the maximum stress on the shear-slip curve of the bond, δ_1 is its corresponding slip, δ_f is the maximum slip and λ_1 and λ_2 are defined by:

$$\lambda_1^2=\frac{\tau_f}{\delta_1 E_p t_p}\left(1+\alpha_y\right) \tag{5.2.30}$$

$$\lambda_2^2=\frac{\tau_f}{\left(\delta_f-\delta_1\right)E_p t_p}\left(1+\alpha_y\right), \tag{5.2.31}$$

where

$$\alpha_y=\frac{b_p E_p t_p}{b_c E_c t_c} \tag{5.2.32}$$

In the solution of Yuan et al. the effective bond length is defined as the value corresponding to the 97% of the load-carrying capacity if L is assumed infinite:

$$L_e=a_0+\frac{1}{2\lambda_1}\ln\frac{\lambda_1+\lambda_2\tan(\lambda_2 a_0)}{\lambda_1-\lambda_2\tan(\lambda_2 a_0)} \tag{5.2.33}$$

where

$$a_0=\frac{1}{\lambda_2}\sin^{-1}\left(0.97\sqrt{\frac{\delta_f-\delta_1}{\delta_f}}\right) \tag{5.2.34}$$

Neubauer & Rostasy [1997a, b] conducted a series of double shear tests on CFRP/concrete bonded joints and concluded that, for both concrete fracture and FRP delamination failures, the shear-slip relationship may be represented by the bi-linear model (figure 5.1.4-e). The fracture energy G_f can be calculated using:

$$G_f = c_f f_{ctm} \tag{5.2.35}$$

where c_f had an average value equal to 0.204mm.
They presented a modified model to Holzenkämpfer:

$$P_u = \begin{cases} 0.64 k_p b_p \sqrt{E_p t_p f_{ctm}}, & if\ L \geq L_e \\ 0.64 k_p b_p \sqrt{E_p t_p f_{ctm}}\ \dfrac{L}{L_e}\left(2 - \dfrac{L}{L_e}\right), & if\ L < L_e \end{cases} \tag{5.2.36}$$

The effective bond length L_e is given by:

$$L_e = \sqrt{\frac{E_p t_p}{2 f_{ctm}}} \qquad \text{[mm]} \tag{5.2.37}$$

Van Gemert [1980], by assuming a triangular shear stress distribution (Figure 5.1.4(b)) in the full bond length, and by calculating the ultimate load through the concrete tensile strength f_{ctm}:

$$P_u = 0.5 b_p L f_{ctm} \tag{5.2.38}$$

This assumption is conceptually misleading because it contradicts the well-established fact that any additional bond length beyond the effective bond length cannot increase the bond strength.

5.2.4 Fracture mechanics-based models with the experimental calibration of parameters

Chen & Teng [2001] proposed a bond strength model by combining fracture mechanics analysis with experimental data. They noted that the shear-slip behaviour of plate to concrete bonded joints may be well represented by a triangular shear-slip model (figure 5.1.4-e) where the typical slip values at failure are $\delta_1 = 0.02mm$ and $\delta_f = 0.2mm$.
The NLFM solution is

$$P_u = \begin{cases} \tau_f b_p / \lambda & if\ L \geq L_e \\ \left(\tau_f b_p / \lambda\right) \sin\left(\lambda L\right) & if\ L < L_e \end{cases} \tag{5.2.39}$$

where

$$L_e = \frac{\pi}{2\lambda} \tag{5.2.40}$$

$$\lambda = \frac{\tau_f}{\delta_f E_p t_p}\left(1 + \alpha_y\right) \tag{5.2.41}$$

with $\alpha_y < 1$.

They also noted that a smaller width of the bonded plate to that of the concrete member leads to a non-uniform stress distribution across the width of the concrete member: when b_p is smaller then b_c higher shear stress can occur at the interface at failure because of contribution from the concrete outside the bond area.

By regression of experimental data, they related the ultimate bond strength to the coefficient β_p:

$$\beta_p = \sqrt{\frac{2 - b_p / b_c}{1 + b_p / b_c}} \tag{5.2.42}$$

They also noted that an accurate measure of the shear-slip properties δ_f and τ_f is very difficult but the experimental data lead to approximate τ_f by the tensile strength of concrete, which is related to the compressive strength of concrete in the form of $\sqrt{f_c'}$.

Chen and Teng approximated the effective bond length by the expression:

$$L_e = \sqrt{\frac{E_p t_p}{\sqrt{f_c'}}} \tag{5.2.43}$$

and proposed a simple expression for the ultimate bond strength:

$$P_u = 0.427\beta_p\beta_L\sqrt{f_c'}b_pL_e \qquad \text{[N]} \qquad (5.2.44)$$

where

$$\beta_L = \begin{cases} 1 & if\ L \geq L_e \\ \sin\left[\pi L/(2L_e)\right] & if\ L < L_e \end{cases} \qquad (5.2.45)$$

Faella et al. [2005] calibrated a bilinear ascending-softening relationship for characterizing the joint behaviour on the basis of the experimental results.
The simplest way for simulating FRP/concrete interface behaviour consists in assuming uncoupled models for shear and normal stresses.
The Equilibrium and compatibility conditions in the z-direction stated as follows:

$$\frac{d\sigma_z}{dz} + \frac{\tau(s)}{t_p} = 0 \qquad (5.2.46)$$

$$\varepsilon = \frac{ds}{dz} \qquad (5.2.47)$$

lead to the following differential equation in terms of shear stress $\tau(s)$ and interface slip s:

$$\frac{d^2s}{dz^2} + \frac{\tau(s)}{E_pt_p} = 0 \qquad (5.2.48)$$

where E_p is the plate Young modulus and t_p is its thickness.
Assuming the bi-linear relationship for $\tau(s)$ represented in Figure 5.2.4 (e), two cases can occur: if $s \leq s_{el}$ throughout all the bonded length (elastic behaviour) the following exponential solution can be derived (Figure 5.2.5 a)):

$$\tau = \alpha_{el}\frac{P}{b_p}\frac{\cosh\left[\alpha_{el}(L-z)\right]}{\sinh(\alpha_{el}L)} \qquad (5.2.49)$$

$$s = \frac{\tau}{k_{el}} = \frac{\alpha_{el}}{k_{el}} \frac{P}{b_p} \frac{\cosh\left[\alpha_{el}\left(L-z\right)\right]}{\sinh\left(\alpha_{el}L\right)} \tag{5.2.50}$$

being

$$\alpha_{el} = \sqrt{\frac{k_{el}}{E_p t_p}} \tag{5.2.51}$$

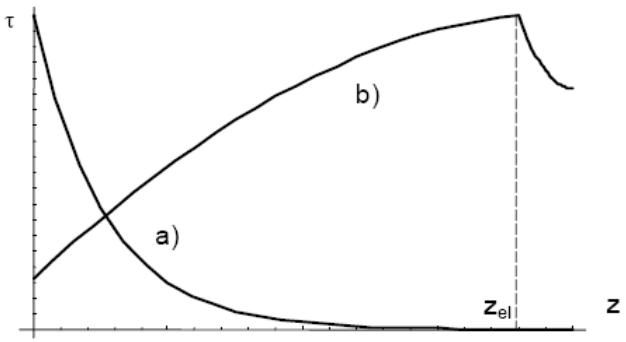

Figure 5.2.5: Interface shear stress: a) at the elastic limit, b) beyond the elastic limit.

The maximum "elastic" interface slip is attained for a force P_{el}:

$$P_{el} = \frac{\tau_{\max}}{\alpha_{el}} b_p \tan\left(\alpha_{el}L\right) \tag{5.2.52}$$

Whenever P overcomes P_{el}, slip in the bond length are greater than sel between the application point of the pulling out force and the abscissa z_{el}, where $s = s_{el}$ (curve b) in Figure 5.2.5).
In this case, two different expressions can be obtained for the two regions of the bonding length:

$$\tau = \begin{cases} \tau_m \cosh\left[\alpha_u \left(z - z_{oc}\right) + \sqrt{k_d k_u s_e} s_i \left[\alpha_u \left(z - z_{ie}\right)\right]\right] t, & if\ z \le z_{el} \\ \tau_m \dfrac{\cosh\left[\alpha_e \left(L - z_i\right)\right]}{\cosh\left[\alpha_{el} \left(L - z_{el}\right)\right]}, & if\ z > z_{el} \end{cases} \tag{5.2.53}$$

being

$$\alpha_u = \sqrt{\frac{\tau_m / \left(s_u - s_e\right)}{E_p t_p}} = \sqrt{\frac{k_u}{E_p t_p}} \tag{5.2.54}$$

The values of the force P (greater than P_{el}) corresponding to the given position of the transition point z_{el} can be obtained by integrating shear stresses along the bonding length. The maximum value P_{max} may be searched by varying the position of z_{el} between 0 and L.

Bi-linear ascending-softening relationship for describing the interface behaviour can by roughly simplified by considering a rigid-softening relationship (Figure 5.2.4 b)) and assuming $k_u' \approx k_u$. Under this hypothesis the ultimate capacity of the FRP/concrete joint can be evaluated as follows:

$$P_{\max} = \tau_{\max} L b_p \frac{\sin\left(\alpha_u L\right)}{\alpha_u L} \tag{5.2.55}$$

with

$$L \le L_{eff} = \frac{\pi}{2\alpha_u} \tag{5.2.56}$$

The inequality in Eq. (5.2.56) means that s is smaller than s_u throughout all the bonding length L of the FRP/concrete joint. When L reaches L_{eff} , s overcomes s_u in the portion of the joint close to the force P; for this reason, no further increase can be obtained for L greater than L_{eff} and the maximum ultimate capacity $P_{\max, L_{eff}}$ can be expressed as follows:

$$P_{\max,L_{eff}} = \tau_{\max}\sqrt{\frac{E_p t_p}{k_u}}b_p \qquad (5.2.57)$$

or

$$P_{\max,L_{eff}} = \sqrt{2G_f E_p t_p}\,b_p \qquad (5.2.58)$$

Guo et al. [2005] used a modified beam test specimen to study the bond behaviour and force transfer of FRP composite adhered to concrete taking into account the influence of bond length, and concrete strength. Based on experimental results on GFRP sheets they proposed three local bond stress-slip constitutive models, as will be described later on. The specimen was a plain concrete beam, simply supported and with the load applied at mid-span. The interfacial slip of section *i* (s_i) is the sum of the difference between the elongation of FRP and the elongation of the equivalent section compounded of concrete and epoxy layer from the free-end of the FRP laminate to section *i*.

They obtained a bond stress-slip curve which has a tendency to become parabolic in form (see Figure 5.2.6): a first steep ascending branch is followed by a plastic or softening region, until an ultimate slip is reached. After the bond stress reaches about 20% to 30% of the peak value, the stiffness of these curves continuously reduces with the increase of bond stress and reaches zero at the peak bond stress. After the peak stress, the curve descends slowly and become parabola in form. The softening branch of the curve predicts the attainment of a linear strain distribution close to peeling and the ultimate slip explains the ductility of the joint.

The local bond stress-slip curve has three key points which include the ultimate bond stress τ_{max} , the slip corresponding to the ultimate bond stress δ_{max}, and the ultimate slip δ_u. The measured ultimate bond stress τ_{max} shows a tendency to increase when the concrete compressive strength increases. The relationship between the ultimate bond stress and the concrete strength was analyzed.

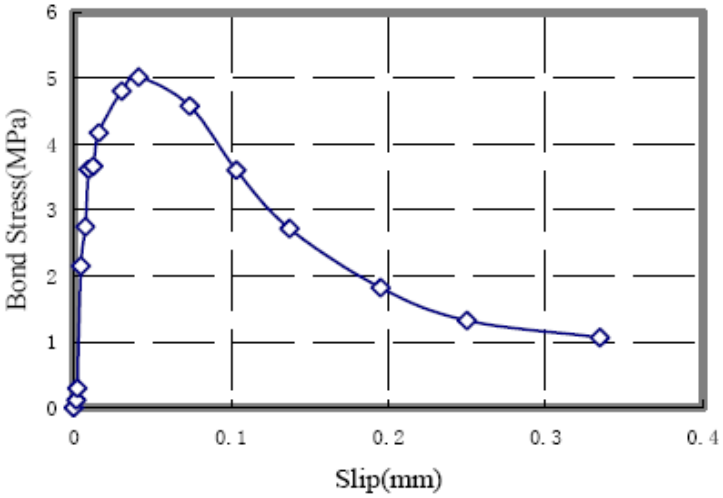

Figure 5.2.6: Experimental bond stress-slip curve [Guo et al. 2005]

The regression analysis of experimental data gave the following expression: $\tau_{\max} = 0.7512 f_{cu}^{0.5}$.

- The equation adopted as logarithmical model is the following:

$$\frac{\tau}{\tau_{\max}} = \begin{cases} \left[\dfrac{1+\alpha_k}{\alpha_k} \ln\left(1+\alpha_k \dfrac{\delta}{\delta_{\max}}\right) - \dfrac{\delta}{\delta_{\max}} \right] \dfrac{\bar{k}_0}{\alpha_k}, & \delta \le \delta_{\max} \\ \dfrac{\dfrac{\delta}{\delta_{\max}}}{a + b\dfrac{\delta}{\delta_{\max}} + c\left(\dfrac{\delta}{\delta_{\max}}\right)^2}, & \delta > \delta_{\max} \end{cases} \tag{5.2.59}$$

where

$$\bar{k}_0 = \frac{k_0 s}{\tau_{\max}} \tag{5.2.60}$$

is the normalised initial stiffness;

$$k_0 = \frac{1}{h_a / G_a + h_c / G_c} \tag{5.2.61}$$

is the initial stiffness; G_a is the shear modulus and t_a is the thickness of adhesive layer, G_c is the shear modulus and t_c is the thickness of concrete; α_k is a coefficient related to the normalised initial stiffness k_0, *a, b, c* are experimental coefficients with $a=c$ and $b=1-2a$. The expression of α_k as function of k_0 by the regression of local bond-slip curve was:

$$\alpha_k = -0.14\bar{k}_0^2 + 0.83\bar{k}_0 + 0.16 \tag{5.2.62}$$

The following conditions are to be satisfied according to the bond stress-slip curve:

$$\left.\frac{\tau}{\tau_{\max}}\right|_{\delta=\delta_{\max}} = 1; \qquad \left.\frac{d(\tau/\tau_{\max})}{d(\delta/\delta_{\max})}\right|_{\delta=0} = \bar{k}_0; \qquad \left.\frac{d(\tau/\tau_{\max})}{d(\delta/\delta_{\max})}\right|_{\delta=\delta_{\max}} = 1 \tag{5.2.63}$$

- The Popovics's equation was used to fit the local bond stress-slip curve. The Popovics's equation shown as follows:

$$\frac{\tau}{\tau_{\max}} = \frac{\delta}{\delta_{\max}} \frac{n}{n-1+\left(\delta/\delta_{\max}\right)^n} \tag{5.2.64}$$

where τ is the bond stress, in MPa; τ_{max} is the ultimate bond stress given by $\tau_{\max} = 0.7512 f_{cu}^{0.5}$; δ is the local slip in mm; δ_{max} is the slip corresponding to the ultimate bond stress; n is the constant coefficient. For the available experimental data the average value of n was 2.018.

- The Hyperbola model was obtained by the regression of the ascending and descending branches of the measured bond stress-slip

curve respectively. The Hyperbola model describes the ascending and descending branches separately using the following equations:

$$\frac{\tau}{\tau_{\max}} = \begin{cases} 1.114\left(\dfrac{\delta}{\delta_{\max}}\right)^{0.488}, & \delta \le \delta_{\max} \\ 1.3424e^{-0.2578\frac{\delta}{\delta_{\max}}}, & \delta > \delta_{\max} \end{cases} \qquad (5.2.65)$$

where τ is the bond stress, in MPa; τ_{max} is the ultimate bond stress given by $\tau_{\max} = 0.7512 f_{cu}^{0.5}$; δ is the local slip in mm; δ_{max} is the slip corresponding to the ultimate bond stress.

5.2.5 Unified analytical approach: Dai et al. model (2005)

The pullout test is a conventional test method for calibrating interfacial shear bond characteristics of FRP/concrete interface. However, due to the small bending stiffness of FRP sheets/strips and the highly non-linear interface fracturing mechanism, a well-recognized analytical approach to the accurate interpretation of the pullout test results remains to be achieved despite extensive studies particularly when the aim is to calibrate a local bond stress-slip model, which is necessary for developing bond strength and anchorage length models avoiding the use of empirical formulations.

This model introduces a newly developed non-linear bond stress-slip model for analyzing full-range strain distributions in FRP and shear bond stress distributions in the interface bond layer during pullout tests.

It is an established technique to obtain the tension-softening diagram of concrete from the load-deflection curve of a notched concrete beam under three-point bending through the *J*-integral method [Li & Ward 1989]. In a similar way, the local τ -*s* constitutive law for the FRP/concrete interface can be obtained from the relationship between pullout load and slip at the loaded point ($P = f(s)$) through simple pullout tests [Dai et al. 2005].

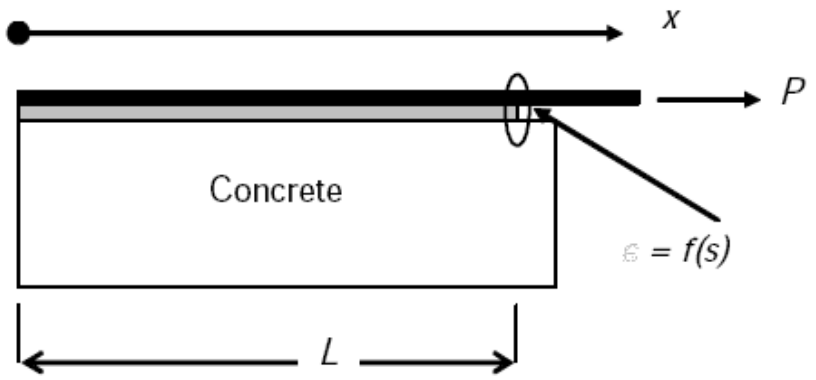

Figure 5.2.7: Sketch of pullout bond test setup

During a pullout test, as shown in Figure 5.2.7, pullout load P in the FRP and slip s between the FRP and the concrete at the loaded point (the circled location in Figure 5.2.7) can be recorded continuously. If FRP stiffness $E_f t_f$ (product of elastic modulus and thickness of FRP) and bond width b_f are known, the relationship between the strain in the FRP and the relative interface slip thus can be obtained as follows:

$$\varepsilon = f(s) \tag{5.2.66}$$

where ε and s are the FRP strain and interface slip at any a location, respectively.
For FRP externally bonded to concrete, the interfacial bond stress can be written as:

$$\tau = E_f t_f \frac{d\varepsilon}{dx} = E_f t_f \frac{df(s)}{ds} f(s) \tag{5.2.67}$$

because

$$\frac{d\varepsilon}{dx} = \frac{df(s)}{ds}\frac{ds}{dx} = \frac{df(s)}{ds}\varepsilon = \frac{df(s)}{ds} f(s) \tag{5.2.68}$$

where τ is the interfacial bond stress.
Using this approach, it is not necessary to get the local τ-*s* relationship by attaching many gages with a small interval on external bonded FRP to record strain distribution.
The effects of coarse aggregates near the interface and local bending of FRP, which are major causes of scatter in the observed FRP strains, can be avoided as well.
For FRP/concrete interfaces with a bond length longer than 300 mm, various pullout bond tests, in which different types of FRP materials, different adhesives and different FRP stiffness [Santos et al. 2003; Dai et al. 2005] a unique form of expression can represent *f*(*s*) and fit the experimental results quite well:

$$\varepsilon = f(s) = A\left(1-\exp\left(-Bs\right)\right) \tag{5.2.69}$$

The local τ-s model can be obtained as follows:

$$\tau = A^2 BE_f t_f \exp\left(-Bs\right)\left[1-\exp\left(-Bs\right)\right] \tag{5.2.70}$$

The physical meaning of A in Eq. (5.2.70) is the maximum strain reached in the FRP when using a long enough bond length in a pullout test and it can be related to the interfacial fracture energy G_f, which is the area underneath the local τ-s curve. The following expression is obtained:

$$A = \sqrt{\frac{2G_f}{E_f t_f}} \tag{5.2.71}$$

Therefore, Eq. (5.2.70) can be rewritten substituting Eq. (5.2.71) as follows:

$$\tau = 2BG_f\left[\exp\left(-Bs\right)-\exp\left(-2Bs\right)\right] \tag{5.2.72}$$

where G_f is expressed in [N/mm] and B in [mm^{-1}].
The theoretical maximum bond force for an FRP/concrete interface with sufficiently long bond length is:

$$P_{\max} = b_f \sqrt{2E_f t_f G_f} \tag{5.2.73}$$

The maximum bond stress and the corresponding slip value which are difficult to calibrate directly from pullout test results, can be determined mathematically as follows:

$$s_{\max} = 0.693/B \tag{5.2.74}$$

$$\tau_{\max} = 0.5BG_f \tag{5.2.75}$$

When the bond length is short, slip at the free-end occurs although strain in the FRP at that location remains zero. Non-zero slip and zero strain at the free-end causes different shapes of strain distributions in reinforcing materials internally or externally bonded to concrete.
An analytical solution to demonstrate different τ-*s* behaviours of the FRP/concrete interface near the free-end in a pullout test, is given as follows. It is assumed (Eq. 5.1.66) that a unified τ-*ε*-*s* expression can be applicable for the FRP-concrete interface as well to describe the different natures of strain distribution in the FRP near and far from the free end:

$$\begin{aligned} \tau = g(\varepsilon) \bullet \tau_0(s) = 2G_f B\left[\exp(-Bs) - \exp(-2Bs)\right] = \\ = 2G_f B \exp(-Bs)\left[1 - \exp(-Bs)\right] \end{aligned} \tag{5.2.76}$$

As a result, the problem in the current analysis is how to get expressions for $g(\varepsilon)$ and $\tau_0(s)$. From Eq. (5.2.66), which is true for the boundary condition of ε= 0, *s* = 0 and τ= 0 (long bond length case), it follows that:

$$\frac{\varepsilon}{A} = 1 - \exp(-Bs) \quad or \quad \exp(-Bs) = 1 - \frac{\varepsilon}{A} \tag{5.2.77}$$

As a consequence, the function for FRP strain, $g(\varepsilon)$ is assumed as follows:

$$g(\varepsilon) = 1 - \frac{\varepsilon}{A} \tag{5.2.78}$$

Substituting Equations (5.2.77) and (5.2.78) into Eq. (5.2.76):
or

$$\tau_0(s) = 2G_f B\left(1-\exp(-Bs)\right) \tag{5.2.79}$$

An important interfacial parameter termed effective bond length is needed for anchorage design of FRP/concrete interfaces. In order to define the effective bond length in a comprehensive way, it needs to have a good understanding of strain distributions in externally bonded FRP or shear stress distributions along the interfaces.
The following differential equation has been popularly used by many researchers to perform stress analysis in bonded connections subjected to shear by neglecting the bending effects of FRP, interfacial normal stress and strain in concrete (i.e., Brosens & Van Gemert [1998], Lorenzis et al. [2001], Wu et al. [2002], Yuan et al. [2004]):

$$\frac{d^2 s(x)}{dx^2} - \frac{\tau(x)}{E_f t_f} = 0 \tag{5.2.80}$$

Eq. (5.2.80) can be rewritten as the following equation with substitution of the bond stress-slip model (Eq. 5.2.72):

$$\frac{d^2 s(x)}{dx^2} = \frac{2BG_f}{E_f t_f}\left[\exp(-Bs) - \exp(-2Bs)\right] \tag{5.2.81}$$

The solution for Eq. (5.2.81) can be obtained as follows:

$$s(x) = \frac{1}{B}\ln\left[\exp B\left(Ax + c_2\right) + 1\right] \tag{5.2.82}$$

Therefore, the strain distribution in FRP can be written as:

$$\varepsilon(x) = \frac{ds}{dx} = A\frac{\exp B\left(Ax + c_2\right)}{\exp B\left(Ax + c_2\right) - 1} \tag{5.2.83}$$

where $A = 2G_f / E_f t_f$, and c_2 is a constant related to the boundary condition at the loaded end.

When pullout force P is exerted at the loaded end, the boundary condition of $= P/(b_f E_f t_f)$ at $x = L$ can be introduced into Eq. (5.2.83), and the constant c_2 can be determined as follows:

$$c_2 = \frac{\ln \dfrac{P}{P_{\max} - P}}{B} - AL \tag{5.2.84}$$

where P_{max} is the theoretical maximum pullout force (Eq. (5.2.73)). By substituting Eq. (5.2.84) into Eq. (5.2.83), the strain distribution of FRP sheets under pullout load P and a long bond length L can be expressed as:

$$\varepsilon(x) = \frac{A}{1 + \dfrac{\exp\left(AB\left(L - x\right)\right)\left(P_{\max} - P\right)}{P}} \tag{5.2.85}$$

Subsequently, shear stress distribution in the bond layer can be obtained as follows:

$$\tau(x) = \frac{E_f t_f P A^2 B \left(P_{\max} - P\right) \exp\left(AB\left(L - x\right)\right)}{\left[P + \left(P_{\max} - P\right)\exp\left(AB\left(L - x\right)\right)\right]^2} \tag{5.2.86}$$

Mathematically, L_e can be expressed as a distance between two locations x_1 and x_2 ($L_e = x_2$-x_1), which bears the pullout force P_{max} (can be taken as a constant that is nearly equal to one). At these two locations, strains of FRP are calculated as follows:

$$\varepsilon_1 = \frac{1-\alpha}{2} A; \quad \varepsilon_2 = \frac{1+\alpha}{2} A; \quad \varepsilon_1 - \varepsilon_2 = \alpha A \tag{5.2.87}$$

The following equation can be obtained from Eq. (5.2.85):

$$L-x=\frac{1}{AB}\left[\ln\left(\frac{A}{\varepsilon(x)}-1\right)-\ln\left(\frac{P_{\max}-P}{P}\right)\right] \tag{5.2.88}$$

By substituting Eq. (5.2.88) into Eq. (5.2.87), the effective bond length can be obtained as follows:

$$L_e=x_2-x_1=(L-x_1)(L-x_2)=\frac{2}{AB}\ln\left(\frac{1+\alpha}{1-\alpha}\right)=\frac{\sqrt{2E_ft_f}}{B\sqrt{G_f}}\ln\left(\frac{1+\alpha}{1-\alpha}\right) \tag{5.2.89}$$

The value increases less and less efficiently as the L_e increases. In other words, with gradual increase in bond length, the load transfer capacity that can be carried increases less and less efficiently.

For a reasonable anchorage strength design, use of the constant 0.96 for α in Eq. (5.2.89) [Ueda & Dai 2004] is suggested. The effective bond length increases with decreases in B and G_f.

For commonly used adhesives, the authors suggested the use of $0.514 f_c^{\,0.236}$ and 10.4 as reference values for G_f (N/mm) and B (mm^{-1}), respectively, based on a large number of experiments [Dai et al. 2005]. Therefore, Eq. (5.2.80) can be simplified as:

$$L_e=\frac{\sqrt{2E_ft_f}}{10.4\sqrt{0.514f_c^{0.236}}}\ln\left(\frac{1.96}{0.04}\right)=0.74\sqrt{\frac{E_ft_f}{f_c^{0.236}}} \tag{5.2.90}$$

When the bond length is shorter than the effective bond length, the bond strength of FRP/concrete interfaces significantly changes with the bond length. The effective bond length is usually used in the bond strength model as a parameter, meaning that the accuracy of the bond strength model is dependent on the manner in which the effective bond length is determined, which may in fact differ greatly among different models.

5.3 STEEL/CONCRETE INTERFACE

Steel concrete interaction influences the crack behaviour of the beam and therefore the performance of the FRP concrete interface and eventually of the entire retrofitted structural element. The mechanism by which forces are transferred between concrete and reinforcement has been widely investigated since reinforced concrete was introduced as a construction material and a detailed discussion of this topic is outside the scope of this work. However, the bond slip behaviour of steel reinforcement is briefly described for completeness and to give the relations used in the finite-element models.

The interaction between concrete and steel bars is characterized by four different steps Figure 5.3.1.

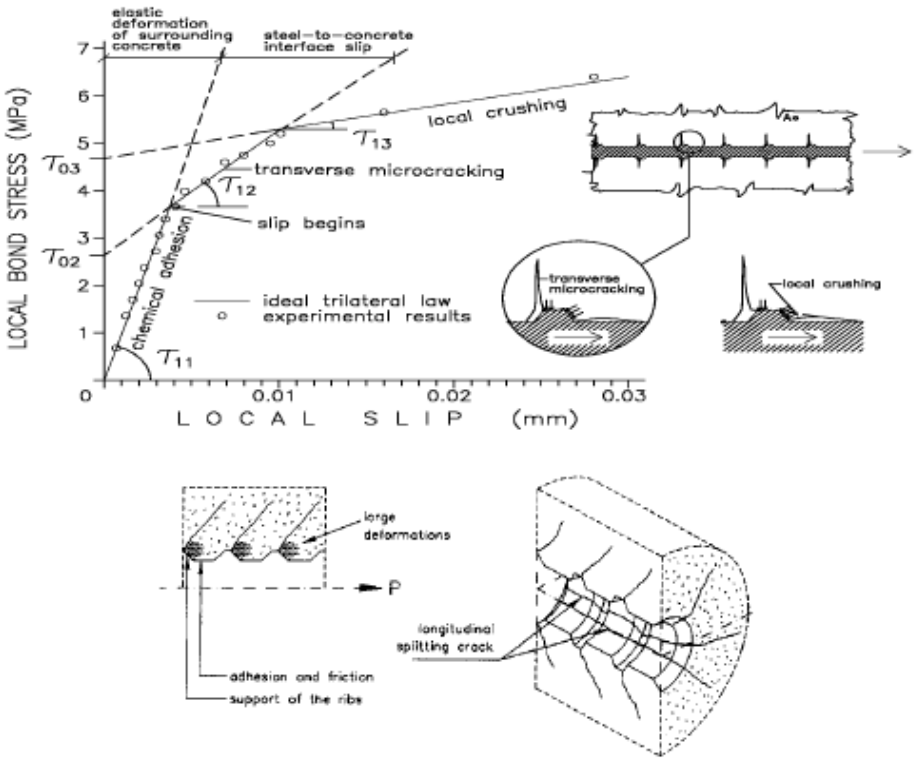

Figure 5.3.1: Local bond slip behaviour [Tassios 1979]

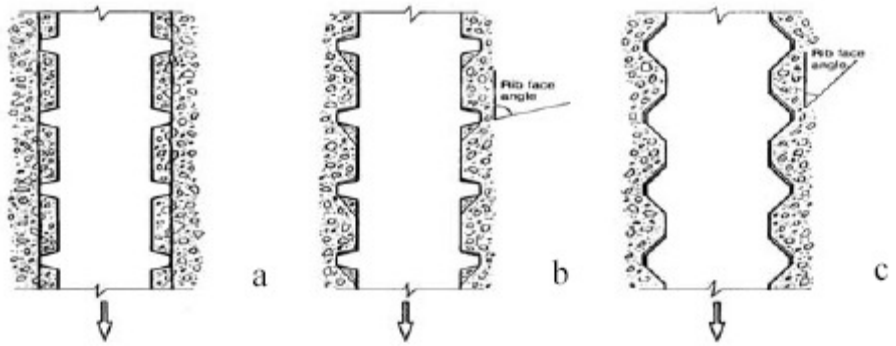

Figure 5.3.2: Modes of bond failure: (a) pull out; (b) splitting-induced pull out accompanied by crushing and/or shearing-off in the concrete under the rib action; (c) splitting accompanied by slip on the rib faces [Coirus & Andreasen 1992].

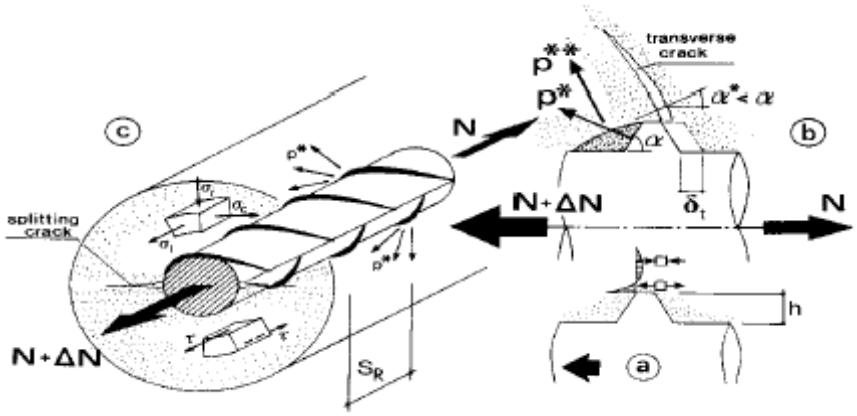

Figure 5.3.3: Bond splitting in reinforced concrete (deformed bars): (a) typical stress peak in the elastic phase; (b) bar concrete slip and wedging action of the bar; (c) main parameters.

- Step I (uncracked concrete): in this stage the bond action is due mainly to chemical adhesion. The bond stresses are characterized by low value, but highly localized stresses may arise close to lug tips (Figures 5.3.1-5.3.3).
- Step II (first cracking): in this stage the chemical adhesion breaks down and the stress transfer is due to mechanical interlocking of the lugs in the surrounding concrete. Large bearing stresses are generated in the

concrete at the lugs Figure (5.3.3). Due to these bearing stresses micro cracks originate at the tips of the lugs allowing the bar to slip as the bond stresses increase.

- Step III (conical struts action): for higher bond stress values, longitudinal cracks start to form originating from initial micro cracks, generating conical struts, Figures 5.3.1-5.3.3. The outward component of the strut action Figure 5.3.3 is resisted by the hoop stresses in the surrounding concrete. The surrounding concrete will exert therefore a confinement action on the bar. Thus, the bond strength and the stiffness are due mostly to the interlocking among the lugs and the surrounding concrete.
- Step IV (residual friction): at this stage the conical struts have failed and only a residual frictional stress transfer is active. The interfacial stresses associated with the interaction mechanisms described, are of different nature and very variable along the bar. For the purpose of the analysis of a reinforced concrete structural element these stresses need to be spatially averaged. By carrying out this spatial averaging we define a bond stress that can be used to define a bond slip relation that simplify considerably the treatment of this problem (Figures 5.3.1-5.3.3).

The mechanisms of stress transfer from step I to step III are considered primary mechanisms as they can be found within the serviceability load limits of the structure. The residual frictional stress transfer of step IV is considered a secondary mechanism (whose effect combined with all the others is present since the beginning of the loading process anyway) as steel bars are considered debonded if this is the only resistance mechanism active.

In Figure 5.3.2 typical failure modes of the concrete surrounding the bars are shown.

In order to establish an appropriate constitutive law for the interface, the bond slip relation should depend, in principle, upon the type of bar, the concrete strength, the confinement regime and the conditions of the materials (rusting of steel, carbonation of concrete). Workmanship of the structure is also relevant.

However, a constitutive low depending only on the concrete strength and confinement regime is given in the CEB-FIP Model Code [1990]. This is based on a work by Ciampi at al. [1982].
In this model the primary zone is non linear and it is modelled by:

$$\tau = \rho_1 s^{\Omega} \tag{5.3.1}$$

where

$$\rho_1 = \frac{\tau_1}{\rho^{\Omega}_1} \tag{5.3.2}$$

is an empirical constant ($\Omega<1$) that describe the shape of the bond stress-slip curve. The model includes a plateau at the peak stresses (τ_1), followed by a linear degradation zone. The bond stress due to the secondary bond mechanism is assumed constant.
The model is characterised by the parameters: s_1, s_2, s_3, τ_1, τ_2, and Ω; these parameters (see Figure 5.3.4) are given in the Model Code as functions of the clear rib spacing of the bars, the concrete strength and the confinement regime. Their expression is reported in Table 5.3.1

Table 5.3.1. Bond-slip law parameters.

	s_1 [cm]	s_2 [cm]	s_3 [cm]	τ_1 [cm]	τ_2 [cm^2]	Ω
Confined concrete	1	3	Clear rib spacing	$2.5(f_{ck})^{1/2}$	$(f_{ck})^{1/2}$	0.4
Unconfined concrete	0.6	0.6	10	$2.0(f_{ck})^{1/2}$	$0.6(f_{ck})^{1/2}$	0.4

For implementation reasons the above relation has been simplified, in the finite-element models, to the one with a linear initial branch followed by linear softening described in Figure 5.3.5.
The parameters characterizing the model adopted have been derived imposing the same peak stress as in the CEB-FIP model, a slip displacement

at the peak stress (s_0) equal to s_1 and a fracture energy Gc equal to the energy obtained integrating the CEB-FIP relation between zero and the slip displacement s_3. This is equivalent to neglecting the residual bond stresses.

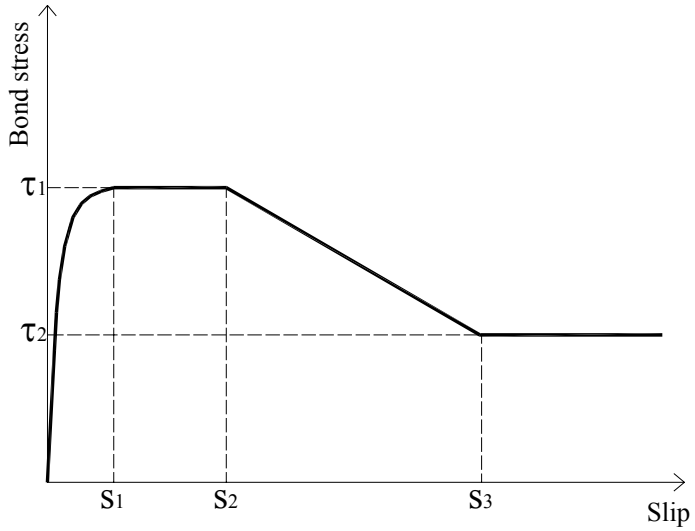

Figure 5.3.4: Analytical model for local bond stress-slip relationship [Ciampi et al. 1981, Eligehausen et al. 1983].

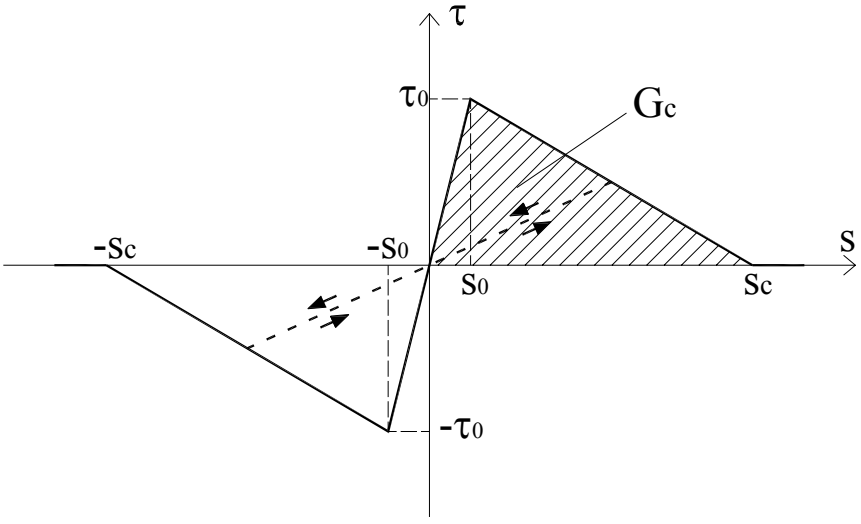

Figure 5.3.5: Bond slip relation used in the finite-element models.

CHAPTER VI
SOLUTION of NON-LINEAR COMPUTATIONAL PROBLEMS

6.1 ITERATIVE PROCEDURES

6.1.1 Introduction

In this section only a brief outline of several solution methods of non-linear problems available in literature and provided by the most important finite-element analysis programs will be made. They was used to solve the non-linear problems of the applications which will be presented in the next section.

The solution of a non-linear problem can be simply understood by considering the external forces, *P*, and the internal (nodal) forces, *I*, acting on a body (see figure 6.1.1(a) and 6.1.1(b), respectively).

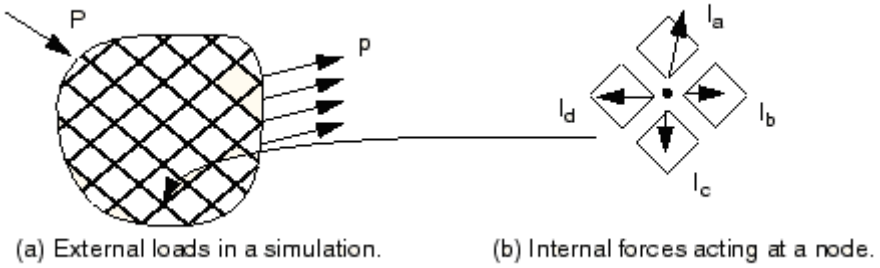

Figure 6.1.1: Internal and external loads on a body.

The internal loads acting on a node are caused by the stresses in the elements that contain that node.

For the body to be in static equilibrium, the net force acting at every node must be zero. Therefore, the basic statement of static equilibrium is that the internal forces, *I*, and the external forces, *P*, must balance each other:

$$P - I = 0 \tag{6.1.1}$$

In a nonlinear analysis the solution cannot be calculated by solving a single system of equations, as would be done in a linear problem. Instead, the solution is found by applying the specified loads gradually and incrementally working
toward the final solution. Therefore, the method breaks the simulation into a number of *load increments* and finds the approximate equilibrium configuration at the end of each load increment.
It is important to clearly understand the difference between an analysis *step*, a load *increment*, and an *iteration*:

- The load history for a simulation consists of one or more *steps*. You can define the steps on the base of the different loads, boundary conditions, analysis procedure and output requests. During the generic step, the loads and boundary conditions do not change;
- An *increment* is part of a step. In nonlinear analyses the total load applied in a step is broken into smaller increments so that the nonlinear solution path can be followed. In solution searching you suggest the size of the first increment. At the end of each increment the structure is in (approximate) equilibrium and results are available for writing to the output database, restart, data, or results files;
- An *iteration* is an attempt at finding an equilibrium solution in an increment when solving with an implicit method. If the model is not in equilibrium at the end of the iteration, you have to try another iteration. With every iteration the solution should be closer to equilibrium; sometimes it may need many iterations to obtain an equilibrium solution. When an equilibrium solution has been obtained, the increment is complete.

These consideration can be related for simplicity to a one-dimensional problem:

$$q_e = f\left(p\right) \tag{6.1.2}$$

where q_e is the load and p is the displacement. We define the tangent stiffness as follows:

$$K_t = \frac{df}{dp} \tag{6.1.3}$$

K_t corresponds to the tangent at the point p-q_e. If we introduce the out-of-balance $g = f(p) - q_e$, for the considered point p-q_e, we obtain for a constant load that:

$$K_t = \frac{dg}{dp} \tag{6.1.4}$$

For a problem with several dimensions, described by the equations $\mathbf{g} = \mathbf{q}_i(\mathbf{p}) - \mathbf{q}_e = 0$, we define the tangent stiffness matrix in the same manner $\mathbf{K}_t = d\mathbf{g}/d\mathbf{p}$.

Different methods can be used in order to solve a non linear problem $\mathbf{g} = \mathbf{0}$. The majority of those methods requires the computation of the variables $\mathbf{g}$ and $\mathbf{K}_t$.

We use the term load control, to indicate that the value of a vector of applied forces $\mathbf{q}_e$ is known at each time of the analysis. Analogously, "displacement control" means that some displacements are prescribed.

Having assigned the history of applied forces or prescribed displacements, an incremental analysis consists of dividing such history in a finite number of increments. We will focus our attention on a "load control" problem, for simplicity, but the treatment would be easily extendable to a "displacement control".

For each increment, the initial values of the displacements $\mathbf{p}_0$ and of the applied forces $\mathbf{q}_{e0}$ are known, as well as the increment of the forces $\Delta\mathbf{q}_{e0}$, and the final value of the displacement is unknown.

Three different approaches for the solution to the incremental problem will be briefly discussed; finally, a brief description of the explicit approach to the solution of a non-linear problem will be given.

6.1.2 Incremental method

Considering for simplicity a one-dimensional example, we know, for each increment, Δq_e, and the initial displacement p_0. With an incremental method, we find the next displacement p_1 as follows:

$$p_1 = p_0 + \Delta p_0 \tag{6.1.5}$$

with

$$\Delta p_0 = K_{t0}^{-1} \Delta q_e \tag{6.1.6}$$

and K_{t0} is computed from p_0.
This method can lead far away from the real solution particularly if the parameter Δq_e is chosen too high or if the function f is quite irregular (Figure 6.1.2 (a))

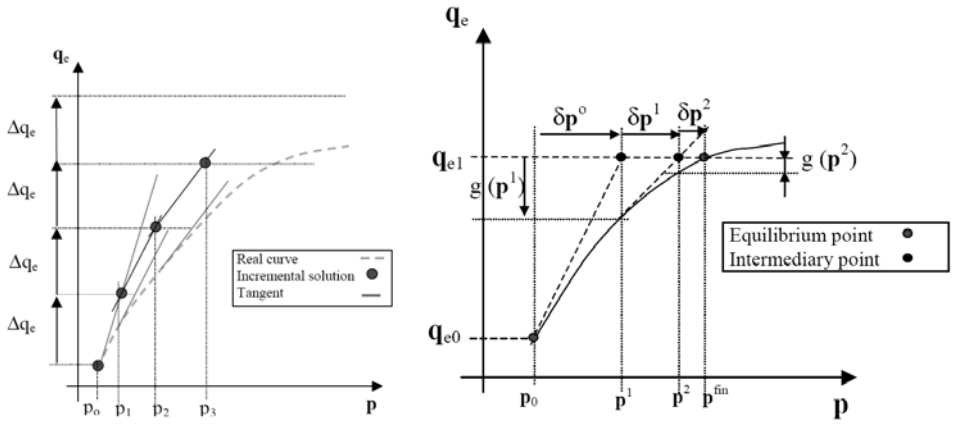

Figure 6.1.2: (a) Incremental method; (b) iterative method

6.1.3 Newton-Raphson method

Considering again, for simplicity, a one-dimensional problem, for the generic increment the applied force will change from the initial value $q_{e,in}$ to the value at the end of the increment, $q=q_{e,in}+\Delta q$.

Denoting as p_0 a "trial" value for the displacement at the end of the increment. The equilibrium equation is generally not satisfied and then a non-zero residual g is computed, $g = f(p) - q_e \neq 0$. Considering the point p_0 for which $g(p_0) \neq 0$, the tangent straight line at this point will be:

$$y = g(p_0) + \frac{dg}{dp}(p_0)(p - p_0) \tag{6.1.7}$$

And for y=0:

$$p = p_0 - \frac{dg}{dp}(p_0)^{-1} g(p_0) \quad with \frac{dg}{dp}(p_0) \neq 0 \tag{6.1.8}$$

Setting:

$$\delta p_0 = -\frac{dg}{dp}(p_0)^{-1} g(p_0) = -K_{t0}^{-1} g(p_0) \tag{6.1.9}$$

Such method is defined as iterative because this procedure continues until δp_i is sufficiently small (depending on the needed precision).
The difference between this method and the last one is that δp_i are iterative changes at the same fixed load level, and the final solution is effectively an equilibrium point (Figure 6.1.2 (b)). The error due to this approximation is about δp_i^2. In fact, expanding g in a Taylor series up to the first order, the following equation can be written:

$$g(p) = g(p_0) + \frac{dg}{dp}(p_0)(p - p_0) + o(p - p_0)^2 \tag{6.1.10}$$

The Newton-Raphson method is called "full" because a new tangent stiffness matrix has to be calculated at each iteration. A simplest method is to always use the tangent stiffness matrix calculated for the first iteration (modified Newton-Raphson method).
One deals with a problem with more dimensions in the same way.

6.1.4 Combined method

The iterative method gives a very good approximation, but some problems can occur if a bad initial parameter is chosen: the CPU time can be very large or K_t might be singular or indefinite for some points.
So one can turn to the use of a combination of the two methods in order to have a good initial parameter given by the incremental method, and at the end, a result very close to the real solution due to the iterative method. The tangential incremental solution can be used as a predictor (Figure 6.1.3).

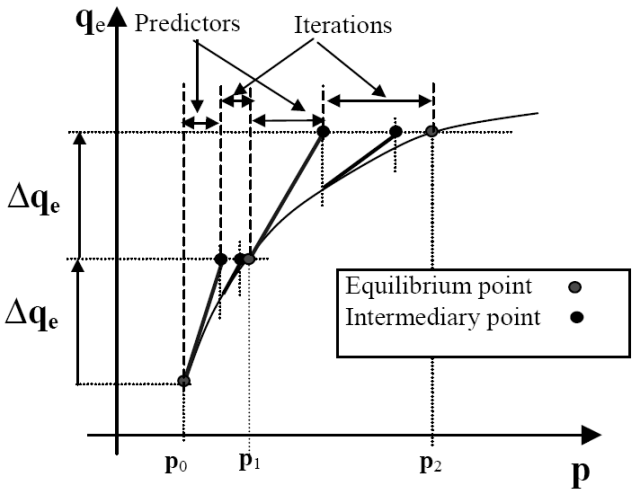

Figure 6.1.3: Combined method

6.1.5 Arc-length method

When the studied function *f(p)* is quite irregular, that is, in mathematical terms, not subjective or not injective, the previous methods can fail to give a solution as it is not possible to pass limit points (i.e., characterised by K_t=0). In Figure 6.1.4 the dashed part is impossible to find with load control, and we can not obtain the plain part with displacement control.

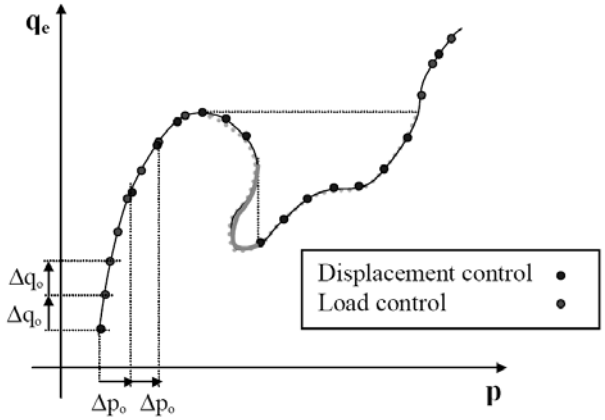

Figure 6.1.4: Failure of classical non-linear method

So a new method that gives the solution in such cases needs to be introduced. Considering the following problem:

$$\mathbf{g}(\mathbf{p},\lambda) = \mathbf{q}_i(\mathbf{p}) - \lambda \mathbf{q}_0 \tag{6.1.11}$$

Where $\lambda \mathbf{q}_0$ are the external forces and $\mathbf{q}_i(\mathbf{p})$ are the internal forces. The external forces are not fixed in this problem and changes linearly with $\mathbf{q}_0$, due to the unknown parameter λ.

Considering a one-dimensional problem it has one equation for two unknowns. In a N-dimensional problem, it will have N+1 unknowns and N equations. So another equation in both cases has to be introduced.

Again, the problem is divided in a finite number of increments. For each of them, the initial values of the displacement vector, $\mathbf{p}_{in}$, and of the local load factor λ_{in}, are known. One way to introduce a new equation is to want the solution at the end of the increment to be, in the plate (or hyperplan) $(\mathbf{p}, \lambda \mathbf{q}_0)$, at a distance $\Delta\lambda$ from the initial point $(\mathbf{p}_{in}, \lambda_{in}\mathbf{q}_0)$. This constraint equation can be expressed as follows:

$$\left\| (\mathbf{p}, \lambda \mathbf{q}_0) - (\mathbf{p}_{in}, \lambda_{in}\mathbf{q}_0) \right\| = \Delta l \tag{6.1.12}$$

Introducing $\Delta\mathbf{p} = \mathbf{p} - \mathbf{p}_{in}$ and $\Delta\lambda = \lambda - \lambda_{in}$, Eq. (6.1.12) becomes:

$$\sqrt{\Delta\mathbf{p}^2 + \left(\Delta\lambda\mathbf{q}_0\right)^2} = \Delta l \qquad (6.1.13)$$

Where Δl is a fixed incremental length. This equation is not dimensionally consistent. Introducing the scaling parameter ψ Eq. (6.1.13) becomes:

$$\sqrt{\Delta\mathbf{p}^2 + \left(\psi\Delta\lambda\mathbf{q}_0\right)^2} = \Delta l \qquad (6.1.14)$$

Now we have enough equations to solve the problem and find the unknowns ($\mathbf{p}$, λ). Because this problem is non-linear, the use of an iterative method is necessary (i.e., combined Newton-Raphson method). The first thing to do is to find the predictor.

At the beginning of an increment, the values $\mathbf{p}_{in}$ and λ_{in} are known and correspond to the last converged solution. Then, the equilibrium solution, which implies $\mathbf{g}(\mathbf{p}, \lambda)=0$, has to be reached. Expanding $\mathbf{g}$ in a Taylor series up to the first order, it results:

$$\mathbf{g}\left(\mathbf{p},\lambda\right) = \mathbf{g}\left(\mathbf{p}_{in},\lambda_{in}\mathbf{q}_0\right) + \frac{\partial\mathbf{g}}{\partial\mathbf{p}_{(\mathbf{p}_{in},\lambda_{in})}}\Delta\mathbf{p} + \frac{\partial\mathbf{g}}{\partial\lambda_{(\mathbf{p}_{in},\lambda_{in})}}\Delta\lambda = 0 \qquad (6.1.15)$$

Because $\left(\mathbf{p}_{in},\lambda_{in}\right)$ is an equilibrium point, $\mathbf{g}\left(\mathbf{p}_{in},\lambda_{in}\right)=0$, it can be written:

$$\frac{\partial\mathbf{g}}{\partial\mathbf{p}_{(\mathbf{p}_{in},\lambda_{in})}}\Delta\mathbf{p} + \frac{\partial\mathbf{g}}{\partial\lambda_{(\mathbf{p}_{in},\lambda_{in})}}\Delta\lambda = 0 \qquad (6.1.16)$$

Knowing that $\frac{\partial\mathbf{g}}{\partial\mathbf{p}_{(\mathbf{p}_{in},\lambda_{in})}} = \mathbf{K}_{t(\mathbf{p}_{in},\lambda_{in})}$ and referring to the equation (6.1.11), it can written $\frac{\partial\mathbf{g}}{\partial\lambda_{(\mathbf{p}_{in},\lambda_{in})}} = -\mathbf{q}_0$.

Finally:

$$\mathbf{K}_{t(\mathbf{p}_{in},\lambda_{in})}\Delta\mathbf{p} - \mathbf{q}_0\Delta\lambda = 0 \qquad (6.1.17)$$

which yields:

$$\Delta\mathbf{p} = \Delta\lambda\Delta\mathbf{p}_t \tag{6.1.18}$$

In this way, $\Delta\mathbf{p}$ is a function of $\Delta\lambda$, which is the only unknown. Substituting Eq. (6.1.18) in the arc-length equation:

$$\Delta\lambda^2\sqrt{\Delta\mathbf{p}^2{}_t + \left(\mathbf{q}_0\psi\right)^2} = \Delta l^2 \Rightarrow \Delta\lambda = \pm\frac{\Delta l}{\sqrt{\Delta\mathbf{p}^2{}_t + \left(\mathbf{q}_0\psi\right)^2}} \tag{6.1.19}$$

This equation has two solutions. One way to choose the best solution is to look at the sign of the determinant of $\mathbf{K}_t\left(\mathbf{p}_{in}, \lambda_{in}\right)$. If this is positive, the positive solution has to be chosen, in order to be on the right part of the tangent straight line (Figures 6.1.5 (a)-(b)).
We have thus found $\mathbf{p}$ and λ but $\mathbf{g}\left(\mathbf{p}, \lambda\right) \neq 0$ (because of the Taylor truncation). In order to obtain a better solution one can use the iterative method for the same increment.
Renaming the last $\mathbf{p}$ as $\mathbf{p}_0$ and the last λ is called λ_0, the next solution can be obtained by calculating the iterative changes $\delta\mathbf{p}$ and $\delta\lambda$ as follows:

$$\mathbf{p} = \mathbf{p}_0 + \delta\mathbf{p}; \quad \lambda = \lambda_0 + \delta\lambda \tag{6.1.20}$$

So, due to the definition of $\Delta\mathbf{p}$ and $\Delta\lambda$, it has $\Delta\mathbf{p} = \Delta\mathbf{p}_0 + \delta\mathbf{p}$ and $\Delta\lambda = \Delta\lambda_0 + \delta\lambda$ where $\Delta\mathbf{p}_0 = \mathbf{p}_0 + \mathbf{p}_{in}$ and $\Delta\lambda_0 = \lambda_0 + \lambda_{in}$ which is the solution of the predictor.
Now, $\mathbf{g}$ can be linearised about $\left(\mathbf{p}_0, \lambda_0\right)$, hence:

$$\mathbf{g}\left(\mathbf{p}, \lambda\right) = \mathbf{g}\left(\mathbf{p}_0, \lambda_0\right) + \frac{\partial\mathbf{g}}{\partial\mathbf{p}_{(\mathbf{p}_0, \lambda_0)}}\delta\mathbf{p} + \frac{\partial\mathbf{g}}{\partial\lambda_{(\mathbf{p}_0, \lambda_0)}}\delta\lambda = 0 \tag{6.1.21}$$

For the same reason as above one can rewrite the equation:

$$\mathbf{g}\left(\mathbf{p}_0, \lambda_0\right) + \mathbf{K}_{t(\mathbf{p}_0, \lambda_0)}\delta\mathbf{p} - \mathbf{q}_0\delta\lambda = 0 \Rightarrow \delta\mathbf{p} = -\left(\mathbf{K}_{t(\mathbf{p}_0, \lambda_0)}\right)^{-1}\mathbf{g}\left(\mathbf{p}_0, \lambda_0\right) + \left(\mathbf{K}_{t(\mathbf{p}_0, \lambda_0)}\right)^{-1}\mathbf{q}_0\delta\lambda \tag{6.1.22}$$

By setting $\delta\mathbf{p}_t = \left(\mathbf{K}_{t(\mathbf{p}_0,\lambda_0)}\right)^{-1}\mathbf{q}_0$ and $\delta\overline{\mathbf{p}} = \left(\mathbf{K}_{t(\mathbf{p}_0,\lambda_0)}\right)^{-1}\mathbf{g}\left(\mathbf{p}_0,\lambda_0\right)$, it results:

$$\delta\mathbf{p} = \delta\overline{\mathbf{p}} + \delta\lambda\delta\mathbf{p}_t \tag{6.1.23}$$

where the only unknown is $\delta\lambda$.

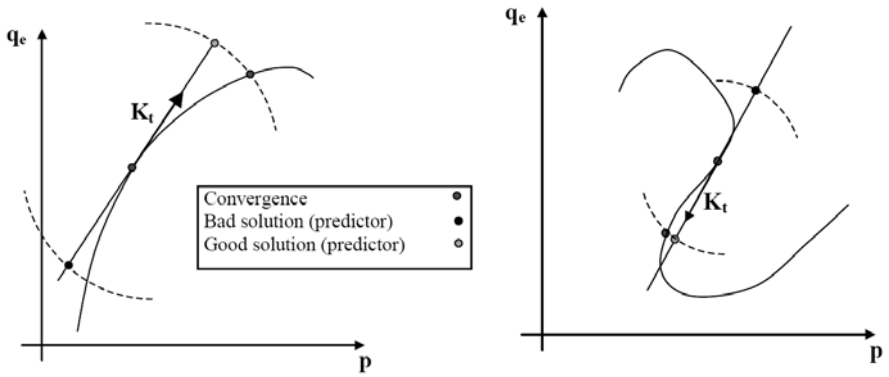

(a) (b)

Figure 6.1.5: (a) Choice of the right value of the predictor(positive tangent); (b) choice of the right value of the predictor (negative tangent)

Substituting expression (6.1.23) in the arc-length equation:

$$\left(\Delta\mathbf{p}_0 + \delta\overline{\mathbf{p}} + \delta\lambda\delta\mathbf{p}_t\right)^2 + \left(\psi\mathbf{q}_0\left(\Delta\lambda_0 + \delta\lambda\right)\right)^2 = \left(\Delta l\right)^2 \Rightarrow a_1\left(\delta\lambda\right)^2 + 2a_2\delta\lambda + a_3 = 0 \tag{6.1.24}$$

where:

$$\begin{aligned} a_1 &= \left(\psi\mathbf{q}_0\right)^2 + \left(\delta\mathbf{p}_t\right)^2 \\ a_2 &= \left[\Delta\lambda_0\left(\psi\mathbf{q}_0\right)^2 + \left(\Delta\mathbf{p}_0 + \delta\overline{\mathbf{p}}\right)\delta\mathbf{p}_t\right] \\ a_3 &= \left(\Delta\lambda_0\psi\mathbf{q}_0\right)^2 + \left(\Delta\mathbf{p}_0 + \delta\overline{\mathbf{p}}\right)^2 - \left(\Delta l\right)^2 \end{aligned} \tag{6.1.25}$$

Eq. (6.1.24) is quadratic and has two solutions, real or complex, distinct or coincident. Ruling out the case that they are non-real (for which a reduction of Δl is required and the analysis must be restarted from the previous converged solution), and assuming that they are distinct, a criterion is then required for choosing the best solution. One can compare the direction of the new vector $\left(\mathbf{p}-\mathbf{p}_{in},\left(\lambda-\lambda_{in}\right)\left(\psi\mathbf{q}_0\right)\right)$ with the vector obtained by the predictor $\left(\mathbf{p}_0-\mathbf{p}_{in},\left(\lambda_0-\lambda_{in}\right)\left(\psi\mathbf{q}_0\right)\right)$. So by calculating the scalar product between the two vectors, the smallest angle will correspond to the nearest vector from the predictor and this might be considered as the best solution. This can be written as:

$$\cos\left(\theta\right)=\frac{\Delta\mathbf{p}_0^T\Delta\mathbf{p}+\Delta\lambda_0^T\Delta\lambda\left(\psi\mathbf{q}_0\right)^2}{\Delta l^2}=\frac{a_4+a_5\delta\lambda}{\Delta l^2} \tag{6.1.26}$$

where:

$$a_4=\Delta\mathbf{p}_0^T\left(\Delta\mathbf{p}_0+\delta\overline{\mathbf{p}}\right)+\Delta\lambda_0^T\Delta\lambda_0\left(\psi\mathbf{q}_0\right)^2 \tag{6.1.27}$$

$$a_5=\Delta\mathbf{p}_0^T\Delta\mathbf{p}_t+\Delta\lambda_0^T\left(\psi\mathbf{q}_0\right)^2 \tag{6.1.28}$$

This method is quite well suited for relatively smooth limit points. But if the limit points are not smooth, this method is inefficient (Figure 6.1.5(b)) and a new criterion has to be adopted. Choosing the root which provides the minimum residual norm $\left\|\mathbf{g}\right\|$, if a convergence criterion is not satisfied (for example $\left\|\mathbf{g}\right\|\geq Tol.$) the above described procedure has to be iterated, by taking the values $\mathbf{p}_0+\delta\overline{\mathbf{p}}+\delta\lambda\mathbf{p}_t$ and $\lambda_0+\delta\lambda$ as new trial solutions $\mathbf{p}_0$, λ_0 (Figure 6.1.6).

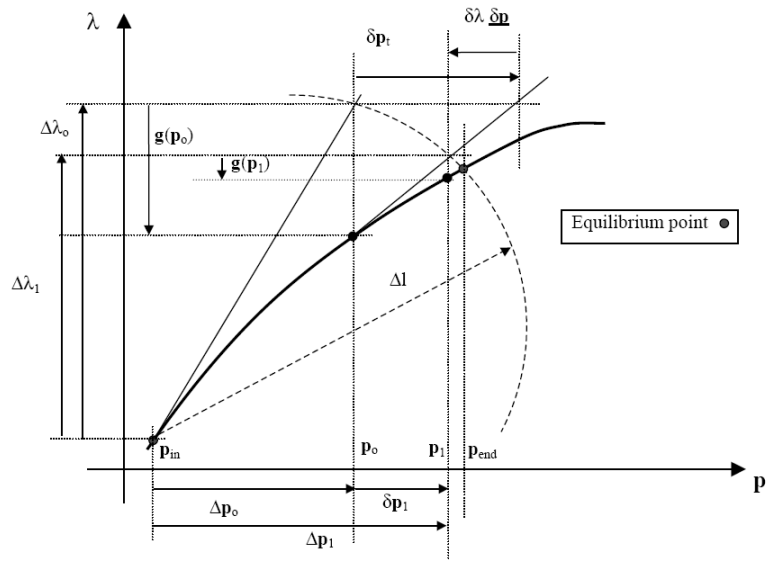

Figure 6.1.6: arc-length method

6.1.6 Linearised arc-length method

Defining a_i as follows:

$$a_i = \Delta l^2 - \left(\Delta \mathbf{p}_i^{\,2} + \left(\psi \mathbf{q}_0 \Delta \lambda_i \right)^2 \right), \tag{6.1.29}$$

linearization about $\left(\Delta \mathbf{p}_{i-1}, \Delta \lambda_{i-1} \right)$ yields:

$$a_i = a_{i-i} - 2\Delta \mathbf{p}_{i-1}{}^T \delta \mathbf{p}_i + 2\Delta \lambda_{i-1} \delta \lambda_{i-1} \left(\psi \mathbf{q}_0 \right)^2 + o\left(\delta \mathbf{p}_i^2, \delta \lambda_i^2 \right) \tag{6.1.30}$$

where a_{i-1} is obtained for $\Delta \mathbf{p}_{i-1}$ and $\Delta \lambda_{i-1}$. Because a_i=0, it has the following equation:

$$\frac{-a_{i-i}}{2} = \Delta \mathbf{p}_{i-1}{}^T \delta \mathbf{p}_i + \Delta \lambda_{i-1} \delta \lambda_{i-1} \left(\psi \mathbf{q}_0 \right)^2 \tag{6.1.31}$$

Taking a_{i-1}=0 in the previous equation, two linearised methods can be applicable.

The Ramm's approach which ensures that the iterative change $\left(\delta\mathbf{p}_i, \delta\lambda_i\left(\psi\mathbf{q}_0\right)\right)$ is orthogonal to the change $\left(\Delta\mathbf{p}_{i-1}, \Delta\lambda_{i-1}\left(\psi\mathbf{q}_0\right)\right)$ is shown in Figure 6.1.7 (a); in the Riks's formulation, the old incremental change $\left(\Delta\mathbf{p}_{i-1}, \Delta\lambda_{i-1}\left(\psi\mathbf{q}_0\right)\right)$ is replaced by the predictor vector, which means that $\left(\delta\mathbf{p}_i, \delta\lambda_i\left(\psi\mathbf{q}_0\right)\right)$ is always orthogonal to the predictor $\left(\Delta\mathbf{p}_0, \Delta\lambda_0\left(\psi\mathbf{q}_0\right)\right)$. The iterative solutions are on the straight line orthogonal to the predictor (Figure 6.1.7 (b)).

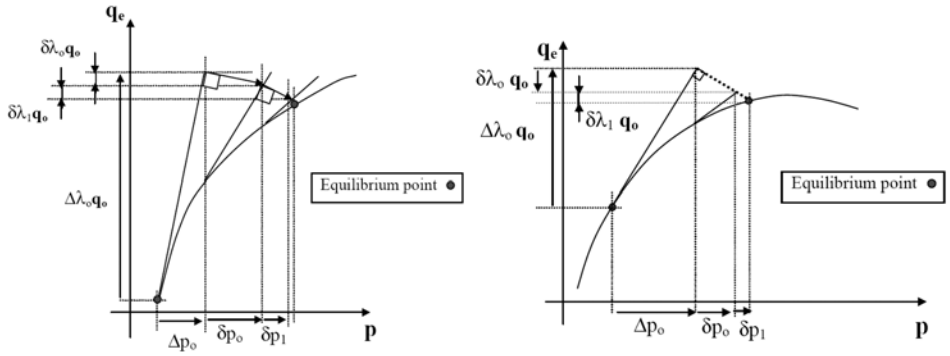

(a) (b)

Figure 6.1.7: (a) Ramm's method; (b) Riks's method

These linearised forms are simpler than the spherical form because we have only one solution. But if the studied function is too irregular the linearised forms fail to converge, unlike the spherical method.

Modifying the value of ψ it is possible to obtain the pure spherical method when ψ=1, and the cylindrical method when ψ=0.

In the arc-length method, the increment size is defined by the value of the arc-length Δl, which is kept fixed in each increment. For the first increment, $\Delta\lambda_0$ is given, and Δl becomes:

$$\Delta l = \Delta\lambda_0 \sqrt{\Delta\mathbf{p}_t^2 + \left(\mathbf{q}_o\psi\right)^2} \qquad (6.1.32)$$

For the next increments, the value of Δl should be select with the aim of having nearly the same number of iteration for each increment. Hence the following equation can be used:

$$\Delta l_j = \Delta l_{j-1} \sqrt{\frac{I_d}{I_{j-1}}}, \tag{6.1.33}$$

where Δl_{j-1} is the length at the previous increment, I_{j-1} is the number of iteration required to achieve convergence at the previous increment, and I_d is the desired number of iterations. This procedure allows us to adaptively choose small arc-lengths when the structural response is strongly non-linear, and large arc-lengths when it is nearly linear

6.2 EXPLICIT DYNAMIC ANALYSIS

6.2.1 Introduction

Very often the convergence of analysis could represent the main problems of the solution of non-linear finite-element analyses.
Sometimes, when for the quasi-static analyses, when the phenomenon occurs in a dynamic way, as for the debonding of the composite reinforcement applied to concrete substratum, it is advantageous to resort to explicit procedures.
The basic advantages of an explicit dynamic analysis can be summarized as follow:

- is computationally efficient for the analysis of large models with relatively short dynamic response times and for the analysis of extremely discontinuous events or processes;
- uses a consistent, large-deformation theory-models can undergo large rotations and large deformation;
- can use a geometrically linear deformation theory-strains and rotations are assumed to be small;
- can be used to perform quasi-static analyses with complicated iteration conditions;

The dynamic equilibrium equation can be expressed by the following equation:

$$P - I = M\ddot{u} \tag{6.2.1}$$

Solving a problem explicitly does not require iterations and proceeds without the formations of tangent stiffness matrices; in fact, the solution of dynamic equilibrium equation needs to explicitly advance the kinematic state from the previous increment.

The explicit central-difference operator satisfies the dynamic equilibrium equations at the beginning of the increment, *t*; the accelerations calculated at time *t* are used to advance the velocity solution to time $t + \Delta t/2$ and the displacement solution to time $t + \Delta t$.

For linear and nonlinear problems alike, explicit methods require a small time increment size that depends solely on the highest natural frequency of the model and is independent of the type and duration of loading. Simulations typically require a large number of increments; however, due to the fact that a global set of equations is not solved in each increment, the cost per increment of an explicit method is much smaller than that of an implicit method.

6.2.2 Explicit dynamics analysis procedure

The explicit dynamics analysis procedure is based upon the implementation of an explicit integration rule together with the use of diagonal ("lumped") element mass matrices. The equations of motion for the body are integrated using the explicit central-difference integration rule:

$$\dot{u}^N_{\left(i+\frac{1}{2}\right)} = \dot{u}^N_{\left(i-\frac{1}{2}\right)} + \frac{\Delta t_{(i+1)} + \Delta t_{(i)}}{2}\ddot{u}^N_{(i)} \tag{6.2.2}$$

$$\dot{u}^N_{(i+1)} = \dot{u}^N_{(i)} + \Delta t_{(i+1)}\dot{u}^N_{\left(i+\frac{1}{2}\right)} \tag{6.2.3}$$

where u^N is a degree of freedom (a displacement or rotation component) and the subscript i refers to the increment number in an explicit dynamics step. The central-difference integration operator is explicit in the sense that the kinematic state is advanced using known values of $\dot{u}^N_{\left(i-\frac{1}{2}\right)}$ and $\ddot{u}^N_{(i)}$ from the previous increment.

The explicit integration rule is quite simple but by itself does not provide the computational efficiency associated with the explicit dynamics procedure. The key to the computational efficiency of the explicit procedure is the use of diagonal element mass matrices because the accelerations at the beginning of the increment are computed by:

$$\ddot{u}^N_{(i)} = \left(M^{NJ}\right)^{-1}\left(P^J_{(i)} - I^J_{(i)}\right) \qquad (6.2.4)$$

where M^{NJ} is the mass matrix, P^J is the applied load vector, and I^J is the internal force vector.

A lumped mass matrix is used because its inverse is simple to compute and because the vector multiplication of the mass inverse by the inertial force requires only n operations, where n is the number of degrees of freedom in the model.

The explicit procedure requires no iterations and no tangent stiffness matrix. The internal force vector, I^J, is assembled from contributions from the individual elements such that a global stiffness matrix need not be formed.

The explicit integration scheme requires nodal mass or inertia to exist at all activated degrees of freedom unless constraints are applied using boundary conditions. More precisely, a nonzero nodal mass must exist unless all activated translational degrees of freedom are constrained and nonzero rotary inertia must exist unless all activated rotational degrees of freedom are constrained.

Another difference between implicit and explicit procedure is in the definition of the boundary conditions applied during an analysis step. It should use through an appropriate amplitude references:

$$u = u_0(t) \tag{6.2.5}$$

If boundary conditions are specified for the step without amplitude references, they are applied instantaneously at the beginning of the step.

6.2.3 Stable time increment

The explicit procedure integrates through time by using many small time increments. Usually the stable time increment for the operator (with damping) is given in terms of the highest frequency of the system as:

$$\Delta t \le \frac{2}{\omega_{\max}}\left(\sqrt{1+\xi_{\max}^2}-\xi_{\max}^2\right) \tag{6.2.6}$$

where $\xi_{\max}$ is the fraction of critical damping in the mode with the highest frequency. It is contrary to the usual engineering intuition according to which the introduction of damping to the solution reduces the stable time increment.

An approximation to the stability limit is often written as the smallest transit time of a dilatational wave across any of the elements in the mesh:

$$\Delta t \approx \frac{L_{\min}}{c_d} \tag{6.2.7}$$

where $L_{\min}$ is the smallest element dimension in the mesh and c_d is the dilatational wave speed in terms of λ_0 and μ_0, defined below.

The stable time increment is defined as the time required to propagate a dilatational wave across the smallest element dimension. If the model contains only one material type, the initial time increment is directly proportional to the size of the smallest element in the mesh, otherwise, if the mesh contains uniform size elements but contains multiple material descriptions, the element with the highest wave speed will determine the initial time increment.

In an isotropic, elastic material the effective Lamé's constants, indicating as $\hat{\lambda}$ and $\hat{G} = 2\hat{\mu}$, can be defined in terms of Young's modulus, *E*, and Poisson's ratio, ν, by:

$$\hat{\lambda} = \lambda_0 = \frac{E\nu}{(1+\nu)(1-2\nu)} \tag{6.2.8}$$

and

$$\hat{\mu} = \mu_0 = \frac{E}{2(1+\nu)} \tag{6.2.9}$$

The time increment used in an analysis must be smaller than the stability limit of the central-difference operator. Failure to not use a small enough time increment will result in an unstable solution. When the solution becomes unstable, the time history response of solution variables such as displacements will usually oscillate with increasing amplitudes. The total energy balance will also change significantly.
In nonlinear problems (those with large deformations and/or nonlinear material response) the highest frequency of the model will continually change, which consequently changes the stability limit. Hence, several explicit procedures account for change in the stability limit by controlling the time increment in each increment.
In order to reduce the in reduce the chance of a solution going unstable, another strategy consists in adjusting the stable time increment computed by a constant scaling factor. This factor can be used to scale the initial global time estimate.

6.2.4 Mass scaling in the quasi-static processes

Although the explicit dynamics procedure is computationally attractive for high-speed dynamic events, where the total dynamic response time that must be modelled is only a few orders of magnitude longer than the stability limit (for example, wave propagation studies or structures subjected to blast loads), it is not ideally suited for analyzing slower (quasi-static) processes.

The computer time involved in running a quasi-static analysis can be very large: the cost of the simulation is directly proportional to the number of time increments required.

The number of increments, n, required is $n = T/\Delta t$ if Δt remains constant, where T is the time period of the event being simulated. Hence, in a two-dimensional analysis refining the mesh by a factor of two in each direction will increase the run time in the explicit procedure by a factor of eight (four times as many elements and half the original time increment size). Similarly, in a three-dimensional analysis refining the mesh by a factor of two in each direction will increase the run time by a factor of sixteen.

In a quasi-static analysis it is expedient to reduce the computational cost by either speeding up the simulation or by scaling the mass.

To reduce the number of increments required, n, the simulation compared to the time of the actual process can be speeded up, that is, one can artificially reduce the time period of the event, T. This will introduce two possible errors. If the simulation speed is increased too much, the increased inertia forces will change the predicted response (in an extreme case the problem will exhibit wave propagation response). The only way to avoid this error is to choose a speed-up that is not too large.

The other error is that some aspects of the problem other than inertia forces (i.e., material behaviour) may also be rate dependent. In this case the actual time period of the event being modelled cannot be changed.

Artificially increasing the material density, ρ, by a factor f^2 reduces n to n/f, just like decreasing T to T/f.

This concept, called “mass scaling,” reduces the ratio of the event time to the time for wave propagation across an element while leaving the event time fixed, which allows rate-dependent behaviour to be included in the analysis. Mass scaling has exactly the same effect on inertia forces as speeding up the time of simulation. Mass scaling is attractive because it can be used in rate-dependent problems, but it must be used with care to ensure that the inertia forces do not dominate and change the solution. Obviously, the mass scaling can be fixed or variable during the analysis.

6.2.5 Bulk viscosity

A small amount of damping can be introduced in the form of bulk viscosity in order to control high frequency oscillations. For the displacement degrees of freedom, bulk viscosity introduces damping associated with volumetric straining.

The bulk viscosity pressure is not included in the material point stresses because it is intended as a numerical effect only, and it is based upon the dilatational mode of each element. The fraction of critical damping in the dilatational mode of each element is given by:

$$\xi = b_1 - b_2 \frac{L_e}{c_d} \min\left(0, \dot{\varepsilon}_{vol}\right) \tag{6.2.10}$$

Linear and quadratic bulk viscosity are used to damp the high frequency so called "ringing" that leads to unwanted noise in the solution or spurious overshoot in the response amplitude.

6.2.5.1 Linear bulk viscosity

Linear bulk viscosity is introduced in order to damp the ringing in the highest element frequency. This damping is sometimes referred to as truncation frequency damping. It generates a bulk viscosity pressure that is linear in the volumetric strain rate:

$$p_{bv1} = b_1 \rho c_d L_e \dot{\varepsilon}_{vol} \tag{6.2.11}$$

where b_1 is a damping coefficient, ρ is the current material density, c_d is the current dilatational wave speed, L_e is an element characteristic length, and $\dot{\varepsilon}_{vol}$ is the volumetric strain rate.

6.2.5.2 Quadratic bulk viscosity

The second form of bulk viscosity pressure is found only for some solid continuum elements. This form is quadratic in the volumetric strain rate:

$$p_{bv2} = \rho\left(b_2 L_e \dot{\varepsilon}_{vol}\right)^2 \qquad (6.2.12)$$

where b_2 is a damping coefficient and all other quantities are as defined for the linear bulk viscosity. Quadratic bulk viscosity is applied only if the volumetric strain rate is compressive.

The quadratic bulk viscosity pressure will smear a shock front across several elements and is introduced to prevent elements from collapsing under extremely high velocity gradients.

Consider a simple one-element problem in which the nodes on one side of the element are fixed and the nodes on the other side have an initial velocity in the direction of the fixed nodes. If the initial velocity is equal to the dilatational wave speed of the material, without the quadratic bulk viscosity, the element would collapse to zero volume in one time increment.

CHAPTER VII
COMPARISONS of NUMERICAL OUTCOMES Vs EXPERIMENTAL RESULTS

7.1 INTRODUCTION

In this section two-dimensional nonlinear finite-element analyses of RC beams retrofitted with FRP have been carried out up to failure in order to correctly model the interaction between FRP and concrete, which is poorly reproduced by conventional RC beam theory.
Furthermore, the results of an experimental campaign on RC beams, either with or without FRP reinforcement, performed in the Department of Structural Engineering laboratory, are reported in the follows. The experimental activity presented in this work has been made both because it represents a typical case of engineering interest and because it provides an useful tool for the validation of the results obtained by the proposed nonlinear numerical models of the RC beams either with or without FRP reinforcement in flexure.
The numerical analyses proposed in this dissertation are encompassing within a general methodology which can be used not only to efficiently integrate available experimental data, but also to get a deeper understanding of the complex failure modes of the reinforced beams.
The modelling of materials behaviours and the interfacial behaviour between parts will be presented in the sequel in details. The effectiveness of the proposed methodology of analysis will be shown by the ability of the model to numerically reproduce the experimental results ad-hoc performed and to well capture the complex mid-span debonding failure.

7.2 EXPERIMENTAL DATABASE

Within a Research Project funded by the Regione Campania (legge 5/2002), an experimental activity has been carried out on RC beams externally

reinforced with FRP sheets. The results of this activity have not yet be published; however, the author of the present dissertation has had the privilege of the availability of the test results for the purpose of the comparisons with numerical results. The tests concerned simple supported beams tested in four-point bending. A set of 16 beams, either with or without external FRP reinforcement, was considered. The beams are divided into 4 groups of 4 beams, which are characterized by the same geometry and steel reinforcement. For each group, two beams were tested without reinforcement and are referred to as A*n*; while the other two reinforced beams are referred to as B*n*. The number *n* from 1 to 8, indicates the group which the beam belongs to. Thus, beams A1, A2, B1 and B2 belong to group I, beams A3, A4, B3 and B4 belong to group II, beams A5, A6, B5 and B6 belong to group III, and beams A7, A8, B7 and B8 belong to group IV.

The beams groups are different in both typology of steel reinforcement and cross-section dimensions. In particular, beams belonging to groups I and III are characterized by smooth steel reinforcing bars, while those belonging to groups II and IV by ribbed steel bars; beams of groups III and IV are characterized by littler dimensions with respect to groups I and II.

The sketch of the tested beams is drawn in Figure 7.2.1, while all the geometrical information are reported in Table 7.2.1.

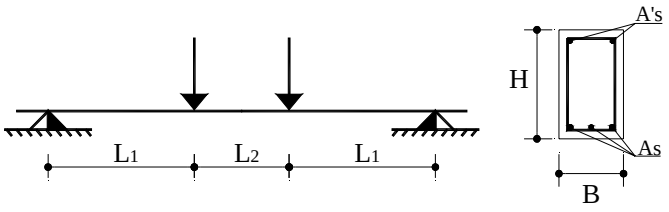

Figure 7.2.1: Sketch of tested beams

Table 7.2.1. Geometrical properties of the RC beams.

BEAM	GROUP	L_1 [cm]	L_2 [cm]	B [cm]	H [cm]	A_S [cm^2]	A'_S [cm^2]	FRP sheet
A1-A2	I	100	60	15	30	304.7	157.1	□
A3-A4	II	100	60	15	30	304.7	157.1	□
A5-A6	III	80	70	15	25	304.7	157.1	□
A7-A8	IV	80	70	15	25	304.7	157.1	□
B1-B2	I	100	60	15	30	304.7	157.1	■
B3-B4	II	100	60	15	30	304.7	157.1	■
B5-B6	III	80	70	15	25	304.7	157.1	■
B7-B8	IV	80	70	15	25	304.7	157.1	■

In Figures 7.2.2 and 7.2.3 all the tested beams are reported in details.
The reinforced beams were reinforced with a pultruded laminate 50mm wide and 1.4mm thick.
The design of the external FRP reinforcement was conducted with the aim of reaching the failure for mid-span debonding; thus, the anchorage length and the cross section dimensions of the composite was proportioned in order to avoid the rupture for extreme traction in the composite or premature failure for the end-peeling delamination.
The mechanical properties of composite sheet have been furnished by the manufacturing industry, while the properties of both smooth and ribbed steel bars were obtained by performing monotonic tensile test on steel specimens. The material properties for the steel bars and FRP sheets are reported in Table 7.2.2.

Table 7.2.2. Material properties for the steel bars and the FRP laminate.

	Young modulus [GPa]	Yield/Failure stress [MPa]
Smooth steel bars	205	380
Ribbed steel bars	205	510
FRP laminate	400	1900
*Yield for steel and failure for FRP		

BEAMS: A1-A2-B1-B2

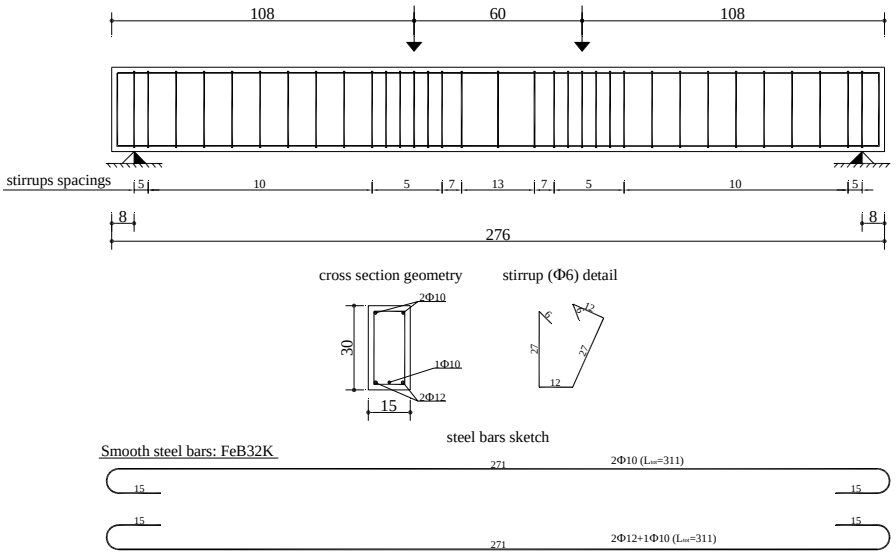

BEAMS: A3-A4-B3-B4

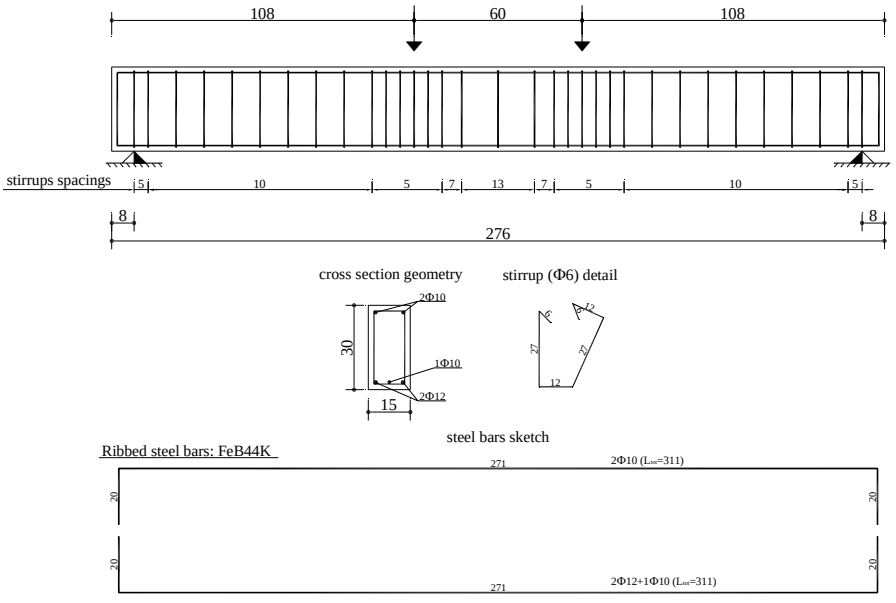

Figure 7.2.2: Details of RC beams belonging to groups I and II

BEAMS: A5-A6-B5-B6

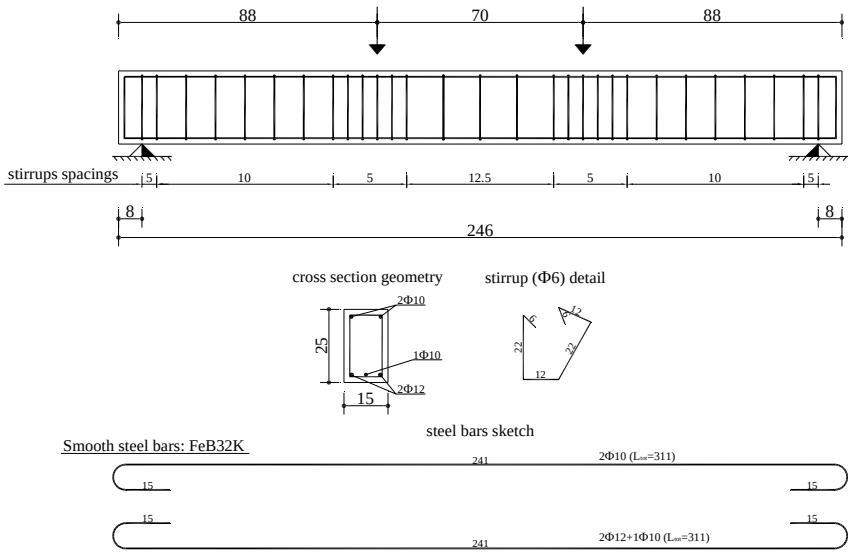

BEAMS: A7-A8-B7-B8

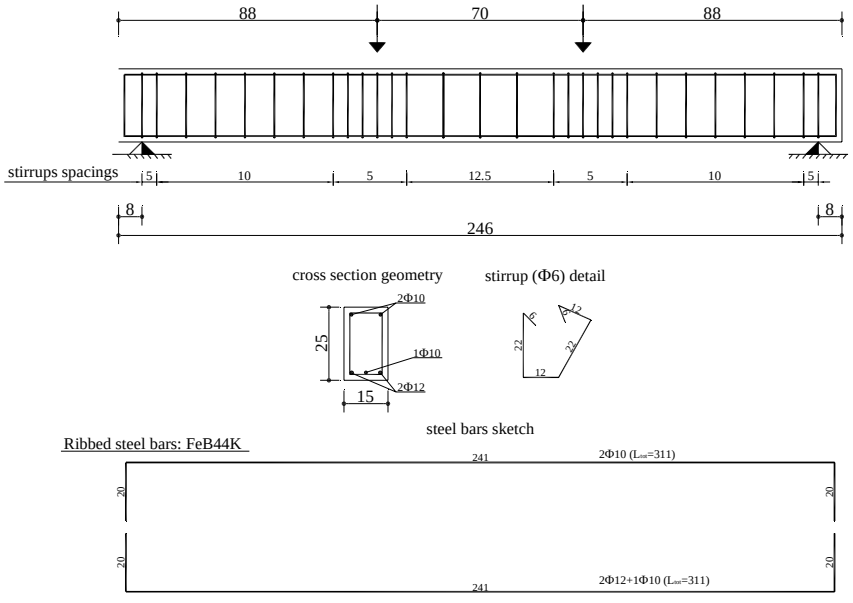

Figure 7.2.3: Details of RC beams belonging to groups III and IV

The mechanical properties of concrete were obtained by carrying out specific experimental monotonic tests in order to evaluate the tensile and compressive strengths, and the Young modulus. The results are summarized in Table 7.2.3.

Table 7.2.3. Experimental results on concrete specimens.

Secant Young Modulus [MPa]	Tangential Young Modulus [MPa]
8063	26000

Compressive Peak Stress [MPa]		Tensile Peak Stress [MPa]	
characteristic	average	characteristic	average
15.89	19.39	1.43	2.00

The test set-up and the concrete specimens are visible in the following figures.

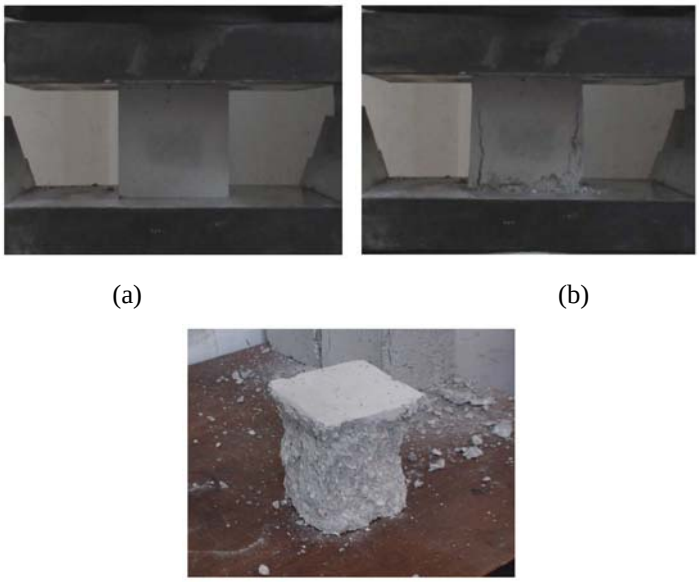

(a) (b)

(c)

Figure 7.2.4: Test for the determination of compressive strength. (a) specimen before crushing. (b) specimen at crushing. (c) specimen after crushing

(a) (b)

Figure 7.2.5: Test for the determination of elastic Young modulus. (a) test set-up. (b) concrete specimens

(a) (b)

Figure 7.2.6: Test for the determination of tensile strength. (a) specimen after rupture. (b) specimen at rupture

Tests were performed in a displacement control mode with an actuator velocity of 0.3 mm/sec. The displacement was assigned through two actuators linked to an hydraulic machine. The mid-span deflection was measured by the readings of two transducers applied in the middle under the beam. The experimental set-up is shown in Figure 7.2.7.

The loading history is sketched in Figure7.2.8. The loading steps can be summarized as follows.

For the beams with no FRP reinforcement (A*n*):

- loading, up to a cracking force (F_{cr}); it is the force corresponding to the cracking bending moment in the middle of the beam, for which the crack configuration along the beam is well defined. This condition corresponds with point *B* in Figure 7.2.8,
- unloading, up to zero (branch *BC*),
- reloading, up to cracking force (branch *CD*),
- reloading, up to failure (branch *DR*).

For the reinforced beams (B*n*):

- loading, up to the complete visualization of crack configuration along the beam (point *B*),
- unloading, up to zero (branch *BC*),
- application of reinforcement,
- reloading, up to cracking force (branch *CD*),
- reloading, up to failure, which happens always for mid-span delamination (branch *DR*).

Figure 7.2.7: Test set-up

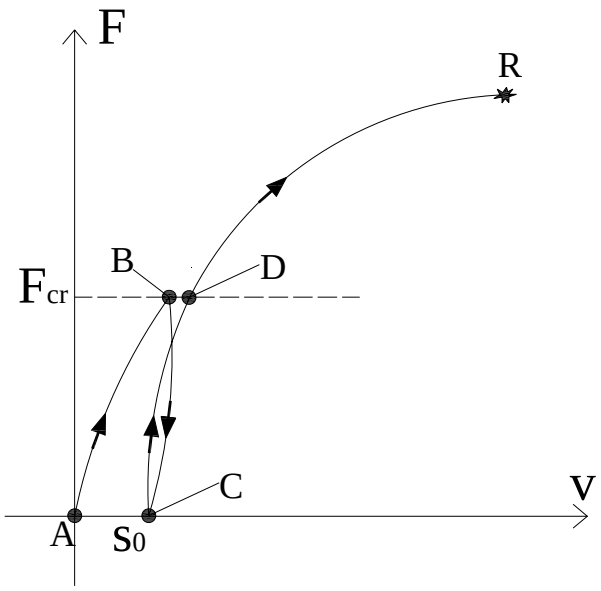

Figure 7.2.8: Force vs. mid-span deflection: loading steps

The basic reason for which the FRP reinforcement was applied after the complete development of cracks along the beams is that this situation is representative of what happens in the practical applications. In fact, generally, the FRP reinforcement is externally applied to an existing beams, when the cracks are already formed, and the presence of cracks is the main cause of mid-span debonding between FRP and concrete.
Figures 7.2.9 and 7.2.10 clearly show the crack configuration for one of the beams of interest, while Figure 7.2.11 shows the beams before the application of the FRP reinforcement, after the cracks opening occurred.

Figure 7.2.9: Cracked beam during test

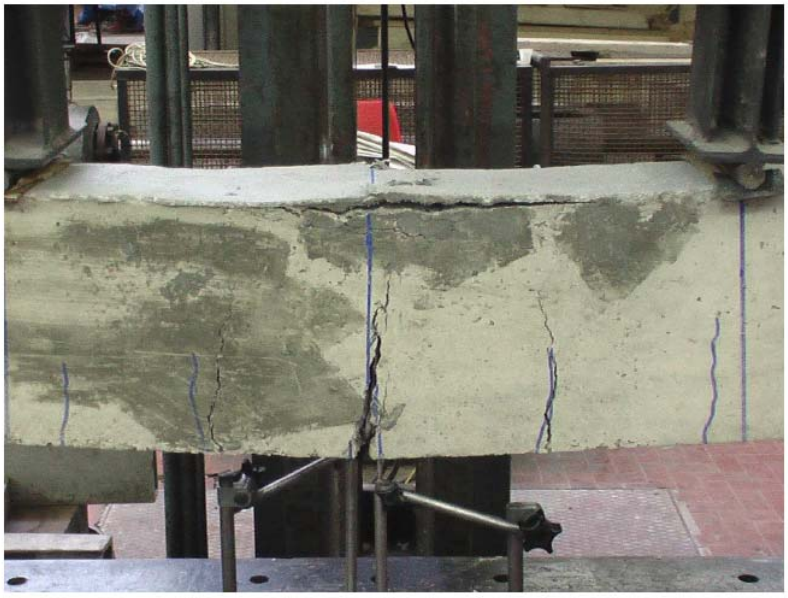

Figure 7.2.10: Detail of cracked beam during test

Figure 7.2.11: View of cracked beams before the application of the composite reinforcement

The experimental outcomes, in terms of load-mid-span deflection curves, are reported in Figures 7.2.12-7.2.15.

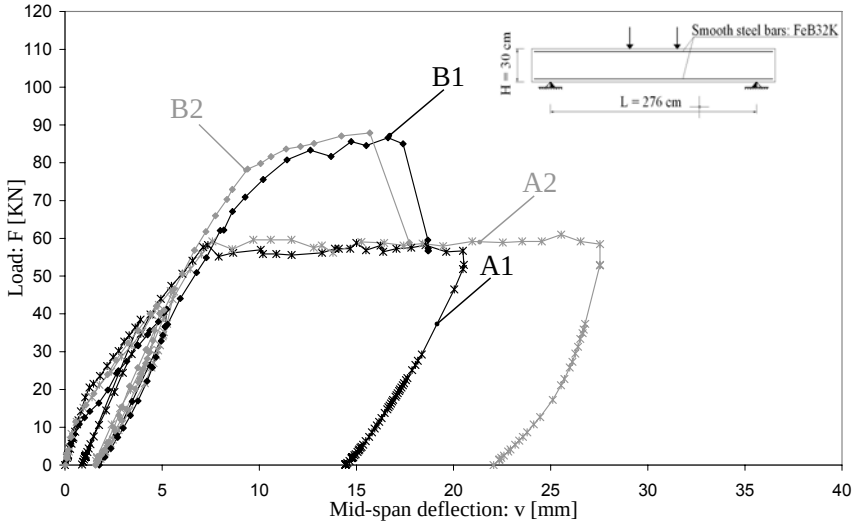

Figure 7.2.12: Experimental results: load/mid-span deflection curves for beams A1-A2 and B1-B2

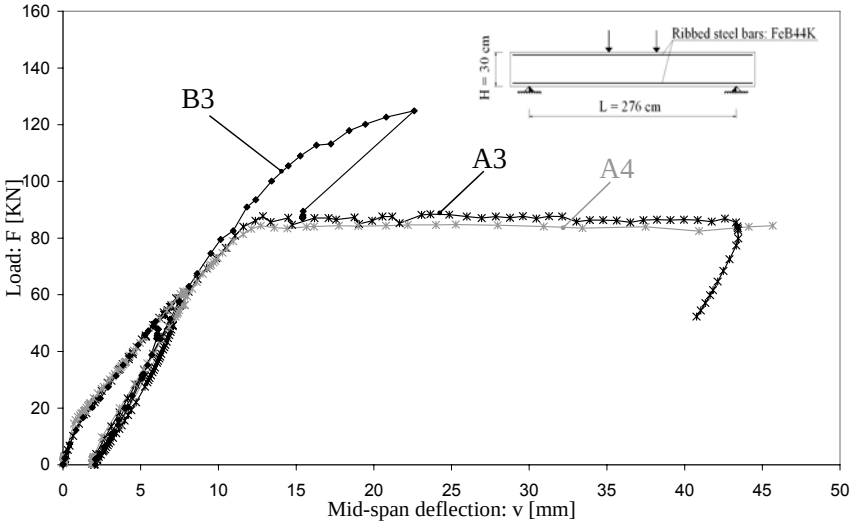

Figure 7.2.13: Experimental results: load/mid-span deflection curves for beams A3-A4 and B3-B4

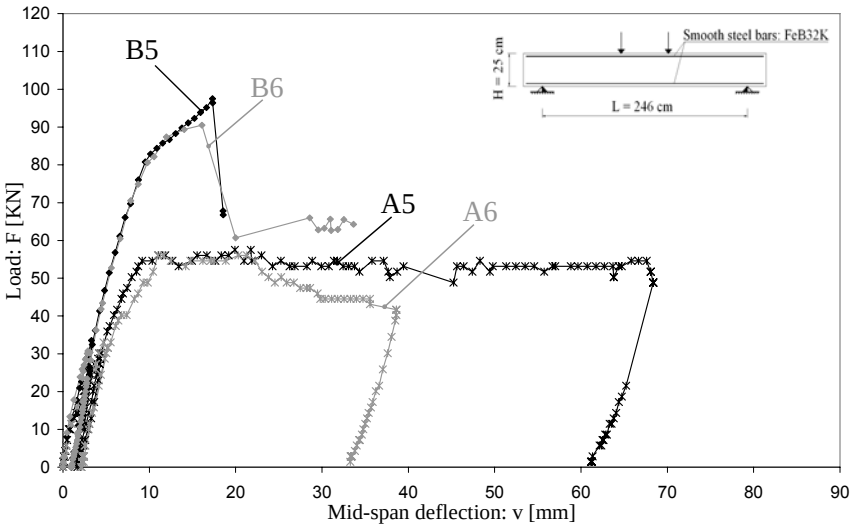

Figure 7.2.14: Experimental results: load/mid-span deflection curves for beams A5-A6 and B5-B6

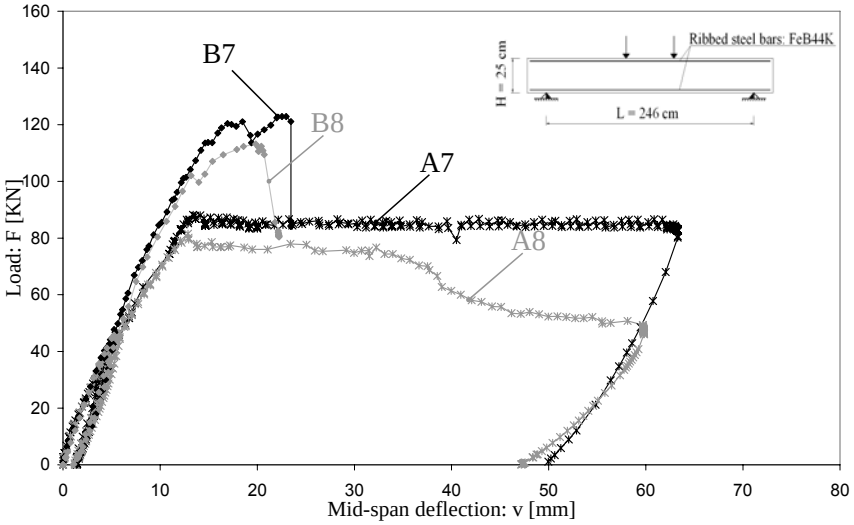

Figure 7.2.15: Experimental results: load/mid-span deflection curves for beams A7-A8 and B7-B8

It can be noticed that, for the longer beams (A1-A2 and A3-A4) the curves are very close, showing an excellent experimental repetitiveness.

The experimental results of beams A6 and A8 are different from the A5 and A7 respectively. They exhibit a softening behaviour just after the steel yielding, showing a less ductile behaviour with respect to beams A5 and A7; this could be due to some problems during the concrete casting phases and concrete crushing close to supports (see Figure 7.2.16). For beam A8, the yielding value is littler with respect to beam A7.

From the visualization of the experimental outcomes of the reinforced beams (B*n*) it clearly appears they exhibit a lower ductile behaviour with respect to analogous beams with no FRP reinforcements.

Only for beam B4 experimental curve is not reported in the paper because of the concrete crushing under the application point of the actuator (see Figure 7.2.17).

In conclusion, for all the beams the experimental behaviour, in terms of applied load/mid-span deflection, of the shorter beams, belonging to group I and II, is very homogeneous, while for the longer ones (group III and IV) the repetitiveness is however acceptable.

Figure 7.2.16: Concrete crushing at support

Figure 7.2.17: Concrete crushing under the actuator

7.3 FINITE ELEMENT MODELLING of RC BEAMS RETROFITTED with FRP

For a rational and safe design of any strengthening work an appropriate analysis method is required. The choice of such a method is not uniquely determined and depends largely on the purpose of the analysis. Usually in engineering simple and conservative models are sought. The intrinsic complexity of structural problems implies that simple models are possible only if strong assumptions are made. This can be done only if there are sufficiently wide experimental grounds to prove that they are acceptable. Also assuming something arbitrarily implies that the model is stripped off of all the features that are deemed not to be relevant in the calculation of the quantities of interest. This means that even though the results calculated are sufficiently accurate the model is not encompassing all the aspects of the physics of the problem and some aspects are missed out or included together with others on an empirical basis. Besides different models are usually used to calculate different quantities pertaining the same structural element.
As the objective of this work is not the determination of a specific quantity but rather the understanding of how RC structures retrofitted with FRP work, In this chapter the modelling of FRP strengthened structures is discussed with a view to defining a model as close as possible to reality, capable of replacing or integrating laboratory testing for the investigation of the structural behaviour. Subsequently, the model developed for the analyses will be described.

7.3.1 Finite Element Modelling of Reinforced Concrete

Suitable Finite Element models are required for reinforced concrete structures. Within the framework of the finite element method reinforced concrete can be represented either by superimposition of the material models for the constituent parts (i.e., for concrete and for reinforcing steel), or by a constitutive law for the composite concrete and embedded steel considered as a continuum at the macro-level.
Models of the first type are more popular and can be employed for virtually all kinds of reinforced concrete structures.

Depending on the application a number of finite element types can be used for concrete. These elements can be continuum elements (solids) or structural elements (shells, beams). The above elements are generally of the same type used for any other material.
Other alternative approaches for modelling of reinforced concrete, not discussed in this dissertation, consist in multilayered shells and fibber beams in which nonlinear behaviour of the main material and in-homogeneities are dealt with by subdividing an element into layers or fibres.

7.3.2 Modelling of reinforcing steel

The reinforcement is modelled either by separate truss or beam elements (*discrete representation*) or by separate elements of the same type as the concrete elements, which are superimposed on the latter (*embedded representation*) or by distribution of reinforcement to thin layers of equivalent thickness (*distributed representation*).
The embedded approach is characterised by incorporating the one-dimensional reinforcing bar into two- or three-dimensional elements. The stiffness matrix and the internal force vector of embedded reinforcement elements only contain the contribution of reinforcement bars. The embedded reinforcement elements are then superimposed on the respective concrete elements.
Since the reinforcement elements and the concrete elements must be assigned the same degrees of freedom, perfect bond between concrete and steel is obtained. The superimposition of concrete and reinforcing steel to model reinforced concrete requires constitutive models to account for bond and dowel action on the concrete-steel interface; instead the discrete representation of reinforcement allows modelling of bond and dowel action by means of special elements connecting adjacent nodes of concrete and steel elements.
The distributed modelling of the reinforcement is characterised by smearing reinforcing bars over an element that is superimposed onto the main concrete element. The correct area of reinforcement along a unit length section of the structure is obtained assuming an equivalent thickness for the

elements. The constitutive equations for such an element with a unidirectional layer of smeared reinforcement are generally referred to the local directions of the element which are parallel and normal to the reinforcing bars.

The distributed representation and the embedded representation of the reinforcement, however, do not permit the use of bond elements, because the displacements of concrete and steel at the interface are presumed to be the same. Consequently, the effect of bond slip can only be accounted for implicitly by modifying the constitutive relations for concrete or steel.

If reinforced concrete is modelled by a constitutive law for the composite concrete and embedded steel considered as a continuum, the material behaviour of reinforced concrete on the macro-level is described such as if this composite material was a single material. Since reinforced concrete is treated as a single material, neither the reinforcement nor the steel-concrete interaction needs to be modelled separately. Models of this type are appropriate only if reinforcement is distributed uniformly.

Discrete representation of the reinforcement is based on modelling the reinforcing bars as separate elements. Commonly, truss or cable elements are used for this purpose. However, for the investigation of structural details, occasionally two-dimensional or even three-dimensional elements are used. Truss and cable elements do not have rotational degrees of freedom and carry only axial forces.

The material behaviour of truss and cable elements is described by means of the one-dimensional constitutive relations. In order to guarantee compatibility of the displacements of the concrete and reinforcement, truss and cable elements must coincide with the boundaries of the concrete elements. The node points of both types of elements must also coincide. Hence, the shape functions for the concrete elements and the truss or cable elements must be of the same order.

The location of the reinforcement elements is obviously determined by the layout of the reinforcement. Consequently, the boundaries of the concrete elements must follow the reinforcing bars. Thus, the layout of the reinforcement has a strong influence on the generation of the finite element mesh for a concrete structure.

Bond slip and dowel action are either disregarded or considered implicitly by modifying the constitutive relations of concrete or steel. However, especially for the investigation of the behaviour of structural details, it may be necessary to model bond slip and dowel action more accurately through the use of concrete-steel continuum interface elements as it has been made in this work in the modelling of FRP/concrete and steel/concrete interface behaviour.
The discrete representation is the only way of accounting for bond slips and dowel action directly. Disadvantages of this approach are the great effort required for the discretization of a structure and the significant increase of the number of degrees of freedom. These disadvantages are the consequence of having to consider each reinforcing bar in the finite element mesh. Therefore, discrete modelling of the reinforcement is generally restricted to the analysis of structural details or single structural elements as beams taken in isolation from the remainder of the structure. It is important to note that opening of localised cracks can be appropriately modelled only by this approach.

7.3.3 2D Finite-Element Models of RC Beams Reinforced with FRP Sheets

In the present work finite-element models have been used to investigate RC beams retrofitted with FRP. Several models have been set up with the sole purpose of providing preliminary results and for the interpretation of the results yielded by more refined models.
These models have been used to explore the potential of finite element analysis in the investigation of RC beams retrofitted with FRP.
For each beam, both with and without external reinforcement, only one half of the geometry has been analysed.
As the detailed distribution of stresses and strains within the beam is of interest, solid elements have been used. The immediate consequence of this choice is that plane sections do not have to remain plane.
In the absence of cracking the assumption that plane sections remain plane is in fact somewhat coarse for sections close to FRP plates or steel

reinforcement ends. The assumption is much more inadequate in presence of cracking. Actually, cracks could not open with the sections remaining plane.
Solid elements are also convenient because the better representation of multi-axial stress states enables the effective use of refined constitutive laws for concrete. Besides, these elements can be attached to interface elements to model bond slip behaviour in an explicit manner. This proved to be very useful both for a good prediction of the overall behaviour of the structural elements and for an accurate evaluation of the interface stresses and strains which are critical in the delamination failure modes of these systems.
Quadratic plane stress two-dimensional solid elements are used for concrete, for steel reinforcement and for FRP plates.
In the sequel an alternative finite-element model which makes use of truss elements have been used in two-dimensional analyses for steel bars and FRP will be presented.
Cracks have been accounted for using a discrete approach: preset cracks have been introduced in the mesh by doubling the set of nodes, so as to introduce a possible discontinuity. The contact between the two faces of any cracks has not been modelled. Hence, the model has not taken into account the possible friction between the cracks tips, even though it basically does not influence the good prediction of the phenomenon because the crack tips tend to separate after the application of the load. The cracks have been introduced in the models following the patterns which are the same as those observable during the experimental tests. As mentioned before, the *a-priori* introduction in the models of the crack patterns, which have really been found during the experiments, is very important in order to analyse in detail the key role played by the presence of cracks in the FRP/concrete debonding process.
Bond slip for both concrete/steel interface and concrete/FRP interface has been explicitly introduced by using interface elements. The in-plane thickness of the interface elements has been assumed equal to 1 mm. It should be borne in mind that the assumed interface model is representative of what happens in a finite volume including the bonding material and a layer of concrete, whose thickness is generally estimated as 20-30 mm, and that the fracture energy and the peak stress of the interface are dependent on

the properties of the concrete. Hence, it is difficult to define the concrete and the interface in the boundary zone, it is reasonable to believe that a refined modelling of the layer of concrete adjacent to the interface can be important for the accuracy of the results. This concept is at the basis of the approach recently used by Lu et al. [2005] to study the concrete/FRP modelling.

With the hypothesis of small deformations, for each beam the analyses have been carried out by applying a prescribed displacement downward to the application point of the actuator during the experiment.

The finite-element models used for the modelling of the tested reinforced beams are shown in Figures 7.3.1-7.3.5.

The two-dimensional finite-element models has been also improved by superimposing an additional part on steel bars and steel/concrete cohesive zone.

The constitutive behaviour of such part is the models. This operation has been introduced in order to take into account the concrete which is adjacent to the sides of reinforcing steel bars because it cannot be adequately modelled by a two-dimensional model. This operation improves also the deformed shape of the cracked part of RC beams: in fact (see Figure 7.5.6), the elements sides along the generic crack lie on the straight line.

Obviously, from the finite-element analysis point of view, the two parts (steel bars-cohesive steel/concrete and lateral concrete) work together by sharing the external nodes, as the following figure clarifies.

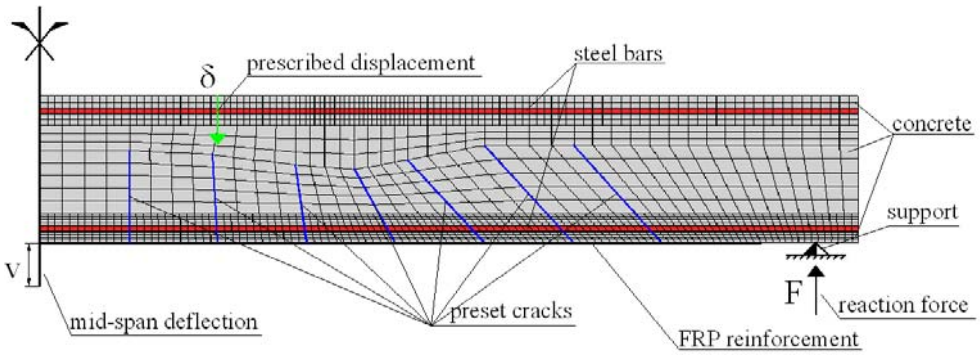

Figure 7.3.1: RC beam (B3-B4): finite-element model

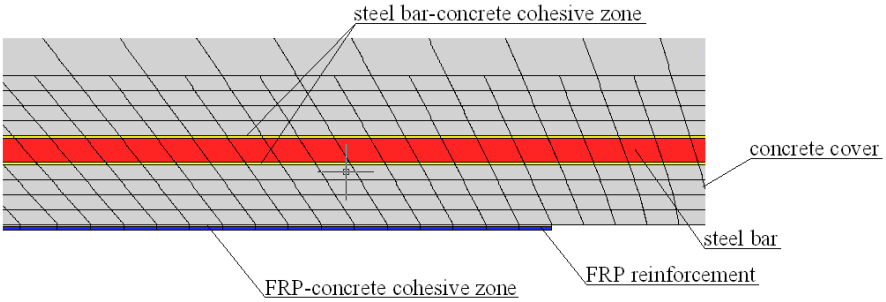

Figure 7.3.2: RC beam (B3-B4): detail of the finite-element model

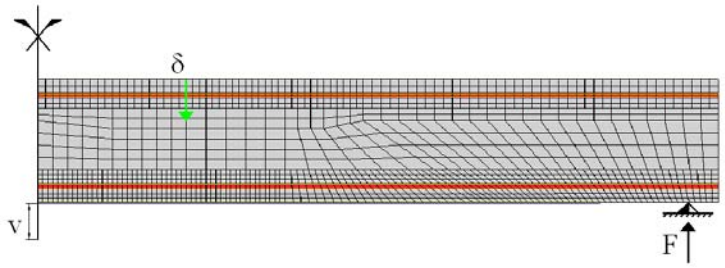

Figure 7.3.3: RC beam (B1-B2): finite-element model

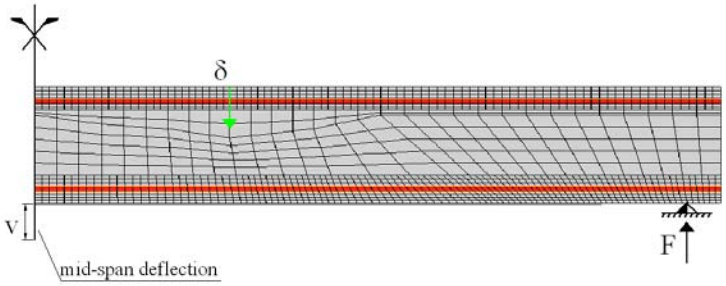

Figure 7.3.4: RC beam (B5-B6): finite-element model

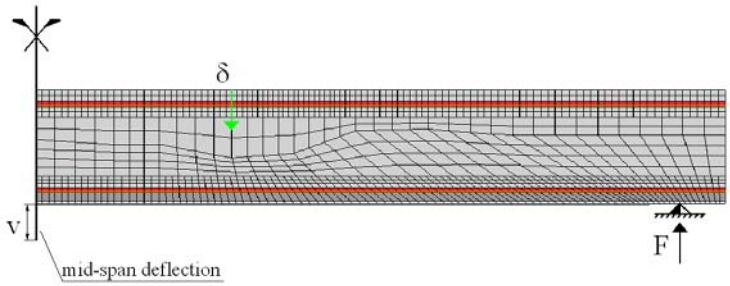

Figure 7.3.5: RC beam (B7-B8): finite-element model

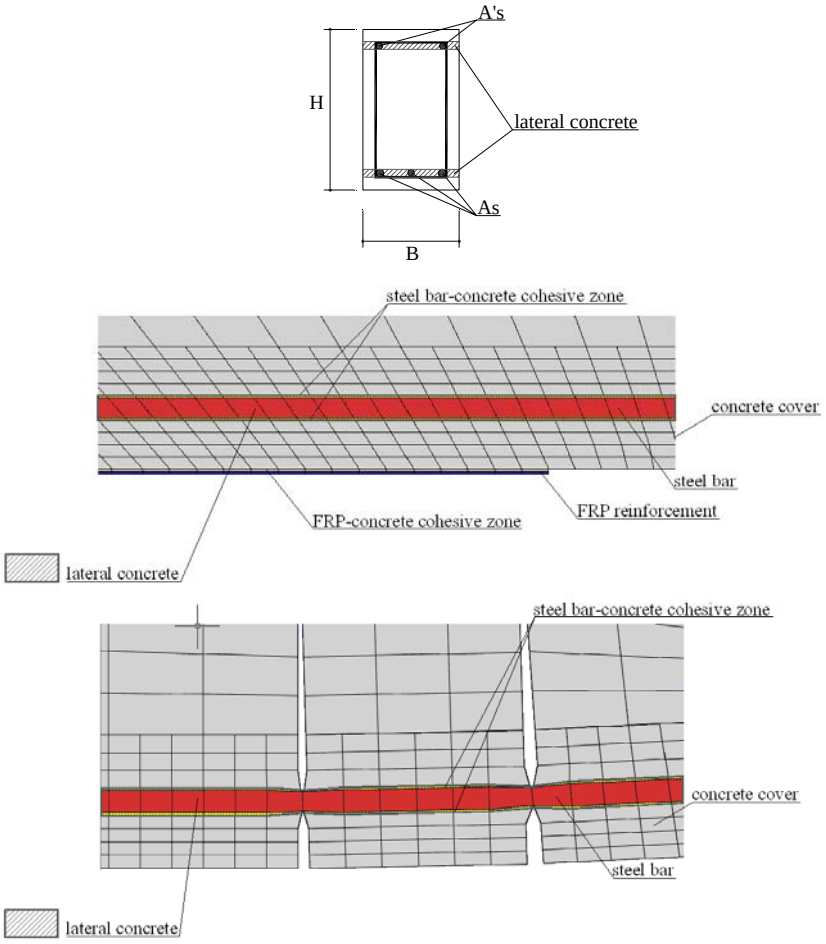

Figure 7.3.6: Additional part in the two-dimensional finite-element models

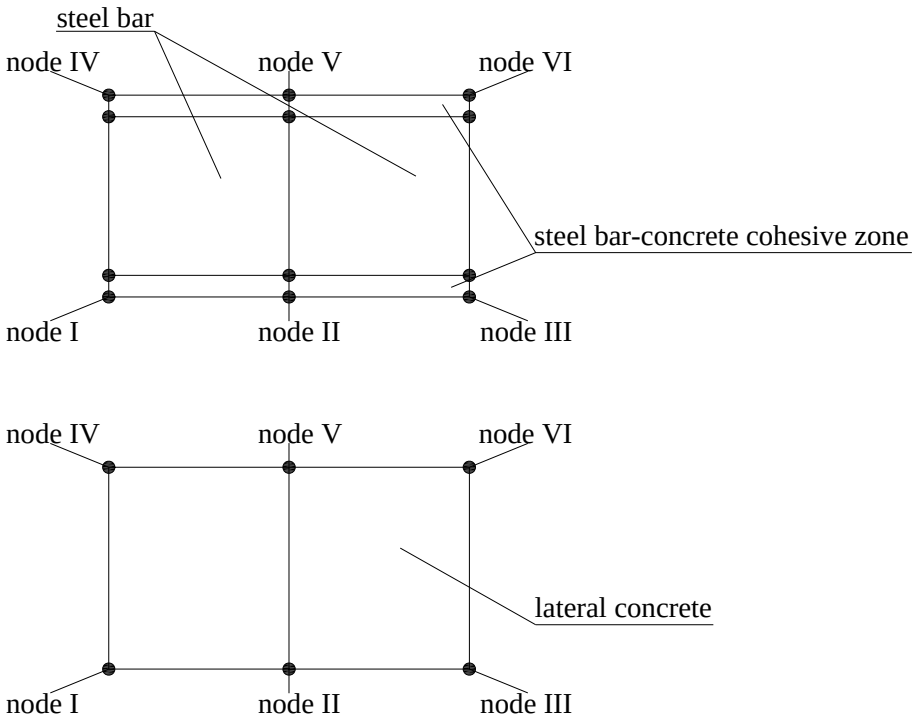

Figure 7.3.7: Sketch of shared nodes of two different parts which are superimposed in the finite-element model

7.4 NUMERICAL RESULTS

The numerical results obtained for a series of simulations concerning the simple supported beams experimentally tested are reported in this section. The bond-slip relationships developed by Camanho & Davila [2002] and the Lubliner et al. [1989] concrete model available in the finite-element code ABAQUS are used for the analyses. They have been illustrated in details in the sections III and V, and will be briefly recapitulated in this section.
Then, the numerical results obtained from the analyses of the two-dimensional models in the hypothesis of plane stress will be compared with experimental findings in order to show that, despite some simplified assumptions made, the models are able to well capture all the main aspects

of the structural response of RC beams retrofitted with FRP composites, both qualitatively and quantitatively, at least in the case of significant interest, which is the problem experimentally investigated in this work.
Finally, a series of considerations will be made in order to understand the influence of the assumptions made and the role of the interface law between concrete and composite on the overall behaviour of this type of retrofitted beams.

7.4.1 Material Properties

The material input data of the problem are those evaluated by specific experimental tests for steel and concrete, and provided by manufacturing industry for the composite reinforcement.
Although the inertia effects can be neglected in this analysis, the actual rate at which the beams are loaded is important because stress-strain curves for steel and concrete are affected by the strain rate.
Even though the experimental loading-rate of 0.3 mm/sec is quite low and this induced to neglect the strain-rate effect for the analysis described in this paper. Hence, rate independent material models are used in this section.

7.4.1.1 Modelling of concrete-steel bars and concrete-FRP interfaces

In order to take into account the bond-slip between concrete and steel bars as well as the possible debonding of the FRP from the concrete, a cohesive-zone model has been used (Camanho & Davila 2002). It is somewhat similar to the approach developed previously by Mi et al. (1998) and Alfano & Crisfield (2001).
Only mode II is involved in both types of decohesion process and the following bilinear, elastic-damage relationship between the tangential stress (τ) and the sliding relative displacement (s) along the interface has been adopted (see Figure 7.4.1):

$$\tau = (1 - D) \cdot K \cdot s \qquad (7.4.1)$$

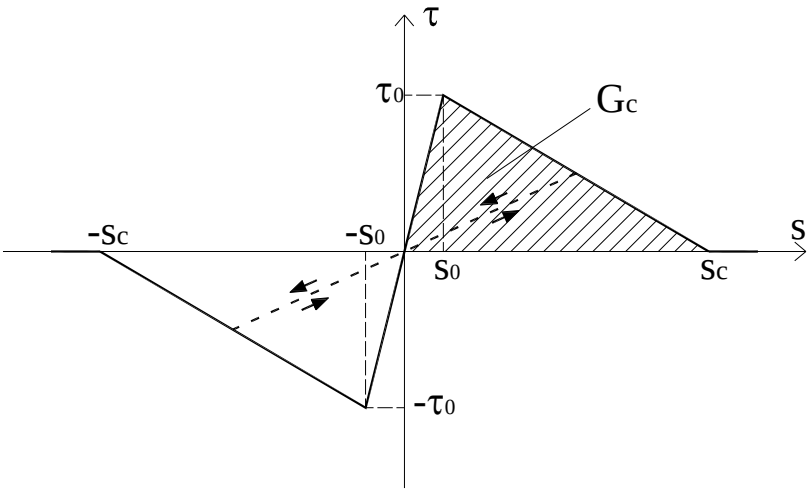

Figure 7.4.1: Mode-II interface relationship

where K is the initial (undamaged) interface stiffness and D is a damage which is greater than zero if the tangential stress fulfils some conditions as Camanho & Davila (2002) indicate.

Input parameters of the law are the area enclosed by the curve, which is taken equal to the dissipated fracture energy (G_c), the peak value of the tangential stress (τ_0) at which the softening part of the law begins and the initial elastic stiffness (K).

The critical sliding relative-displacement s_c and the "first cracking" value s_c are related to the input parameters as follows:

$$K = \tau_0 / s_0 ; \qquad s_c = 2G_c / \tau_0 \tag{7.4.2}$$

Further details on the adopted cohesive-zone model can be found in Camanho & Davila [2002].

In absence of detailed information about the interface properties required in the model, the values entering the bar bond-slip relationships and concrete/FRP bonding (as shown in Figure 7.4.1) are chosen on the basis of the experimental-numerical comparisons in terms of load-mid span displacement curve, which will be shown later on.

The values so obtained for the interface parameters are reported in Tables 7.4.1 and 7.4.2: they are referred to unit beam width, consistently with the plane-model hypothesis.

Table 7.4.1. Mechanical properties for the concrete/steel bar interface.

	τ_0 [MPa]	s_0 [mm]	$G_C^{numerical}$ [N]
Smooth	10.0	1.0	50.0
Ribbed	12.0	1.0	75.0

Table 7.4.2. Mechanical properties for the concrete/FRP interface.

BEAM	τ_0 [MPa]	s_0 [mm]	$G_C^{numerical}$ [N]
B1-B2	3.8	0.0001	1.33
B3-B4	5.0		0.85
B5-B6	5.0		0.60
B7-B8	4.0		0.60
Average values	*4.5*	*0.0001*	*0.85*

From Table 7.4.2 it appears clear that the value chosen for s_0 in the case of concrete/FRP interface is very small; this is consistent with the view to obtaining a high stiffness value which approximately models the almost rigid behaviour of the undamaged interface.

7.4.1.2 Concrete model

The model used in the finite-element model for concrete makes use of the yield function of Lubliner et. al. [1989], with the modifications proposed by Lee and Fenves [1995] to account for different evolutions of the strength under tension and compression. The yield surface is controlled by the tensile and compressive equivalent plastic strain $\tilde{\varepsilon}_c^{pl}$ and $\tilde{\varepsilon}_t^{pl}$.
In terms of effective stresses, the yield function takes the form:

$$F = \frac{1}{1-\alpha}\left(\bar{q} - 3\alpha\,\bar{p} + \beta\left(\tilde{\varepsilon}^{pl}\right)\left\langle\hat{\bar{\sigma}}_{\max}\right\rangle - \gamma\left\langle\hat{\bar{\sigma}}_{\max}\right\rangle\right) - \bar{\sigma}_c\left(\tilde{\varepsilon}_c^{pl}\right) = 0 \quad (7.4.3)$$

with

$$\alpha = \frac{\left(\sigma_{b0}/\sigma_{c0}\right)-1}{2\left(\sigma_{b0}/\sigma_{c0}\right)-1} \qquad with \quad 0 \le \alpha \le 0.5 \quad (7.4.4)$$

$$\beta = \frac{\bar{\sigma}_c\left(\tilde{\varepsilon}_c^{pl}\right)}{\bar{\sigma}_t\left(\tilde{\varepsilon}_t^{pl}\right)}(1-\alpha) - (1+\alpha) \quad (7.4.5)$$

$$\gamma = \frac{3(1-K_c)}{2K_c - 1} \quad (7.4.6)$$

where $\hat{\bar{\sigma}}_{\max}$ is the maximum principal effective stress; σ_{b0}/σ_{c0} is the ratio of initial equi-bi-axial compressive yield stress to initial uni-axial compressive yield stress; K_c, in the deviatoric plane, is the ratio between the second stress invariant on the tensile meridian ($q_{(TM)}$) and that on the compressive meridian ($q_{(CM)}$), at initial yield for any given value of the pressure invariant (p) such that the maximum principal effective stress is negative. It must also satisfy the condition $0.5 \le K_c \le 1.0$, where $\bar{\sigma}_c\left(\tilde{\varepsilon}_c^{pl}\right)$ and $\bar{\sigma}_t\left(\tilde{\varepsilon}_t^{pl}\right)$ are the effective compressive and tensile stress, respectively, which are functions of equivalent plastic strains.
The effective stress is defined as:

$$\bar{\sigma} = D_0^{el} : \left(\varepsilon - \varepsilon^{pl}\right) \quad (7.4.7)$$

where D_0^{el} is the initial (undamaged) elastic stiffness of the material.
As Eq. (7.4.3) shows, the yield surface makes use of two stress invariants of the effective stress tensor, namely the hydrostatic pressure stress,

$$\bar{p} = -\frac{1}{3}\left(\bar{\sigma}_1 + \bar{\sigma}_2 + \bar{\sigma}_3\right) \quad (7.4.8)$$

and the Mises equivalent effective stress,

$$\bar{q} = \sqrt{3/2\left(\bar{S} : \bar{S}\right)} \tag{7.4.9}$$

where $\bar{S}$ is the effective stress deviator, defined as

$$\bar{S} = \bar{\sigma} + \bar{p}I \tag{7.4.10}$$

The concrete damaged plasticity model assumes a non-associated potential plastic flow rule:

$$\dot{\varepsilon}^{pl} = \dot{\lambda}\frac{\partial G\left(\bar{\sigma}\right)}{\partial \bar{\sigma}} \tag{7.4.11}$$

The flow potential *G* used for this model is the Drucker-Prager hyperbolic function:

$$G = \sqrt{\left(e\sigma_{t0}tg\psi\right)^2 + \bar{q}^2} - \bar{p}tg\psi \tag{7.4.12}$$

which makes use of two stress invariants of the effective stress tensor, like yield surface.

Parameter ψ is the dilation angle measured in the *p*–*q* plane at high confining pressure; σ_{t0} is the uni-axial tensile stress at failure; and *e* is an eccentricity parameter, which defines the rate at which the function approaches the asymptote (the flow potential tends to a straight line as the eccentricity tends to zero). When the value of *e* increases, the curvature to the flow potential becomes greater, implying that the dilation angle increases more rapidly as the confining pressure decreases. This flow potential, which is continuous and smooth, ensures that the flow direction is always uniquely defined. The parameters values used in the analysis are summarized in table 7.4.3.

Table 7.4.3. Elastic and plastic properties for the concrete model.

Young modulus [GPa]	Poisson ratio [-]
26000	0.2

f_{cm} [MPa]	Ψ [°]	e [-]	σ_{b0}/σ_{c0} [MPa/MPa]	K [-]
19.39	35.0	0.01	1.1	0.65

For the uni-axial compressive stress-strain behaviour, the Kent-Park model [1971], with the modifications of Yashin [1994], have been used; while the use of Belarbi-Hsu model [1994] seems to be efficient for the definition of the uni-axial tensile constitutive behaviour. Accordingly, the non-linear elastic perfectly-plastic relationship and a linear elastic softening branch have been considered in compression and in tension, respectively. The stress-strain curves are plotted in Figure 7.4.2.

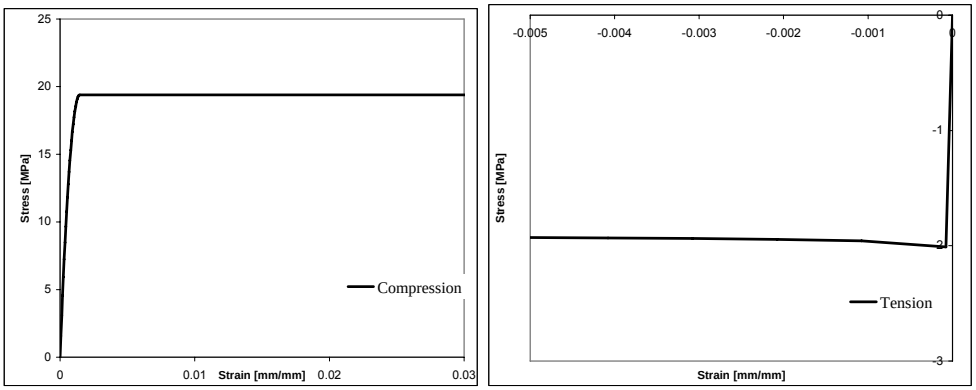

Figure 7.4.2: Compressive tensile monotonic constitutive law for concrete

7.4.1.3 Steel and FRP laminate model

For the reinforcing steel bars a linear elastic-perfectly plastic model has been adopted, while the behaviour of the FRP laminates has been assumed as linear elastic up to failure.
The material properties chosen for the numerical analyses was obtained from experimental tensile tests for steel, and provided by the manufacturing industry. They are reported in Table 7.4.4.

Table 7.4.4. Material properties for the steel bars and the FRP laminate.

	Young modulus [GPa]	Yield/Failure* stress [MPa]
Smooth steel bars	205	380
Ribbed steel bars	205	510
FRP laminate	400	1900
* yield for steel and failure for FRP		

7.4.2 Results and discussion

Figures 7.4.3-7.4.6 show the load displacement curves obtained for all the beams, with and without FRP reinforcement, by plotting the value of each reaction force (F) vs. the mid-span displacement (v).
It is important to observe that the a-priori introduction of the cracks entails some inaccuracies of the results in the early stage of analysis which correspond to reloading portion *CD* of the Figure 7.4.1. Such inaccuracies are due to the absence of the modelling of contact behaviour between the cracks tips. However, this is accepted because the aim of the analyses is to investigate, up to failure, on the key role played by the presence of cracks in the FRP delamination, and thus, on the behaviour of the beam after that cracking has developed.
The experimental-numerical comparisons of the RC beams with no FRP reinforcement highlight a good agreement of the numerical curves with the shapes of the experimental curves after the concrete cracking (portion *DR* of the diagram in Figure 7.4.1); in fact, the finite-element models well capture

the sharp elbow of experimental curves which is due to the yielding of the steel bars.

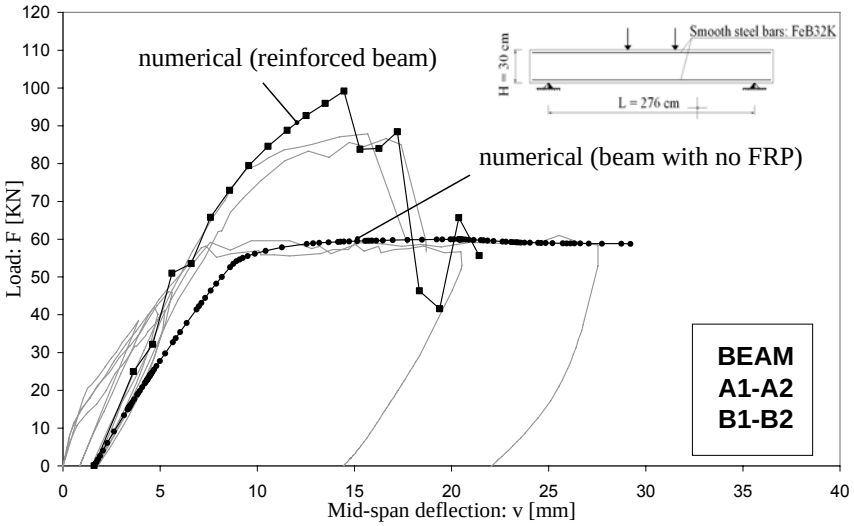

Figure 7.4.3: Numerical-experimental comparisons: load/mid-span deflection for beams A1-A2 and B1-B2

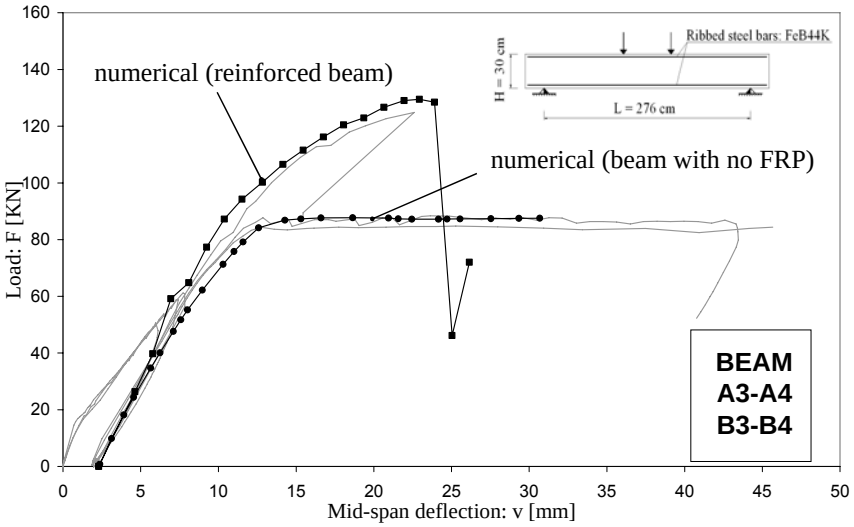

Figure 7.4.4: Numerical-experimental comparisons: load/mid-span deflection for beams A3-A4 and B3-B4

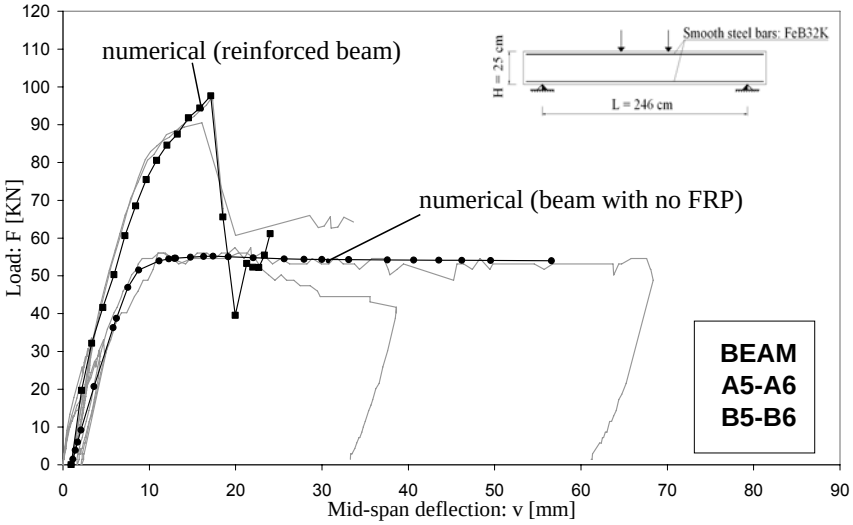

Figure 7.4.5: Numerical-experimental comparisons: load/mid-span deflection for beams A5-A6 and B5-B6

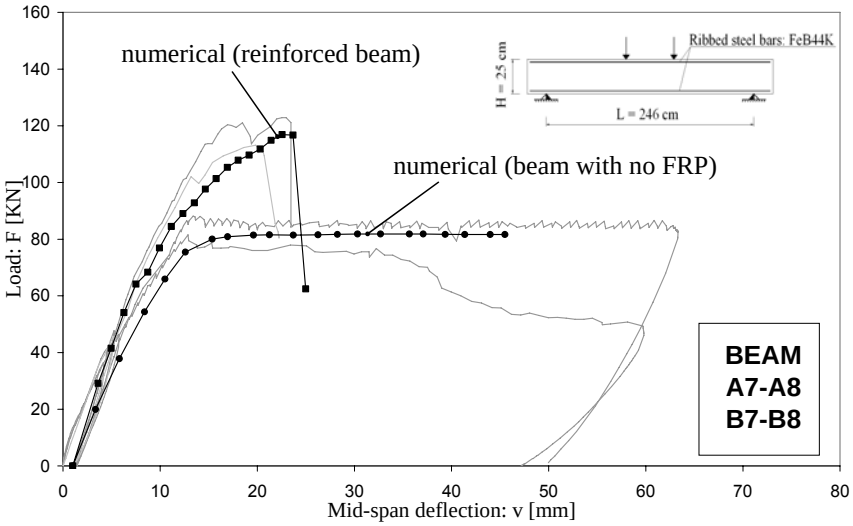

Figure 7.4.6: Numerical-experimental comparisons: load/mid-span deflection for beams A7-A8 and B7-B8

The figures show also a good agreement between experimental and numerical results for all the reinforced beams. The descending part of the load-displacement curves is well reproduced by the numerical model, showing the effectiveness of the proposed methodology of analysis.
For the analyses of the beams with no FRP reinforcement (A*n*) the simple application of the Newton-Raphson approach has led to excellent results.
The unstable debonding between concrete and FRP, for the reinforced beams, led to convergence problems for the numerical analysis. Thus, the numerical analyses have been performed through dynamic explicit procedures (as it is already illustrated in Chapter VI) in order to follow the structural behaviour in the post-peak part of the equilibrium path: it is clearly shown how the explicit approach performs better in presence of delamination.
However, the analyses of the reinforced beams have been repeated through the use of arc-length method in order to confirm the output of the explicit analyses results before the start of debonding between concrete and FRP.
Figure 7.4.7 shows the comparison between the explicit analysis and arc-length method results for the reinforced beam B3-B4. The curve obtained by using the arc-length method does not reach the peak part of the curve because of convergence problems.
In order to understand the sensitiveness of the parameters used in the elasto-plastic damaged model for concrete, in Figures 7.4.8-7.4.9 the load-displacement curves obtained for beams A3-A4 by plotting the force vs. the mid-span deflection are shown. In Figure 7.4.8 three values have been assumed for the eccentricity (*e*), while in Figure 7.4.9 three values have been assumed for the parameter referred to as K_c, previously defined.
The dilation angle (ψ) and the material parameter α ($\alpha = f\left(\sigma_{b0}/\sigma_{c0}\right)$) have a very negligible influence on the overall behaviour of the beam, and hence, the corresponding comparisons have not been reported in this dissertation. The values suggested for concrete by Lubliner et al. [1989] have been chosen for ψ and α, they are reported in Table 7.4.3.

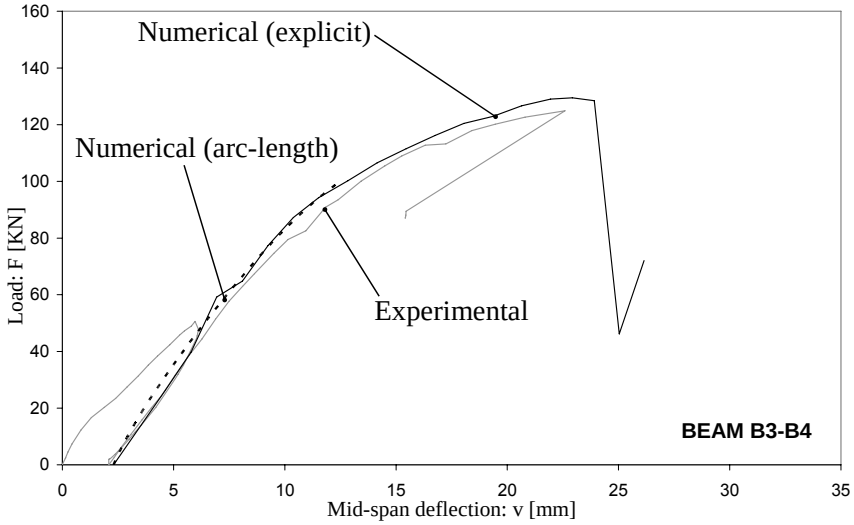

Figure 7.4.7: Numerical results of arc-length method and explicit analysis for the reinforced beam B3-B4

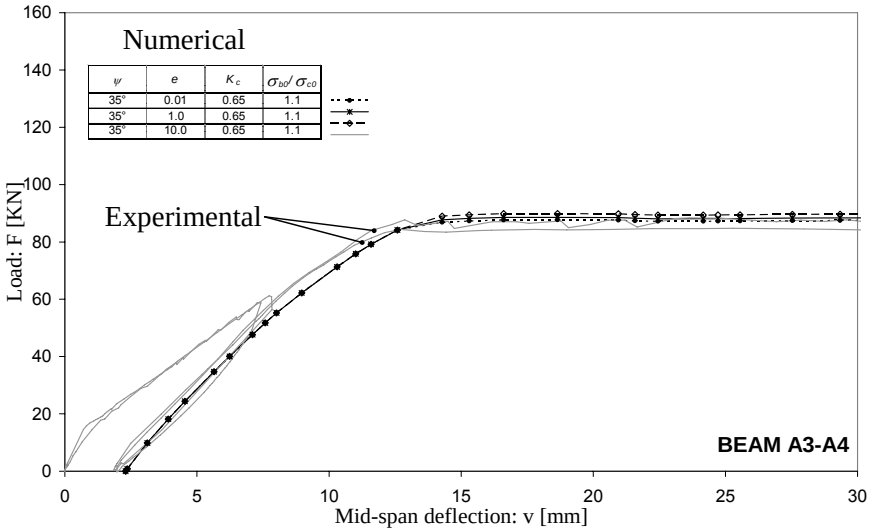

Figure 7.4.8: Numerical-experimental comparisons: load/mid-span deflection for beams A3-A4, with different values of the eccentricity *e*

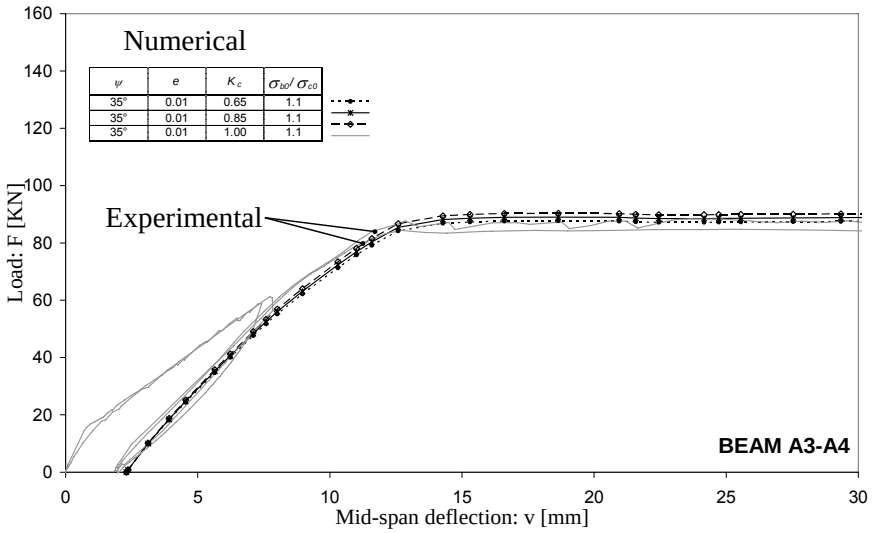

Figure 7.4.9: Numerical-experimental comparisons: load/mid-span deflection for beams A3-A4, with different values of K_c

In the case of a RC beams with no FRP reinforcement the eccentricity and K_c have little influence after steel yield has occurred, and almost no influence on the elastic part of the overall behaviour of the beam.

The same curves as in Figures 7.4.8-7.4.9 have been reported in Figures 7.4.10-7.4.11 for the reinforced beams B3-B4. In these cases the two parameters (e and K_c) have greater influence on the results in terms of strength and delamination failure. This underlines that the assumed interface model is representative of what happens in a finite volume including the bonding material and a layer of concrete, and hence, the fracture energy and the peak stress of the interface are dependent on the properties of the concrete. This induces to believe that a refined modelling of the layer of concrete adjacent to the interface can be important for both the accuracy of the results and a good prediction of delamination failure [Simonelli 2005].

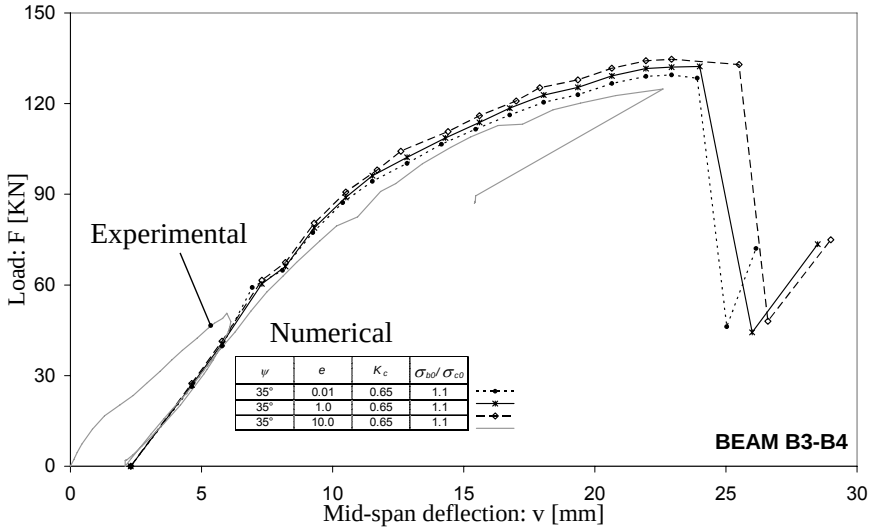

Figure 7.4.10: Numerical-experimental comparisons: load/mid-span deflection for beams B3-B4, with different values of the eccentricity *e*

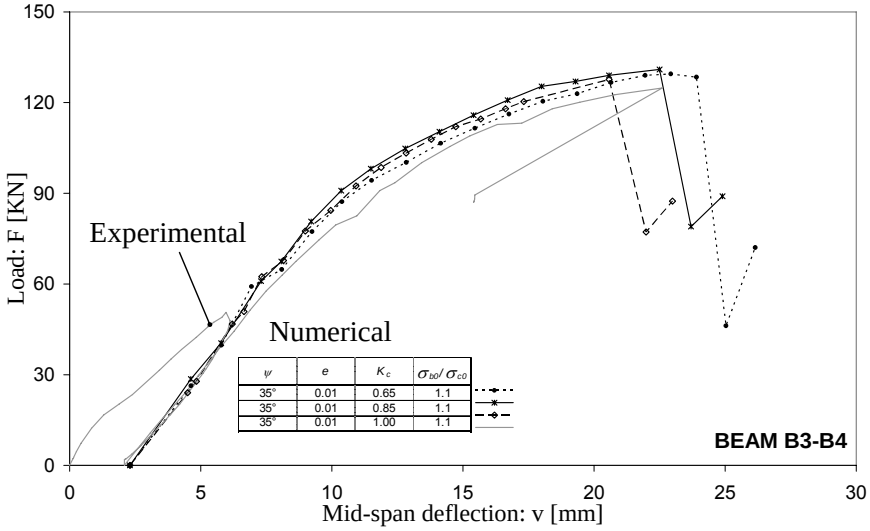

Figure 7.4.11: Numerical-experimental comparisons: load/mid-span deflection for beams B3-B4, with different values of K_c

However, the best results are achieved with the values reported in Table 7.4.3.

In order to understand the importance of some of the assumptions made in the finite-element model for the beams A3-A4 and B3-B4, the results of some analyses done with the modification of some initial hypotheses will be illustrated in the follows. The set of hypotheses are summarized in Table 7.4.5.

Table 7.4.5. Set of hypotheses.

BEAM		CRACKS	BAR SLIP	FRP SLIP
A3-A4	Hypoth. 1	□	□	-
	Hypoth. 2	■	□	-
	Hypoth. 3	■	■	-
B3-B4	Hypoth. 1	□	□	□
	Hypoth. 2	■	■	□
	Hypoth. 3	■	□	□
	Hypoth. 4	■	■	■

In particular, two and three further analyses have been carried out for the beams A3-A4 and B3-B4, respectively. Figures 7.5.12 and 7.4.13 show the comparisons of the numerical results.

For the beams A3-A4:

- with the first assumption (referred to as hypoth. 1), the cracks have been eliminated in the finite-element model by constraining with perfect bond the couple of nodes on the adjacent crack faces, and the bilinear bond-slip relationship for the concrete/steel bars has been replaced with a perfect bond assumption,
- with the second assumption (referred to as hypoth. 2), the initial cracks have been retained and a perfect bond assumption has been made for bond-slip relationship for the concrete/steel bars interface,
- with the third assumption (referred to as hypoth. 3), the initial cracks and the bilinear bond-slip relationship for the concrete/steel bars

interface have been retained: it coincides with the analysis reported for comparison in Figure 7.4.4.

For the beams B3-B4:

- with the first assumption (referred to as hypoth. 1), the cracks have been eliminated and the assumption of perfect bond has been made for the concrete/FRP and concrete/steel bars interfaces,
- with the second assumption (referred to as hypoth. 2), the initial cracks and the bilinear bond-slip relationship for the concrete/steel bars interface have been retained, while a perfect bond assumption has been made for the concrete/FRP interface,
- with the third assumption (referred to as hypoth. 3), the initial cracks have been retained, while the assumption of perfect bond behaviour has been made for both concrete/steel bars and concrete/FRP interfaces,
- with the fourth assumption (referred to as hypoth. 4), the initial cracks and the bilinear bond-slip relationships for the concrete/steel bars and concrete/FRP interfaces have been retained: it coincides with the analysis reported for comparison in Figure 7.4.4.

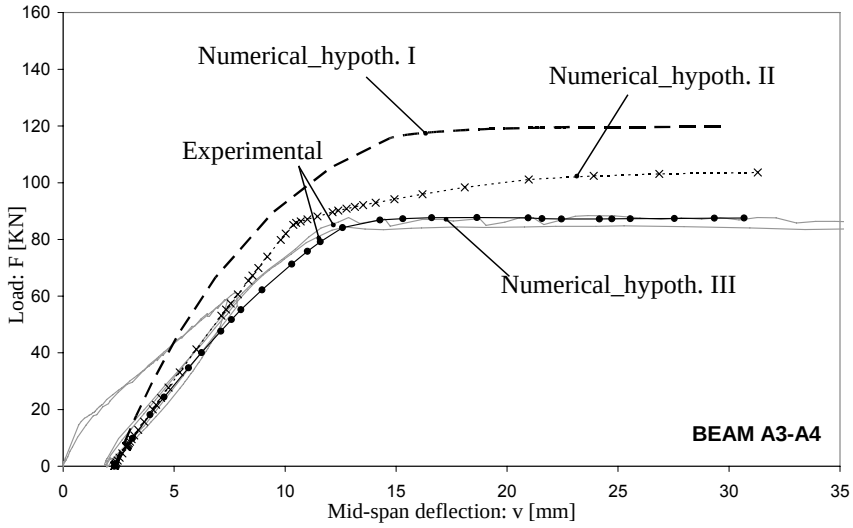

Figure 7.4.12: Numerical results for the bema A3-A4 with no FRP reinforcement, obtained with different sets of hypotheses

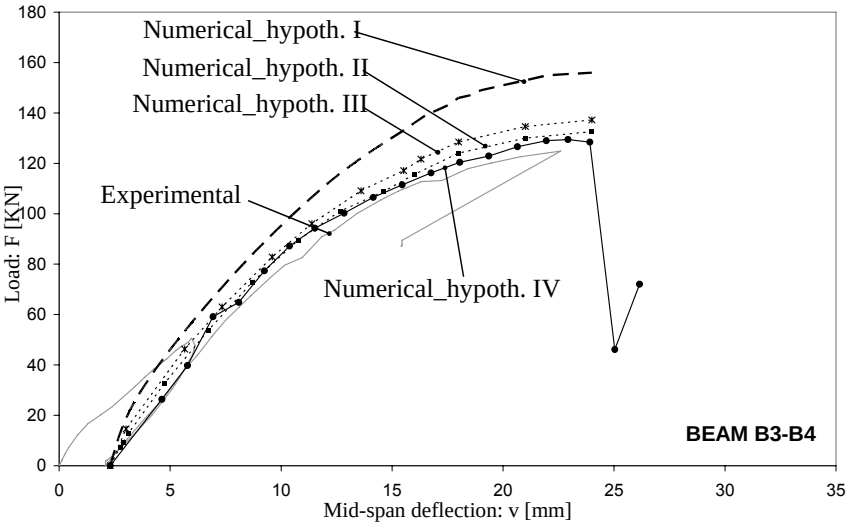

Figure 7.4.13: Numerical results for the reinforced beam B3-B4 obtained with different sets of hypotheses

It appears from Figures 7.4.12 and 7.4.13 that the numerical results are able to reproduce the increasing stiffness of the finite-element model associated with the closure of the cracks and with the perfect bond of the concrete with steel bars and FRP reinforcement.

Furthermore, all the considered hypotheses, that are the presence of initial cracks and the correct modelling of concrete/steel bars and concrete/FRP interfaces through a cohesive relationship, are important in order to achieve a good appreciation of structural behaviour in terms of load-displacement curve.

One of the aims of this work is to focuses in detail on the interfacial stresses at the FRP/concrete interface and the effect of localized cracks on these.

A lot of works have been done on the interface performance [Rasheed & Pervaiz 2002; Yang et al. 2004] and analytical solutions, which are only applicable prior to cracking, have been provided. The nonlinear model developed in this work is capable of capturing the effects of cracking on the interface stresses.

The set of results presented in Figure 7.4.14 represents a series of diagrams showing the stresses at the FRP/concrete interface in the reinforced beam B3-B4, for several values of the applied load. The stress values correspond to points *C1*, *C2*, *C3*, *C4* and *C5*, on the load-displacement curve plotted in Figure 7.4.15. Finally, Figure 7.4.16 shows the evolution of the deflection of the numerical model during the analysis.

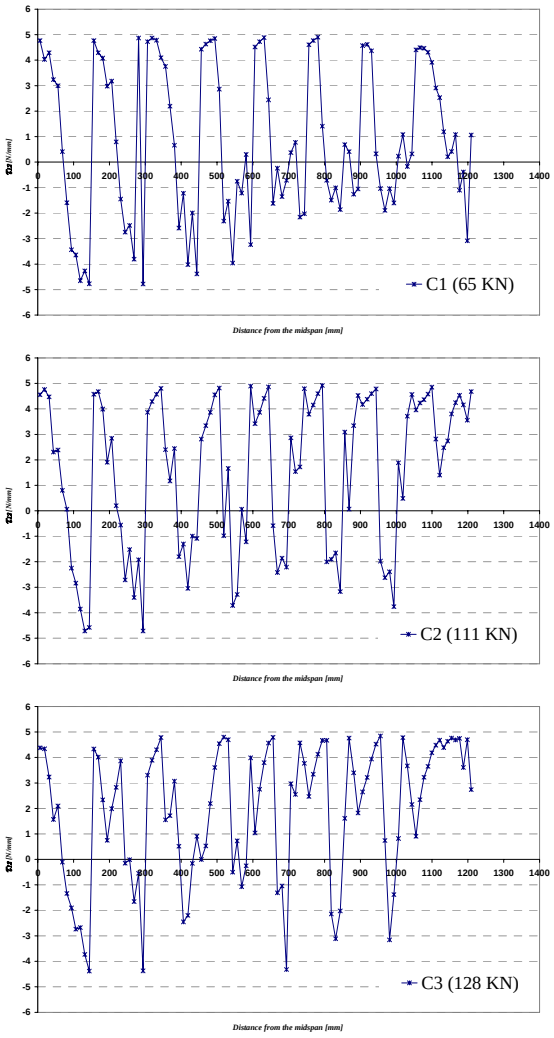

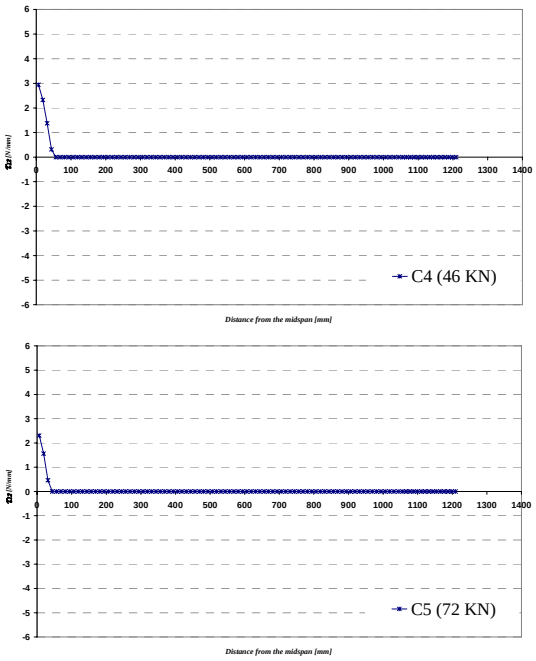

Figure 7.4.14: Evolution of bond stresses at the interface FRP/concrete for the reinforced beam B3-B4 carried out by model I: interface stress profiles

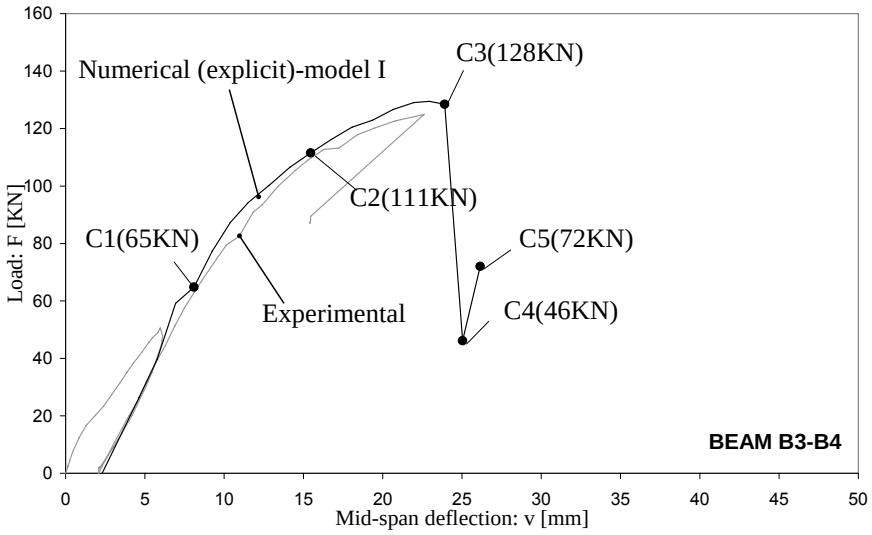

Figure 7.4.15: Evolution of bond stresses at the interface FRP/concrete for the reinforced beam B3-B4 carried out by model I: corresponding load-displacement curve

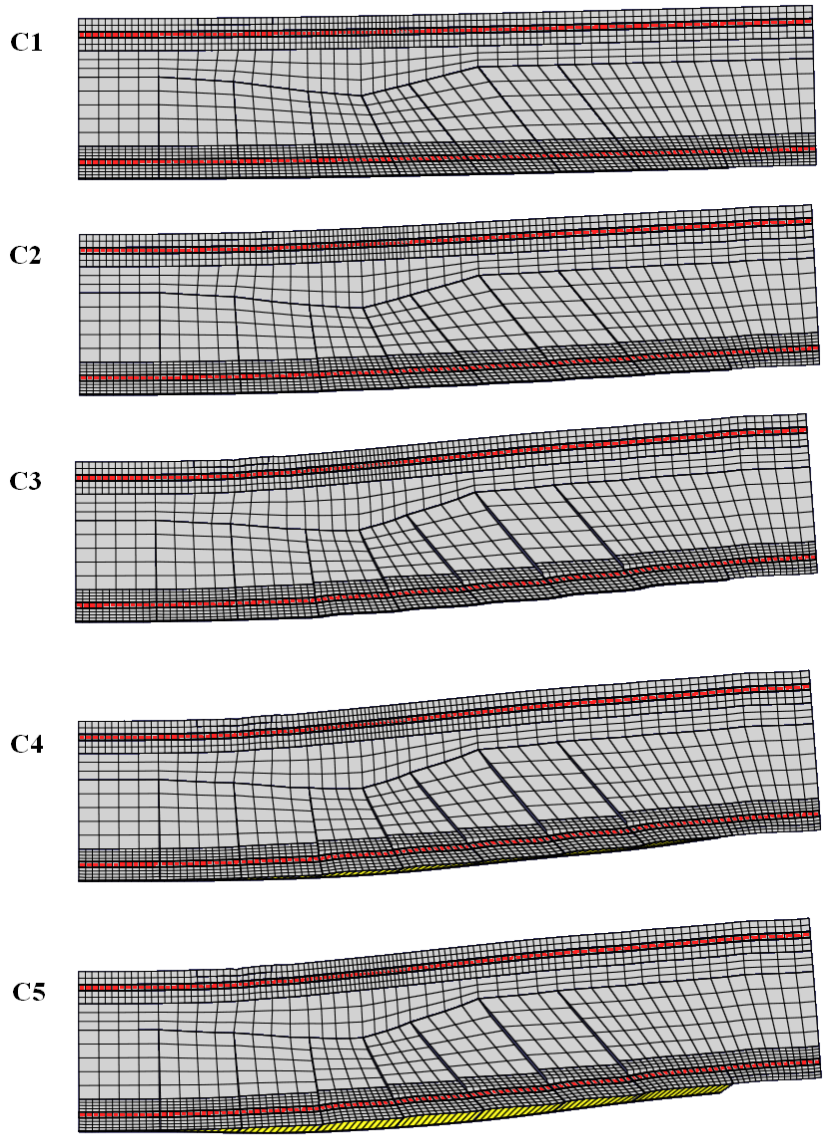

Figure 7.4.16: Evolution of bond stresses at the interface FRP/concrete for the reinforced beam belonging to group II: deformed configurations of beam

The progressive decohesion of the laminate from the concrete face, is triggered in the area near to the point of application of the prescribed

displacement, and propagates in the vicinity of the terminal zones, as it is visible in Figure 7.4.16.

7.5 INFLUENCE of CONCRETE/FRP INTERFACE LAW

The finite-element model used for the experimental-numerical comparisons is now used for simulating explicit numerical analysis in order to investigate on the role of the interface law between the concrete substratum and FRP reinforcement on the overall behaviour of reinforced beam.
The bilinear elastic-damage relationships considered for this goal are reported in the following table.

Table 7.5.1. FRP stress-bond slip relationships for beam B5-B6.

TEST	τ_0 [N/mm]	G_C [N]	S_C [mm]
LAW 1	2.1	0.52	0.50
LAW 2	4.5	0.56	0.25
LAW 3	4.8	0.55	0.23
LAW 4	4.8	0.72	0.30
LAW 5	4.5	0.72	0.32
LAW 6	4.5	0.90	0.40
LAW 7	4.0	1.00	0.50
LAW 8	5.0	0.50	0.20
LAW 9	5.0	0.60	0.24
LAW 10	3.0	0.60	0.24

Such laws, which have been also plotted in Figure 7.5.1, have been introduced in the material properties of the cohesive-zone elements adopted for the modelling of the concrete/FRP interface. The load-displacement curves carried out by performing explicit analysis on the reinforced beam B5-B6 will be reported in Figures 7.5.2 and 7.5.3.

In particular, Figure 7.5.2 focuses on the influence of the fracture energy of the concrete/FRP relationship on the global structural behaviour, and hence, on delamination. The numerical curves obtained by selecting the interface laws characterized by the same fracture energy (laws from 1 to 5) are compared. It can be underlined that:

- the laws with the same fracture energy do not imply the same load-deflection curve, in particular the overall ductility of the reinforced beam tends to decrease with the decreasing of the peak stress,
- the increasing of the fracture energy corresponds in the load-deflection curve to an increasing in the ductility;

Figure 7.5.3 indeed focuses on the influence of the peak stress (τ_0) of the concrete/FRP relationship on delamination. It confirms what already underlined about fracture energy:

- the laws with the same peak stress do not imply the same load-deflection curve, in particular the overall ductility of the reinforced beam tends to decrease with the decreasing of the fracture energy,
- the increasing of the peak stress corresponds to an increasing in the overall ductility.

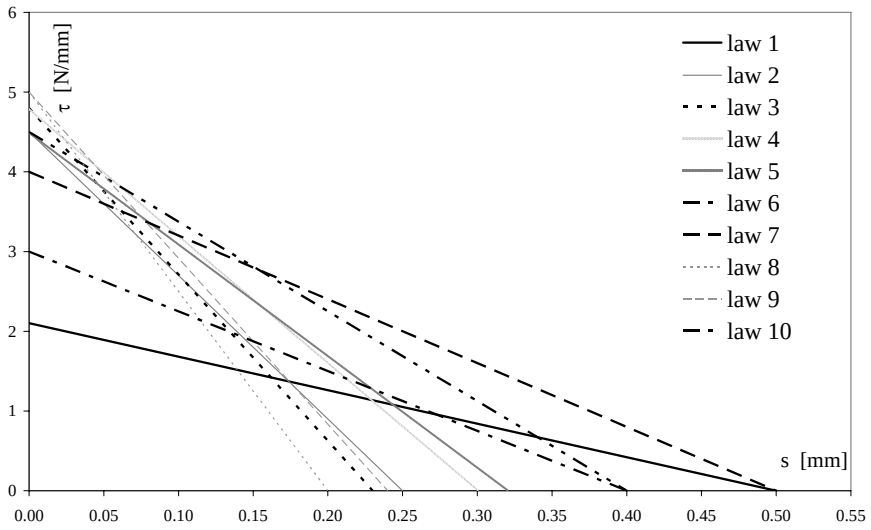

Figure 7.5.1: Mode-II interface relationships

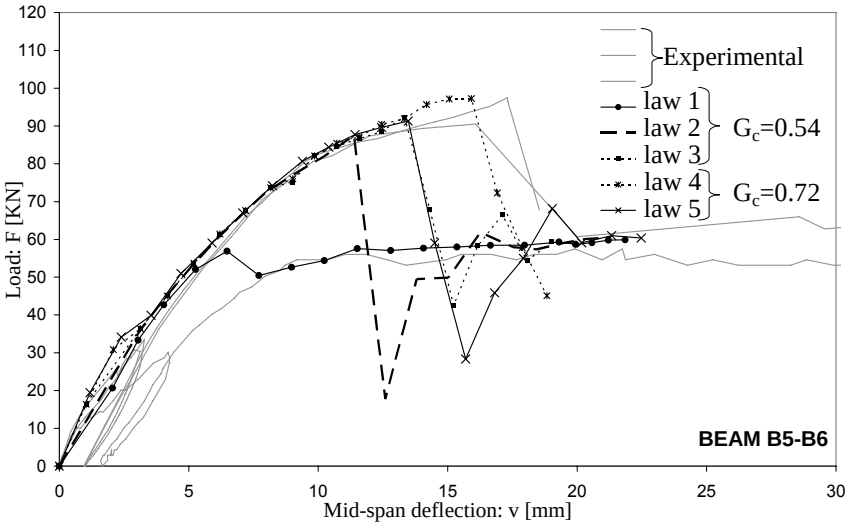

Figure 7.5.2: Numerical results. Influence of interface law between FRP/concrete on global behaviour of reinforced beam

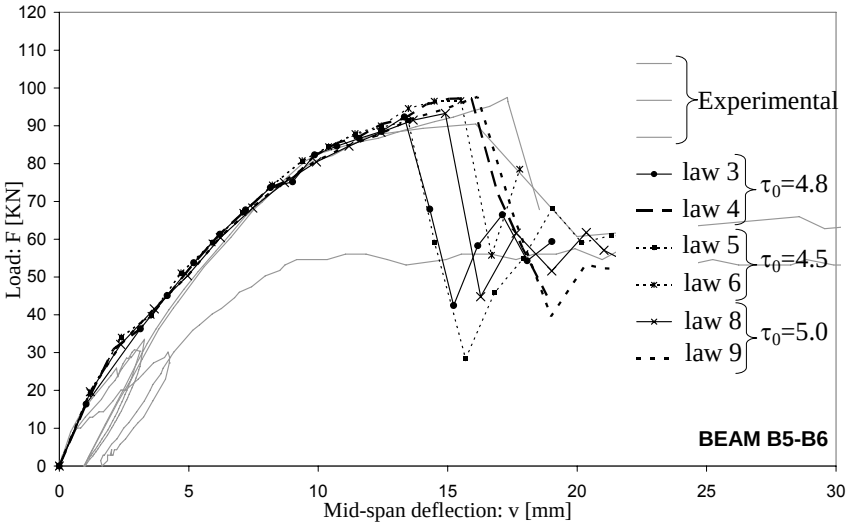

Figure 7.5.3: Numerical results. Influence of interface law between FRP/concrete on global behaviour of reinforced beam

Figure 7.5.4, highlights the perfect agreement of the numerical results corresponding to laws 3, 5 and 7. It suggests an interesting result: in fact, the laws 3, 5 and 7 are characterized by a decreasing of the peak stress passing from law 3 to law 7, on the contrary, the fracture energy progressively decreases passing from law 3 to law 7.
It means that the decreasing of the fracture energy and the consequently increasing of the peak stress can lead to the same global behaviour of the reinforced beam.
Further studies could be turned to investigate on the influence of the fracture energy and the shape of the bond-slip relationship on the global structural behaviour of a RC beam retrofitted with composite.

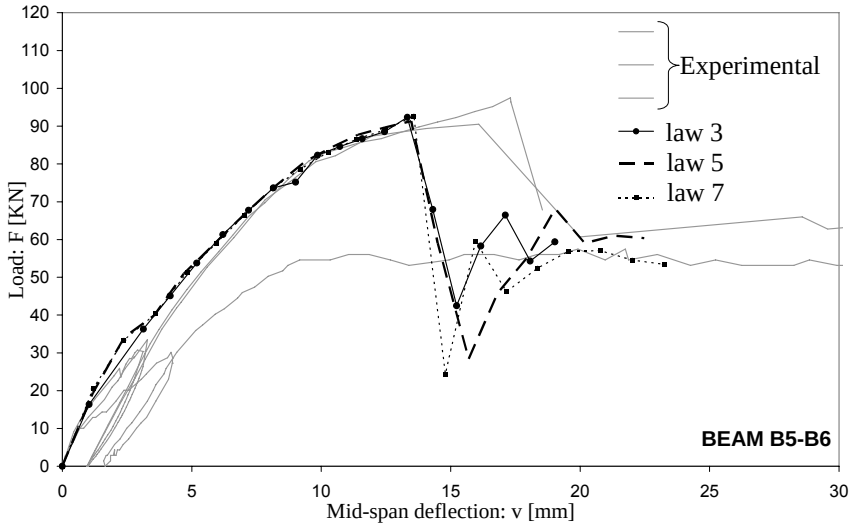

Figure 7.5.4: Numerical results. Influence of interface law between FRP/concrete on global behaviour of reinforced beam

The same analysis have been performed for the reinforced beam B3-B4: the numerical results confirm all the findings just found for the reinforced beam B5-B6. For brevity, only the curves obtained by adopting the interface laws characterized by the same peak stress (τ_0) are reported in Figure 7.5.5.

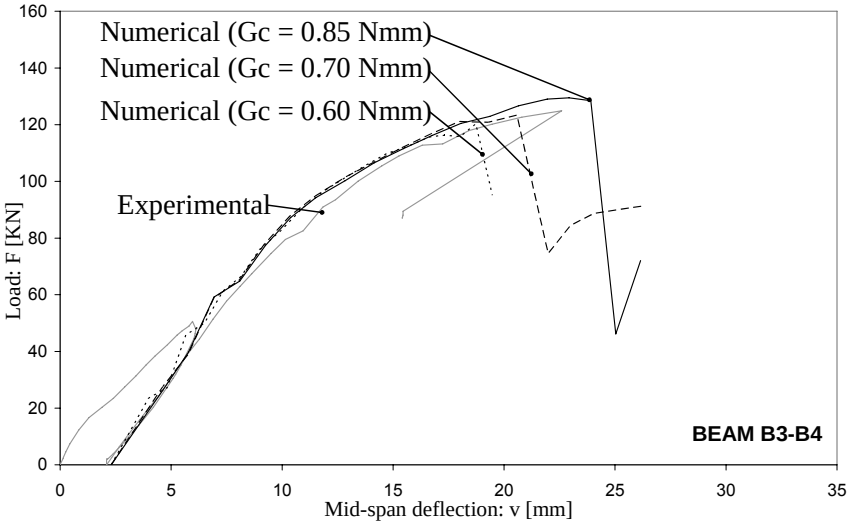

Figure 7.5.5: Numerical results. Influence of interface law

7.6 INFLUENCE of the FINITE-ELEMENT MODEL

The aim of this section is to validate the numerical results in order to understand if few changes in the finite-element model can induce variations in the prediction of the global and local behaviour of retrofitted RC beams.
The numerical results previously described are now compared with the results obtained by considering a new model (referred to as model II) only for the reinforced beam B3-B4.
The new finite-element model used is shown if Figures 7.5.1 and 7.5.2.
The steel bars and the FRP reinforcement have been modelled with 3-noded truss elements, while for the concrete 8-noded quadrilateral plane stress elements have been used. Furthermore, a new less refined mesh has been used for this new model.
Figures 7.6.3 and 7.6.4 show the load-displacement curves obtained from the two finite-element models.

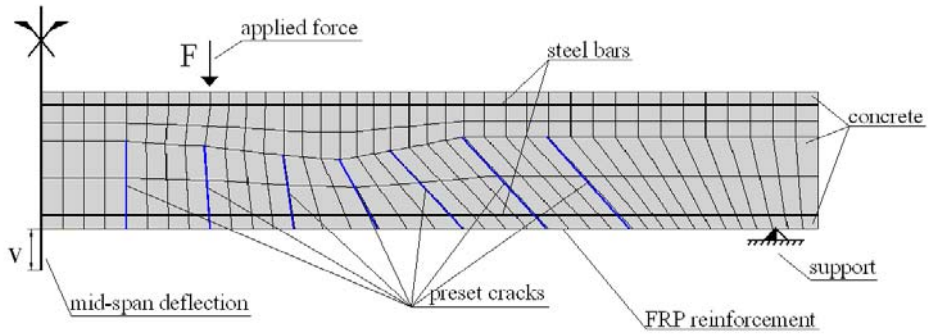

Figure 7.6.1: RC beam (B3-B4): finite-element model II

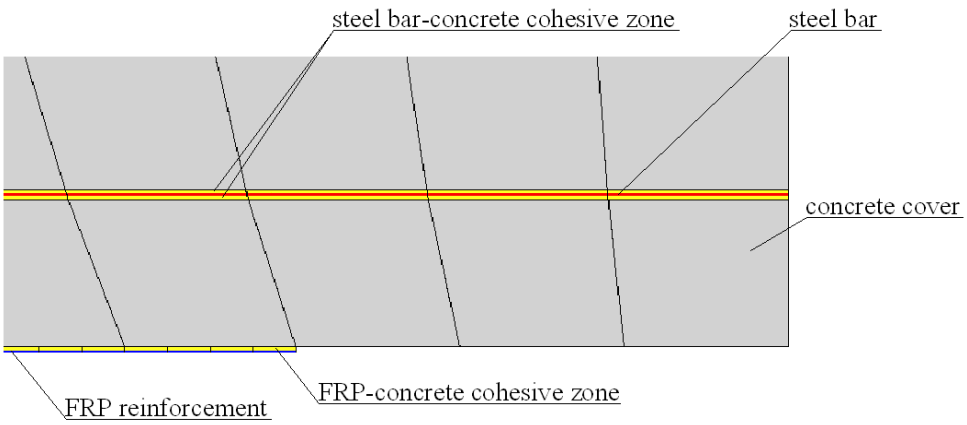

Figure 7.6.2: RC beam (B3-B4): detail of the finite-element model II

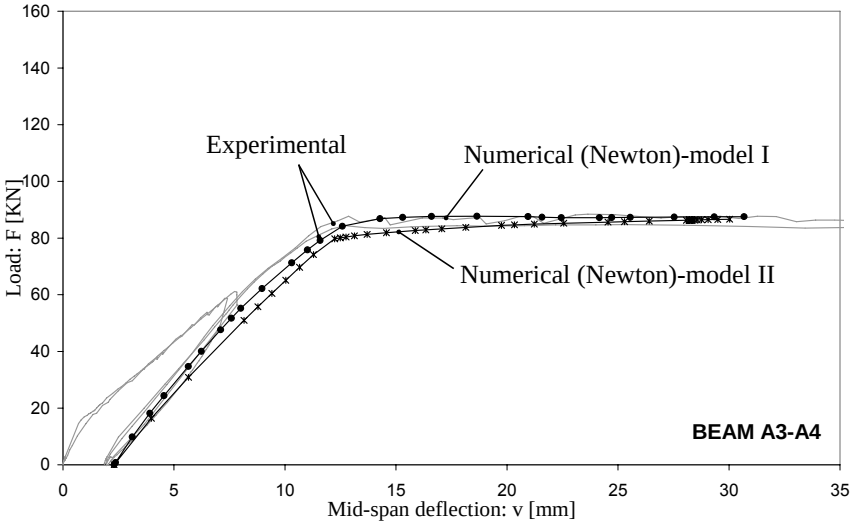

Figure 7.6.3: Comparisons of numerical results obtained by adopting two models for the beam A3-A4 with no FRP reinforcement

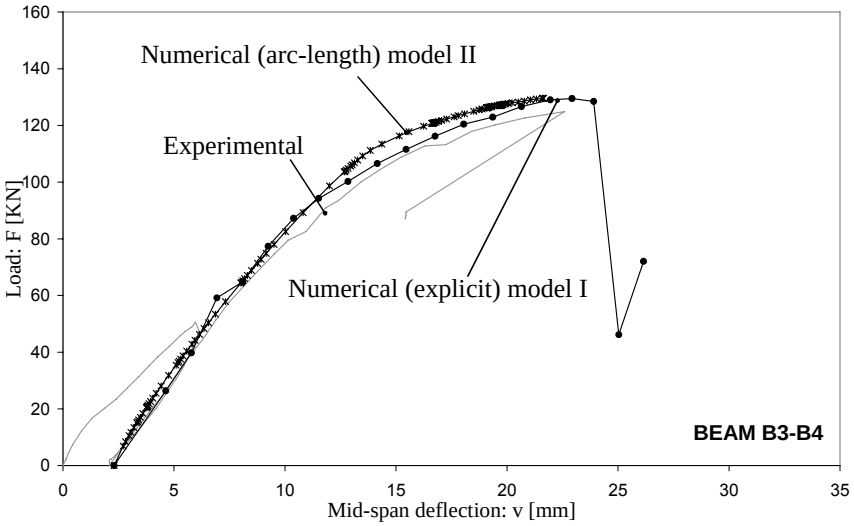

Figure 7.6.4: Comparisons of numerical results obtained by adopting two models for the reinforced beam B3-B4

They underline the good degree of accuracy achieved by the new finite-element model in the modelling of the nonlinear behaviour of the reinforced beam B3-B4.
As Figures 7.6.3 and 7.6.4 clarify, simplifying the finite-element model, the arc-length method represents a good alternative procedure for partially solving the analysis convergence problems when debonding occurs.
Now, analyzing the interfacial stresses at the FRP/concrete interface in the reinforced beam B3-B4 and the effect of localised cracks on these, the set of results obtained by model II are reported in Figure 7.6.5 for several values of applied load.

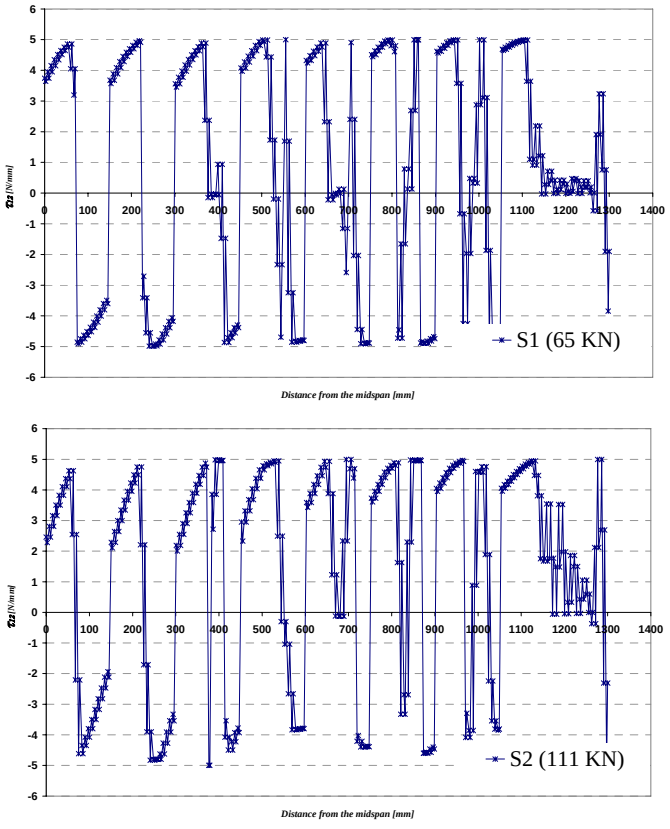

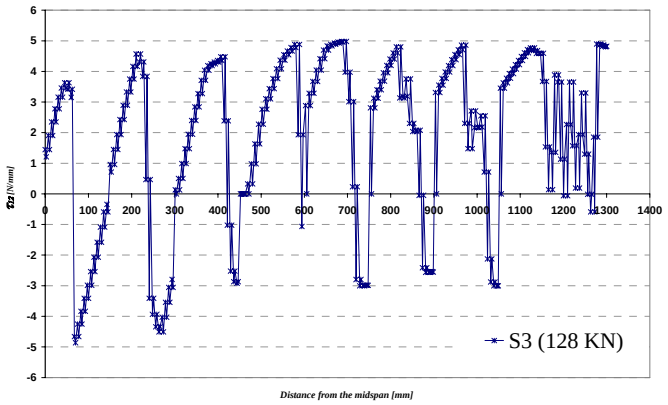

Figure 7.6.5: Evolution of bond stresses at the interface FRP/concrete for the reinforced beam B3-B4 carried out by model II: interface stress profiles

These values are also reported in Figure 7.6.6 near the corresponding points of the load-displacement curve.

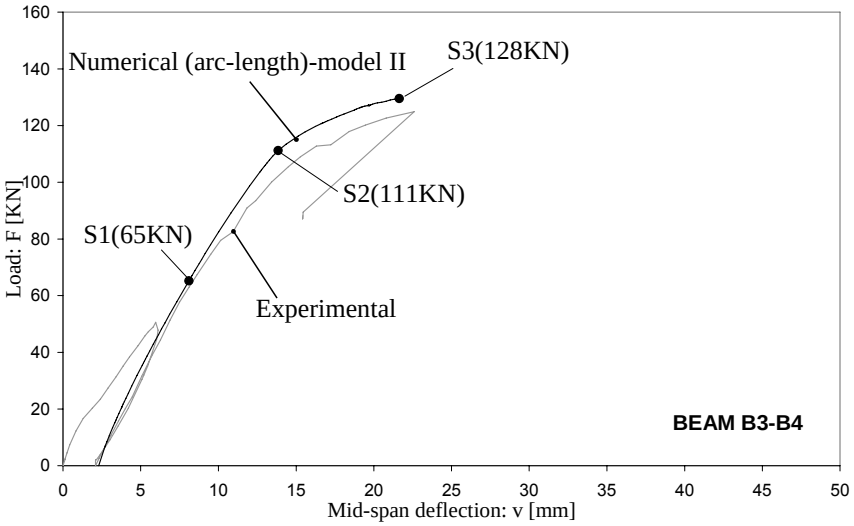

Figure 7.6.6: Evolution of bond stresses at the interface FRP/concrete for the reinforced beam B3-B4 carried out by model II: corresponding load-displacement curve

The evolution of the debonding process for the reinforced beam B3-B4 can appear clearer by reasoning in terms of displacements. In Figure 7.5.7 the evolutions of the absolute and the relative displacements of the two adjacent layers of the cohesive-zone elements along the beam are reported.
From the figures it is clear that debonding is triggered in the area near the point of application of the prescribed displacement and propagated toward the anchorage of the FRP-reinforced zone.
The numerical results of model II validate all the numerical findings illustrated previously obtained by the original finite-element model.

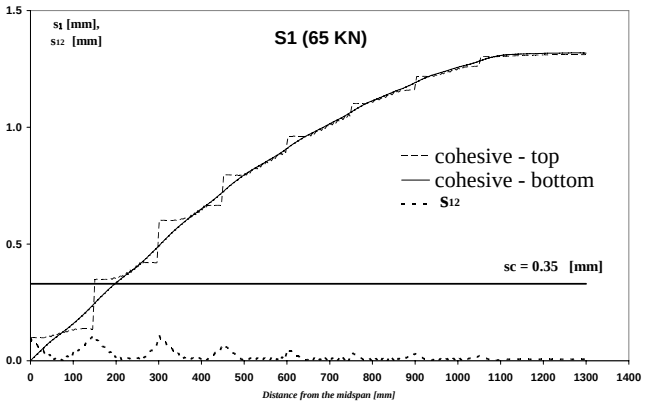

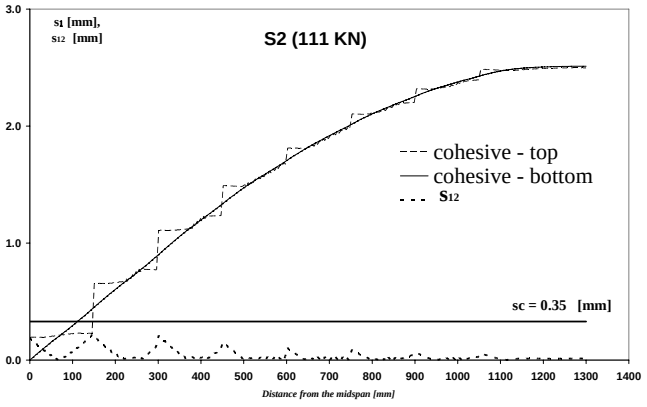

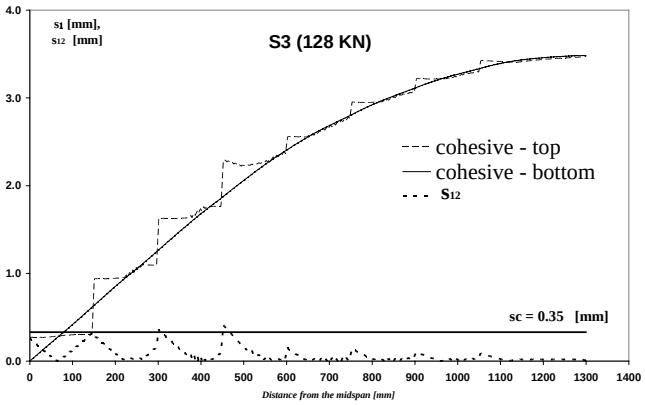

Figure 7.6.7: Evolution of bond stresses at the interface FRP/concrete for the reinforced beam B3-B4 carried out by model II: interface displacements profiles

CHAPTER VIII
CODE PROVISIONS and ANALYTICAL RESULTS

8.1 INTRODUCTION

For failure modes in which adhesion between FRP and concrete is maintained up to rupture (full composite action), so that failure occurs for concrete crushing, shear or FRP brittle rupture, it is widely accepted that the conventional RC theory for the ultimate limit state analysis can be easily applied by simply adding the composite as additional resisting element in traction. However, two cases of failure due to the loss of adhesion between composite and FRP (loss of composite action) can be observed during experimental tests on RC beams externally reinforced with FRP materials.
In some cases, it occurs because the composite debonding starts in proximity of vertical flexural cracks or of inclined cracks due to shear with or without flexure and propagates towards the end of the beam, it is usually named mid-span delamination; in other cases, delamination may start at the end of the composite laminate (end peeling) due to the insufficiency or even the lack of anchorage, with the crack sometimes propagating up to the reinforcing bars so that the entire covercrete debonds. For each of these cases the codes of practice propose different analytical models based on the extensive research done in the last two decades. Furthermore, the proposed models all involve different types of approximation and often different proposed methods yield quite different results. For this reason, the results of analytical calculations based on the models proposed in the codes of practice are presented in this section and will provide a further element of comparison and discussion with the numerical results obtained by finite-element analysis and, hence, by the experimental results.
The current guidelines for the design of this type of strengthening works tend to extend the principles of the design of standard RC elements to the case of FRP retrofitted ones. When FRP sheets are applied to the structural elements though, the behaviour of the assembly becomes by far more complex and aspects that are negligible in the assessment of the overall

performance of a standard RC element are to be taken into account. In the present section the analytical approaches provided by European [Fib bulletin 14, 2001] and International code, with referring to documents provided by the American Concrete Institute [ACI 440-2R, 2008] and Japan Society of Civil Engineers [JSCE Recommendations, 2001] will be discussed. Furthermore, the analytical results obtained by using the recommendations available in the Italian code [CNR DT-200, 2004] will be also shown and discussed.

8.2 CODE PROVISIONS

Before the analytical methods will be discussed it is useful to observe that the experimental results reported in the literature induce to consider the following mechanisms of failure for the RC beams strengthened with FRP:

- Concrete crushing after the steel yielding
- Concrete crushing
- Failure of the anchorage
- Failure of the FRP/concrete interface due to the growth of flexural and shear cracks

The first two failure modes the checks consist in quantifying the flexural capacity of the reinforced section assuming the perfect interaction between the concrete section and the FRP reinforcement. In this case, the computation of the ultimate strength of the reinforced section is carried out considering, for the steel and concrete strains, the values usually adopted for the evaluation of the flexural capacity of common RC elements. Only the last case will be analysed in the follows.

8.2.1 ACI 440 (2008)

A first method for the check for the debonding of FRP reinforcement consists in limiting the ultimate deformations of the composite. In particular, in order to prevent the intermediate crack-induced debonding failure mode, the code [ACI 440 2R 2008] introduces a limitation to the effective strain in FRP reinforcement ε_{fd} which depends on the specific

stiffness of the composite in terms of product between the Young modulus (E_f) and the thickness (t_f) of the composite reinforcement.

$$\varepsilon_{fd} = 0.41\sqrt{\frac{f_c'}{nE_f t_f}} \leq 0.9\varepsilon_{fu} \qquad (8.2.1)$$

Eq. (8.2.1) takes a modified form of the debonding strain equation proposed by Teng et al. [2001-2004] that was only based on committee evaluation of a significant database for flexural beam tests exhibiting FRP debonding failure. The proposed equation was calibrated using average measured values of FRP strains at debonding and the database for flexural tests experiencing intermediate crack-induced debonding to determine the best fit coefficient of 0.41.
Eq. (8.2.1) recognizes that laminates with greater stiffness are more prone to delamination; in fact, the limited deformations (ε_{fd}) decrease with the increasing of the axial stiffness $E_f t_f$, as it is clearly shown in Figure 8.2.1(a). The limitation of the strains induces implicitly a limitation in terms of stresses in the composite layer. In Figure 8.2.1(b) it is shown how the stresses are to be limited in order to comply with adherence conditions, in particular for high values of the composite thickness.

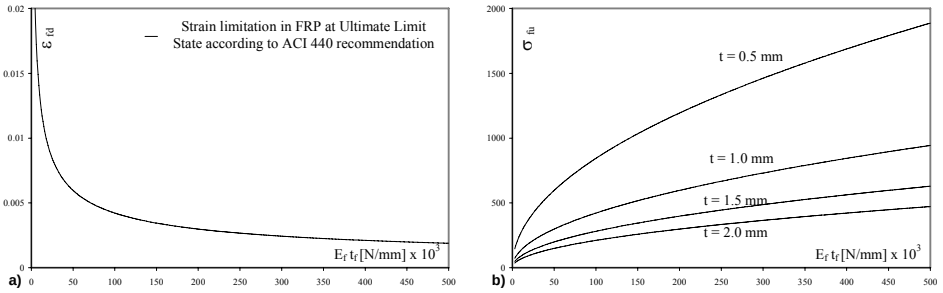

Figure 8.2.1: Limitation on FRP strain (a) and relative limitation on FRP stress (b) according to prescriptions of ACI committee 440

In fact, in order to prevent the mid-span debonding failure, the admissible values for the FRP stress are very low with respect to the rupture stresses of the reinforcement, which can reach also 2000÷3000 MPa.
The ultimate bending moment diagrams along the reinforced beam B3-B4 evaluated both by assuming the full composite action and by using the limit recommended in the ACI for the stress in the FRP reinforcement are reported in Figure 8.2.2.
Furthermore, the safe factor (SF) for mid-span debonding failure evaluated as the ratio between the ACI failure load and experimental force is also reported in Figure 8.2.2.

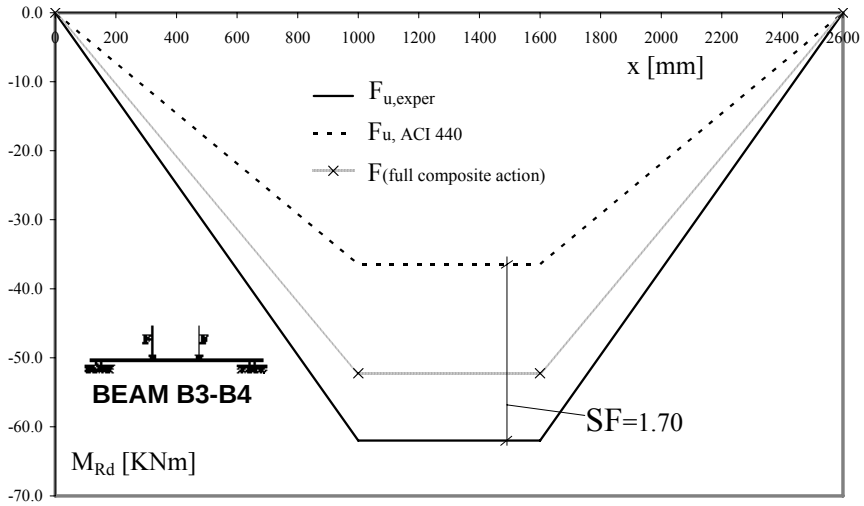

Figure 8.2.2: Bending moment diagrams corresponding to failure and Safe Factor evaluated in accordance with the ACI 440 provisions, for the reinforced beam B3-B4

For the evaluation of the analytical failure load (F_u) the concrete crushing is assumed to occur if the compressive strain in the concrete reaches its maximum usable strain ($\varepsilon_{cu}=0.003$); furthermore, the reliability of FRP contribution to flexural strength is addressed by incorporating an additional strength reduction factor for FRP ψ_f in addition to the strength reduction factor ϕ suggested by ACI 318 [2005] for structural concrete, defined by:

$$\phi = \begin{cases} 0.90 & for\ \varepsilon_t \geq 0.005 \\ 0.65 + \dfrac{0.25\left(\varepsilon_t - \varepsilon_{sy}\right)}{0.005 - \varepsilon_{sy}} & for\ \varepsilon_{sy} < \varepsilon_t < 0.005 \\ 0.65 & for\ \varepsilon_t \leq \varepsilon_{sy} \end{cases} \qquad (8.2.2)$$

8.2.2 CNR DT-200 (2004)

The simplified procedure adopted by the Italian code of practice provides to compute the maximum strain in the composite and to compare this value with the following limitation of the strain:

$$\varepsilon_{f,\max} = \frac{k_{cr}}{\gamma_{f,d}\sqrt{\gamma_c}}\sqrt{\frac{2G_c}{E_f t_f}} \qquad (8.2.3)$$

In the above formula $\gamma_{f,d}$ is the material factor for FRP, taken equal to 1.2 in the present analysis (for a certificated reinforcement according to CNR provisions); γ_c is the material factor for concrete, taken equal to 1.5, in line with the recent European codes of practice; k_{cr} is an empirical coefficient that, in absence of further data, can be taken as high as 3.0; finally E_f and the t_f are the Young modulus and the thickness of the composite lamina.
Finally, G_c is the fracture energy of the interface behaviour between FRP reinforcement and concrete; in the CNR Bulletin it can be assumed as:

$$G_c = 0.03 \cdot k_b \sqrt{f_{ck} \cdot f_{ctm}} \qquad (8.2.4)$$

where k_b is a geometrical factor which takes into account the ratio between the beam and reinforcement widths:

$$k_b = \sqrt{\frac{2 - \dfrac{b_f}{b}}{1 + \dfrac{b_f}{400}}} > 1 \qquad (8.2.5)$$

The mechanical properties of concrete (f_{ck}, f_{ctm}) in Eq. (8.2.4) are taken from experimental outcomes already reported in the previous section.
The evaluation of the axial stress can be made on the basis of the conventional theory of RC beam.
The bending moment diagrams along the reinforced beam B3-B4 induced by applying the failure loads F_u, evaluated both assuming the full composite action and using the bound for the FRP strain recommended in the CNR, with two different values for the fracture energy, are reported in Figure 8.2.3.
The two values considered for the fracture energy are:

- the value suggested by the Italian CNR
- the value come out of the numerical-experimental comparisons

The safe factors (SF) are also reported in the figure.

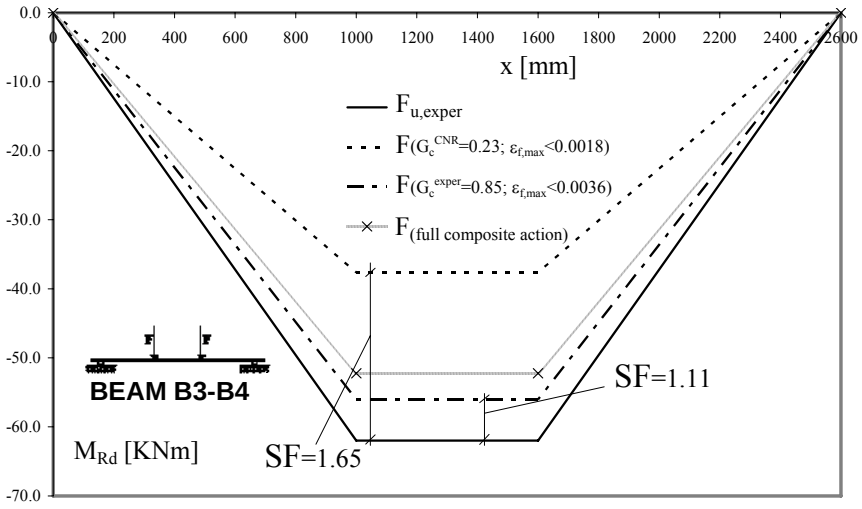

Figure 8.2.3: Bending-moment diagrams corresponding to failure and Safe Factors evaluated in accordance with CNR DT-200, considering two values for fracture energy, for the reinforced beam B3-B4,

8.2.3 JSCE (2001)

The Japanese recommendations introduce a different procedure for the evaluation of the ultimate force corresponding to debonding. A double check along the beam is assumed in order to take into account the last two mechanisms summarized before. For each case, only the axial stresses are considered in the evaluation of the section capacity, and the check in conducted by verifying the compatibility of the axial stresses variation with mechanical characteristics of the adhesive layer.

At the end of the beam, the debonding check is conducted by controlling that the stress in the composite, at a predefined distance from the end of the reinforcement, is smaller than $\sigma_{f,max}$ given by:

$$\sigma_{f,\max} = \sqrt{\frac{2G_f E_f}{t_f}} \tag{8.2.6}$$

with G_f the fracture energy of the FRP/concrete interface (suggested equal to 0.5 N/mm). The second right-end member of the Eq. (8.2.6) represents the maximum stress which can be applied to an adhesive joint FRP/concrete, provided with a fracture energy G_f, when its length de so called "transfer length": this topic is quite known in the theory of fracture energy applied to the retrofitting of structures. Further details can be found in a work published by Faella et al. [2003].

The same approach is used for the debonding checks along the beam. The procedure requires to compute the axial stress variation $\Delta\sigma_f$ in the composite between two adjacent cracks, assuming a distance between cracks equal to s_{rm} (ranging in the field 150-250 mm, for the JSCE), and to compare such value with the capacity of the FRP/concrete interface ($\Delta\sigma_{f,max}$):

$$\Delta\sigma_f \le \Delta\sigma_{f,\max} = \sqrt{\frac{2G_f E_f}{t_f}} \tag{8.2.7}$$

The evaluation of the axial stress can be made on the basis of the conventional theory of RC beam.

The bending moment diagrams along the reinforced beam B3-B4 induced by applying the failure loads F_u, evaluated both assuming the full composite action and using the procedure provided by the JSCE recommendation, with three different values for the fracture energy, are reported in Figure 8.2.4.
The three values considered in the procedure are:

- the value suggested in the Japanese
- the value suggested in the Italian CNR
- the value come out of the numerical-experimental comparisons

The safe factors (SF) are also reported in the figure.
Finally, in Figure 8.2.5 the current approach is shown graphically: the stresses in the FRP lamina and the admissible increments are reported along the reinforced beam B3-B4, assuming for the adherence law and crack spacing the values suggested in the Japanese code. Furthermore, the stress variation in tensile stress ($\Delta\sigma_f^i$) and the maximum variation carried by the FRP lamina ($\Delta\sigma_{f,max}^i$) are indicated for the i^{th} portion between two consecutive cracks.

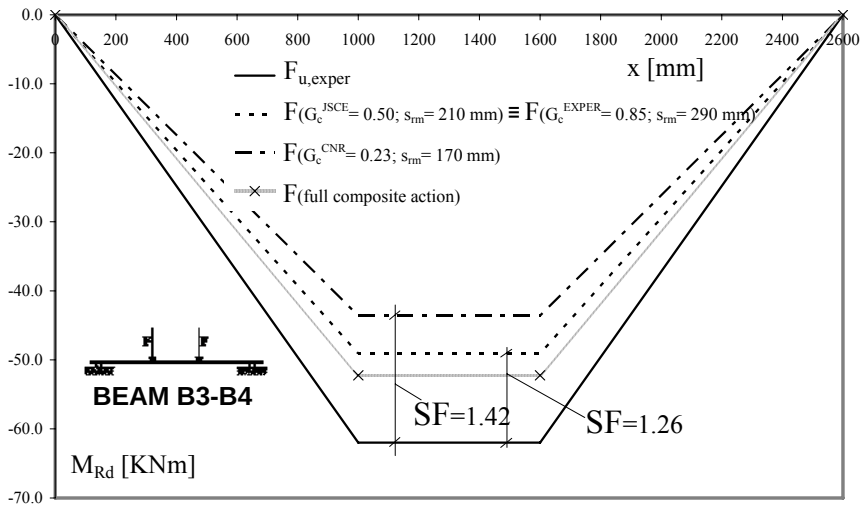

Figure 8.2.4: Bending-moment diagrams corresponding to failure and Safe Factors evaluated in accordance with Japanese Recommendations, considering three values for fracture energy, for the reinforced beam B3-B4

In Figure 8.2.5 it is clear that in the present case the analysis reveals that the critical zone in which debonding first is triggered is that under the applied force. This is confirmed also by the evolution of the stress profiles obtained by the numerical analyses discussed in the previous section.

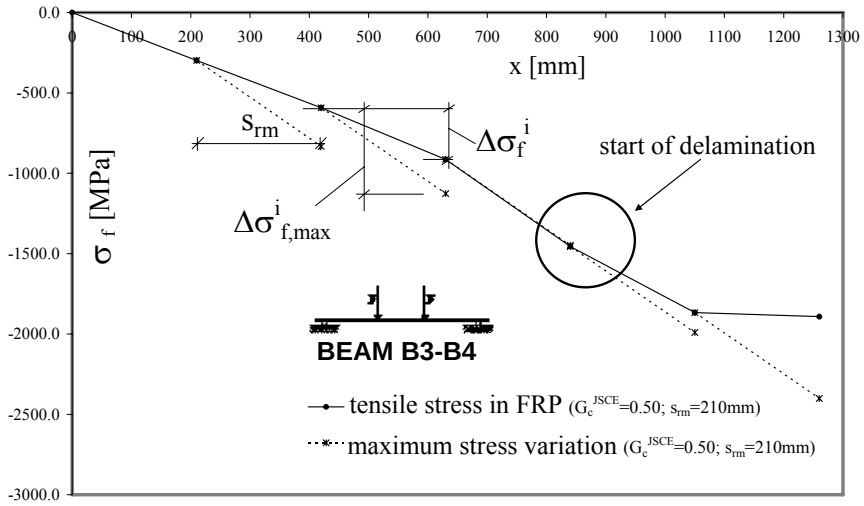

Figure 8.2.5: Diagrams of the maximum possible increase in tensile stress (JSCE) and tensile stress in the FRP reinforcement along the beam B3-B4

8.2.4 FIB Bulletin n.14 (2001)

The only European reference code is the document drawn up by the Federation International du Beton in 2001 [Bulletin n.14, 2001]. The debonding checks at limit states are dealt with three different approaches summarized in the follows.

8.2.4.1 Approach I

The approach I consider only the end-peeling debonding check; it basically refers to the recommendations provided by the Japanese code of practice for the estimation of the anchorage. In order to prevent peeling-off, the approach restricts the ultimate tensile strain $\varepsilon_{f,lim}$ at Ultimate Limit State to a certain value, which ranges from 0.0065 to 0.0085.

In the following figure the bending moment diagrams along the reinforced beam B3-B4 induced by applying the failure loads F_u , evaluated both assuming the full composite action and using the lower and the upper bounds for the FRP strain recommended in the approach I of the Fib Bulletin, on the beam are reported.
The diagrams obtained by assigning the above limits and that induced by assuming the full composite action overlaps because of concrete crushing.
Furthermore, the safe factor (SF) for mid-span debonding failure with respect to experimental action is also reported in the figure.

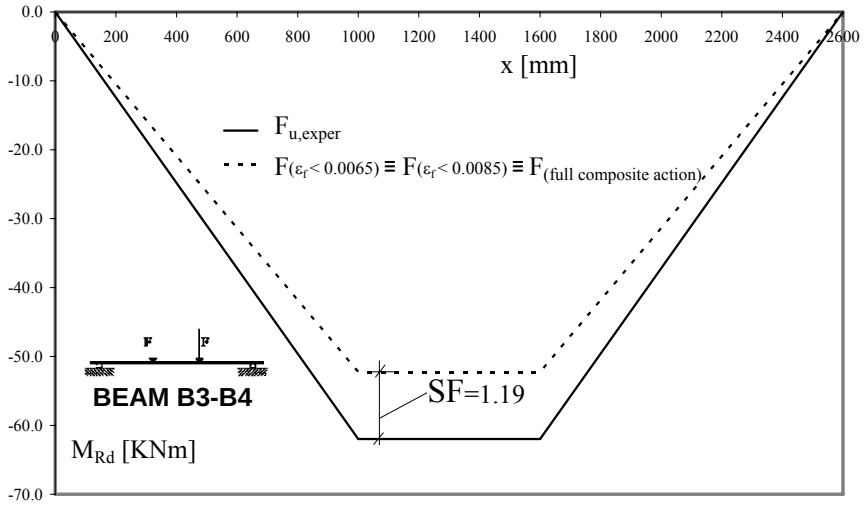

Figure 8.2.6: Bending-moment diagrams corresponding to failure and Safe Factor evaluated in accordance with approach I of Fib Bulletin 14, for the reinforced beam B3-B4

8.2.4.2 Approach II

The procedure is very similar to that provided by the JSCE, previously discussed, even though in the European code the debonding check between two adjacent cracks is more conservative. This method is based on a model developed by Niedermeier [2000]. To determine whether a given load does not produce mid-span debonding, Niedermeier's procedure requires to compute the maximum admissible increase in the tensile stress for the

composite between two adjacent cracks, assuming a bilinear relationship between shear stress and interface slip on the FRP/concrete interface. This value is then compared with the actual increase obtained for the given load level, and iterations are performed on the load level to make the two values coincide. The maximum stress variation ($\Delta\sigma_{f,max}$) can be synthetically expressed as a function of:

$$\Delta\sigma_{f,max} = f\,(\sigma_{fd},\ \tau\text{-}s \text{ relationship},\ s_{rm}) \qquad (8.2.8)$$

where, σ_{fd} is the minimum stress on the cracks, s_{rm} is the distance between cracks.

Basically, the approach consists of three steps (Figure 8.2.7):

- Determination of the most unfavourable spacing of flexural cracks.
- Determination of the tensile force within the Externally Bonded Reinforcement (EBR) between two subsequent cracks according to the conventional RC beam theory.
- Determination of the maximum possible increase in tensile stress in the EBR.

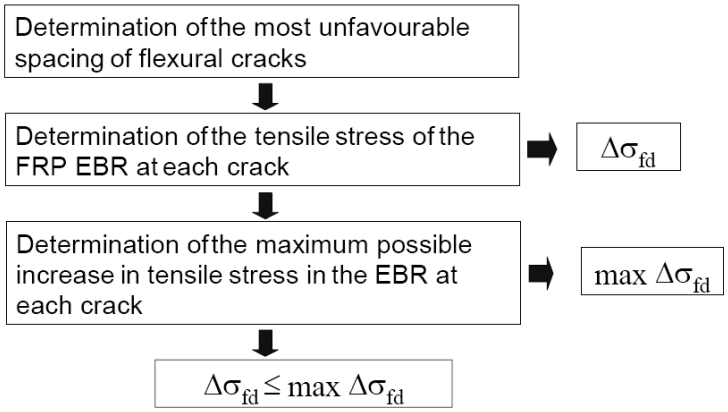

Figure 8.2.7: Basic approach-flow chart [Fib Bulletin 14 2001]

- <u>Determination of the most unfavourable spacing of flexural cracks</u>

The crack spacing between two subsequent cracks is evaluated on the basis of the RC tie-beam theory provided by CEB Manual on Cracking and Deformations [1985], taking also into account the presence of the FRP sheet externally bonded.
Hence, the crack spacing is equals one to two times the transmission length (l_t) and may be calculated assuming constant mean bond stresses of both the internal and the external reinforcement. The mean bond stress of the internal reinforcement (τ_{sm}) can be determined according to EC2 [1998] in case of high bond action:

$$\tau_{sm} = 2.25 f_{ctk,0.95} = 1.85 f_{ctm} \tag{8.2.9}$$

whereas the mean bond stress of the external reinforcement can be estimated with:

$$\tau_{fm} = 0.44 f_{ctm} \tag{8.2.10}$$

The transmission length may be calculated with:

$$l_t = \frac{M_{cr}}{z_m} \frac{1}{\left(\sum \tau_{fm} b_f + \sum \tau_{sm} d_s \pi\right)} \tag{8.2.11}$$

where M_{cr} is the bending moment causing cracking:

$$M_{cr} = \frac{k \cdot f_{ctk,0.95} \cdot bh^2}{6} \tag{8.2.12}$$

In Eq. (8.2.12) the factor k takes into account, among others, the higher value of the flexural tensile strength when compared to the axial tensile strength or the tensile strength of the concrete surface. In this case k should equal 2.0 [Eurocode 2, 1998].
The mean lever arm z_m may be determined taking into account the axial stiffness of the different layers of reinforcement through the equation:

$$z_m = 0.85 \frac{\left(A_f h E_f + A_{sl} d E_s\right)}{\left(A_f E_f + A_{sl} E_s\right)} \qquad (8.2.13)$$

To simplify the calculation, a constant crack spacing over the whole length of the flexural member may be assumed. As the bond stresses which can be transferred in an uncracked concrete zone (i.e. anchorage zone or between two subsequent cracks) is restricted due to the limitation of fracture energy, large crack spacing is unfavourable. Hence the crack spacing may correspond to two times the transmission length:

$$s_{rm} = 2l_t = 2\frac{M_{cr}}{z_m}\frac{1}{\left(\sum \tau_{fm} b_f + \sum \tau_{sm} d_s \pi\right)} \qquad (8.2.14)$$

- Determination of the tensile stress of the FRP EBR at each crack

In accordance with Eurocode 2 [1998] procedures, the tensile stress has to be calculated taking into account strain compatibility and internal force equilibrium.

- Determination of the maximum possible increase in tensile stress in the EBR

To verify that the growth in tensile stresses between two subsequent cracks as prescribed in the Eurocode 2 [1998] does not exceed the maximum possible increase determined by the bond stresses, the achievable increase has to be estimated. This has to be done for the region where flexural cracks occur as well as for the anchorage zone, but in this study only the debonding along the beam is focused on.

The analysis of the bond behaviour of the composite reinforcement based on a simplified bilinear bond stress-slip relation which leads to equations which can be used to calculate the maximum increase in tensile stress $\Delta\sigma_{f,max}$ in an element between two cracks is based on the findings of Niedermeier [2000], as it has just anticipated at the beginning of this section.

The maximum possible increase in tensile stress increment ($\Delta\sigma_{f,max}$) depends on the tensile stress (σ_{fd}) as determined based on strain

compatibility and force equilibrium at the section where the lower tensile stresses act (Figure 8.2.8).

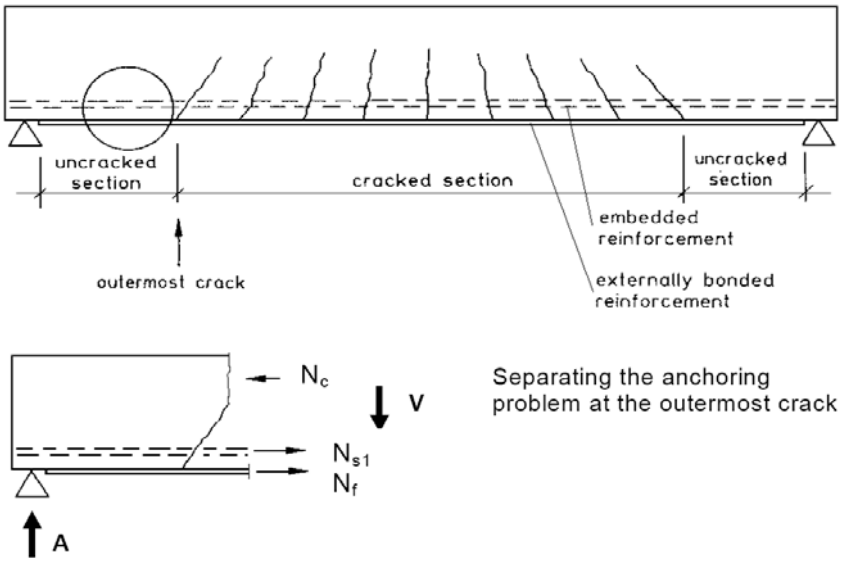

Figure 8.2.8: Element between two subsequent cracks. Analysis of peeling-off at flexural cracks [Fib Bulletin 14 2001]

In Figure 8.2.9 the maximum possible increase depending on a specific crack spacing is shown.
The code gives the closed form expressions of the red line shown in Figure 8.2.9.
The point *A* shown in the figure corresponds to the verification at the end anchorage where $\sigma_{fd} = 0$. The maximum anchorable tensile stress, if the anchorage length is greater than an effective anchorage length indicated as $l_{b,max}$ in the Fib Bulletin, can be estimated by:

$$\Delta\sigma_{f,\max}^{(A)} = \frac{c_1}{\gamma_c}\sqrt{\frac{E_f\sqrt{f_{ck}f_{ctm}}}{t_f}} \qquad (8.2.15)$$

The matching maximum increase in stress corresponding to the point *B* may be estimated using the following equations:

$$\Delta\sigma_{f,\max}^{(B)} = \frac{1}{\gamma_c}\left[\sqrt{\frac{c_1^2 E_f \sqrt{f_{ck} f_{ctm}}}{t_f} + \left(\sigma_{fd}^{(B)}\right)^2} - \sigma_{fd}^{(B)}\right] \qquad (8.2.16)$$

$$\sigma_f^{(B)} = \frac{c_3 E_f}{s_{rm}} - c_4 \sqrt{f_{ck} f_{ctm}}\,\frac{s_{rm}}{4t_f} \qquad (8.2.17)$$

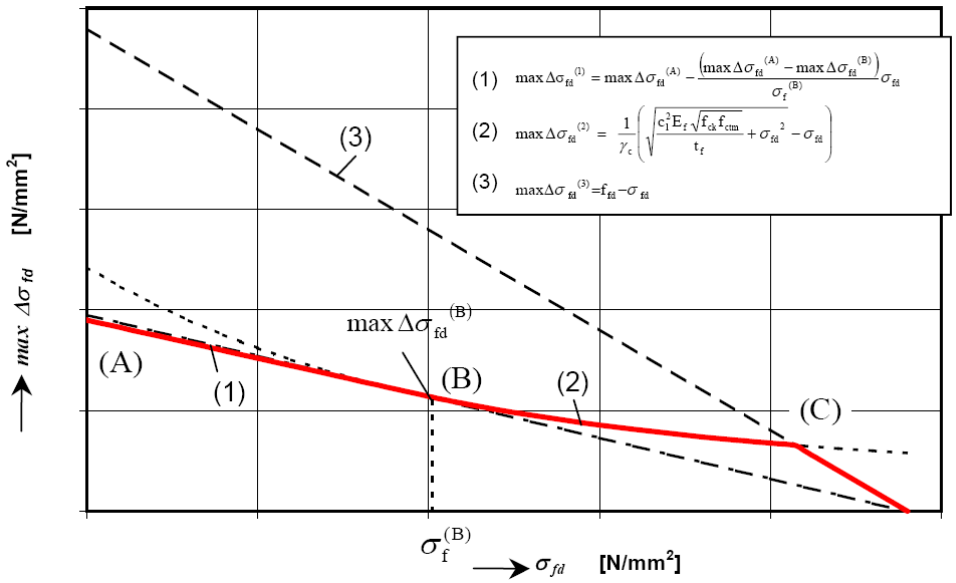

Figure 8.2.9: Diagram of the maximum possible increase in tensile stress between two subsequent cracks [Niedermeier, 2000]

The linear decrease between points *A* and *B* can then be described by the following equation:

$$\Delta\sigma_{f,\max}^{(1)} = \Delta\sigma_{f,\max}^{(A)} - \frac{\Delta\sigma_{f,\max}^{(A)} - \Delta\sigma_{f,\max}^{(B)}}{\sigma_f^{(B)}}\sigma_{fd} \qquad (8.2.18)$$

And the graph between *B* and *C* is determined by:

$$\Delta\sigma_{f,\max}^{(2)} = \frac{1}{\gamma_c}\left[\sqrt{\frac{c_1^2 E_f \sqrt{f_{ck} f_{ctm}}}{t_f} + \sigma_{fd}^2} - \sigma_{fd}\right] \qquad (8.2.19)$$

For high tensile stresses, the upper limit of the increase in stresses is determined by the tensile strength of the FRP as follows:

$$\Delta\sigma_{f,\max}^{(3)} = f_{fd} - \sigma_{fd} \qquad (8.2.20)$$

The design tensile strength f_{fd} is given by the equation:

$$f_{fd} = \frac{f_{fk}}{\gamma_f}\frac{\varepsilon_{fue}}{\varepsilon_{fum}} \qquad (8.2.21)$$

The value of the FRP material safety factor γ_f is suggested equal to 1.20 for the application of prefab carbon FRP reinforcement under normal quality control conditions. It is mainly based on the observed differences in the long-term behaviour of FRP (basically depending on the type of fibres), as well as on the influence of the application method (as the Italian CNR suggests). The ratio $\varepsilon_{fue}/\varepsilon_{fum}$ takes into account the difference between the effective ultimate FRP strain ε_{fue} expected in-situ and the mean strain ε_{fum} obtained through uniaxial tensile testing, and also the possible variations accounted for in the FRP material safety factor γ_f; it is normally takes equal to 1.

However, in the Fib Bulletin not all the details of the procedure are given, and the original publication is a doctoral thesis not easily available to the wide community. In particular, the maximum admissible increase in the tensile stress in the FRP between two cracks depends on the smaller of the initial values of the FRP stress on either of the adjacent cracked sections, as well as on three coefficients (c_1, c_3, c_4) which are not clearly given in document.

In absence of further data, the values suggested for the five factors are 0.23, 0.185 and 0.285, respectively.

Furthermore, the methods is quite sensitive to the input parameters as beyond the load value corresponding to yielding in the tensile steel bars, the composite is the only element that takes all the additional tensile stresses.
Anyway, the Fib Bulletin suggests simplified bond tests for calibrating the proposed factors by means of a linear regression analysis. The three equations reported in the follows are furnished by the code in order to define the parameters once the basic bond stress-slip relationship has been carried out:

$$\tau_0 = \frac{c_4}{\gamma_c}\sqrt{f_{ck} f_{ctm}} \text{ , maximum bond stress} \qquad (8.2.22)$$

$$s_c = c_3 = \frac{c_1^2}{c_4} \text{, slip where debonding occurs} \qquad (8.2.23)$$

$$G_c = \tfrac{1}{2}\tau_0 s_c = \tfrac{1}{2}\frac{c_1^2}{\gamma_c}\sqrt{f_{ck} f_{ctm}} \text{ , fracture energy} \qquad (8.2.24)$$

Anyway, they are subject to further study and may change in the future when more test data will become available.
In the follows the approach II of the Fib Bulletin will be applied to the reinforced beam B3-B4, considering for the factors c_1, c_3 and c_4 the values suggested by the Fib and those deduced by the experimental-numerical comparisons. They are reported in Table 8.2.1 with the corresponding interface laws.

Table 8.2.1. Interface law and respective numerical factors suggested by the Fib Bulletin and deduced by the experimental-numerical comparisons, for reinforced beam B3-B4.

	τ_0 [N/mm]	S_C [mm]	G_C [N]	C_1	C_3	C_4
Coefficients come out by the experimental-numerical comparisons	5.0	0.34	0.85	0.70	0.34	1.46
Coefficients suggested by Fib Bulletin	0.97	0.185	0.090	0.23	0.185	0.285

In Figure 8.2.10 the curves which represent the relationships between the maximum stress variation of the FRP between two consecutive cracks ($\Delta\sigma_{f,max}$) and the minimum tensile stress in the FRP on the considered cracks (σ_{fd}) is reported for the beam B3-B4, using for the three parameters (c_1, c_3 and c_4) the values both suggested by the Fib Bulletin and deduced by the experimental-numerical comparisons. In Figure 8.2.11 the bending moment diagrams i analytical and experimental failure loads, with the corresponding safe factors, are reported.

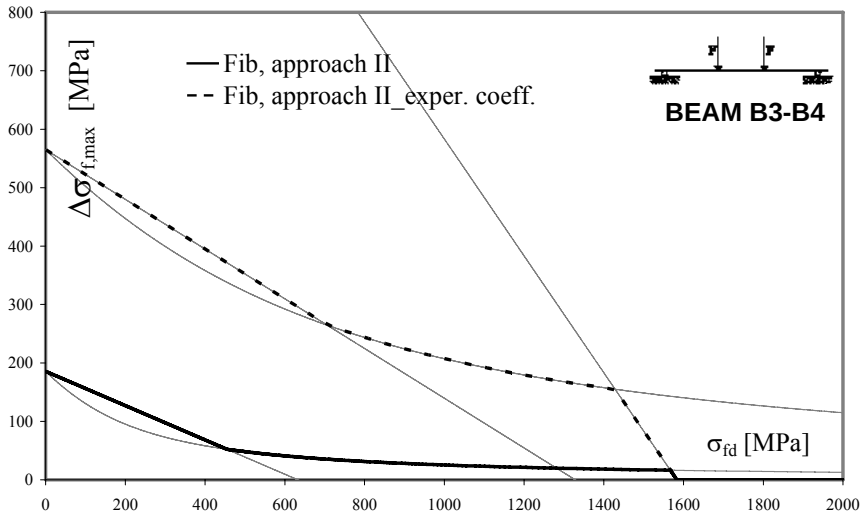

Figure 8.2.10: Diagrams of the maximum possible increase in tensile stress between two subsequent cracks obtained by considering the coefficients suggested by Fib and those evaluated experimentally

In Figures 8.2.12 and 8.2.13 the stresses and the admissible increasing in tensile stress in the composite are reported considering the values suggested by the Fib and those experimentally evaluated, respectively.

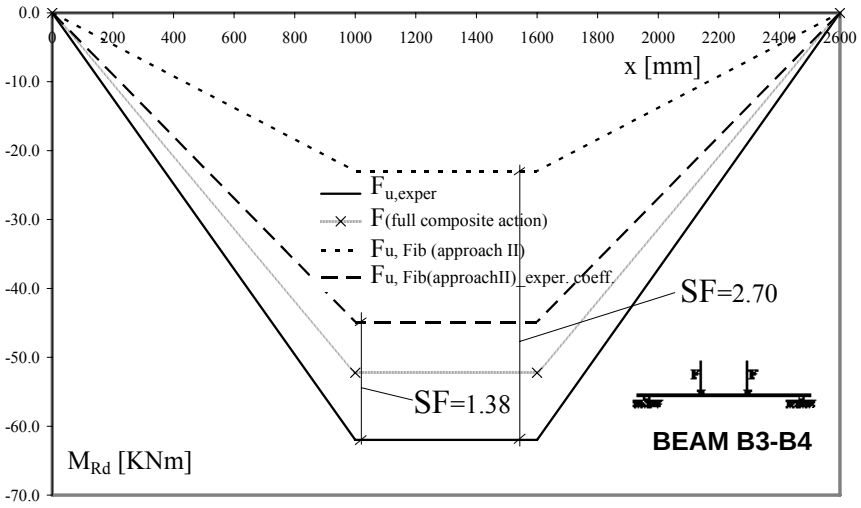

Figure 8.2.11: Bending-moment diagrams corresponding to failure and Safe Factor for the reinforced beam B3-B4, evaluated in accordance with the approach II of Fib Bulletin 14, considering the coefficients suggested by Fib and those evaluated experimentally

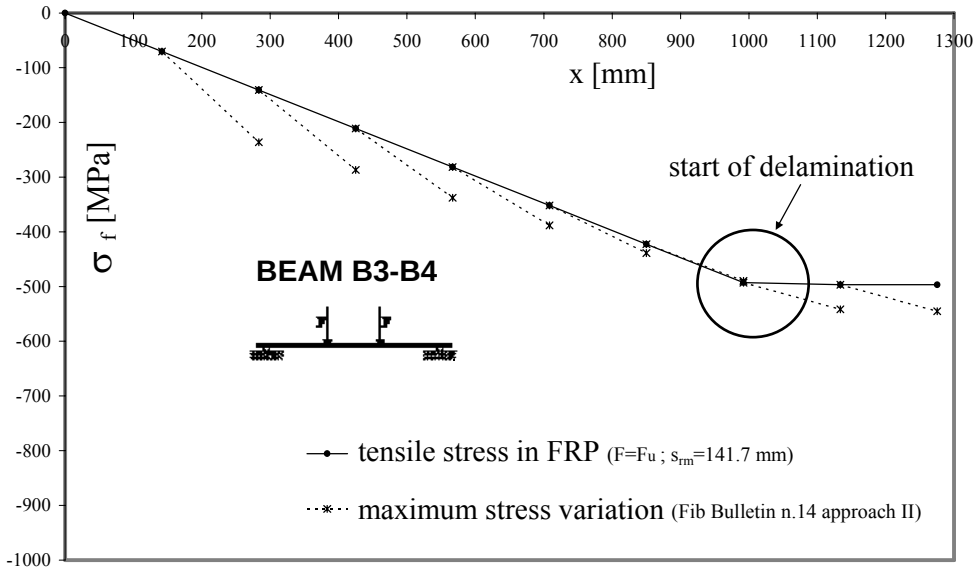

Figure 8.2.12: Diagrams of the maximum possible increase in tensile stress (Fib Bulletin 14) and tensile stress in the FRP reinforcement along the beam B3-B4

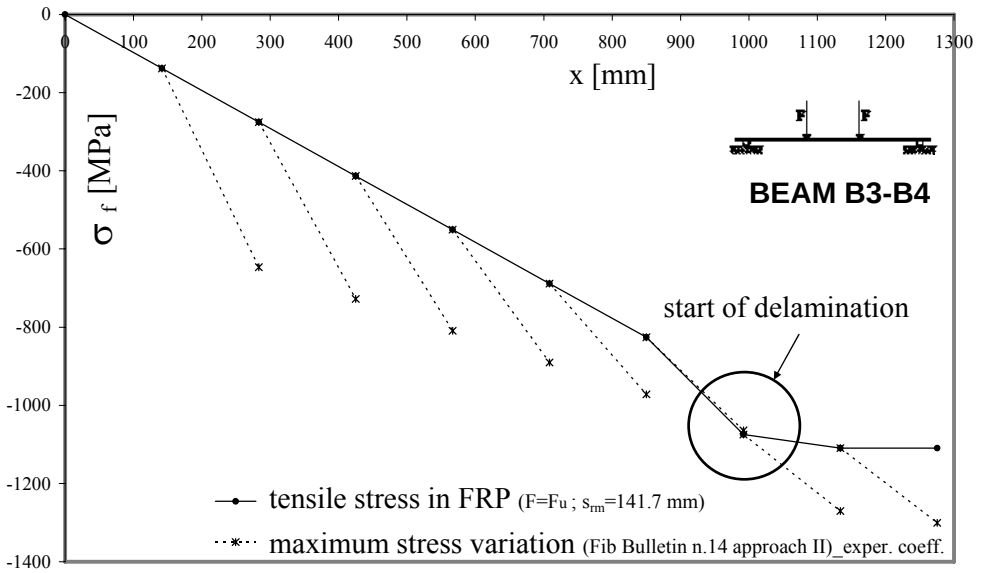

Figure 8.2.13: Diagrams of the maximum possible increase in tensile stress (Fib Bulletin 14) and tensile stress in the FRP reinforcement along the beam B3-B4

In either cases the analyses reveals that the critical zone in which debonding first is triggered is that under the applied force. This is confirmed also by the JSCE procedure and by the evolution of the stress profiles obtained by the numerical analyses, discussed in the previous section.

The role of the crack spacing on the safe factor (SF) is not discussed in detail in the code. The closed-form expressions provided by the Fib Bulletin can be used to evaluate the trend of the a-dimensionless strength $\Delta\sigma_{f,max}/\sigma_{fu}$ when the cracks spacing varies considering several values of the minimum stress on the cracks (σ_{fd}) (see Figures 8.2.14 and 8.2.15).

It can be observed that the strength decreases when the cracks spacing increases, and such decreasing is as much strong as the tensile stress in the FRP on cracks is large. This leads to the observation that the adherence checks are generally as much conservative as the cracks spacing is large.

In the same figures the maximum stress variation assumed by the Japanese recommendations is also reported, considering the same basic bond stress-slip relationship, and hence the same fracture energy. It is constant when the

stress level in the lamina changes, and corresponds to the value considering a tensile stress equal to zero. Hence, it underlines that the values of the fracture energy provided by the approach II of the Fib Bulletin are significantly smaller than those suggested by the JSCE recommendations.
For this reason, as a possible choice, one could consider the maximum cracks spacing which can occur when a RC beam is not externally reinforced, in accordance with the indications provided by the CEB Manual on Cracking and Deformations [1985]. Such choice is justified by the fact that, in the practical applications, the RC element is already cracked when it is externally reinforced.

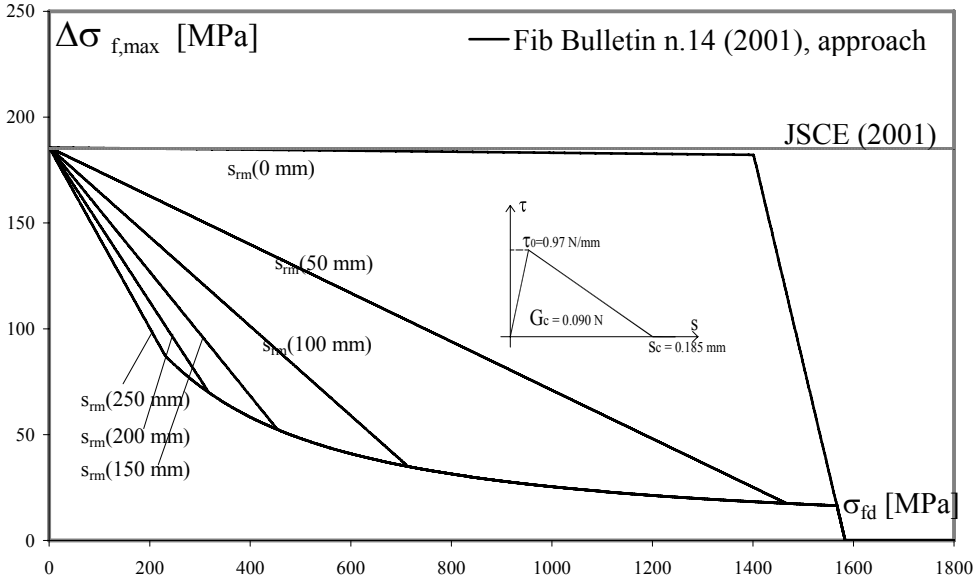

Figure 8.2.14: Diagrams of the maximum possible increase in tensile stress between two subsequent cracks obtained considering different values for cracks spacing

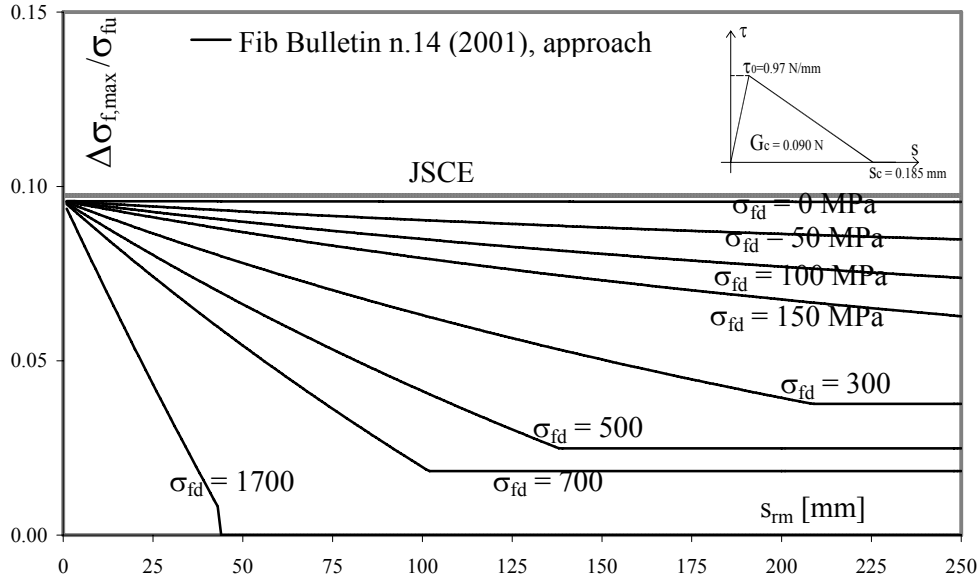

Figure 8.2.15: Diagrams of the a-dimensional tensile strength vs. cracks spacing obtained considering different values for minimum tensile stress in the FRP

8.2.4.3 Approach III

This approach comprises two steps. The first involves verification of the end anchorage, as prescribed by Japanese recommendations. In the second step it should be verified that the shear stress τ_{bc} at the FRP-concrete interface, resulting from the change of tensile force along the FRP, is limited [Matthys, 2000]. Considering two cross sections at distance Δx, subjected to moments M_d and $M_d+\Delta M_d$, τ_{bc} is equals to:

$$\tau_{bc} = \frac{\Delta N_{fd}}{b_f \Delta x} \tag{8.2.25}$$

where ΔN_{fd} is the change in FRP axial force between the two sections. For the verification of the Ultimate Limit State the shear stress τ_{bc} should be restricted to the design bond shear strength, which is equal (in most practical cases) to the bond shear strength of concrete, f_{cbd}. Adopting the Mohr-

Coulomb failure criterion in the case of zero normal stress, the bond strength equals about *1.8* times the tensile strength, that is:

$$f_{cbd} = 1.8\frac{f_{ctk}}{\gamma_c} \tag{8.2.26}$$

Eq. (8.2.25) can be simplified considering that $N_{rd}=M_d/z_m$ and $N_{rd}=N_{fd}+N_{sd}$. Assuming that $\varepsilon_{sl}/\varepsilon_f \approx 1$, with $\Delta M_d/\Delta x \approx V_d$ (design shear force) and $z_m = (z_s+z_f)/2 \approx 0.95d$, this gives the following conditions:

$$\tau_{bc} = \begin{cases} \dfrac{V_d}{0.95\cdot d\cdot b_f\left(1+\dfrac{A_{sl}E_s}{A_fE_f}\right)} & \varepsilon_{sl} < \varepsilon_{yd} \\ \dfrac{V_d}{0.95\cdot d\cdot b_f} & \varepsilon_{sl} \geq \varepsilon_{yd} \end{cases} \tag{8.2.27}$$

where τ_{bc} is influenced by the area of longitudinal bars A_{sl} only if the steel of longitudinal bars is yielded ($\varepsilon_{sl} < \varepsilon_{yd}$).

In Figures (8.2.16) and (8.2.17) the bending moment and the shear stresses along the beams induced by analytical and experimental failure loads are reported, respectively. The corresponding safe factor is also indicated in the figures.

In conclusion, the second and third procedures provided by the Fib Bulletin 14 coincide as the spacing of flexural cracks tends to zero. In fact, Figure 8.2.15 shows how the curves in the plane ($\Delta\sigma_{f,max}/\sigma_{fu}$, s_{rm}) are directed to the same point as s_{rm} tends to zero. This value can be evaluated from the equilibrium condition of an infinitesimal portion of a lamina in the horizontal direction; it is equal to the ratio between the maximum stress τ_{max} and the thickness of the FRP lamina t_f. According to this consideration, the procedure suggested by the approach II is equivalent to a local check of the tangential stresses (approach III) as s_{rm} tends to zero. Even though, from the practical point of view, the equivalence is not valid because the value assumed by approach II (τ_{max}) is different from f_{cbd} assumed in approach III.

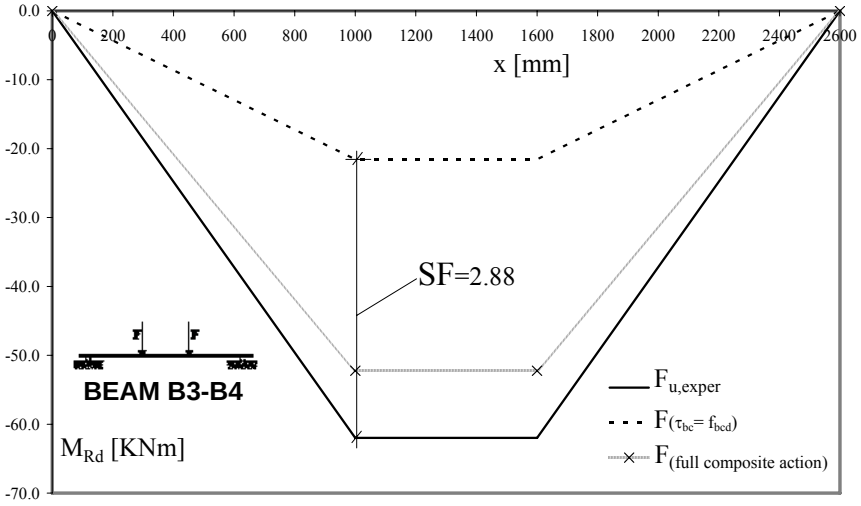

Figure 8.2.16: Bending moment diagrams corresponding to failure and Safe Factor for the reinforced beam B3-B4, evaluated in accordance with approach III of Fib Bulletin 14

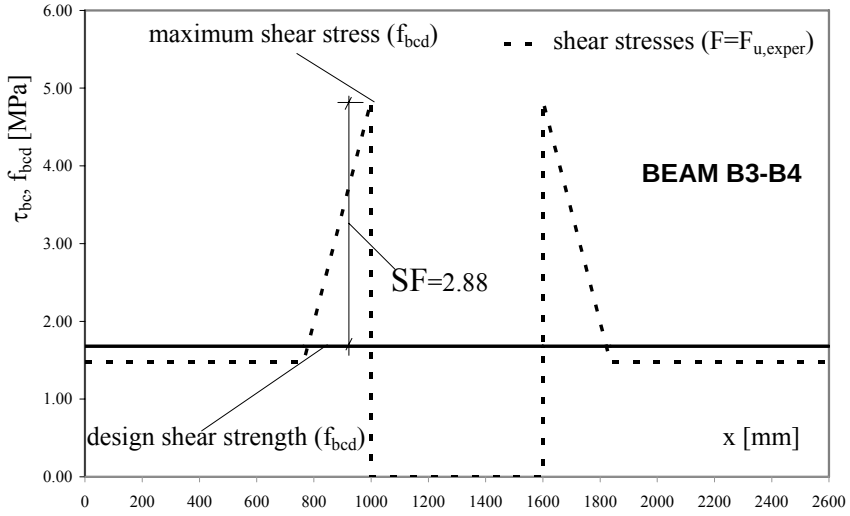

Figure 8.2.17: Shear stresses at concrete/FRP interface along the reinforced beam B3-B4

In Table 8.2.2 all the analytical results obtained from this brief outline of the code provisions are summarized for only the reinforced beam B3-B4: the

mid-span debonding failure loads (F_u) and the corresponding stresses in the composite (σ_{fu}) are reported in the table in order to prove the discrepancies in term of safe factor (SF) between the analytical estimation and the experimental value of failure load.
Furthermore, the failure load evaluated under the assumption of full composite action and in also reported for the beam B3-B4. As shown in the table, in the case of full composite action, the stress in the composite is less than $\sigma_{f,max}$ which is given by the manufacturing industry equal to 1900 MPa.

Table 8.2.2. Mid-span delamination failure loads and safe factors evaluated in accordance with Code provisions for reinforced beam B3-B4.

BEAM	F_u [KN]	σ_{fu} [MPa]	S.F.
Full composite action	52.2	1235	1.19
Fib Approach I (ε_f<0.0065)	52.2	1235	1.19
Fib Approach I (ε_f<0.0085)	52.2	1235	1.19
Fib Approach II (c_1=0.23; c_3=0.185; c_4=0.285)	23.0	493	2.70
Fib Approach II (c_1=0.70; c_3=0.34; c_4=1.46)	44.9	1075	1.38
Fib Approach III	21.5	508	2.88
CNR (G_c^{CNR}=0.23)	37.6	737	1.65
CNR (G_c^{exper}=0.85)	56.0	1423	1.11
JSCE	43.6	840	1.26
ACI 440	36.5	713	1.70

CONCLUSIVE REMARKS

The use finite-element models with preset localized cracks in association with an appropriate stress-slip model for FRP reinforcement proved to be the most effective strategy for the study of typical failure mode of RC beams retrofitted with FRP as the mid-span debonding, which is associated with the mechanisms of force transfer between concrete and FRP.

In fact, such beams are structures highly sensitive to cracking of concrete. A discrete crack model should be used to predict the local stress concentrations in the FRP/concrete interface at crack mouths and consequently the correct mechanism of debonding between the two materials.

Two-dimensional nonlinear finite-element models of RC beams retrofitted with FRP in flexure have been implemented and analysed in the finite-element program ABAQUS. The damaged elastic-plastic behaviour for concrete has been modelled by means of the Lubliner et al. criterion modified by Lee and Fenves, while crack configuration before the application of FRP strips has been explicitly introduced in the finite-element model. Furthermore, suitably specialized cohesive-zone interface laws have been considered for modelling bond-slip between concrete and the reinforcing steel bars as well as debonding between concrete and FRP.

The proposed nonlinear numerical models beams is capable of capturing many important aspects of the behaviour of these structural systems, up to failure. The agreement with the experimental results reported in this work is excellent both for beams with no FRP reinforcement, and for the reinforced beams. In particular, the mid-span debonding failure can be well predicted by the models. The computational cost and the convergence problems of the numerical analysis are to be taken into account when studying complex phenomena like the mid-span debonding failure due to stress concentration in correspondence of discrete cracks, for which the use of a refined finite-element model with damaged non-linear constitutive laws represent the best choice. The explicit analysis performs better then the iterative procedures (i.e., Newton-Raphson and Arc-length method) even for pseudo-static analyses, provided to well define the time period of the analysis and the

bulk viscosity in order to either avoid an excessive computational cost or control the high frequency of oscillation, respectively.

From the comparisons of numerical and experimental results with analytical ones obtained by considering the formulations available in the main codes of practice, it is interesting to underlined that, among all methods, Niedermeier's approach (Fib Bulletin 14 approaches II) appears to have the soundest theoretical bases, and provides a unified treatment of mid-span debonding and end-peeling failure modes, as the procedure can be applied along the entire beam span. In particular, it is also able to predict the exact location where debonding first is triggered, which is also confirmed by the numerical results.

Other simplified methods proposed in most codes of practice (i.e., ACI 440, CNR DT-200, Fib Bulletin 14 approaches I and III) to evaluate mid-span debonding failure load are based on the limitation on the stress or on the strain in the composite, and therefore give only a crude approximation of the failure load for mid-span delamination. Such simple methods do not always furnish the most conservative estimation of failure load with respect to more sophisticated ones.

Moreover, this work has underlined some issues which need to be investigating in the future. In particular, the important influence of the crack pattern in concrete, especially for the prediction of the FRP debonding, suggests that a higher degree of accuracy may be obtained by modelling the initiation and propagation of cracks.

Other possible enhancements will include the introduction of friction along the crack faces, especially of inclined cracks related to shear, even though it should not alter the ultimate behaviour of a reinforced RC beams close to failure. Furthermore, the development of full 3D models could lead to understand the influence of FRP width.

The outcomes of an experimental activity conducted previously has been presented in this dissertation; they represents an useful tool which is available in the future for the scientific community in order to validate the analytical and numerical results. The promising results presented in this dissertation will stimulate the development of other experimental and numerical activities.

REFERENCES

ABAQUS Theory Manual, Version 6.7, SIMULIA Program.

ABAQUS Analysis User's Manual, Version 6.7, SIMULIA Program.

ACI 318-05, *Building Code Requirements for Structural Concrete and Commentary*. American Concrete Institute (ACI) Committee 318-05, 2005.

ACI 440 2R-08 "*Guide for the Design and Construction of Externally Bonded FRP Systems for Strengthening Concrete Structures*". American Concrete Institute (ACI) Committee 440. 2R-08, 2008.

Alfano G. & Crisfield M.A.: "Finite element interface models for the delamination analysis of laminated composites: mechanical and computational issue". *International Journal for Numerical Methods in Engineering*. 50 (7): 1701-1736, 2001.

Alfano G. & Rosati L.: "Analysis of the interface debonding through a damage/visco-plastic cohesive-zone model". *Proceeding of the 7th International Conference on Computational Plasticity* (*COMPLAS*), Barcelona, 2003.

Alfano G. & Sacco E.: "Combing interface damage and friction in a cohesive-zone model". *International Journal for Numerical Methods in Engineering*. 168, 542-582, 2006

Allix O., Ladveze P. & Corigliano A.. "Damage analysis of interlaminar fracture specimens". *Composite Structures*. 31(1): 61-74, 1995.

Allix O. & Corigliano A.: "Modelling and simulation of crack propagation in mixed-modes interlaminar fracture specimens". *International Journal of Fracture*. 77: 111-140, 1996.

Allix O. & Corigliano A.: “Geometrical and interfacial non-linearities in the analysis of delamination in composites”. *International Journal of Solids and Structures*. 36(15): 2189-2216, 1999.

Babu R.R., Benipal G.S. & Singh A.K.: “Constitutive modelling of concrete an overview”. *Asian Journal of Civil Engineering* (*Building and Housing*). 6(4): 211-246, 2005.

Barrenblatt G.I.: “Mathematical theory of equilibrium cracks in brittle failure”. *Advances in Applied Mechanic*. No. 7, 1962.

Bazant Z.P. & Oh B.H.: “Crack band theory for fracture concrete”. *Materials and Structures*. RILEM, Paris, 16: 155-176, 1983.

Bedard C. & Kotsovos M.D.: “Fracture process of concrete for NLFEA methods”, *Journal of Structural Engineering - ASCE*. 112(3): 573-587, 1986.

Belarbi H. & Hsu T.C.C.: “Constitutive laws of concrete in tension and reinforcing bars stiffened by concrete”. *ACI Structural Journal*. 91(4): 465-474, 1994.

Benzeggagh M.L. & Kenane M. “Measurement of mixed mode delamination fracture toughness of unidirectional Glass/Epoxy Composites with mixed-mode bending apparatus ”. *Composite Science and Technology*. 56: 439-449, 1996.

Bizindavyi L.: “Étude expérimentale et analytique du comportement de l’interface entre les structures en béton armé et les plaques de renfort externe en polymères renforcés de fibres”. Ph.D. Thesis, Université de Sherbrooke, France, 1999.

Bolzon G. & Corigliano A.: “A discrete formulation for elastic solids with damaging interfaces”. *Computer Methods in Applied Mechanics and Engineering*. 140: 329-359, 1997.

Brosens K. & Van Gemert D.: "Anchoring stresses between concrete and carbon fibre reinforced laminates". Non-Metallic (FRP) reinforcement for Concrete Structures, *Proceedings of the 3rd International Symposium*, Sapporo, Japan, 1997.

Brosens K. & Van Gemert D.: "Plate end shear design for external CFRP laminate ". *Proceedings of FRAMCOS-3*, Gifu, Japan, 1998.

Bronsen K. & Van Gemert D.: "Anchorage of externally bonded reinforcements subjected to combined shear/bending action". *CICE 2001, International Conference on FRP Composites in Civil Engineering*, Hong Kong, 2001.

Buyukozturk O. & Hearing B.: "Failure behaviour of pre-cracked concrete beams retrofitted with FRP". *Journal of Composites for Construction – ASCE*. 2(3): 138-144, 1998.

Camanho P.P, Davila C.G & Ambur D.R.: "Numerical simulation of delamination growth in composite material". NASA-TP-211041, 2001.

Camanho P.P. & Davila C.G.:" Mixed-mode decohesion finite elements for the simulation of delamination in composite material". NASA-TM-2002-211737: 1-37, 2002.

CEB. "*Design Manual on Cracking and Deformations*". Comitè Euro-International du Bèton, 1985.

CEB-FIB (1993). "*CEB-FIP Model Code 1990 - Design Code*" Thomas Telford, Lausanne, Switzerland.1990.

Chaboche J.L., Girard R. & Schaff A.: "Numerical analysis of composite systems by using interphase/interface models". *Computational Mechanics*. 20: 3-11, 1997.

Chajes M.J., Finch W.W., Januszka T.F. & Thomson T.A.: “Bond and Force Transfer of Composite-Material Plates Adhered to Concrete“. *ACI Structural Journal*. 93 (2): 208-217, 1996.

Champaney L. & Valoroso N.: “Evaluation of interface models for the analysis of non-linear behaviour of adhesively bonded joints”. *Proceedings of the European Conference on Computational Mechanics ECCM-2001*, Cracow, Poland, 2001.

Chandra N., Li H., Shet C. & Ghonem H.: ”Some issues in the application of cohesive zone models for metal-ceramic interfaces”. *International Journal of Solids and Structures*. 39(10): 2827-2855, 2002.

Chang G.A. & Mander J.B.: ”Seismic energy based fatigue damage analysis of bridge columns: Part I - evaluation of seismic capacity”. NCEER Technical Report No. NCEER-94-0006. State University of New York, Buffalo, New York, 1994.

Chen W.F. & Saleeb A.F.: “Constitutive equations for engineering materials” Wiley, New York, U.S., 1992.

Chen J., Crisfield M.A., Kinloch J., Busso E.P., Matthews F.L. & Qiu Y.: “Predicting progressive delamination of composite materials speciments via interface elements”. *Mechanics of Composite Materials and Structures*. 6: 301-317, 1999.

Chen, W.F. & Han D.J.: “Plasticity for structural engineers.” Springer-Verlag, New York, U.S., 1988.

Chen J.F. & Teng J.G.: “Anchorage Strength Models for FRP and Plates Bonded to Concrete”. *Journal of Structural Engineering - ASCE*. 127(7): 784-791, 2001.

Ciampi V., Eligehausen R., Bertero V.V. & Popov E.P.: “Analytical model for concrete anchorages of reinforcing bars under generalized excitations”,

Report No. UCB/EERC 82-83, University of California, Berkeley, US, 1982.

Collins P.M. & Mitchell D.: ”Prestressed concrete structures”. Prentice Hall. Upper Saddle River, New Jersey, 1991.

CNR DT-200: “*Istruzioni per la progettazione, l’esecuzione e il controllo di interventi di consolidamento statico mediante l’utilizzo di compositi fibrorinforzati*”. Consiglio nazionale delle ricerche (CNR), Rome, 2004.

Corigliano A.: “Formulation, identification and use of interface models in the numerical analysis of composite delamination”. *International Journal of Solids and Structures*. 30(20): 2779-2811, 1993.

Corigliano A. & Ricci M.: ”Rate-dependent interface models: formulation and numerical applications”. *International Journal of Solids and Structures*. 38(4): 547-576, 2001.

Cruz J.S., Barros J. & Azevedo A.: “Elasto-plastic multi-fixed smeared crack model for concrete”. Report 2004.

Cui W., Wisnom M.R. & Jones M.: “A Comparison of Failure Criteria to Predict Delamination of Unidirectional Glass/Epoxy Specimens Waisted Through the Thickness”. *Composites*. 23(3): 159-166, 1992.

Dai J., Ueda T. & Sato Y.: “Unified analytical Approaches for determining Shear Bond characteristics of FRP-concrete Interface through Pullout Tests”. *Journal of Advanced Concrete Technology*. 4(1): 133-145, 2005.

Davila C.G., Camanho P.P. & Moura M.F.: “Mixed-Mode Decohesion Elements for Analyses with Progressive Delamination”. *42nd AIAA/ASME/ASCE/AHS/ASC Structures, Structural Dynamics and Materials Conference*, Seattle, Washington, USA, 2001.

"*Design guidance for strengthening concrete structures using fiber composite materials*". Technical Report TR-55. Concrete society, Berkshire, UK, 2000.

DIN 1048 (Deutches Institut für Normung), *Ausgabe 6.91, Teil 2, Prüfverfahren für Beton, Festbeton in Baumwerken und Bauteilen*, Beuth Verlag, Berlin, Germany, 1991.

Dugdale D.S.: "Yielding of steel sheets containing Slits". *Journal of Mechanics and Physics of Solids*. 8:100-104,1960.

Etse G. & Willam R.L.: "Fracture energy formulation for inelastic behaviour of plain concrete". *International Journal for Numerical Methods in Engineering*. 120(9): 1983-2011, 1994.

Eurocode 2 - Part 1: "*Design of concrete structures*: *general rules and rules for building*". European Committee for Standardization (CEN), ENV 1998-3.

Faella C., Martinelli E., Nigro E., Salerno N., Sabatino M. & Mantegazza G.: "Aderenza tra calcestruzzo e fogli di FRP utilizzati come placcaggio di elementi inflessi - Parte prima: risultati sperimentali" (in Italian). *Proceedings of the XIV C.T.E. Conference*, Mantua, Italy, 2002.

Faella C., Martinelli E. & Nigro E.: "Interface Behaviour in FRP Plates Bonded to Concrete: Experimental Tests and Theoretical Analyses". *ECI2003, Conference on Advanced Materials for Construction of Bridges, Buildings and Other Structures III*, Davos, Switzerland, 2003.

Fib: Bulletin d'information n. 14: "*Externally bonded FRP reinforcement for RC structures*". July, 2001.

Flanning P.J. & Kelly O.: "Smeared Crack Models of RC Beams with Externally Bonded CFRP Plates". *Computational Mechanics*. 26(4): 325-332, 2000.

Guo Z.G., Cao S.Y., Sun W.M. & Lin X.Y.: "Experimental study on bond stress-slip behaviour between FRP sheets and Concrete". *Proceedings of the International Symposium on Bond Behaviour of FRP in Structures, 2005.*

Hoek E. & Brown E.T.: "Empirical strength criterion for rock masses". *Journal of the Geotechnical Engineering Division*. 106(9): 1013-1035, 1980.

Holzenkämpfer O. "*Ingenieurmodelle des Verbundes geklebter Bewehrung für Betonbauteile*", Dissertation. TU Braunschweig, 1994.

Horigucki T. & Saeki N.: "Effect of Test Methods and Quality of Concrete on Bond Strength of CFRP Sheet". *Proceedings of the 3rd International Symposium on Non-Metallic (FRP) Reinforcement for Concrete Structures*, Sapporo, Japan, 1997.

Horigucki T. & Wu Z.: "Analysis of debonding fracture properties of CFS strengthened member subject to tension". *Proceedings of the 3rd International Symposium on Non-Metallic (FRP) reinforcement for Concrete structures*, Sapporo, Japan, 1997.

Hsu. T.T.C. & Zhang.: "Tension stiffening in reinforced concrete membrane elements". *ACI Structural Journal*. 93(1): 108-115, 1996.

Hsu T.T.C. & Zhu R.R.H.: "Softened membrane model for reinforced concrete elements in shear". *ACI Structural Journal*. 99(4): 460-469, 2002.

Hughes T.J.R. & Winget J.: "Finite rotation effects in Numerical Integration of Rate Constitutive Equations Arising in Large-Deformation Analysis". *International Journal for Numerical Methods in Engineering*. Vol. 15, 1962.

Yang Z.J., Chen J.F. & Proverbs D.: "Finite Element Modelling of Concrete Cover Separation Failure in FRP Plated RC Beams". *Construction and Building Materials*. 17(1): 3-13, 2003.

Yang J., Teng J.G. & Chen J.F.: "Interfacial stresses in soffit-plated reinforced concrete beams". *Proceedings of ICE - Structures and Buildings*, 157(3): 77-89, 2004.

Yang Q.S., Peng X.R. & Kwan A.K.H.: "Finite Element Analysis of Interfacial Stresses in FRP-RC Hybrid Beams". *Mechanics Research Communications*. 31(3): 331-340, 2004.

Yao J., Teng J.G. & Chen J.F.: "Experimental study on FRP-to-concrete bonded joints". *Composites - PartB*: *engineering*. Vol. 36, 2005.

Yassin M.H.M.: "*Non-linear analysis of prestressed concrete structures under monotonic and cyclic loads*". Dissertation. University of California, Berkeley, California, 1994.

Yuan H., Teng J.G., Seracino R., Wu Z.S. & Yao J.: "Full-range behaviour of FRP-to-concrete bonded joints". *Engineering Structures*. 26(5): 553-564, 2004.

Yuan H. & Wu Z. "Interfacial fracture theory in structures strengthened with composite of continuous fiber". *Proceedings of symposium of China and Japan, Science and technology of 21st Century*. Tokyo, Japan, 1999.

Yuan H., Wu Z.S. & Yoshizawa H.: "Theoretical solutions on interfacial stress transfer of externally bonded steel/composite laminates". *Journal of Structural Mechanics Earthquake Engineering - JSCE*. No. 675/1-55: 27-39, 2001.

Jirasek M. & Bazant Z.P.: "Inelastic Analysis of Structures". John Wiley & Sons, UK, 2002.

Jirasek M. & Zimmermann T.: "Embedded crack model: Basic formulation" *International Journal for Numerical Methods in Engineering*. 50: 1269-1290, 2001.

Jones R., Swamy R.N. & Charif A.: "Plate Separation and Anchorage of Reinforced Concrete Beams Strengthened by Epoxy-bonded Steel Plates". *The Structural Engineer*, 66 (5): 85-94, 1988.

JSCE: *"Recommendations for upgrading of concrete structures with use of continuous fiber sheets"*. Concrete Engineering Series 41, 2001.

Kent D.C. & Park R.: "Flexural members with confined concrete". *Journal of Structural Division - ASCE*. 97: 1969-1990, 1971.

Kotsovos M.D. & Newman J.B. "Generalized stress-strain relation for concrete". *Journal of Engineering and Mechanics - ASCE*. 104: 845-856, 1977.

Kotsovos M.D. "Fracture processes of concrete under generalised stress states". *Materials and Structures*. 12(6): 431-437, 1979.

Kupfer H., Hilsdorf H.K. & Rush H.: "Behaviour of concrete under biaxial stresses". *ACI Journal*. 66: 656-666, 1969.

Lee J. & Fenves G.L.: "Plastic-damage model for cyclic loading of concrete structures". *Journal of Engineering Mechanics*. 124(8): 892-900, 1998.

Li V.C. & Ward R.J.: "A novel testing technique for post-peak tensile behaviours of cementitius material". *Fracture Toughness and Fracture Energy*. Balkema, 1989.

Lorenzis L., De L., Miller B. & Nanni A.: "Bond of Fiber-Reinforced polymer laminate to concrete ". *ACI Material Journal*. 3: 279-286, 2001.

Lu X.Z., Ye L.P., Teng J.G. & Jiang J.J.: "Meso-scale finite element model for FRP sheets/plates bonded to concrete". *Engineering Structures*. 27(4): 564-575, 2005.

Lu X.Z., Teng J.G. & Jiang J.J.: "Bond-slip models for FRP sheets/plates bonded to concrete". *Engineering Structures*. 27(6): 920-937, 2005.

Lubliner J., Oliver J., Oller S. & Oñate E.: ”A plastic damage model for concrete”. *International Journal of Solids and Structures*. 25: 229-326, 1989.

Maeda T., Asano Y., Sato Y., Ueda T. & Kakuta Y. “A study on debond mechanism of carbon fiber sheet”. *Non-Metallic (FRP) reinforcement for Concrete structures, Proceedings of the 3rd International Symposium,* Sapporo, Japan, 1997.

Malek A.M., Saadatmanesh H. & Ehsani M.R.: “Prediction of failure load of R/C beams strengthened with FRP plate due to stress concentration at the plate end”. *ACI Structural Journal*. 95(2): 140-152, 1998.

Mander J.B., Priestley M. J. N. & Park R.: ”Theoretical stress-strain model for confined concrete”. *Journal of Structural Engineering - ASCE*. 114(8): 1804-1826, 1988a.

Mander J.B., Priestley M. J. N. & Park R.: “Observed stress-strain model of confined concrete”. *Journal of Structural Engineering - ASCE*. 114(8): 1827-1849, 1988b.

Mansour M., Lee J. & Hsu T.T.C. : “Cyclic stress-strain curves of concrete and steel bars in membrane elements”. *Journal of Structural Engineering - ASCE*. 127(12): 1402-1411, 2001.

Matthys S., Taerwe L. & Audenaert K.: ”Tests on axially loaded concrete columns confined by FRP sheet wrapping”. *Proceedings of the 4th International Symposium on FRP for Reinforced Concrete Structures,* Baltimore, USA, 1999.

Menetrey P. & William K.: “Triaxial failue criterion and its generalization” *ACI Structural Journal*. 92(3): 311-317, 1995.

Mi Y., Crisfield M.A., Davies G.A.O. & Hellweg H.B.: “Progressive delamination using interface elements”. *Journal of Composite Material*. 32: 1246-1272, 1998.

Möes N. & Belytschko T.: "Extended finite element method for cohesive crack growth". *Engineering Fracture Mechanics*. 69: 813-833, 2002.

Nakaba K., Kanakubo T., Furuta T. & Yoshizawa H.: "Bond behaviour between Fiber-Reinforced Polymer Laminates and Concrete". *ACI Structural Journal*. 98, 2001.

Needlemann A.: "An analysis of tensile decohesion along an interface". *Journal of the Mechanics and Physics of Solids*. 38(3): 289-324, 1990.

Neubauer U. & Rostasy F.S.: "Bond Behaviour of CFRP-Laminates for the Strengthening of Concrete Members". *Proceedings of Composite Construction - Conventional and Innovative*. Innsbruck, Austria, 1997a.

Neubauer U. & Rostasy F.S.: "Design aspects of concrete structures strengthened with externally bonded CFRP plates". *Proceedings of the 7th International Conference on Structural Faults and Repairs*. Edinburgh, UK, 1997b.

Niedermeier R.: "Stellungnahme zur Richtlinie für das Verkleben von Betonbauteilen durch Ankleben von Stahllaschen-Entwurf März 1996". *TU München* .1996.

Niedermeier R.: "*Zugkraftdeckung bei klebearnierten bauteilen (Envelope line of tensile forces while using externally bonded reinforcement)*". PhD Dissertation. *TU München*, 2000.

Niu H. & Wu Z.: "Numerical Analysis of Debonding Mechanisms in FRP-strengthened RC Beams". *Computer-Aided Civil and Infrastructure Engineering*. 20(5): 354-368, 2005.

Ngo D. & Scordelis A.C.: "Finite Element Analysis of reinforced concrete Beams". *ACI Journal*. 64(3): 152-163, 1967.

Oliver J., Huespe A.E., Pulido M.D.G., Blanco S. & Linero D.: "Recent advances in computational modelling of material failure". *ECCOMAS 2004*, Jyvskyl, Finland, 2004.

Oliver J., Cervera M., Oller S. & Lubliner J.: "Isotropic Damage Models and Smeared Crack Analysis of Concrete", *Proceedings of the 2nd International Conference on Computer Aided Analysis and Design of Concrete Structures*, Vol. 2, 1991.

Orakcal K., Massone L.M. & Wallace J.W.: "Analytical Modelling of Reinforced Concrete walls for Predicting flexural and coupled-shear-flexural responses". PEER Report 2006/07.

Pang X.D. & Hsu T.T.C.: "Behavior of reinforced concrete membrane elements in shear". *ACI Structural Journal*. 92(6): 665-679, 1995.

Pesic N. & Pilakoutas K.: "Concrete Beams with Externally Bonded Flexural FRP-reinforcement: Analytical Investigation of Debonding Failure". *Composites*: *part B*, 34(4): 327-338, 2003.

Rahimi H. & Hutchinson A.: "Concrete Beams Strengthened with Externally Bonded FRP Plates". *Journal of Composites for Construction - ASCE*, 5(1): 44-56, 2001.

Rasheed H.A. & Pervaiz S.: "Bond-slip analysis for fiber-reinforced polymer-strengthened beams". *Journal of Engineering Mechanics - ASCE*, 128(1): 78-86, 2002.

Rashid Y.R.: "Analysis of prestressed concrete pressure vessels nuclear". *Engineering and Design*, 7(4): 334-344, 1968.

Richart F.E., Brandtzaeg A. & Brown R.L.: "Failure of plain and spirally reinforced concrete in compression". *Bullettin 190*. University of Illinois, Champain, 1929.

Rizkalla S.H. & Hwang L.S.: "Crack prediction for members in uniaxial tension". *ACI Journal*. 81(6): 572-579, 1984.

Roberts T.M.: "Approximate analysis of shear and normal stress concentrations in the adhesive layer of plated RC beams". *The Structural Engineer*. 66(5): 85-94, 1988.

Rosati L. & Valoroso N.: "A Return map algorithm for general isotropic elasto/visco-plastic materials in principal space". *International Journal for Numerical Methods in Engineering*. 60(2): 461-498, 2004.

Santos A.C., Bittencourt T.N. & Gettu R.: "Experimental analysis of interface between CFRP and concrete using cylindrical specimens". *Proceedings of FRPRSC-6*. Singapore, 2003.

Sato Y., Kimura K. & Kobatake Y.: "Bond Behavior between CFRP Sheet and Concrete". *Journal of Structural and Construction Engineering*. 500: 75-82, 1997.

Sato Y., Ueda T., Kakuta Y. & Tanaka T.: "Shear reinforcing effect of carbon fibre sheet attached to side of reinforced concrete beams". *Proceedings of the 2nd International Conference on Advanced Composite Materials in Bridges and Structures*. Quebec, Canada, 1996.

Scott B.D., Park R. & Priestley M.J.N.: "Stress-strain behavior of concrete confined by overlapping hoops at low and high strain rates". *ACI Journal*. 79(1): 13-27, 1982.

Sebastian W.M.: "Significance of mid-span debonding failure in FRP-plated concrete beams". *Journal of Structural Engineering - ASCE*. 127(7): 792-798, 2001.

Simonelli G.: "*Finite-element analysis of RC beams retrofitted with fibre reinforced polymers*". PhD Dissertation. University of Naples "Federico II", 2005.

Smith S.T. & Teng J.G.: "FRP-strengthened RC beams. Part II: assessment of debonding strength models". *Engineering Structures*: 397-427, 2002.

Schellekens J.C.J. & de Borst R.: "A non-linear finite element approach for the analysis of mode-I free edge delamination in composites". *International Journal of Solids and Structures*. 30(9): 1239-1253, 1993.

Täljsten B.: "*Plate Bonding. Strengthening of existing concrete structures with epoxy bonded plates of steel or fibre reinforced plastics*". PhD Dissertation. Lulea University of Tecnology, 1994.

Täljsten B.: "Strengthening of Beam by Plate Bonding". *Journal of Materials in Civil Engineering - ASCE*. 9(4): 206-212, 1997.

Tanaka T.: "*Shear resisting mechanism of reinforced concrete beams with CFS as shear reinforcement*". Graduation Thesis. Hokkaido University, 1996.

Tassios T.P.: "Properties of bond between concrete and steel under load cycles idealizing seismic actions", *Proceedings AICAP-CEB Symposium*, Rome, Italy, 1979.

Tsai W.T.: "Uniaxial compressional stress-strain relation of concrete". *Journal of Structural Engineering - ASCE*. 114(9): 2133-2136, 1988.

Tvergaard V. & Hutchinson J.W.: "The relation between crack growth resistance and fracture process parameters in elastic-plastic solids". *Journal of the Mechanics and Physics of Solids*. 40(6):1377-1397, 1992.

Tvergaard V. & Hutchinson J.W.: "The influence of plasticity on mixed mode interface toughness". *Journal of the Mechanics and Physics of Solids*. 41(6): 1119-1135, 1993.

Ueda T. & Dai J.G.: "New shear Bond model for FRP-Concrete Interface-Form modeling to application". *Proceedings of the 2nd International*

Conference on FRP Composites in Civil Engineering CICE-2004. Adelaide, Australia, 2004.

Van Gemert D. “Force transfer in epoxy-bonded steel-concrete joints”. *International journal of adhesion and* adhesives. 1: 67-72, 1980.

Vecchio F.J. & Collins M.P.. “*The response of reinforced concrete to in-plane shear and normal stresses*”. Publication No. 82-03, Department of Civil Engineering, University of Toronto. Toronto, Canada, 1982.

Vulcano A., Bertero V.V. & Colotti V.: “Analytical modelling of RC structural walls”. Proceedings, 9th World Conference on Earthquake Engineering (6). Tokyo-Kyoto, Japan, 1988.

Wang W. & Li G.:” Experimental study and analysis of RC beams strengthened with CFRP laminates under sustaining load”. International Journal of Solids and Structures, 43 (6): 1372-1387, 2006.

Wells G.N. & Sluys L.J.: ”A new method for modeling cohesive cracks using finite elements”. *International Journal for Numerical Methods in Engineering*. 50(12): 2667-2682, 2001.

Wendel M.S.:” Significance of mid-span debonding failure in FRP-plated concrete beams”. Journal of Structural Engineering - ASCE. 20 (5): 354-368, 2005.

White T.W., Soudki K.A. & Erki M.: “Response of RC Beams Strengthened with CFRP Laminates and Subjected to a High Rate of Loading”. Journal of Composites for Construction - ASCE, 5 (3): 153-162, 2001.

Wight R.G., Green M.F. & Erki M.A.:” Prestressed FRP sheets for post strengthening reinforced concrete beams”. Journal of Composites for Construction - ASCE , 5 (4): 214-220, 2001.

Wu E.M. & Reuter R.C. “Crack extension in Fiberglass reinforced plastic”. T&AM report No.275. University of Illinois. 1965.

Wu Z.S. & Yin J.: ”Fracturing behaviors of FRP-strengthened concrete structures”. *Engineering Fracture Mechanics*. 70(10): 1339-1355, 2003.

Wu Z.S., Yuan H. & Niu H.D.: ”Stress transfer and fracture propagation in different kinds of adhesive joints”. *Journal of Engineering Mechanics - ASCE*. 128(5): 562-573, 2002.